Measurement and Interpretation of Higgs Boson Differential Cross Sections in the Diphoton Decay Channel and Measurement of the Photon Identification Efficiency in the ATLAS Experiment

Dissertation

zur Erlangung des Doktorgrades
an der Fakultät für Mathematik, Informatik und
Naturwissenschaften
Fachbereich Physik
der Universität Hamburg

vorgelegt von
Früd Braren

Hamburg

2020

Gutachter/innen der Dissertation:	Prof. Dr. Kerstin Tackmann Prof. Dr. Peter Schleper
Zusammensetzung der Prüfungskommission:	Prof. Dr. Kerstin Tackmann Prof. Dr. Peter Schleper Prof. Dr. Dieter Horns Prof. Dr. Elisabetta Gallo Dr. Thomas Konstandin
Vorsitzende/r der Prüfungskommission:	Prof. Dr. Dieter Horns
Datum der Disputation:	7. 8. 2020
Vorsitzender Fach-Promotionsausschusses PHYSIK:	Prof. Dr. Günter Sigl
Leiter des Fachbereichs PHYSIK:	Prof. Dr. Wolfgang Hansen
Dekan der Fakultät MIN:	Prof. Dr. Heinrich Graener

Abstract

The properties of the scalar boson that was first found in 2012 by the ATLAS and CMS experiments at the LHC are so far consistent with those of the Higgs boson, predicted by the Standard Model of particle physics. Further investigations of the boson's properties with increased accuracy are of immediate interest, as any deviation from Standard Model predictions could lead the way to a more fundamental theory of nature. The comparison of predicted and measured cross sections, both inclusive and differential, allows important tests of the Standard Model. One of the decay channels of the Higgs boson that is particularly well suited for measurements of Higgs boson production cross sections is the decay into a pair of photons, $H \to \gamma\gamma$.

Based on proton-proton collision data collected with the ATLAS experiment in the data-taking periods in 2015 – 2017 at a center-of-mass energy of $\sqrt{s} = 13\,\text{TeV}$, corresponding to an integrated luminosity of 79.8/fb, inclusive and differential Higgs boson production cross sections are measured in the $H \to \gamma\gamma$ decay channel in a fiducial phase-space volume. The observed fiducial inclusive cross section of Higgs production with the Higgs decaying to a pair of photons corresponds to (60.4 ± 8.6) fb, which is in good agreement with the Standard Model prediction of (63.5 ± 3.3) fb.

The differential cross section in the Higgs boson transverse momentum, p_{T}^{H}, is sensitive to the Yukawa couplings between the Higgs boson and quarks; therefore, limits for these couplings can be set by performing a fit on the observed p_{T}^{H} distribution. In this work, limits are set on the Yukawa couplings between both bottom and charm quarks and the Higgs boson, using ATLAS pp collision data collected in the years 2015 – 2018, corresponding to an integrated luminosity of 139.0/fb. The charm quark Yukawa coupling modifier, $\kappa_c = y_c/y_c^{SM}$, has been constrained to $\kappa_c \in [-19, 25]$ at 95 % CL, while for the bottom quark Yukawa coupling modifier, $\kappa_b = y_b/y_b^{SM}$, the corresponding confidence interval was determined to be $\kappa_b \in [-6, 16]$.

The measurement of photon identification efficiencies and a comparison with efficiencies in simulation are an important input for photon-based analyses of ATLAS data such as the above mentioned measurement of $H \to \gamma\gamma$ cross sections. Using the data recorded in the years 2015 – 2017, corresponding to an integrated luminosity of 79.8/fb, photon identification efficiencies are measured using a method that relies on applying transformations to variables parametrizing the

shape of the electromagnetic showers of electrons and photons. A pure and unbiased sample of electrons to which these transformations are applied is selected with a tag-and-probe method. The transformed electrons are photon-like objects and as such can be used to measure photon identification efficiencies. Depending on the considered region of pseudorapidity and photon transverse momentum, the uncertainties on these efficiencies range from 0.5 % to 3 %.

Zusammenfassung

Das skalare Boson, das im Jahr 2012 vom ATLAS- und CMS-Experiment am LHC entdeckt wurde und dessen Eigenschaften in den Jahren seither mit steigender Präzision vermessen wurden, entspricht bislang innerhalb der Messgenauigkeiten den Erwartungen für das Higgs-Boson im Standardmodell der Teilchenphysik. Weiterführende und genauere Untersuchungen der Eigenschaften des Bosons sind von großem Interesse, da etwaige Abweichungen von den Vorhersagen des Standardmodells den Weg zu einer fundamentaleren Beschreibung der Natur weisen könnten. Der Vergleich von vorhergesagten und gemessenen Wirkungsquerschnitten, sowohl differenziellen als auch inklusiven, erlaubt entsprechende Tests des Standardmodells. Einer der Zerfallskanäle, die besonders gut für die Messung der Eigenschaften des Higgs-Bosons geeignet sind, ist der Zerfall des Higgs-Bosons in ein Photonenpaar, $H \to \gamma\gamma$.

Basierend auf Proton-Proton-Kollisionsdaten des ATLAS-Experiments aus den Jahren 2015 bis 2017, die einer integrierten Luminosität von 79.8/fb bei einer Schwerpunktsenergie von $\sqrt{s} = 13\,\text{TeV}$ entsprechen, wurden inklusive und differentielle Wirkungsquerschnitte für Higgs-Boson-Produktion mittels des $H \to \gamma\gamma$ Zerfallskanals in einem Phasenraumvolumen gemessen, welches in guter Näherung mit der Detektorakzeptanz übereinstimmt. Der gemessene inklusive Produktions-Wirkungsquerschnitt für Higgs-Bosonen, welche in ein Photonenpaar zerfallen, beträgt im betrachteten Phasenraumvolumen (60.4 ± 8.6) fb. Dieser Wert stimmt gut mit dem vom Standardmodell vorhergesagten Wert von (63.5 ± 3.3) fb überein.

Der differentielle Wirkungsquerschnitt im transversalen Impuls des Higgs-Bosons, p_{T}^{H}, ist sensitiv auf die Yukawa-Kopplungen zwischen dem Higgs-Boson und den Quarks, weshalb durch eine Analyse der p_{T}^{H}-Verteilung Informationen über jene Kopplungen erlangt werden können. Unter Verwendung der ATLAS-Daten, die in den Jahren 2015 – 2018 gesammelt wurden und einer integrierten Luminosität von 139.0/fb entsprechen, wurden Konfidenzintervalle für die Yukawa-Kopplungen zwischen dem Higgs-Boson und dem Bottom-Quark sowie dem Charm-Quark bestimmt. Das resultierende 95 % CL-Konfidenzintervall für den Kopplungsmodifikator $\kappa_c = y_c/y_c^{SM}$ entspricht $\kappa_c \in [-19, 25]$, wohingegen es im Falle von $\kappa_b = y_b/y_b^{SM}$ durch das Intervall $\kappa_b \in [-6, 16]$ gegeben ist.

Die Messung von Photon-Identifikationseffizienzen und der Vergleich gemessener Werte mit Effizienzen aus Simulationen sind ein wichtiger Beitrag für photonbasierte Analysen von ATLAS-Daten, wie beispielsweise oben erwähnten Messungen von $H \to \gamma\gamma$ - Wirkungsquerschnitten. Photon-Identifikationseffizienzen wurden gemessenen auf Grundlage von 79.8/fb an Daten, welche in den Jahren 2015 – 2017 genommen wurden. Die angewandte Methode stützt sich auf Transformationen von Variablen, welche die Form der elektromagnetischen Schauer von Elektronen und Photonen parametrisieren. Werden solche Transformationen auf Elektronen angewandt, die in Daten mittels einer *Tag-and-Probe*-Methode gesammelt wurden, resultieren Objekte, deren Schauerformen denen von Photonen entsprechen. Auf Grundlage solcher photon-ähnlichen Objekte können Photon-Identifikationseffizienzen gemessen werden. Die Unsicherheiten für die gemessenen Effizienzen liegen im Bereich von 0.5 % bis 3 %.

Acknowledgment

I would like to thank Kerstin Tackmann very much for giving me the opportunity to work in a wonderful group on several engaging topics. She gave invaluable guidance, support and expertise. Moreover, I am very grateful for the encouragement to participate in several scientific conventions, and to engage in work in the ATLAS control room during data-taking, which was a very interesting experience. In general, the degree of supervision and free exploration of ways to solve a problem was perfect. Also, I very much appreciate the supervision of Peter Schleper, who already in my time as a master student helped me to understand the grand field of particle physics by giving lectures at the university, and contributed important guidance in my doctorate.

I am grateful to Dieter Horns for being the chair of the PhD examination commission. Moreover, I would like to express my gratitude to Elisabetta Gallo and Christophe Grojean for having agreed to being part of the commission.

I want to thank: Kurt Brendlinger, for giving superb advice and feedback on many topics and for having coordinated the photon identification measurements with great proficiency.
Lydia Brenner, for great supervision and advice in the measurement and interpretation of Higgs boson production cross sections.
Daniela Börner, for great advice and important feedback.
Frank Tackmann, whose insight into the field of cross section predictions was indispensable for my studies on the heavy-quark Yukawa couplings.
Jim Lacey, for helping me to dive into the measurement of Higgs boson production cross sections and matters of Monte Carlo simulation.
Roger Naranjo, for giving me instructive feedback.
Florian Bernlochner, for insights in interesting features in the fit results within the context of the Yukawa coupling measurements.

The ATLAS group at DESY and Ingrid-Maria Gregor as the group leader in particular created a positive and supportive atmosphere, which I appreciate very much. I would also like to thank Daniel Rauch and Shuo Han, with whom I had the pleasure to share office, for helpful discussion and advice. I would like to extend my gratitude to the ATLAS secretaries, present and former, Sabine Krohn, Ramona Matthes, and Carolin Grötzinger, who helped me with administrative matters. Thomas Schörner-Sadenius was my mentor during my time as a PhD candidate; I want

to thank him for that and for the pleasant and interesting conversations we had over coffee. Many thanks also go to David South, who has been very helpful in distributing and maintaining the computing resources that have been necessary for the results of this thesis.

The work in ATLAS is a very connected process; therefore, the list of those deserving gratitude is certainly longer than what has been written. I am grateful for every single of the numerous instances of help and advice I received.

I feel honored for having the support of amazing and dear friends. Finally, I have an infinite gratitude for my family. Thank you for everything, Volkert, Maren, Jana and Antje.

This thesis has received funding from the European Research Council (ERC) under the European Union's Horizon 2020 research and innovation programme (grant agreement No 678215: HiggspT – Differential Higgs distributions as a unique window to New Physics at the LHC).

Eidesstattliche Erklärung

Hiermit versichere ich an Eides statt, die vorliegende Dissertationsschrift selbst verfasst und keine anderen als die angegebenen Hilfsmittel und Quellen benutzt zu haben. Die eingereichte schriftliche Fassung entspricht der auf dem elektronischen Speichermedium. Die Dissertation wurde in der vorgelegten oder einer ähnlichen Form nicht schon einmal in einem früheren Promotionsverfahren angenommen oder als ungenügend beurteilt.

Hamburg, 1.7.2020

Früd Braren

Declaration on oath

I hereby declare, on oath, that I have written the present dissertation by my own and have not used other than the acknowledged resources and aids.

Hamburg, 1.7.2020

Früd Braren

Contents

1. Introduction

Based on observations of nature and the scientific method, it has been discovered that the world is at its basis governed by several forces and consists of elementary particles, all of which can be described by mathematical equations. Gravity may be the most obvious example of a force to us. It became apparent, however, that there exists an *electromagnetic force*, which accounts for a wide array of natural phenomena such as light, electricity and magnetism. In the last century, processes have been studied that can neither be accounted for by gravity or electromagnetism, in the course of which two more forces have been discovered: the *weak* and the *strong interaction*. In parallel, a multitude of elementary particles have been found. Our current best understanding of the subatomic world, excluding the realm of gravity, is the *Standard Model of particle physics* (SM). In the SM, both matter and forces are described in terms of *quantum fields*. While it describes the subatomic world with unmatched precision, is not consistent with the *general theory of relativity*, which describes gravity and the cosmos on large scales successfully. Moreover, from cosmological observations it is assumed that a significant fraction of the matter of the universe does not consist of SM particles. Therefore, further studies of the validity of the SM are well motivated.

A central building block of the SM is the Higgs field, which plays the central role in the generation of masses of elementary particles and is the only elementary scalar field of the SM. The *Higgs boson*, the quantized excitation of the Higgs field, has a mass of approximately 125 GeV. It has been discovered in the year 2012 by two experiments [1, 2] located at the *Large Hadron Collider* (LHC), a proton-proton collider ring that, in recent years, was operating at a center-of-mass energy of $\sqrt{s} = 13\,\text{TeV}$. The experiments that led to the discovery of the Higgs boson, CMS (short for *Compact Muon Solenoid*) and ATLAS (short for *A Toroidal LHC Apparatus*), are large multi-purpose detectors that are able to detect a variety of different collision-event signatures.

Given a measurement of the mass of the Higgs boson, the SM predicts the Higgs boson's couplings to all other particles in the SM. By measuring production cross sections and decays of the Higgs boson, these predictions can be tested.

The analysis of events in which the Higgs boson decays into two photons, one of the several possible decay channels of the Higgs boson, has proven to be a valuable method for the discovery and the detailed analysis of its properties. The good energy resolution of the reconstructed photons in the ATLAS detector enables a robust background subtraction of the sizable background contributions in a signal-plus-background fit of the diphoton invariant-mass spectrum.

The Higgs boson production cross section can be measured almost model-independently in a fiducial volume of phase space that closely resembles the acceptance of the ATLAS detector and the event selection. Predictions that take into account the same fiducial phase-space volume can be directly compared to the measurements. Both the total cross section in this phase-space region and the differential cross sections of variables such as the Higgs boson transverse momentum are important observables for tests of the SM.

Because the distribution of the Higgs boson transverse momentum depends on the coupling of the Higgs boson to the b- and c-quark, these couplings can be constrained by comparing the measured distribution with predictions. The effect of the b- and c-quark coupling strength can be seen predominantly at low transverse momentum of the Higgs boson. However, also the region of high transverse momentum is interesting as it is sensitive to the presence of heavy particles that couple to the Higgs, including possible non-SM particles.

Photon candidates that are used in analyses as described above are reconstructed based on clusters of energy depositions in the ATLAS calorimeter. However, photons are not the only particles that create such clusters: the most important background results from hadronic particles, which are produced in large amounts in LHC collision. A *photon identification* selection is applied to reconstructed clusters of energy depositions in order to minimize this background and to select a sample of photon candidates that contains only a relatively small fraction of clusters that do not result from photons. Knowledge of the photon identification efficiency and the corresponding uncertainty is an important ingredient for photon-based analyses of ATLAS data. One of the methods to determine the identification efficiency in the ATLAS experiment is the *electron extrapolation* method, which is based on the transformation of variables parametrizing the shape of electromagnetic showers of electrons. The aim of these transformations is to obtain

a sample of photon-like objects, based on which the photon identification efficiency can be measured. A pure and unbiased sample of electrons to which the transformations are applied can be collected with a tag-and-probe method from Z-boson decays into electron-positron pairs.

Chapter 2 of this thesis gives an overview of the SM and its limitations, and introduces basic techniques to predict Higgs boson production cross sections. In Chapter 3, the LHC collider, the ATLAS detector and the analysis objects that are relevant for this thesis are described. The measurement of photon identification efficiencies is detailed in Chapter 4. Chapter 5 discusses the measurement of fiducial Higgs boson production cross sections in the $H \to \gamma\gamma$ decay channel. An interpretation of the measured differential cross section of the Higgs boson transverse momentum with respect to the Yukawa couplings of the c- and b-quark is shown in Chapter 6. The thesis is summarized in Chapter 7.

2. Theoretical Foundations

2.1. Introduction

The underlying theory of high energy physics is the Standard Model, which is a quantum field theory and as such a combination of quantum theory with the *special theory of relativity* [3]. Interactions and kinematics of SM particles are fundamentally described by means of a *Lagrangian density* $\mathcal{L}$. The field equations that determine the behavior of fields are derived by extremizing an action S, which is a functional of the Lagrangian density. This is called the *principle of least action* [4]. The SM describes all known interactions between matter, except the gravitational force, i.e. the strong interaction and the electroweak interaction, where the latter describes both electromagnetic phenomena and effects of the weak force.

The electromagnetic interaction is a long-range force. Both magnetic and electric fields in the classical regime are described by the theory of electromagnetism. Light and as its equivalents in different energy regimes such as X-rays or radio waves are electromagnetic phenomena as well, corresponding to oscillations of the electric and magnetic field that propagate through space – electromagnetic waves. The weak interaction is very short-ranged and is responsible for a certain type of radioactive decays and also plays a crucial role in the fusion process that powers stars. The strong interaction is the force that confines the constituents of atomic nuclei to a very small region, overpowering the repulsive effects of same-signed electric charges of the confined protons (and their constituents) and leading to strongly bound composites of multiple protons and electrically neutral neutrons. It is also the strong force that results in large energy releases in processes of nuclear fission and fusion, as found both in artificial reactors and stars. The weak and strong interactions act on short distances only, which made their discovery more challenging than that of the electromagnetic force.

Both matter and interactions are described by means of quantum fields that extend over time

and space: For each point in space-time, a harmonic oscillator for each type of field is defined and can be excited in interactions with other fields [3]. Quantized excitations of these fields correspond to what is commonly called particle.

Fermions and Bosons

In general, two types of particles exist in the SM: Fermions and bosons. These two types differ in spin, an angular momentum that is an intrinsic property of particles. Bosons are particles with integer spin, while fermions carry half-integer spin. Systems of multiple fermions and systems of multiple bosons behave each in very distinct ways: not more than one fermion can occupy a given quantum state, as stated in the Pauli exclusion principle, while any number of bosons can condensate into one state [5].

Elementary fermions with spin 1/2 constitute matter. Each fermion has a mirrored version of itself with the opposite charges, which corresponds to *antimatter*. The group of elementary fermions can be further divided into two sets of particles called *leptons* and *quarks*, depending on the interactions they participate in. Both fermion types interact electroweakly, but only quarks interact in addition via the strong interaction.

In Table 2.1 all fermions of the SM are listed. The first two lines contain the leptons, and the two lower lines contain the quarks. The most common examples of leptons are electrons, which in combination with the atomic nucleus constitute the atom. In addition to electrically charged particles like the electron, the category of leptons also contains neutrinos – particles that interact only via the weak interaction. Accordingly, neutrinos hardly interact with other particles.

Quarks cannot be found in an unbound state; instead, they are confined with other quarks to composites called *hadrons*. Protons and neutrons are the most common examples of hadrons, each consisting of a combination of two different quark types. Two up-quarks and one down-quark bound together by the strong interaction correspond to a proton, with the fractional charges as shown in Table 2.1 adding up to the positive equivalent of the electron's charge. Two down-quarks and one up-quark correspond to a neutron. However, there are more quarks to be found than just up- and down-quarks, although it needs higher energies to probe them and to create such more exotic hadrons.

An important feature of both leptons and quarks is that they come in three generations of

1st Generation	2nd Generation	3rd Generation	Electric charge [e]
Electron e	Muon μ	Tau τ	-1
Electron neutrino ν_e	Muon neutrino ν_μ	Tau neutrino ν_τ	0
Up-quark u	Charm-quark c	Top-quark t	+2/3
Down-quark d	Strange-quark s	Bottom-quark b	-1/3

Table 2.1. | Fermions of the SM, grouped in three generations, and their electric charge. The first line contains the electrically charged leptons, and the second line contains the leptons without electric charge. The two gray-shaded lines contain the up-type quarks and the down-type quarks, with fractional electric charges [6].

which each generation contains two particle types, also called *flavor*, as seen in Table 2.1. Each *up-type* quark (u, c, t) is paired with a corresponding *down-type* quark (d, s, b), and similarly each charged lepton is paired with a corresponding neutrino. Via the weak interaction, a charged lepton can be transformed to a neutrino, and vice versa, and similarly an up-type quark can be transformed to a down-type quark, and vice versa. Such transformations between different fermion types are one of the reasons for radioactive decays of atomic nuclei. The flavor-changing transformations can not only happen between particles of the same generation, but with a smaller probability also between particles from different generations. This is because the eigenstates of mass, which defines the particle, are not the eigenstates of the weak interaction.

The group of elementary SM bosons can be divided into two types: particles with spin 1, and one instance of a particle with spin 0, a scalar. Those that have unit spin are commonly called *vector bosons* or *gauge bosons*. These fields are the mediators of the SM interactions. While gauge bosons are all created by the same dynamic principle, called the *gauge principle*, the scalar field is stated ad hoc as basic ingredient of the *Higgs mechanism*, which was added to the SM in order to allow non-zero masses of elementary particles. In Table 2.2, all elementary bosons of the SM are listed in combination with their mass and electric charge.

Name	Mass [GeV]	Electric charge [e]
Photon γ	$< 10^{-27}$	0
Z-boson	91.188 ± 0.002	0
$W^{\pm}$-boson	80.379 ± 0.012	± 1
Gluon g	0	0
Higgs boson H	125.09 ± 0.24	0

Table 2.2. | Bosons of the SM [6][7]. Except for the Higgs boson, all bosons mediate *gauge interactions*, as described in Section 2.2.

2.2. Interactions in the Standard Model

Interactions in the SM are based on symmetry principles. By imposing the constraint of preserving certain symmetries of the Lagrangian that describes naively only non-interacting matter, vector fields have to be introduced to the theory, which have the effect of mediating a force. Because these vector fields are products of the constraint of being able to freely choose a "gauge", that is, products of a demand for symmetry, they are called *gauge bosons*. They can be seen as mediators of SM forces. The kind of symmetry that is considered in this context is that of *Lie symmetry groups* acting on internal degrees of freedom of the quantum fields, which generally contain an infinite number of symmetry transformations [3].

If a theory is symmetric under a transformation identical for all points in space-time, one speaks of a global symmetry. If a theory is said to be locally invariant under a given symmetry group, one can apply a different element of the symmetry group for each point in space-time without changing the Lagrangian [4]. The existence of a local symmetry implies the existence of a global symmetry of the same type. The Noether theorem states that for each global and differentiable symmetry a conserved quantity exists, meaning that in corresponding interactions this quantity does not change. Such a conserved quantity is generally called *charge* [4].

Depending on the symmetry to be preserved, different dynamics entail. The simplest example of a gauge theory in the SM is the theory of electromagnetic interactions, which follows from a local symmetry of type $U(1)$. Transformations of this symmetry group correspond to changes in the phase of a complex number by multiplication with a complex number $e^{ig\alpha(x)}$. In this simple example, $\alpha(x)$ is a real number that specifies the transformation, and g is the *generator* of the symmetry group. The defining property of the set of generators, which in this simple case

contains only one element, is that with a linear combination of the set elements every element of the symmetry group can be expressed.

Such a transformation can be generalized to fields with more than one component. The most general case of a gauge symmetry is to assume a field with n components, $\psi(x) = (\psi_1(x), \psi_2(x), ..., \psi_n(x))^{\mathrm{T}}$, and a symmetry group that acts upon this field [4]. A symmetry transformation of such a group can be represented by a unitary, complex-valued $n \times n$ matrix with unit determinant. Unitary matrices obey $M^\dagger M = I$. A transformation corresponding to such a matrix preserves the Euclidean norm of the field on which the transformation acts. A generic transformation of that type can be written as

$$\psi(x) \to e^{ig\alpha^k(x)T^k}\psi(x), \tag{2.1}$$

where summation over the index k is implicit. The T^k are the generators of the symmetry group, and the $\alpha^k(x)$ are real numbers that act as coefficients for the generators, resulting in a linear combination of the generators acting on the field $\psi(x)$.

The special case where $n = 1$ is called *Abelian*. In this case, the order in which multiple transformations are applied is irrelevant. In the case $n \geq 2$, the order of the application of group elements is generally of importance; such symmetry groups are called *non-Abelian*. Whether a symmetry is Abelian or non-Abelian has significant consequences for the dynamics of the resulting interaction; if an interaction corresponds to a non-Abelian symmetry group, its gauge bosons can couple to each other [4].

A Lagrangian typically contains derivatives $\partial_\mu = (\partial/\partial t, \vec{\nabla})$ of the field $\psi(x)$. In order to preserve gauge invariance for such terms, these original derivatives ∂_μ are substituted by a *covariant derivative* D_μ that transform like the fields ψ under gauge transformations. In the case of a $U(1)$ gauge theory, the covariant derivative is given by $D_\mu = \partial_\mu + igA_\mu(x)$, which involves a newly introduced vector field A_μ that compensates for the changes brought by the $U(1)$ gauge transformation. This *gauge field* $A_\mu(x)$ itself is subject to gauge transformations: $A_\mu(x) \to A_\mu(x) - \frac{1}{g}\partial_\mu\alpha(x)$.

In the case of the SM, three gauge symmetries are postulated in order to account for all known

forces except gravity. The combination of these reads [4]

$$\mathrm{SU(3)_c} \times \mathrm{SU(2)_L} \times \mathrm{U(1)}_Y \,. \tag{2.2}$$

The first part, $\mathrm{SU(3)_c}$, corresponds to the strong force, and the combination of the $\mathrm{SU(2)_L}$ and $\mathrm{U(1)}_Y$ symmetries to the electroweak interaction. The subscript c in $\mathrm{SU(3)_c}$ indicates that the so-called *color* is the conserved quantity of the resulting interaction. In the case of the $\mathrm{SU(2)_L}$ symmetry group, the subscript L indicates that this interaction acts only on particles of left-handed chirality[1]. The charge of the interaction related to the $\mathrm{SU(2)_L}$ symmetry is one of the three components of the *weak isospin*, usually chosen to be the third, i.e. the z-component. For the $\mathrm{U(1)}_Y$ symmetry group, the conserved quantity Y is called *weak hypercharge*.

In general, the number of gauge fields that result from a gauge symmetry $\mathrm{SU}(N)$ is given by $N^2 - 1$. Hence, there are 8 gauge bosons that mediate the strong force, and four gauge bosons in the case of the electroweak force. The gauge bosons of the strong force are called *gluons* and are massless. The strong interaction is non-Abelian, which implies that gluons carry color charge themselves and couple to each other. Similarly, there are interactions between the electroweak gauge bosons. Three of the four gauge bosons corresponding to the $\mathrm{SU(2)_L} \times \mathrm{U(1)}_Y$ gauge symmetry are massive ($W^{\pm}$, Z), while one of them, the photon, is massless. The massive electroweak gauge bosons mediate the weak interaction, and the photon mediates the electromagnetic interaction. A non-zero mass of gauge bosons generally leads to a reduced range of the corresponding interaction. As can be seen in Table 2.2, the massive electroweak gauge bosons have masses of the order $O(10^2)$ GeV, corresponding to a range of about $2.5 \cdot 10^{-18}$ m [8]. Despite a mass of zero, the range of the strong interaction is small, which is discussed in Section 2.5.

2.3. Electroweak Theory and the Higgs Mechanism

The theory of electroweak interactions is strongly linked to the Higgs mechanism, which is responsible in the SM for generating masses of elementary particles, including those of the gauge

[1] For massless particles the chirality corresponds to handedness, the projection of the spin on the momentum vector. The chirality of a system is changed by application of the parity transformation $P : (x, y, z) \rightarrow (-x, -y, -z)$.

bosons of the weak interaction. The Higgs mechanism requires the existence of a scalar field with a non-vanishing expectation value. Without an ingredient like the Higgs mechanism, neither masses for gauge bosons nor masses for elementary fermions are possible without explicitly breaking the gauge symmetry. In case of the gauge bosons, this is because not only fermion fields but also the gauge fields themselves are subject to gauge transformations. If an explicit mass term for the gauge boson would be part of the Lagrangian, the combination of it with the aforementioned gauge transformation would explicitly break gauge invariance. In the case of fermions, a naive mass term of the form $m(\overline{\psi}_L\psi_R + \overline{\psi}_R\psi_L)$ would destroy gauge invariance because the products in this term involve both fields with left-handed and right-handed chirality, which transform differently under gauge transformations of $\mathrm{SU(2)_L}$.

2.3.1. The Electroweak Interaction

The gauge symmetry of the electroweak interaction is $\mathrm{SU(2)_L} \times \mathrm{U(1)}_Y$. Its gauge fields are denoted by W^i_μ, with $i \in \{1, 2, 3\}$, and B_μ, where the W^i_μ result from the $\mathrm{SU(2)_L}$ symmetry, and the B_μ from the $\mathrm{U(1)}_Y$ symmetry. The mass eigenstates of the $\mathrm{SU(2)_L} \times \mathrm{U(1)}_Y$ gauge bosons are linear combinations of the fields W^i_μ and B_μ. Three of the four mass eigenstates are massive. The massless photon is denoted by γ or A, the two massive gauge bosons that carry electrical charge by $W^\pm$, and the electrically neutral massive gauge boson by Z.

Photons and Z-bosons mediate *neutral currents*, interactions in which the flavor of the interacting particle does not change. *Charged currents* correspond to interactions with $W^\pm$ bosons, which change particle flavor and carry electrical charge. An example for this would be the emission of a W^- boson by an electron, by which the electron is transformed into an electron neutrino. The gauge bosons of $\mathrm{SU(2)_L}$ only couple to fermions of left-handed chirality. Right-handed neutrinos have so far not been observed. Of all other fermions, right-handed versions are known to exist. These are singlets under $\mathrm{SU(2)_L}$ transformations, corresponding to zero weak isospin, while left-handed fermions belong to a doublet of weak isospin. The electric charge is the charge that the photon couples to; it is given by the sum of the z-component of the weak isospin and on the weak hypercharge, $eQ = e(T_z + Y)$ [4].

The initial Lagrangian without interactions can be transformed to an electroweakly interacting theory by replacing the derivatives ∂_μ with the covariant derivative of $\mathrm{SU(2)_L} \times \mathrm{U(1)}_Y$, which

contains terms with gauge fields and is given by

$$\begin{aligned} D_\mu &= \partial_\mu + i\frac{g}{2}\sigma^i W_\mu^i + ig'\frac{Y}{2}B_\mu \\ &= \partial_\mu + \frac{i}{2}\begin{pmatrix} gW_\mu^3 + g'B_\mu & g(W_\mu^1 - iW_\mu^2) \\ g(W_\mu^1 + iW_\mu^2) & -gW_\mu^3 + g'B_\mu \end{pmatrix}. \end{aligned} \tag{2.3}$$

The σ_i represent the three Pauli matrices. As there are two gauge symmetries involved, two interaction strengths play a role, g for $\mathrm{SU(2)_L}$, and g' for $\mathrm{U(1)}_Y$. Based on Eq. (2.3), the following definitions of mass eigenstates for the gauge fields can be introduced:

$$\begin{aligned} W_\mu^\pm &= \frac{1}{\sqrt{2}}(W_\mu^1 \mp iW_\mu^2) \\ Z_\mu &= \frac{1}{\sqrt{g^2+g'^2}}(gW_\mu^3 - g'B_\mu) \\ A_\mu &= \frac{1}{\sqrt{g^2+g'^2}}(gW_\mu^3 + g'B_\mu). \end{aligned} \tag{2.4}$$

2.3.2. The Higgs Field

If gauge invariance of the Lagrangian is required, the inclusion of simple, ad hoc mass terms is not permitted. Because fermion masses are generally non-zero, and several of the electroweak gauge bosons are massive, a way had to be found to allow a dynamical mass generation of these particles. One solution for this is to assume the existence of a particular scalar field with non-zero expectation value for its field strength. The coupling of elementary particles to such a scalar field would create particle masses without explicitly breaking gauge invariance. This scalar field is a weak-isospin doublet and complex-valued, corresponding to a total of four scalar fields ϕ_i:

$$\phi = \begin{pmatrix} \phi^+ \\ \phi^0 \end{pmatrix} = \frac{1}{\sqrt{2}}\begin{pmatrix} \phi_1 + i\phi_2 \\ \phi_3 + i\phi_4 \end{pmatrix}. \tag{2.5}$$

As a weak-isospin doublet, it participates in the $\mathrm{SU(2)_L}$ interaction. Moreover, it carries a weak hypercharge Y. In order to have a doublet of which one component has zero electrical charge and accordingly does not couple to photons and provides the possibility of an electrically neutral ground state of the scalar field, the Higgs field needs to have a value for the weak hypercharge of

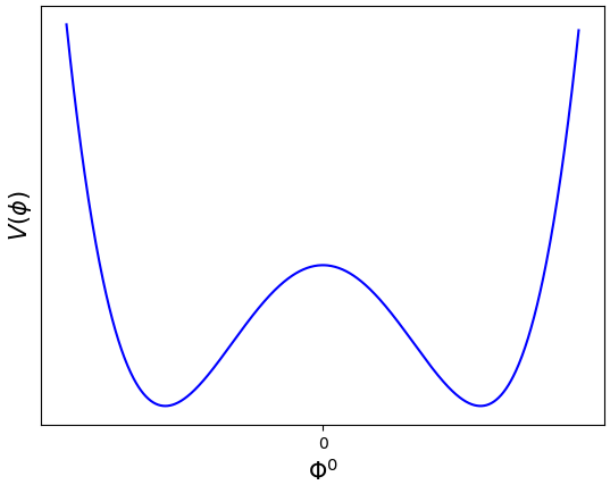

Figure 2.1. | Higgs potential as a function of the field strength. For the sake of the presentation, the Higgs potential is drawn as a function of only one of the four real-valued Higgs field components. Its potential is minimal at a field strength of $|\phi^+|^2 + |\phi^0|^2 = \frac{\mu}{\sqrt{2\lambda}}$, see Eq. (2.6).

$Y = \frac{1}{2}$ [4]. The Lagrangian that describes this field is given by

$$\begin{aligned} \mathcal{L}_{\mathrm{H}}^{\mathrm{free}} &= \partial_\mu \phi^\dagger \partial^\mu \phi - V(\phi) \\ &= \partial_\mu \phi^\dagger \partial^\mu \phi + \mu^2 \phi^\dagger \phi - \lambda (\phi^\dagger \phi)^2 , \end{aligned} \tag{2.6}$$

where ϕ is given by Eq. (2.5) and $V(\phi)$ is the term describing the potential of the field. Two real-valued parameters enter this Lagrangian, μ^2 and λ. Both have to be positive under the requirement of having a stable vacuum state with a non-vanishing vacuum expectation value. In that case, the potential has a form as shown in Figure 2.1. By computing the field configuration at which the potential energy is minimal, one obtains the non-vanishing expectation value for the Higgs field strength.

The vacuum or ground state can be chosen from a degenerate four-dimensional circle that has a radius of $\mu/\sqrt{2\lambda}$. By assuming one of the field configurations of the ground state, the initial $\mathrm{SU(2)_L \times U(1)}_Y$ symmetry of the system is hidden. Such a situation is called *spontaneous symmetry breaking*. As a consequence of such a breaking of a continuous symmetry, massless scalar bosons arise. The reason that these massless bosons are not seen in experiment is that the corresponding degrees of freedom are absorbed into the definitions of the $W^\pm$ and Z-bosons, increasing their number of degrees of freedom from two to three. This additional degree of

freedom corresponds to a mode with longitudinal polarization, whereas the original two degrees of freedom described the transversal modes of polarization of a massless vector boson. The remaining $4-3=1$ degree of freedom from the introduction of the doublet of scalar fields is equivalent to the Higgs boson.

Since the global $\mathrm{SU(2)_L}\times\mathrm{U(1)}_Y$ symmetry exists irrespective of the spontaneous symmetry breaking, one can gauge the ground state in a way that results in a charged component of the Higgs field with vanishing expectation value and one electrically neutral component of which only the real part has a non-vanishing expectation value, see Eq. (2.7). In this ground state, the Higgs field is given by

$$\phi = \begin{pmatrix} 0 \\ \frac{1}{\sqrt{2}}(v+H(x)) \end{pmatrix}, \tag{2.7}$$

where $v/\sqrt{2}$ corresponds to the expectation value of the Higgs field in its ground state. An oscillation around this value is represented by $H(x)$ and correspond to the Higgs boson.

2.3.3. Masses of Gauge Boson

To understand the interactions of the Higgs field with the gauge bosons and itself, it is instructive to further analyze the Lagrangian in Eq. (2.6). First, one replaces the derivative with its covariant version given by Eq. (2.3) to make it invariant under $\mathrm{SU(2)_L}\times\mathrm{U(1)}_Y$ gauge transformations. This leads to

$$\begin{aligned}\mathcal{L}_{\text{Higgs}} &= (D_\mu\phi)^\dagger(D^\mu\phi) + \mu^2\phi^\dagger\phi - \lambda(\phi^\dagger\phi)^2 \\ &= (\partial_\mu\phi)^\dagger(\partial^\mu\phi) + \mu^2\phi^\dagger\phi - \lambda(\phi^\dagger\phi)^2 \\ &\quad + \frac{1}{4}\phi^\dagger(gW_\mu^a\sigma^a + g'B_\mu)(gW_\mu^b\sigma^b + g'B_\mu)\phi\,. \end{aligned} \tag{2.8}$$

When evaluating the Pauli matrices and assuming the ground state given by Eq. (2.7), this Lagrangian becomes

$$\begin{aligned}\mathcal{L}_{\text{Higgs}}^{\text{vac}} &= \frac{1}{2}(\partial_\mu H)^\dagger(\partial^\mu H) - \mu^2H^2 - \lambda vH^3 - \frac{1}{4}\lambda H^4 \\ &\quad + \frac{1}{8}(v+H)^2\left[g^2\left((W_\mu^1)^2 + (W_\mu^2)^2\right) + (-gW_\mu^3 + g'B)^2\right]. \end{aligned} \tag{2.9}$$

With the definitions of the gauge boson mass eigenstates (2.4) one obtains a Lagrangian from which the following gauge boson masses can be determined:

$$\begin{aligned} m_W &= \frac{v}{2} g \\ m_Z &= \frac{v}{2} \sqrt{g^2 + g'^2} \\ m_\gamma &= 0 \,. \end{aligned} \tag{2.10}$$

It follows that the masses of the W-bosons and Z-bosons are proportional to the vacuum expectation value of the Higgs field, which can thus be computed based on the measured masses of the heavy gauge bosons, e.g. the W-boson: $v = 2 m_W / g = 246\,\mathrm{GeV}$ [6]. The ratio of the masses of the W-boson and Z-boson is fixed by the relations (2.10):

$$\frac{m_W}{m_Z} = \frac{g}{\sqrt{g^2 + g'^2}} \,. \tag{2.11}$$

Not only do the $W^\pm$ and Z-bosons become massive by the introduction of the Higgs field, there are also interactions between those massive bosons and the Higgs boson as well as self-interactions of the Higgs boson:

$$\begin{aligned} \mathcal{L}_{\text{int.}} = &-\lambda v H^3 - \frac{1}{4}\lambda H^4 \\ &+ \frac{g^2}{4} H^2 (W_\mu^\pm)^2 + \frac{g^2}{2} H (W_\mu^\pm)^2 + \frac{g^2 + g'^2}{8} H^2 (Z_\mu)^2 + \frac{g^2 + g'^2}{4} H (Z_\mu)^2 \,. \end{aligned} \tag{2.12}$$

2.3.4. Masses of Fermions

Since explicit mass terms of fermions would involve mixing the left-handed and the right-handed versions of the fermion fields, which behave differently under $\mathrm{SU(2)_L} \times \mathrm{U(1)}_Y$ gauge transformations, such mass terms would break gauge invariance explicitly. The Higgs field can be used to generate fermion masses without explicitly breaking gauge invariance. This is done by assuming *Yukawa interactions* between the Higgs field and elementary fermions. For example, a mass for the electron can be introduced by adding the following term to the Lagrangian:

$$\mathcal{L}^e_{\text{Yukawa}} = \text{-}\lambda_e \left(\bar{E}_L \phi e_\mathrm{R} + \bar{e}_\mathrm{R} \phi^\dagger E_L \right) , \tag{2.13}$$

with the left-handed $SU(2)_L$ doublet

$$E_L = \begin{pmatrix} \nu_e \\ e^- \end{pmatrix}_L . \tag{2.14}$$

The right-handed component e_R is a singlet under $SU(2)_L$. The factor λ_e denotes the Yukawa coupling strength of the Higgs field to the electron. Assuming the vacuum state given by Eq. (2.7), the Lagrangian given in Eq. (2.13) becomes

$$\mathcal{L}^e_{\text{Yuk}} = -\lambda_e \frac{v}{\sqrt{2}} (\bar{e}_L e_R + \bar{e}_R e_L) . \tag{2.15}$$

It follows that by introducing Yukawa couplings between elementary fermions and the Higgs field gauge-invariant mass terms for these fermions follow. In general, the mass of an elementary fermion from a Yukawa coupling is given by

$$m_f = \frac{\lambda_f v}{\sqrt{2}} , \tag{2.16}$$

where λ_f is a free parameter of the theory which can be chosen such that the measured fermion masses are reproduced.

Neutrinos are different from the other fermions because it was originally assumed that they are massless. However, neutrino mixing has been observed; therefore, they must have non-zero masses [9]. A way to implement this in the SM is to assume the existence of right-handed neutrinos that interact neither electromagnetically nor weakly [3].

2.4. The Higgs Boson

2.4.1. Higgs Boson Properties

The Higgs boson's mass is given by $m_H = \sqrt{2}\mu$, as follows from the Lagrangian in Eq. (2.9). Since μ is not known but a free parameter of the theory, it does not predict the mass of the Higgs boson, making it necessary to measure it by experiment. The Higgs boson has been observed in 2012 by both the CMS and ATLAS experiment [1, 2]. Its mass has been measured to be $m_H = (125.09 \pm 0.21\,(\text{stat.}) \pm 0.11\,(\text{syst.}))$ GeV [7]. The experimental signature of the Higgs

boson is a resonance, and can be measured in various decay channels, including the decay to two photons. The fact that the observed boson can decay to a system of two photons implies that this boson cannot be a spin-1 particle, as a diphoton system cannot be constructed in a way that leads to a combined spin of 1 [10, 11]. Spin 0 and spin 2 are the remaining options. In Reference [12] hypotheses about the spin and the behavior under CP-transformations have been tested. All hypothesis except the one that corresponds to the SM assumption, i.e. a CP-even boson with spin 0, have been excluded with more than 99.9 % CL.

2.4.2. Higgs Boson Decays

Given the Higgs boson mass of approximately 125 GeV, the Higgs boson is predicted to decay quickly, with a mean lifetime of $\tau = (1.60 \pm 0.02 \cdot 10^{-22})$ s, corresponding to the inverse of the decay width $\Gamma = \sum_i \Gamma_i = (4.10 \pm 0.06)$ MeV, where Γ_i denotes the partial decay width of decay channel i [13]. The branching ratios of the various Higgs boson decays are given by [14]

$$\mathcal{B}_i = \frac{\Gamma_i}{\Gamma}. \tag{2.17}$$

In Table 2.3, the predicted branching ratios for a Higgs boson with a mass of 125.09 GeV are shown. The coupling of the Higgs boson to other particles grows with increasing particle mass. Therefore, the Higgs boson tends to decay to a pair of particles with the highest possible mass. Due to the uncertainty principle $\Delta t \cdot \Delta E \geq 2\pi$, the Higgs boson can not only decay to a pair of particles with a mass smaller than half of the Higgs boson mass, but also to a pair of heavier particles [9]. In such a case, at least one of the particles from the Higgs boson decay must violate the energy-momentum relation $E^2 = \vec{p}^2 + m^2$. The larger this violation is, the more suppressed is the process.

As can be seen in Table 2.3, most Higgs bosons decay to a pair of b-quarks. However, it is challenging to observe this decay due to the large QCD background of the $H \to b\bar{b}$ signature. Consequently, this decay mode has only recently been experimentally observed [15, 16]. The decay channels that were used to discover the Higgs boson were those to pairs of gauge bosons, in particular $H \to \gamma\gamma$, $H \to ZZ^* \to 4\ell$, and $H \to WW^* \to \ell^+\nu\ell^-\bar{\nu}$ [2], where ℓ denotes either an electron or muon. The two former channels can be used for the measurement of the Higgs boson mass, while the latter is limited in this regard because the inability to fully reconstruct neutrino

Decay Channel	Branching ratio	Relative uncertainty [%]
$b\bar{b}$	0.58	$^{+1.2}_{-1.3}$
W^+W^-	0.22	$^{+1.5}_{-1.5}$
gg	0.082	$^{+5.2}_{-5.1}$
$\tau\tau$	0.063	$^{+1.7}_{-1.6}$
$c\bar{c}$	0.029	$^{+5.6}_{-2.0}$
ZZ	0.026	$^{+1.5}_{-1.5}$
$\gamma\gamma$	0.0023	$^{+2.1}_{-2.1}$
$\mu\mu$	0.000 22	$^{+1.7}_{-1.7}$
$Z\gamma$	0.0015	$^{+5.8}_{-5.8}$

Table 2.3. | SM predictions for Higgs boson branching ratios for a Higgs boson mass of 125.09 GeV [13]. Decays with boson pairs in the final state are highlighted in gray. The uncertainties are computed by quadratically summing the individual theoretical and parametric uncertainties.

four-momenta in the ATLAS detector prevents the reconstruction of the invariant mass of all decay products.

Of particular relevance for this thesis is the decay of the Higgs boson to a pair of photons. While the Higgs boson does not directly couple to photons, it does couple indirectly to them via a loop of $W^{\pm}$ bosons or a loop of massive, charged fermions, see Figure 2.2. (All Feynman diagrams in this work have been created using Reference [17].)

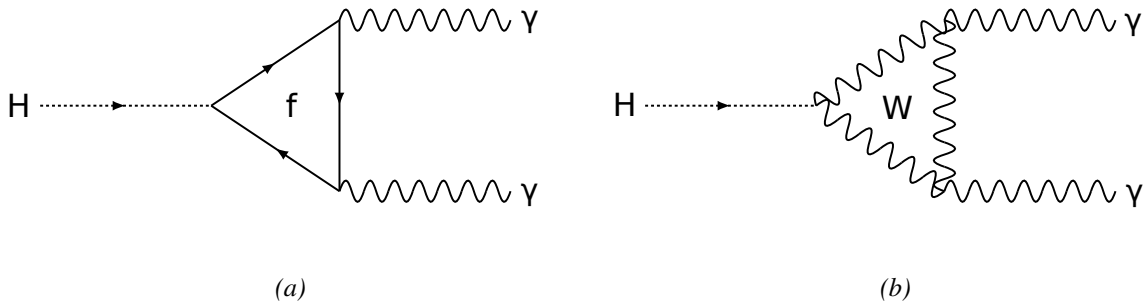

(a) *(b)*

Figure 2.2. | Feynman diagrams for $H \to \gamma\gamma$ decays. (a) Decay via a loop of electrically charged fermions, particularly heavy fermions, denoted by f, such as t-quarks. (b) Decay via a loop of $W^{\pm}$ bosons.

2.4.3. Higgs Boson Production Processes

In proton-proton collisions at the LHC, Higgs bosons can be produced in various processes with different cross sections; see Section 2.6 for an introduction to the concept of the cross section and its computation. In Figures 2.3, 2.4, 2.5 and A.1 (see Appendix A), the leading-order[2] Feynman diagrams for Higgs boson production are shown. These processes will be briefly described below. For the quoted predicted cross sections a Higgs boson mass of $m_H = 125.09\,\text{GeV}$ and a center-of-mass energy of $\sqrt{s} = 13\,\text{TeV}$ has been assumed.

Gluon fusion

Gluon fusion is the dominant Higgs boson production mode for proton-proton collisions at the LHC. Two gluons lead to a heavy-quark loop which can couple to a Higgs boson, see Figure 2.3 (a). Because of its relatively large cross section of $48.51^{+2.72}_{-3.61}$ pb [13, 18–36] and the presence of a loop at leading order that could involve particles beyond the SM, this production mode is of particular interest. For more details on the computation of the gluon fusion cross section, see Section 2.6.4.

Vector-boson fusion

In the vector-boson fusion process two incoming quarks each emit massive gauge bosons which fuse into a Higgs boson, see Figure 2.3 (b). With a cross section of $3.779^{+0.083}_{-0.082}$ pb, this production mode has the second-largest cross section [13, 18, 37–44].

Associated *WH* production

In the process of associated WH production, two quarks fuse into a W-boson that has sufficient high virtuality to emit a Higgs boson, see Figure 2.3 (c). This process has a cross section of $1.369^{+0.027}_{-0.028}$ pb [13, 18, 37, 40, 45].

[2]For a given process, the leading-order diagram corresponds to the diagram of minimal order in perturbation theory that leads to a non-zero process cross section.

Associated *ZH* production

Associated ZH production corresponds to diagrams in which a pair of quarks fuse into a Z-boson which emits a Higgs boson, see Figure 2.3 (c); it additionally includes diagrams with a pair of gluons in the initial state ($gg \rightarrow ZH$). See Figure 2.3 (d) for the leading-order diagrams representing the gluon-initiated associated ZH production. The combined cross section amounts to $0.882^{+0.036}_{-0.030}$ pb [13, 18, 37, 40, 45–49].

Higgs boson production in association with a pair of *t*-quarks

In associated $t\bar{t}H$ production, two gluons split each into a $t\bar{t}$-pair, leading to four t-quarks, of which two fuse into a Higgs boson, resulting in a final state with two top quarks and a Higgs boson. The leading-order diagrams are given in Figure 2.4. This process has a predicted cross section of $0.507^{+0.035}_{-0.050}$ pb [13, 18, 50–62].

b-quark-initiated Higgs boson production

In b-quark-initiated Higgs boson production, two b-quarks fuse into a Higgs boson, with a predicted cross section of $0.52^{+0.05}_{-0.05}$ pb [63]. In Figure 2.5 (a), one of the leading-order diagrams in the *4-flavor-scheme* is depicted. Here, b-quarks are not taken into account by the proton *parton distribution functions* (PDF), see Section 2.6.2; instead, gluon splittings into pairs of b-quarks are necessary for the realization of a $b\bar{b}H$ vertex. In the *5-flavor-scheme*, the proton PDF includes the b-quark; the corresponding leading-order diagram is shown in Figure 2.5 (b). More details on flavor schemes are given in Section 2.6.2.

c-quark-initiated Higgs boson production

Similar to the b-quark-initiated Higgs boson production process, a pair of c-quarks can fuse into a Higgs boson in the final state, with a predicted cross section of $0.077^{+0.004}_{-0.004}$ pb [13, 64]. See Figure 2.5 (b). Unlike b-quarks, it is uncommon to not take c-quarks into account via the PDF set.

Higgs boson production in association with a single *t*-quark

The production of Higgs bosons in association with a single t-quark generally involves a W-boson. One distinguishes between diagrams in which the W-boson has negative virtuality (t-channel), diagrams in which the W-boson has positive virtuality (s-channel), and diagrams in which the W-boson has vanishing virtuality, i.e. in which it is on-shell and is produced in association with the Higgs boson and the t-quark. See Figure A.1 in Appendix A for the leading-order diagrams; (a) and (b) are the t-channel diagrams, (c) and (d) the s-channel diagrams, and (e), (f) and (g) correspond to the associated production of an on-shell W-boson. In the t-channel, the cross section is predicted to be $0.074^{+0.006}_{-0.011}$ pb [13, 18, 65], and in the s-channel, it is predicted to be $2.875^{+0.094}_{-0.082}$ fb [13, 18, 65]. The associated Higgs boson production with a single t-quark and an additional $W^{\pm}$ boson is expected to have a cross section of $0.015^{+0.001}_{-0.001}$ pb (assuming a Higgs boson mass of 125.0 GeV) [18, 66].

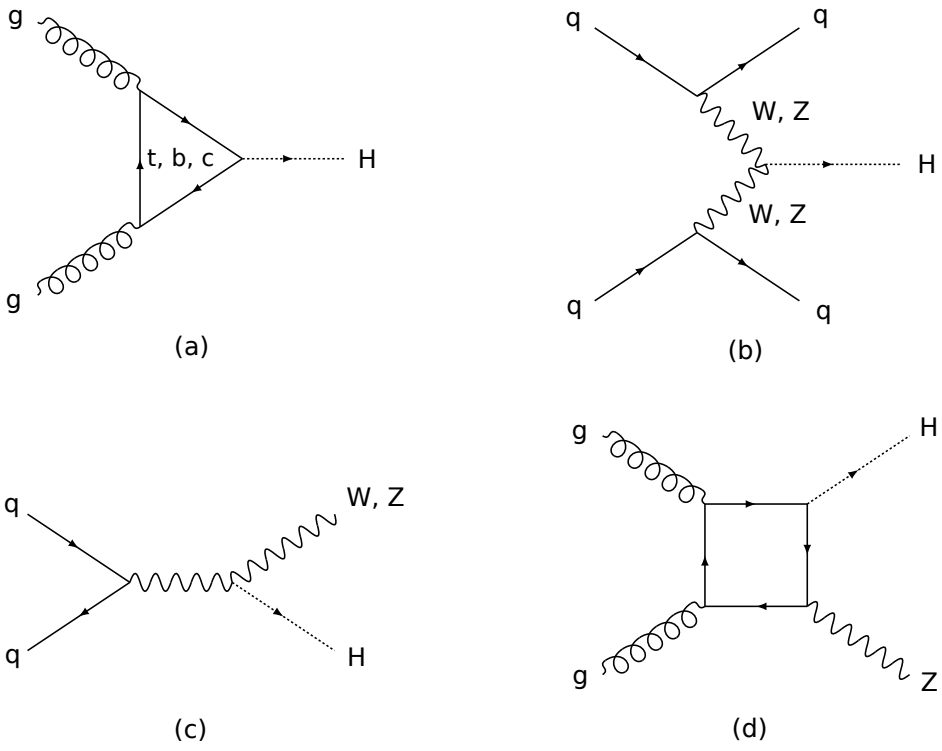

Figure 2.3. | The leading-order Feynman diagrams for (a) gluon fusion (ggF), (b) vector-boson fusion (VBF), and (c), (d) associated vector-boson production (VH in general, the latter $gg \to ZH$).

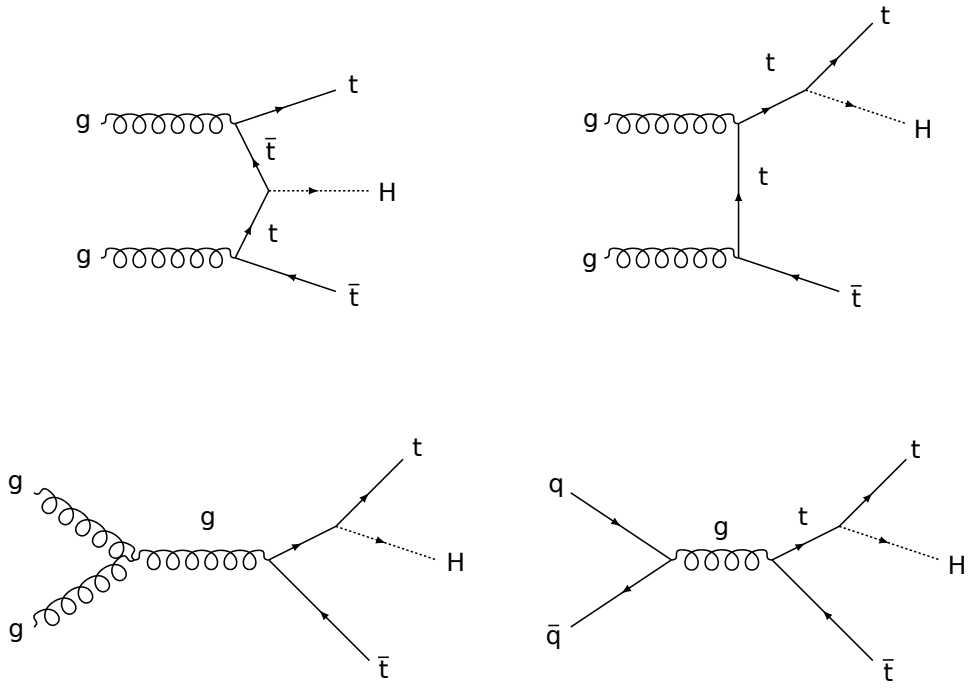

Figure 2.4. | The leading-order Feynman diagrams for Higgs boson production in association with $t\bar{t}$ pairs ($t\bar{t}H$).

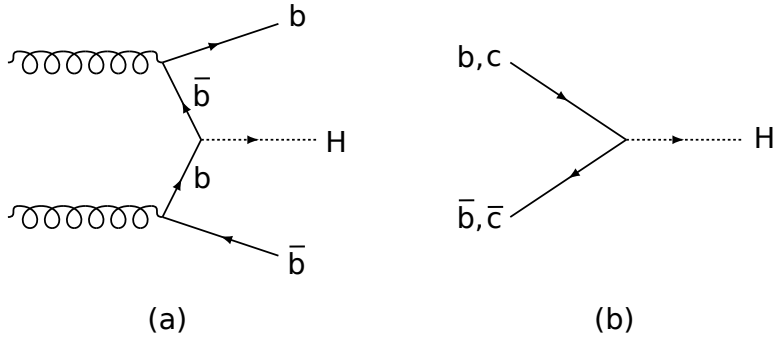

Figure 2.5. | The leading-order Feynman diagrams for b- and c-quark-initiated Higgs boson production ($b\bar{b} \to H$, $c\bar{c} \to H$). b-quark-initiated Higgs boson production can be treated differently by either assuming the b-quark to be or not to be a constituent of the proton. The former case is referred to as the 5-flavor-scheme and one of the corresponding leading-order diagrams is shown in (a). The latter case is referred to as the 4-flavor-scheme. In this case, the structure of the diagram is identical for b- and c-quark-initiated Higgs boson production, see the diagram (b). See Section 2.6.2 for more details on the two flavor schemes.

2.5. Quantum Chromodynamics

The strong interaction can be derived from a $SU(3)_c$ gauge symmetry. Quarks and gluons are charged under this interaction. Quarks carry one of three different QCD charges, called color, conventionally denoted by *red*, *green*, and *blue*. Gluons carry both color and anti-color. As is the case for all gauge interactions in the SM, the strength of the coupling depends on the momentum-transfer scale Q of the process. The coupling strength of the strong interaction increases with decreasing Q, or, equivalently, with increasing distance of the interacting particles. This *running* of the QCD coupling strength α_s with changing scale is given in the lowest perturbative order by

$$\alpha_s \approx \frac{2\pi}{(11 - \frac{2}{3}N_f)\ln\left(\frac{Q}{\Lambda_{\mathrm{QCD}}}\right)}, \tag{2.18}$$

where N_f corresponds to the number of quark flavors, and Λ_{QCD} is the scale at which the coupling strength is divergent. The predicted and measured running of α_s with Q is shown in Figure 2.6, in which the rise of α_s towards low values of Q is well visible. At a scale equal to the mass of the Z-boson, α_s is given by 0.1181 ± 0.0011 [6].

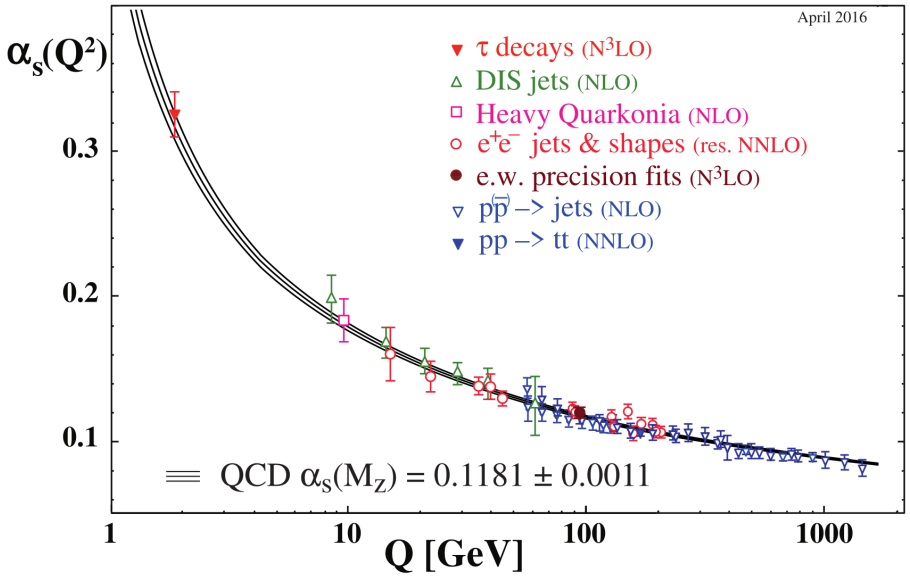

Figure 2.6. | Comparison of measured values for the strong coupling α_s for different values of the interaction scale Q with the prediction. Taken from Reference [6].

Using an expression for α_s that includes higher orders in perturbation theory than Eq. (2.18), one obtains by experiments a value $\Lambda_{\mathrm{QCD}} \approx 0.2\,\mathrm{GeV}$ [3], corresponding to a distance of approxi-

mately 1 fm. The application of perturbation theory is not valid at large values of α_s, i.e. if Q is close to Λ_{QCD}.

Related to the running of α_s, it is impossible to create free colored objects such as single quarks [3]: with increasing distance between color-carrying particles, the interaction strength increases, with the result that all the particles end up in bound states without net color charge. This process is called *hadronization*. Because it involves QCD interactions at a low scale, perturbative techniques are not sufficient to describe it. Instead, phenomenological models typically are used to describe such low-Q processes. In the limit of very large Q, the coupling strength of the strong interaction vanishes, corresponding to what is called *asymptotic freedom*.

2.6. Computation of Cross Sections

A collision in an experiment such as performed at the LHC experiments at CERN consists in the scattering of particles at high center-of-mass energies. Different final states that result from such scattering have different probabilities to occur. These probabilities depend on the properties of the particles that take part in the scattering. The cross section is a quantity that encapsulates the probability that a process with a given initial and final state occurs. Typically, the cross section does not include branching ratios from decays. This factorization of production and decay is possible due to the narrow decay width of the Higgs boson.

2.6.1. Cross Section and Luminosity

The cross section σ relates the number of events N corresponding to a given process to the *integrated luminosity* $\int L \mathrm{d}t$ by

$$N = \sigma \int L \mathrm{d}t, \tag{2.19}$$

The luminosity L is a measure of the number of particles per unit time and per unit area that are given the chance to interact with each other. In a collider experiment, the luminosity can be computed as [67]

$$L = \frac{n_b \cdot N_1 \cdot N_2 \cdot f_{\mathrm{rev}}}{2\pi \cdot \sqrt{\sigma_{1x}^2 + \sigma_{2x}^2} \cdot \sqrt{\sigma_{1y}^2 + \sigma_{2y}^2}} \cdot F \cdot W. \tag{2.20}$$

The denominator corresponds to the cross-sectional area to which the beams are confined. Under the assumption of a Gaussian beam profile, the beam widths of the two beams in the transverse plane are given by σ_{ix} and σ_{1y}, $i \in \{1, 2\}$. The numerator gives the number of colliding particles per unit time. The number of particle bunches per beam is given by n_b; these revolve with a frequency f_{rev} in the beam pipe. Each bunch of the first and second beam consists of N_1 and N_2 particles, respectively. While the number of bunches is constant in a collider run, the number of particles per bunch and beam i, N_i, decreases exponentially over time due to occurring collisions. The factors F and W quantify the reduction of luminosity due to a non-zero beam crossing angle and due to a possibly non-zero transverse offset between the beam axes, respectively.

2.6.2. Perturbation Theory and Factorization

Perturbation Theory

In general, a cross section computed in QCD can be written as an expansion in the coupling of the strong interaction, α_s:

$$\sigma = \sigma_0 + \alpha_s \sigma_1 + \alpha_s^2 \sigma_2 + \cdots , \tag{2.21}$$

where σ_i is the coefficient for the i^{th} term in the expansion in α_s. The order of the computation in perturbation theory is given by the number of terms $\alpha_s^i \sigma_i$ included in the computation. If only the first nonzero term is included, one speaks of a leading order (LO) computation. If the following term is included as well, one speaks of *next-to-leading order* (NLO) computation, and so on.

When α_s is sufficiently small, i.e. $\alpha_s \ll 1$, and there are no large logarithmic factors that could counteract a small size of α_s, it is generally appropriate to truncate this series after few terms to obtain a fixed-order result for the cross section. If, however, these conditions are not given, such a truncation becomes inadmissible because of a lack of convergence of the perturbation series. Large logarithms can arise when the computed quantity is sensitive to soft or collinear emissions [67]. Another possible reason of large logarithms that can spoil the convergence of the perturbative series is a restriction of the phase space, which prevents a complete cancellation of diverging virtual and real-emission contributions. That way, coefficients involving logarithms L or L^2 arise, where L is the logarithm of a ratio of a process-dependent mass scale and the constrained kinematic variable. If L is sufficiently large it can lead to contributions proportional

to $\alpha_s L^2 \gg 1$, spoiling the convergence of the perturbative expansion. The process of accounting for dominant logarithmic contributions for all orders in α_s is called *resummation* and can improve the accuracy of the computation significantly.

Parton Distribution Functions

The results that will be shown in this thesis are based on high-energy collisions of protons. Protons are composite particles; they consist of quarks and gluons, jointly denoted as *partons*. The momentum P of a proton thus is the sum of the momenta of the constituting partons, $x_i \cdot P$, where i denotes the considered parton and x_i is the fraction of the proton momentum that parton carries. These momentum fractions are distributed according to parton distribution functions $f_{i/h}(x, \mu)$. Such a PDF can, to leading order, be interpreted as the probability density for finding a parton of type i with a fraction x of the momentum of the hadron h at the resolution given by the scale μ [68]. PDFs cannot be computed based on perturbation theory. Instead, they are determined using fits of data from collider experiments involving scattering of protons with particles such as electrons, protons or antiprotons [3]. The PDFs encapsulate the non-perturbative aspects in the calculation of cross sections. In general, the PDFs depend on the momentum transfer Q of the scattering process. PDFs at different scales are related to each other via the DGLAP equations [69–72]. Each parton type has its own PDF. As can be seen in Figure 2.7, a gluon tends to carry a low fraction of the total proton momentum, and u-quarks and d-quarks tend to carry large fractions of the total proton momentum. Three u- and d-quarks that are, in a way, the substrate of the proton are called *valence quarks*. In addition to these three u- and d-quarks, other quark types can be found in a proton when a gluon splitting $g \to q\bar{q}$ into a virtual quark-antiquark pair occurs and the resolution scale is high enough to probe these virtual *sea quarks*.

The b-quark content of the proton deserves special consideration. One distinguishes between two flavor schemes which differ by the treatment of b-quarks in the initial state. In the 5-flavor scheme (5FS), b-quarks can be generated by a perturbative computation from the gluon- and light-quark content of the proton above a given energy threshold [68]. The largest contribution comes from the above mentioned gluon splitting, $g \to b\bar{b}$, which is taken into account in the b-quark PDF. Accordingly, b-quarks can be part of the initial state in the 5FS and are treated as

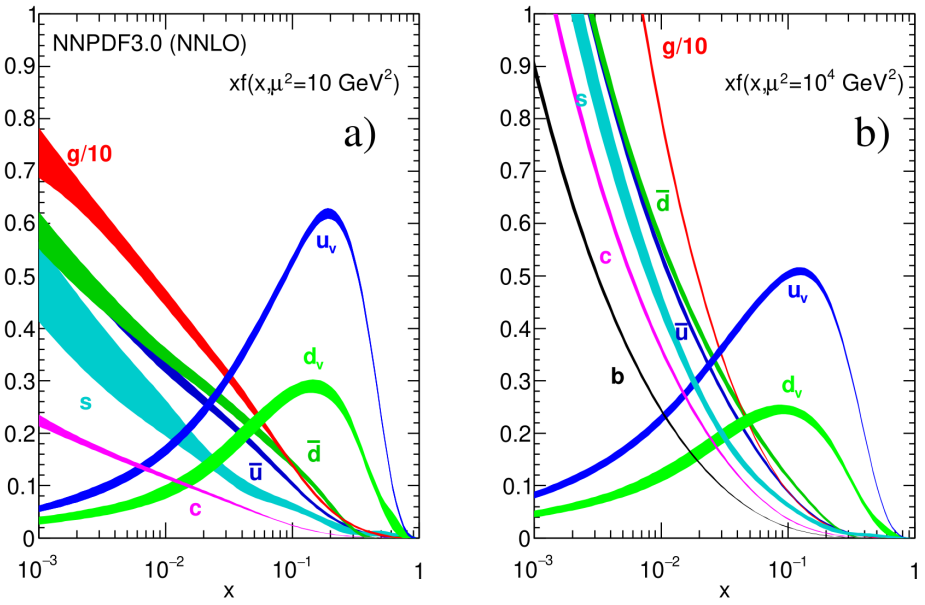

Figure 2.7. | PDFs for different parton types at a momentum transfer of $Q^2 = 10\,\mathrm{GeV}^2$ (a), and at $Q^2 = 10^4\,\mathrm{GeV}^2$ (b). Taken from Reference [6].

massless particles in that context. In the 4-flavor-scheme, on the other hand, b-quarks cannot be a part of the initial state and can only be produced via gluon splitting that needs to be taken into account in the matrix element of the considered process.

Hard-Scattering Cross Section

By factorizing the perturbative and non-perturbative aspects of the cross section computation, the scattering cross section of two colliding hadrons can be written as [68, 73, 74]:

$$\sigma_{2\to n} = \sum_{a,b} \int_0^1 \mathrm{d}x_a \mathrm{d}x_b \, f_{a/h_1}(x_a, \mu_\mathrm{F}) \cdot f_{b/h_2}(x_b, \mu_\mathrm{F}) \cdot \hat{\sigma}_{ab\to n}(\mu_\mathrm{F}, \mu_\mathrm{R}), \tag{2.22}$$

The sum runs over all contributing partons in the initial state, $a, b \in \{g,\ u,\ d \ldots\}$, and the integral over the momentum fractions of these initial-state partons. At which momentum scale the PDF is evaluated is controlled by the *factorization scale*, denoted by μ_F [68]. The hard-scattering cross section at parton level, computed perturbatively, is denoted by $\hat{\sigma}_{ab\to n}(\mu_\mathrm{F}, \mu_\mathrm{R})$. This parton-level cross section depends on both the factorization scale and on the resummation scale μ_R. The resummation scale μ_R is the scale at which the coupling strength is evaluated. Both μ_F and μ_R must be chosen adequately for the process in consideration. For example, in processes involving

a Higgs boson, the chosen scales typically are of the order m_H. These scales are unphysical in their nature, and yet they are useful variables for the calculation of cross sections. With increasing perturbative accuracy, the dependence of the cross section on these scales decreases. The residual dependence of the cross section on these scales is used to estimate the potential size of contributions from higher-order terms that have not been taken into account.

2.6.3. Monte Carlo Simulation

The calculation of cross sections involves the computation of phase-space integrals. Collision events typically have numerous particles in the final state, which necessitates the calculation of a phase-space integral with a large number of degrees of freedom. With n particles in the final state, the phase-space integral is of dimension $3n-4$, where the subtraction of 4 is takes into account the constraints from the conservation of energy and momentum [75]. Such integrals typically are not solvable by analytic methods and call for numeric approaches such as *Monte Carlo* (MC) simulations. Such simulations allow the numeric computation of high-dimensional integrals, with a statistical uncertainty on the result that decreases with the number of generated events as $1/\sqrt{N}$, independent of the number of considered integral dimensions. Therefore, typically many events are generated in order to perform the integration, using random numbers to sample the phase space over which the integral is defined. With this procedure not only the cross section can be determined, but one also obtains a sample of individual events that resemble collision events and can be analyzed to obtain information about distributions of final-state observables. When the predicted cross sections are to be compared with measurements, experimental selection cuts on the phase space need to be considered in the predictions. In MC simulations, it is relatively simple to compute cross sections within complicated phase-space regions by rejecting those generated events that fail the selection cuts. For the simulation of LHC collision events, different simulations for various steps are used:

- a simulation that takes into account the matrix element of the hard interaction,
- a simulation that describes the evolution of an outgoing parton from a high scale to lower scales by emission of further partons, a process called *parton shower*,
- a simulation of the transformation of partons to hadrons (hadronization),
- a simulation of the detector response to the simulated particles.

Ideally, the matrix element would include many real emissions and virtual loops; however, a large number of loops and emissions in the matrix element complicate its computation considerably. Moreover, the description of soft emissions involves large values of α_s, which has a negative impact on the convergence of the perturbative series. A parton shower, on the contrary, can model arbitrarily many emissions due to simplifying assumptions regarding kinematics, helicity structure and interferences between processes. Emissions of soft particles can be well described by parton showers; however, they are not the method of choice for the description of hard emissions or emissions at wide angles since the parton shower approximations are not warranted in these cases. The PYTHIA8 program is commonly used to model the parton shower [76, 77]. Once the scale decreases to values as low as approximately 1 GeV, where the strong coupling α_s becomes divergent and the hadronization of partons into hadrons takes place, the showering process of the parton shower simulation stops and a modeling of non-perturbative effects is applied. This modeling can be performed by PYTHIA8 as well by applying an implementation of the *Lund string* model [78–80].

The parton shower algorithm applied to the final-state partons from the hard interaction corresponds to performing a resummation of large logarithmic terms in the expression for the matrix element. In the case of a cross section determination using MC simulation with diagrams beyond LO, a *matching* [75] of radiative corrections to the LO matrix element with parton shower emissions need to be implemented in order to avoid double-counting of emissions as represented in the matrix element and in the parton shower.

2.6.4. Gluon-Fusion Production Cross Sections

Using techniques as described above, Higgs boson production cross sections in various phase-space regions can be computed. Among the various Higgs boson production modes, gluon fusion stands out because at the LHC it has the largest expected cross section and for that reason needs to be modeled with particular care. QCD corrections to the LO cross section prediction are sizable. Large efforts have been made to take these into account, resulting in achieving next-to-next-to-next-to-leading order (N^3LO) accuracy for the inclusive gluon fusion cross section as of today [19]. Differential gluon fusion cross sections are currently available at next-to-next-to-leading order (NNLO), as described in Section 2.6.4.

In Figure 2.3 (a) the leading-order diagram for the gluon fusion process is depicted: a pair of gluons leads to a loop of a heavy quark, which in turn produces a Higgs boson. The amplitude of this type of diagram is proportional to the Yukawa coupling of the Higgs boson to the quark in the loop. Because the top quark is the heaviest quark, the gluon fusion diagram with a t-quark in the loop gives the dominant contribution to the gluon fusion cross section. However, the gluon fusion diagrams with a b-quark or c-quark in the loop contribute to the cross section as well, in particular their interference with the gluon fusion diagram with a t-quark in the loop.

Inclusive Cross Section

In the calculation of the inclusive gluon fusion cross section, terms up to $\mathrm{N^3LO}$ are included [13, 19]. Results of NLO QCD corrections are described in References [23–25]. NNLO QCD corrections have been discussed in References [26–32]. References [33–36] present electroweak corrections to the gluon fusion cross section. Finally, the $\mathrm{N^3LO}$ QCD corrections are described in References [20–22].

Ideally, the exact quark masses enter the calculations at each order of perturbation theory. At low scales, however, the dominant t-quark-loop contribution can be safely treated as a point-like interaction that effectively couples two gluons to a Higgs boson, i.e. the t-quark loop can be integrated out by taking $m_t \to \infty$, which greatly simplifies the cross section computation. However, progress in the computation of matrix elements has allowed incorporating effects of a finite t-quark mass up to NNLO. The exact dependence on m_t is taken into account up to NLO [24, 25], whereas at NNLO an expansion in $1/m_t$ is used to correct for finite-m_t effects [29–32]. Similarly, at LO and NLO, the complexity of the calculation is sufficiently small to include also the exact effects from other quarks such as b, and c-quarks [24, 25, 81–86]. The contributions of b-quark or c-quark gluon fusion diagrams beyond NLO, including their interference with the t-quark loop, are not known. An estimate of the effect on the gluon fusion cross section of omitting these corrections has been computed in Reference [19] based on NLO results and is of the order of 1 %.

Differential Cross Sections

Differential cross sections are collections of cross sections in different phase-space regions as defined by a kinematic variable such as the Higgs boson transverse momentum p_{T}^{H}. See Section 3.2.2 for an introduction of some basic kinematic variables, including the transverse momentum. The perturbative expansion for non-inclusive cross sections tends to be less accurate than in the inclusive case. At the same time, the restriction of the phase space to the boundaries of the individual exclusive region as defined by the variable in consideration (*bin*) can make a resummation in some regions of phase space necessary.

In Chapter 6, an analysis of the p_{T}^{H} distribution aiming at extracting limits on quark Yukawa couplings is shown, which makes it worthwhile to discuss predictions for the p_{T}^{H} distribution in more detail. State-of-the-art predictions for the differential gluon fusion cross section in Higgs boson transverse momentum are of perturbative order NNLO in α_s and include logarithmic terms up to next-to-next-to-leading logarithms (NNLL). While the t-quark-loop contribution to the gluon fusion cross section and its dependence on the t-quark mass is a well understood problem, the calculation of the contribution of the b-quark loop to the gluon fusion differential cross sections is more challenging. At transverse momenta below the t-quark mass, the t-quark loop can be integrated out, which simplifies the computation by removing one loop from the considered diagram. In this approximation, NNLO accuracy was achieved. A similar approach for the b-quark loop is not possible except for transverse momenta below the b-quark mass, which is approximately 4 GeV at the relevant scales [87]. For transverse momenta above the b-quark mass, such approximation is invalid, and one has to consider the resolved b-quark loop. The resulting complexity of the calculation currently restricts the accuracy to NLO. Even though the b-quark Yukawa coupling is considerably smaller than the t-quark Yukawa coupling, the b-quark contributions to the transverse momentum distribution should not be neglected, as they can be enhanced by large logarithmic factors of the form $\ln(m_H^2/m_b^2)$ and $\ln(p_{\mathrm{T}}^2/m_b^2)$ [87]. Therefore, a resummation to all orders of these terms could be indicated; however, this has not been achieved so far. Similarly, a resummation of equivalent terms including the mass of the c-quark would be advantageous, although less important due to the smaller contribution to the gluon fusion cross section.

Below, the predictions for distributions in several kinematic variables that are presented in

comparison with the measured differential cross sections in Chapter 5 are outlined. The different predictions differ in matters such as resummation procedure and in some cases are specialized to describe particular distributions well. Several predictions of differential cross sections are obtained by means of a *soft-collinear effective theory* (SCET) [88, 89], which is an effective theory of QCD and can be used to resum logarithmic terms associated with emissions of soft and collinear gluons.

POWHEG NNLOPS

The gluon fusion MC simulation that has been used in the measurement of inclusive and differential cross sections in Section 5 is POWHEG NNLOPS [90], interfaced with the PYTHIA8 parton showering program [76, 77]. Gluon fusion production cross sections with different jet multiplicities in the final state are combined using the MINLO *merging* scheme [91]. Events are reweighted according to the Higgs boson rapidity such that resulting inclusive distributions are accurate to NNLO [92, 93]. Afterwards, a comparison of the resulting distribution in p_{T}^{H} with a prediction at NNLO accuracy of the p_{T}^{H} distribution as obtained by HRES [94, 95] is made, ensuring that both distributions agree within uncertainties. The masses of t- and b-quark are considered at LO and NLO [96]. The central renormalization and factorization scales have been chosen to be $m_H/2$.

SCETLIB+MCFM8

The MC simulation program MCFM8 [97] enables an NNLO calculation of the differential cross section in the rapidity of the Higgs boson. In this calculation, a regularization of the divergences of soft and collinear radiation is necessary. Both virtual loop corrections and radiative corrections involving soft or collinear partons lead to divergences in the computation if considered separately. In this prediction, a measure of the soft emission intensity is given by the observable τ_0, which quantifies how much an event appears like an event without jets [98]. Logarithmic terms of the form $\ln^2(-1) = -\pi^2$ are introduced to the gluon form factors[3][99, 100], which are sufficiently large to impede the convergence of the perturbative expansion. The coefficients of those logarithmic terms are related to infrared singularities and exist at all orders in α_s. By resumming those logarithmic terms with NNLL'_{ϕ} accuracy, the resulting cross section

[3]Form factors are terms that encapsulate the effect of a non-point-like charge distribution in scattering objects at a given four-momentum transfer.

is more accurate and the perturbative uncertainties are reduced. The prime in NNLL$'_\phi$ means that also some parts of N^{3}LL resummation contributions are taken into account, while the subscript ϕ signifies that the resummation is performed in the gluon form factor.

SCETLIB(STWZ)

The SCETLIB(STWZ) prediction is a NNLO prediction of the differential distribution in the momentum of the leading jet, $p_{\mathrm{T}}^{j_1}$ [101]. The SCET framework is used [100], and the corresponding resummation of logarithms of the form $\ln(p_{\mathrm{T}}^{j_1}/m_H)$ takes into account logarithms up to next-to-next-to-leading logarithm and some α_s^2 corrections that are not part of the resummation (NNLL$'$).

NNLOJET+SCET

The NNLOJET+SCET prediction [102] for the differential cross section in p_{T}^H consists of an NNLO QCD computation of the gluon fusion process in the limit of an infinite t-quark mass. The large logarithmic terms $\log(p_{\mathrm{T}}^H/m_H)$ at low transverse momentum of the Higgs boson are resummed to all orders, using SCET and includes sub-leading logarithmic terms up to the third level (N^{3}LL) [103].

RadISH

The RadISH (short for *Radiation off Initial State Hadrons*) gluon fusion prediction [104] for the differential cross section in p_{T}^H as used in this thesis has NLO accuracy in QCD perturbation theory. It is obtained through differentiation of the resummed NNLL + NNLO result in the total phase space. Details on the treatment of quark masses are described in Reference [105].

2.6.5. Quark-Initiated Higgs Boson Production Cross Section

The b-quark-initiated Higgs boson production (c-quark-initiated Higgs boson production) denotes the production of a Higgs boson via a $b\bar{b}H$ ($c\bar{c}H$) Yukawa coupling, excluding diagrams that contain a gluon fusion loop as shown in Figure 2.3 (a). The b-quark-initiated Higgs boson production cross section can be computed in two different calculation schemes, the 4FS and 5FS, see also Section 2.6.2. In Figures 2.5 (a) and (b) the LO diagrams are shown for the 4FS and 5FS, respectively. In the 4FS, the b-quark is treated as a massive particle that is not part of the proton, meaning that it can not appear in the initial state of a matrix element. Instead, b-quarks

can only appear via the splitting of a gluon into a $b\bar{b}$ pair. This flavor scheme allows more precise information about the kinematics of b-quarks in the final state, as final-state b-quarks are already described at LO, while in the case of the 5FS NLO corrections need to be taken into account in order to obtain information about final-state b-quarks. Due to collinear gluon splitting [106] logarithms of the form $\alpha_s^k \ln^k(m_b/Q)$ appear at each order of perturbation theory in the 4FS, where Q is the hard scale of the interaction [107]. At sufficiently large scales, these logarithmic terms can become sizable and can have a detrimental effect on the convergence of the perturbative series. It is possible, however, to resum these logarithms to all orders by assuming a vanishing kinematic b-quark mass and by absorbing these logarithmic terms into a b-quark PDF that is non-zero above a scale given by the b-quark mass. At the same time, the assumption of a vanishing kinematic mass does not affect the Yukawa coupling to the Higgs boson. This scheme corresponds to the 5FS, depicted in Figure 2.5 (b) for b-quark-initiated Higgs boson production. In this case, the detrimental effect of possibly large logarithmic terms on the perturbation series is reduced. Moreover, the complexity of the calculation is reduced since fewer final-state particles need to be described at LO. As a consequence, the computation of the inclusive cross section in the 5FS has been achieved at NNLO [108], while only at NLO in the 4FS so far [107, 109, 110]. On the downside, simplifying kinematic approximations have to be made in order to resum the logarithmic terms into a b-quark PDF. Moreover, the accuracy of the description of final-state b-quarks in the 5FS is worse than in the 4FS. An additional potential disadvantage of the 5FS is that power-suppressed terms of the form m_b^2/Q^2 are not included. These may be relevant at low values of the scale Q^2. Power-suppressed terms (as well as logarithmic terms) arise when two different scales such as the scale Q of the hard interaction and the b-quark mass m_b enter the calculation of a matrix element [111]. If all orders of the perturbative expansion in α_s would be included in the calculations, the 4FS and 5FS could yield identical results, as they merely represent different arrangements of the terms of the perturbation series [111]. However, at fixed order, the results generally differ. Both schemes contain complementary information and are justified in different kinematic regions. Therefore, a combination of both approaches generally is advisable. The state-of-the-art prediction [63] includes such a combination.

The picture is more complicated for differential cross sections, as additional energy scales must be considered. For the simulation of this production mode that is used in the measurement of differential cross sections as described in Chapter 5, the 4FS has been chosen, using the

POWHEG-Box framework combined with the PYTHIA8 parton shower program [112]. With this, a relatively precise description of final-state b-quarks is possible, which is advantageous since also a distribution of a b-quark-related variable is measured. For the simulation of b-quark-initiated Higgs boson production in the context of the measurement of quark Yukawa couplings in Chapter 6, however, the 5FS has been chosen in order to be on an equal footing with the prediction of c-quark-initiated Higgs boson production. The c-quark is generally taken into account in the proton PDF. Within the context of the measurement of the b- and c-quark Yukawa couplings, the MADGRAPH5_aMC@NLO software in connection with the PYTHIA8 parton shower was used [113] to predict p_{T}^{H} distributions of b-quark- and c-quark-initiated Higgs boson production cross sections; the corresponding inclusive cross sections are scaled such they match the state-of-the-art NNLO predictions [63, 64].

2.7. Limitations of the Standard Model

The SM describes the processes occurring in collider experiments at currently available center-of-mass energies well. Except for the observation of neutrino oscillations, which require non-zero, i.e. non-SM neutrino masses, the SM is compatible with all laboratory-based experiments conducted so far. There are aspects of nature, however, that can not be explained by the SM. Two major examples of these are outlined below.

2.7.1. Gravity

At scales probed with current particle colliders, gravity is negligible when compared to the interactions described in the SM [114], and can be safely omitted when performing calculations for such experiments. However, the fact that the combination of the SM with a theory of gravity has so far not been achieved should not be forgotten entirely.

While the SM is not able to describe gravity, the *general theory of relativity* (GTR) [115] is well capable of that. The GTR, however, cannot be reconciled with the SM. One of the difficulties in reconciling gravity and the SM is that the concept of time is different in quantum theory and in the GTR: in the former, time is an external, absolute element, while in the latter, it is a dynamical object. Therefore, a unification of quantum theory with the GTR would have

to involve a modification of the concept of time [114]. Another complication in the interplay of the currently prevailing theories of quantum physics and gravity is called the *black hole information paradox*. When combining quantum physics with the GTR by considering quantum field theory in a curved spacetime in the vicinity of black holes, one obtains the result that by the radiative decay of black holes in the form of *Hawking radiation* a general postulate of quantum theory is violated. This postulate says that the quantum-mechanical state of a system at a given time allows the determination of the state at any other time. With a black hole's complete evaporation by emission of Hawking radiation, whose characteristics are independent of the elements that became part of the black hole, many initial configurations would point to only one final configuration. This is in conflict with unitarity [116], a core element of quantum theory. Another problem, although not a problem of mathematical inconsistency, is the presence of singularities, for example in the center of black holes. Such singularities could hint at the existence of a more fundamental theory of gravity [114].

The interactions in the SM are quantized; likewise, it is attempted to quantize the gravitational interaction, leading to a theory containing spin-2 gravitons as quanta of the gravitational force. What has been obtained so far is only a non-renormalizable perturbative theory of quantum gravity [114], breaking down at strong gravitational fields such as in the center of a black hole. Several theories of quantum gravity that also describe the behavior at large gravitational fields have been conceived, but experimental tests of those theories are notoriously difficult, as conditions with sufficiently strong gravitational fields and large energy densities are not easily created or found in nature, except in black holes, which are presumably inaccessible in the near future. A particle collider that could provide the necessary energy density would have a size far larger than Earth itself[4].

Some theories of quantum gravity predict deviations at low energy from the predictions of the classical theory that the GTR is. Such deviations could show up when analyzing the gravitational interaction within a system of a set of particles in a quantum superposition. As the gravitational pull in the classical theory of gravitation depends on an exact distance between sources of gravity and the particles in the quantum states would have a non-pointlike localization, one can expect to gain information about the quantum properties of gravitation by measuring the gravitational

[4]With current technology, such a collider would have to be of the size of several thousand light-years in order to be able to probe scales as high as the Planck mass scale of about 10^{19} GeV and is out of reach for that reason [114].

field of a superposition of quantum states [117].

2.7.2. Dark Matter

Observations of galaxies and clusters of galaxies led to the insight that their kinematic properties are not as one would expect from the visible sources of gravity in these galaxies and galaxy clusters: velocities of stars in galaxies and velocities of galaxies in galaxy clusters tend to be higher than one would assume for a system that is exclusively bound by the gravitational force of these stars and galaxies, respectively [118]. In addition, phenomena such as the angular substructure of the *cosmic microwave background* and the structure formation in the early ages of the Universe give evidence of a cosmos that is not sufficiently described by SM-only matter which interacts as predicted by the GTR. From this it follows that either there are sources of gravitational pull that effectively do neither emit nor absorb electromagnetic radiation and hence do not interact electromagnetically, or that the gravitational force is not described well by the GTR in all situations, particularly in those of very low gravitational acceleration [118]. Both of these possibilities present some problems; however, currently the favored option is to assume the existence of *dark matter* constituted by non-SM particles such as weakly interacting massive particles with masses between 10 GeV and several TeV [6] or sterile massive neutrinos, for which constraints from structure formation of the cosmos require a minimum mass of several keV [119, 120]. Generally, numerous extensions of the SM have been put forward which give candidates for dark matter particles. In the absence of a detection of such particles by LHC and other experiments, the nature of dark matter is not known at this point.

2.8. Summary

The SM is a highly successful quantum field theory of the interaction of fundamental particles. It has been tested in countless experiments, and thus far, no significant deviation has been observed. The SM comprises the electroweak and strong interactions. Both are gauge theories and as such they operate on symmetry principles applied to an internal space of the interacting quantum fields. The quantum of the Higgs field, which enables elementary particles to have non-zero masses within the context of the SM, was the last remaining part to be discovered, until 2012. In that

year, the CMS and ATLAS experiments discovered a scalar resonance at a mass of approximately 125 GeV. Within present uncertainties, this boson appears consistent with being the SM Higgs boson. One of the discovery channels, and one that can well be used to study the properties of the Higgs boson in detail, is the Higgs boson decay to two photons.

In order to predict Higgs boson production cross sections in proton-proton collisions and to compare those to measured cross sections, accurate QCD calculations are necessary. Here, both inclusive cross sections and differential cross sections are of interest. The prediction of cross section requires the use of the several computational techniques such as the factorization of perturbative and non-perturbative aspects, MC simulation, and the resummation of large logarithms that can spoil the convergence of the perturbative series.

If one attempts to combine the SM with the theory of general relativity, inconsistencies arise, and so far, attempts at a combination were not successful. The SM does not provide a candidate for the explanation of the phenomenon of dark matter, which shows its effect in many astronomic and cosmological observations. These problems hint at the existence of a more fundamental theory, which can incorporate more of the observed phenomena of nature. From the perspective of particle physics, it is a well-motivated endeavor to study the properties of the most recently discovered fundamental particle and only fundamental scalar of the SM, the Higgs boson.

3. The ATLAS Experiment

3.1. The Large Hadron Collider

3.1.1. Introduction

The *Large Hadron Collider* (LHC) is a proton accelerator and collider located at CERN (Geneva, Switzerland). At the present time, it is the world's largest collider, having a circumference of 26.7 km [121]. This large radius allows a proton energy of currently up to 6.5 TeV, corresponding to a center-of-mass energy of $\sqrt{s} = 13\,\text{TeV}$. The two proton beams rotate in opposite direction in two beampipes. At four locations around the ring the beams cross, resulting in proton-proton collisions. Detector experiments are located at each of the four beam intersection. Besides proton-proton collisions, the LHC can also be used to study collisions of heavy ions and collisions of protons with heavy ions. For this thesis, only proton-proton collisions are relevant.

3.1.2. Acceleration and Collision

The LHC is the end of a chain of several accelerators [122] which are used to bring low-energy protons up to an energy of 6.5 TeV. The initial proton source feeds into the *linac*, a linear accelerator that accelerates protons to an energy of 50 MeV. At that point, the protons enter a circular accelerator called *booster*. Here, the protons are brought to an energy of 1.4 GeV and are subsequentially injected into the *proton synchrotron*, in which protons reach an energy of 25 GeV. The remaining acceleration that brings the protons to an energy of 450 GeV, which is sufficient for injection into the LHC, is performed by the *super proton synchrotron*.

The proton beams are divided into *bunches*. A bunch is a collection of protons that is contained within one bucket of the radio-frequency field used for acceleration. Each bunch contains about 10^{11} protons. The number of bunches per beams depends on the data-taking period; in 2015

and 2016, the beams were constituted by 2232 and 2208 bunches, respectively, while in 2017 and 2018 the number of bunches per beam was 2254. The radio-frequency field is shaped via superconducting cavities. Superconducting dipole magnets are used to keep the proton bunches on their trajectory. At the time of injection of protons into the LHC ring, the magnetic field that is necessary to keep the protons on their path has a magnetic flux density of 0.5 T. The magnetic field then is gradually ramped up in order to match the increasing energy of the proton beams. At a proton energy of 7 TeV, the necessary magnetic flux density would amount to 8.3 T [121]; however, since a reduced energy of 6.5 TeV at collision has been chosen, the required magnetic flux density is reduced by a factor of $E/E_{\text{max}} = 6.5/7$. In order to obtain focused beams, quadrupol magnets are used, which confine the beams in both horizontal and vertical direction. By a system of quadrupole magnets, the beams are confined to a small cross-sectional area. Before entering the interactions points within the detectors, the beams are squeezed to an RMS beam size of approximately 17 µm [121].

3.1.3. Pileup

The average number of proton-proton interactions in a bunch crossing during normal data-taking during the years 2015 – 2018 is significantly higher than 1, as can be seen in Figure 3.1, which gives information about the mean number of proton-proton interactions per bunch crossing for the different data-taking periods. Averaging over the four years, a typical bunch crossing results in more than 30 proton-proton interactions.

The proton-proton interaction that triggers the recording of an event is typically the interaction in which the largest momentum transfer occurs, the *hard interaction*. When additional proton-proton interactions occur in the same bunch crossing, one speaks of *in-time pileup*. Such pileup interactions result most frequently in emissions of particles with low transverse momentum. Particles from pileup interactions result in additional signatures in the detector, which can complicate the reconstruction of particles and the calibration of the measurement of their energy. *Out-of-time pileup* occurs due to detector components which are influenced by previous bunch crossings or due to a readout time of detector information longer than 25 ns [124].

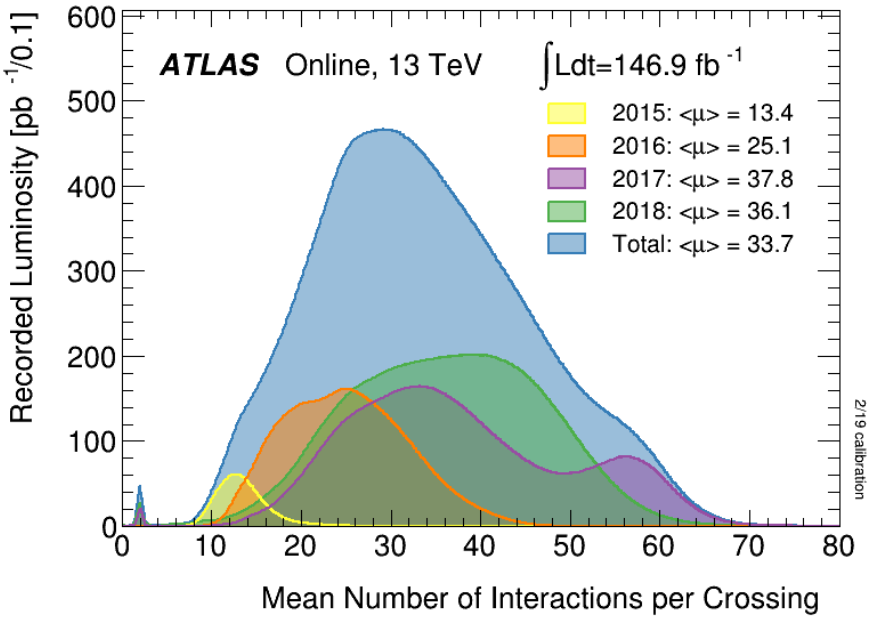

Figure 3.1. | Distribution of recorded luminosity as a function of the mean number of interactions per bunch crossing for the data-taking periods from 2015 to 2018. Taken from Reference [123].

3.2. The ATLAS Detector

3.2.1. Introduction

The ATLAS experiment is one of the four large detector experiments located at the LHC. ATLAS is a general-purpose detector, meaning that it can be used to analyze a broad range of possible types of physics events, including phenomena such as decays of Higgs bosons or events involving physics beyond the SM. For this, the detector needs to be able to detect as many particle types as possible and allow the reconstruction of corresponding physics objects for later analysis. In order to achieve this, several detector systems need to be combined, which is due to the fact that different types of particles interact differently with matter. Moreover, different detector components are used to measure different particle properties, such as trajectories, momentum, and energy. A good resolution of these measurements is important for many aspects of physics analyses.

Neutrinos leave the detector without a direct trace, as would some hypothetical non-SM particles. The conservation of momentum helps to detect such particles: the initial state of the colliding proton-proton system has effectively no transverse momentum component. Due to

conservation of momentum, the final state should have net-zero transverse momentum as well. By balancing the transverse momenta of all particles from a given proton-proton interaction against each other, missing transverse momentum resulting from particles such as neutrinos can be registered. In order to measure the missing transverse momentum as accurately as possible, the detector needs to be as hermetic as possible. The finite extent of the beam line is a limiting factor in this regard; particles that are emitted in an angle very close to the beam line cannot be detected, which is a limiting factor in the resolution of the measurement of missing transverse momentum.

Besides a large degree of hermeticity, a requirement for the ATLAS detector is the ability to withstand large amounts of radiation. This requirement is particularly important in the regions close to the beam pipe since this part of the detector is subject to the highest particle flux.

Concretely, the ATLAS detector consists of three major subdetector systems, each of them dedicated to another purpose. From the innermost to the outermost detector layer:

- The *inner detector* is used to detect charged particles and to measure their momentum and charge sign, making use of a solenoidal magnetic field.
- The *calorimeter* is used to measure the energy of particles, except the energy of neutrinos and muons.
- Most of the charged particles that can traverse and leave the calorimeter are muons. Their momentum is measured with the *muon spectrometer* using a toroidal magnetic field.

An overview of the ATLAS detector, in which these subdetectors and their components are depicted, is given in Figure 3.2.

3.2.2. Coordinate System and Kinematic Observables

As protons of both beams carry the same energy, the ATLAS detector is designed in a way that is symmetric in both beam directions. Moreover, the detector has an azimuthal symmetry since no transversal direction is in any way distinguished from another one by physical principles. Correspondingly, the ATLAS detector has a cylindrical shape. The Cartesian coordinate system that is used to describe the detector is aligned as follows: the z-axis is parallel to the beam directions. Both x- and y-axes are perpendicular to the z-axis. The x-axis is pointing towards the middle of the LHC ring, and the y-axis is pointing upwards [126]. An additional and often

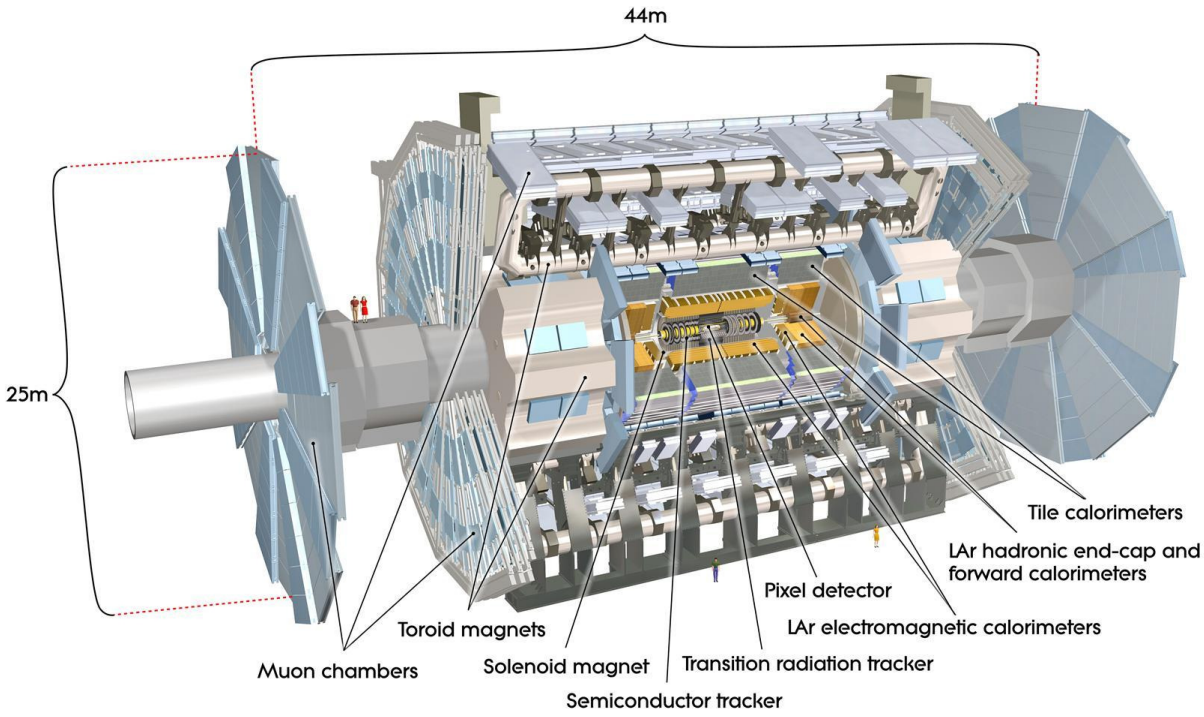

Figure 3.2. | Sketch of the ATLAS detector. Taken from Reference [125].

more useful way of describing the detector structure is a cylindrical coordinate system. In that case, a location in the detector is fully specified by the radius R, the azimuthal angle ϕ, and the z-coordinate along the beam axis. The azimuthal angle is defined by $\tan(\phi) = \Delta y/\Delta x$. It is convenient to define a polar angle $\tan(\theta) = \sqrt{(\Delta x)^2 + (\Delta y)^2}/\Delta z$.

The trajectory of particles in the ATLAS detector can be reconstructed based on the coordinates of the energy depositions the particles leave in the different subdetectors. The momentum then can be determined by observing the curvature of the trajectory in the magnetic field. Particularly the transverse momentum, $p_\mathrm{T} = \sqrt{p_x^2 + p_y^2}$, is a useful quantity when analyzing collisions of composite particles such as protons. The total momentum of a particle is given by $|\vec{p}| = \sqrt{p_\mathrm{T}^2 + p_z^2}$, where p_z denotes the longitudinal component of the particle's momentum. Because the initial longitudinal momenta of the incoming partons within the colliding protons are unknown, the longitudinal momentum of a particle emerging from a proton-proton interaction is of limited relevance for later analyses. Large transverse momenta on the other hand are indicative of interactions with a large momentum transfer, which are of particular relevance if processes involving considerable energy scales such as the Higgs boson mass are considered.

A variable closely related to the polar angle is the *rapidity*, given by

$$y = 0.5 \ln\left(\frac{E + p_z}{E - p_z}\right), \tag{3.1}$$

where E denotes the energy of the particle. Unlike differences in polar angles, differences in rapidity are invariant under Lorentz boosts in the longitudinal direction, i.e. along the z-axis. When the mass of the particle is much smaller than its energy, it is useful to consider the pseudorapidity instead of the rapidity because it only depends on the polar angle, not on the particle's energy, and correspondingly is easier to determine:

$$\eta = -\ln\left(\tan\left(\frac{\theta}{2}\right)\right). \tag{3.2}$$

The relation between η and θ is illustrated in Figure 3.3.

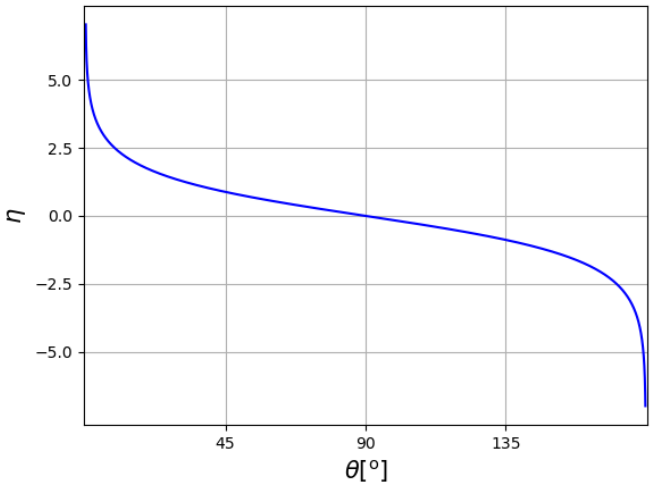

Figure 3.3. | Pseudorapidity η as function of the polar angle θ.

3.2.3. The Inner Detector

Introduction

The primary function of the inner detector is the tracking of the trajectory of charged particles. Making use of the curvature of trajectories of charged particle in a solenoidal magnetic field, the trajectory can be used to determine particle momenta and the sign of their electric charge. The

curvature of a particle with charge q in a solenoidal magnetic field with flux density B is given by

$$R_{\text{curv}} = \frac{p_{\text{T}}}{q\,B}\,. \tag{3.3}$$

Accordingly, the more the trajectory of a particle with a given charge is bent by the magnetic field, the smaller is its transverse momentum. The sign of the electrical charge is determined based on the direction in which the trajectory is bent. Another important task that can be performed with tracking information from the inner detector is the reconstruction of proton-proton interaction vertices and displaced vertices, the latter resulting from decays of relatively long-lived hadrons. Additionally, secondary vertices from interactions of neutral particles like photons with the inner-detector material can be reconstructed.

Because dense materials tend to alter the trajectory of particles significantly and consequently reduce the reliability of the momentum and charge-sign determination, materials with a sufficiently low density must be used in the inner detector. Both silicon semiconductor detectors and gaseous ionization detectors are employed as tracking detectors in ATLAS. The material distribution of the components of the inner detector is shown in Figure 3.4 in terms of *radiation lengths* X_0. The radiation length gives the distance for a given material in which electron energies decrease due to particle-material interactions by a factor of $1/e$. Below a pseudorapidity of about $|\eta| \approx 0.6$, the cumulative amount of inner-detector material is below $0.5\,X_0$, while it is typically in the range of $1\,X_0$ to $2\,X_0$ at pseudorapidities between 0.6 and 4.

The magnetic field in the inner detector is generated by a superconducting solenoid that surrounds the inner detector and has a magnetic flux density of $B = 2\,\text{T}$ [126]. The solenoidal field configuration, which consists in a magnetic field that is aligned with the beam direction to a good approximation in the central region of the detector (*barrel* region), enables the measurement of the transverse momentum of a charged particle. At larger radii in the *endcap* regions of the inner detector, the spurious radial component of the magnetic field reaches its maximum, which is about one order of magnitude lower than the longitudinal component [126].

The shape of the inner detector is that of a cylinder with a radius of 1.08 m and a length of 7 m. The acceptance in terms of pseudorapidity is $|\eta| < 2.5$. Three subdetectors are part of the inner detector (from innermost to outermost), see Figure 3.5 and 3.6:

- Pixel detector

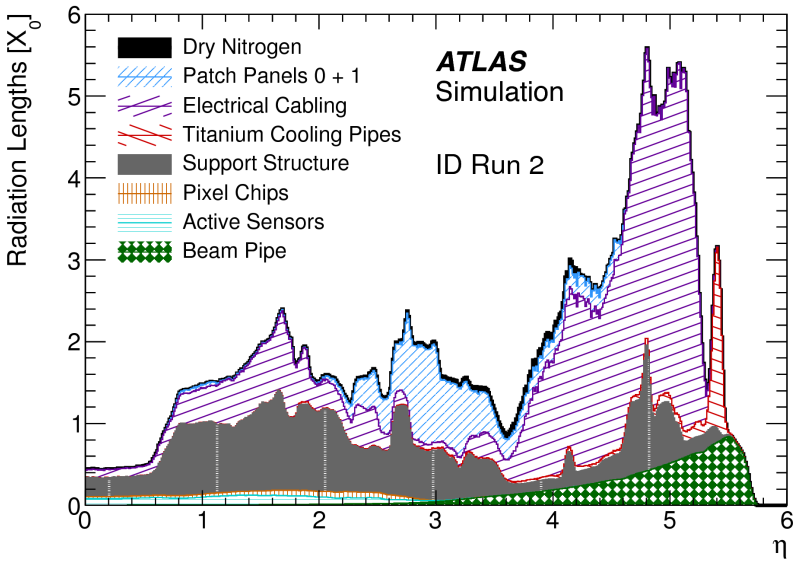

Figure 3.4. | Material distribution of the inner-detector components in terms of the radiation length X_0 as a function of pseudorapidity. Taken from Reference [127].

- Semiconductor Tracker (SCT)
- Transition Radiation Tracker (TRT)

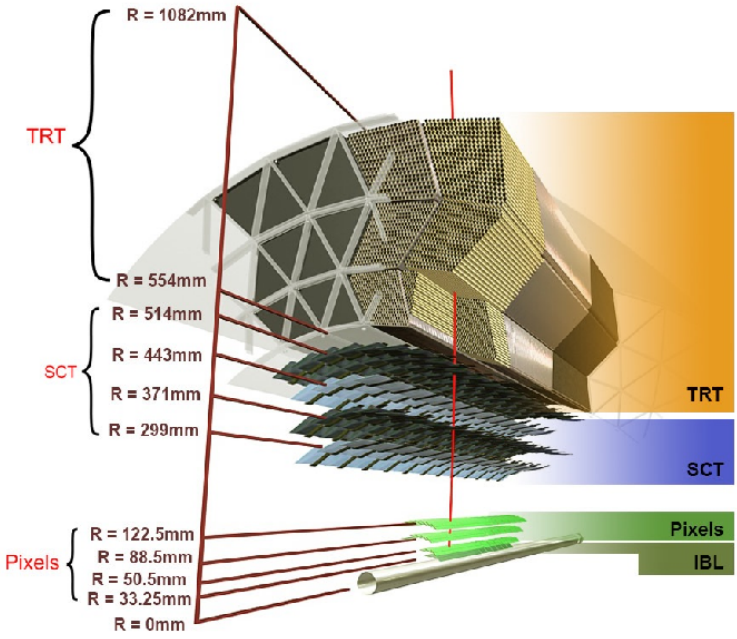

Figure 3.5. | Representative segment of the inner-detector barrel with a particle leaving the interaction point at $R = 0\,\text{mm}$ and traversing the inner detector. Taken from Reference [128].

Both pixel detector and SCT are based on doped silicon sensors which allow a very accurate

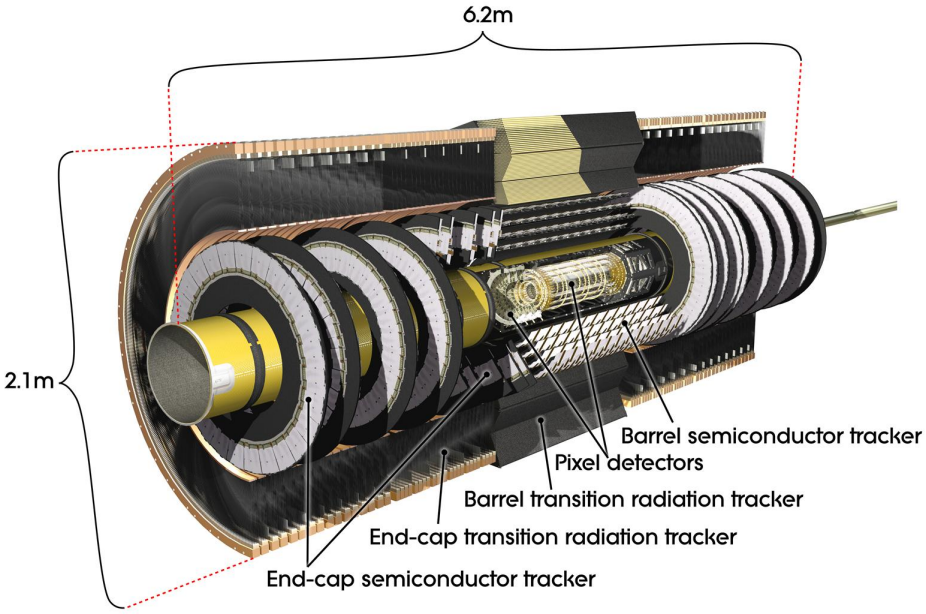

Figure 3.6. | A sketch of the inner detector. Taken from Reference [129].

determination of the localization of an energy deposition by an energetic particle due to the fine segmentation of the silicon sensor modules. By connecting the silicon sensors of the pixel detector and the SCT to high voltage, energetic charged particles traversing these sensors result in measurable electric signals, based on which the tracks of these particles can be reconstructed. When traversing charged particles deposit energy in the sensor material, *electron-hole pairs* are created. *Holes* are non-occupied electronic states of the semiconductor which effectively behave as positively charged particles.

In the case of the SCT, a voltage of 150 V is applied in most modules. Due to radiation damage, in some segments of the SCT a voltage of 200 V or 250 V is applied in order to retain a high detection efficiency. The high voltage in the pixel detector is chosen differently for different parts: in order to compensate radiation damage effects, it has been raised over the course of data-taking in the years 2015 – 2018 to up to 400 V in the IBL and B-layer, and to 250 V in the other layers and in the endcaps.

The TRT detector is a gaseous detector. When an energetic charged particle travels through the gas in the detector, gas molecules or atoms are ionized, leading to free charge carriers. The application of a high voltage leads then to an electric current, which can be read out. In addition to serving as a tracking detector like the pixel and SCT detectors, the TRT can also be used to

discriminate between electrons and hadrons, based on the amount of electromagnetic radiation that is emitted when a charged particle of a given mass moves between regions of different refractive index. The amount of this *transition radiation* depends on the particle mass, and, as a consequence, on the particle type.

The Pixel Detector

The pixel detector comprises four (barrel) and three (endcaps) silicon pixel layers that are located close to the beamline. Thanks to the small distance to the interaction point, the pixel detector is of paramount relevance for the determination of the points from which particles emerge. In the barrel region, the layer closest to the beam pipe is located at a radial position of 3.3 cm, and the outermost layer at a radial position of 12.3 cm. In the endcaps, three disk-shaped layers of pixel sensors are installed; the disk closest to the interaction point is located at $z = 49.5\,\text{cm}$, the most distant disk at $z = 65.0\,\text{cm}$ [130]. The small size of pixel sensors results in a very good spatial resolution of localized energy depositions, called *hits*, from particles. In both barrel and endcaps, the intrinsic resolution in $R-\phi$-direction is 10 µm [126][130]. The resolution of the second coordinate measured by the pixel detector, z in the barrel and R in the endcaps, is of the order 115 µm [126].

The SCT

The inner-detector component that follows the pixel detector both in radial proximity to the beam pipes and in spatial resolution of track hits is the SCT. Unlike the pixel detector, the SCT sensors consist of silicon microstrips and not silicon pixels. Layers of microstrips alone would not enable measuring two coordinates, which, in combination with information about the location of the sensor module, would allow the determination of 3-dimensional coordinates of energy depositions. However, by attaching two microstrip modules on top of each other with a small stereo-angle of 40 mrad, the readout from both modules can be used to extract information about the location in which a particle traversed the microstrip modules. In the barrel, there are four double layers of silicon microstrips, while in the endcaps, nine double-layer disks are installed. The resolution which is achieved by the SCT in $R-\phi$-direction is 17 µm [126]. In the barrel region, the z-coordinate is measured as second coordinate, while in the endcaps it is the radial

coordinate R, in both cases with a resolution of 580 µm.

The TRT

The TRT uses gas as medium, which is contained in proportional drift tubes, called *straw tubes*, with a diameter of 4 mm [131]. Their inner surface is coated with an aluminum layer. In the center of the straw tubes is a thin gold-plated wire anode. High voltage of 2 kV [126] is applied between the wire and the aluminum coating, such that free charge carriers produced by energetic particles traversing the gas lead to a measurable current. Although the spatial resolution of energy depositions in the straw tubes is worse than in the silicon detectors, the TRT provides important input for the determination of particle trajectories, owing to the large number of straw tubes.

Due to the arrangement of the straw tubes, in the barrel region only $(R-\phi)$ coordinates are measured. The only information about the z-coordinate here is given by the fact that the barrel TRT is divided in the center, at $z = 0$. The $(R-\phi)$ resolution is of the order 100 µm [126]. In the endcaps, the TRT provides information about the $z-\phi$ coordinates of tracks, but not about the radial position. The TRT has an acceptance of $|\eta| < 2.0$.

The TRT can be used to discriminate between electrons and more massive charged particles, most notably charged pions. For this, the straw tubes are interlaced with polypropylene or polyethylene. The transition of a charged particle between materials with differing dielectric constants such as gas-filled straw tubes and plastics leads to the emission of electromagnetic radiation called transition radiation. The intensity of this radiation is related to the Lorentz factor of the traversing particle. Typically, transition radiation photons have energies of the order keV, sufficient to ionize the noble-gas atoms, which are a major component of the gas mixture in the straw tubes. The additional ionization due to transition radiation enhances the signal, which allows an estimation of the Lorentz factor of the traversing particle. By combining this estimate with the measured momentum of the particle, its mass can be estimated, which allows discriminating between electrons and more massive particles. Two signal thresholds are set for the TRT operation: a value for the energy deposition above which a hit for tracking is recorded, and a greater value that is used to discriminate between electrons and more massive particles based on transition radiation. In Figure 3.7 an event display containing different kinds of hits in

the inner detector is shown, highlighting hits in TRT that exceed the transition radiation signal threshold.

The gas mixture in the straw tubes consists mostly of a noble gas, carbon dioxide and oxygen [126]. At the beginning of LHC operation, a xenon-based gas mixture was used in all straw tubes. Due to several leaks in the gas distribution system that developed in 2012, it was decided to operate the TRT with an argon-based gas in the affected parts of the TRT, as argon is considerably less expensive than xenon [132]. Compared to the xenon-based gas mixture, the argon-based gas mixture results in a worse electron identification performance due to a smaller efficiency of absorbing transition radiation.

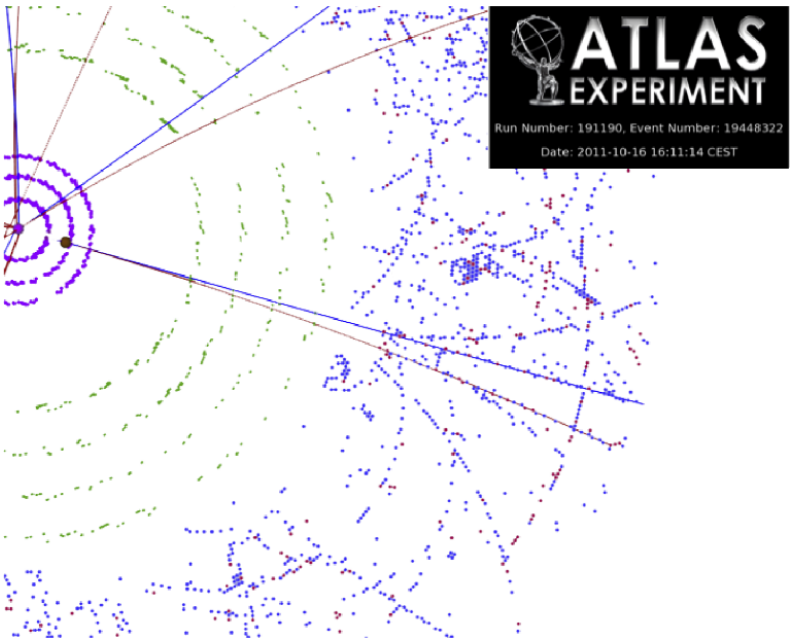

Figure 3.7. | An event display illustrating hits from particles and reconstructed tracks in the inner detector, projecting the pseudorapidity region $-1 < \eta < 0$ to a plane. Hits in the pixel detector are shown in purple, SCT hits in green. TRT hits with signals above the tracking threshold are colored blue, those with signals above the transition radiation threshold are colored red. The black dot in the pixel section corresponds to a reconstructed photon conversion vertex. Taken from Reference [132].

3.2.4. The Calorimeter

Introduction

The ATLAS calorimeter is an instrument that measures the energy of particles. In order to perform this measurement, the incoming particle needs to distribute its energy in a cascade of

interactions with the calorimeter material, producing a detectable electric signal and completely stopping the primary particle and its secondary particles.

The calorimeter used in the ATLAS detector consists of several sub-calorimeters, all of which are *sampling* calorimeters. In a sampling calorimeter the *active*, i.e. detecting material is interleaved with *passive* material whose purpose is to interact with the particles as intensely as possible, creating a *shower* of secondary particles. This showering leads to a transfer of the energy of the incoming particle to electrically detectable energy deposits in the sampling calorimeter through a multitude of ionization processes. A part of this energy is deposited in the active calorimeter layers, and the rest in the passive calorimeter layers. Therefore, one needs to extrapolate from the energy deposited in the active material to the total deposited energy. In order to achieve a complete absorption of the energy of the initial particle, which is advantageous for a good energy resolution, the calorimeter must be sufficiently thick. Such an approximate hermeticity allows assigning imbalances in summed transverse energy reliably to neutrinos or other tracelessly leaving particles. Moreover, the muon detector that surrounds the calorimeter relies on the assumption that effectively no charged particle except muons can reach it, which means that all other charged particles should be stopped in the calorimeter.

Particles that interact via the strong force have other showering properties than electrons and photons, which disperse their energy exclusively via electromagnetic interactions. In order to measure the energy of both exclusively electromagnetically interacting particles and strongly interacting particles as accurately as possible, several types of calorimeters are used in ATLAS. A particle on its way from the primary interaction point encounters first the *electromagnetic calorimeter* (EM calorimeter), and next, if not already absorbed by the EM calorimeter, the *hadronic calorimeter*.

Electromagnetic Showers and the Electromagnetic Calorimeter

Once a particle such as an electron or photon enters the electromagnetic calorimeter, a shower consisting of secondary photons and electrons is initiated. For high-energy electrons, the relevant scattering process with the detector material is *bremsstrahlung*,

$$e^{\pm} + X \rightarrow e^{\pm} + \gamma + X \,,$$

where X represents a constituent of the calorimeter material. In case of photons, the relevant interaction with the detector material is electron-positron pair production,

$$\gamma + X \rightarrow e^+ + e^- + X\,.$$

By subsequent occurrences of these two processes, an electromagnetic shower with a multitude of constituting secondary particles is created. In each scattering process the energy of the incoming photon or electron is further divided and is thus dissipated among a larger number of particles. At some point the energy of the products of these two basic interaction types has decreased to the point that it is not sufficient to produce further secondary particles, and the showering stops. What remains of the kinetic energy is then absorbed by the material by Compton scattering or the photo-electric effect in the case of photons or ionization in the case of electrons [133].

The ability of a material to impede the propagation of an incoming particle by initiating the development of an electromagnetic shower can be quantified in terms of the radiation length X_0, as introduced in Section 3.2.3. It depends on the *atomic number* of the material, that is, on the number of protons in the material's nuclei, which in turn directly relates to the amount of electric charge that interacts with the incoming charged particles.

Liquid argon (LAr) is used in the EM calorimeter as active material, and lead, which has a radiation length of $X_0 = 5.6\,\text{mm}$, as passive material. The mean free path λ of an energetic photon before undergoing a pair-production interaction is directly proportional to the radiation length of the material, $\lambda = X_0 \cdot 9/7$.

The EM calorimeter is located between the inner detector's solenoid magnet and the Hadronic Calorimeter. In Figure 3.8, the EM calorimeter is shown in context with the inner detector and the hadronic calorimeter. It consists of a barrel part and two endcap parts. In order to sample the particle showers multiple times in depth and in order to have a homogeneous response in the whole azimuthal range, an *accordeon* shape of the active and passive layers has been chosen, see Figure 3.9. The EM calorimeter is encompassed by a cryostat whose purpose is to keep the argon in a liquid state.

Copper anodes are submerged in the layers of LAr between the lead absorbers. Traversing energetic particles ionize argon atoms and thereby create free charge carriers, which, in the presence of a high voltage of 2 kV [126], leads to a detectable current based on which energy

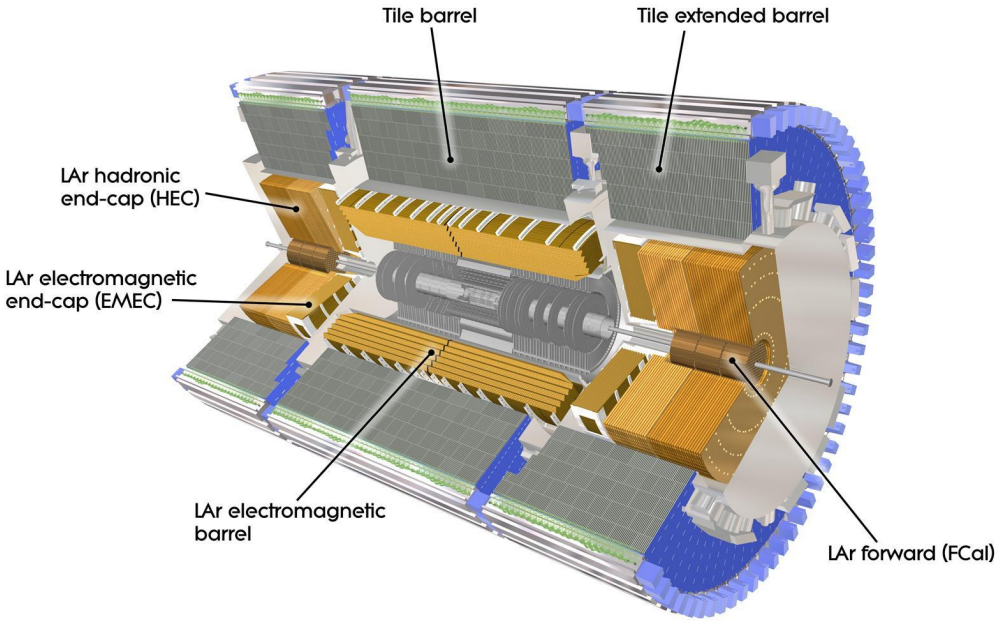

Figure 3.8. | Sketch of the ATLAS calorimetric systems. The EM calorimeter consists of the LAr electromagnetic barrel and the LAr electromagnetic endcap. Taken from Reference [126].

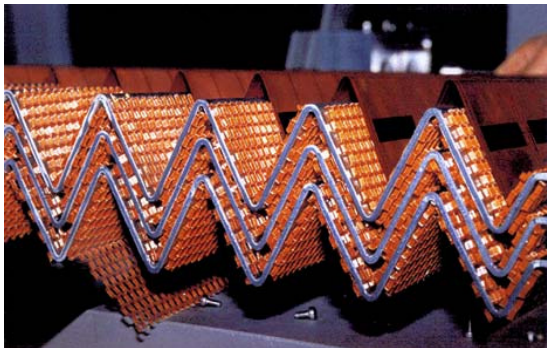

Figure 3.9. | Illustration of the sampling structure of the EM calorimeter. Taken from Reference [134].

depositions can be measured.

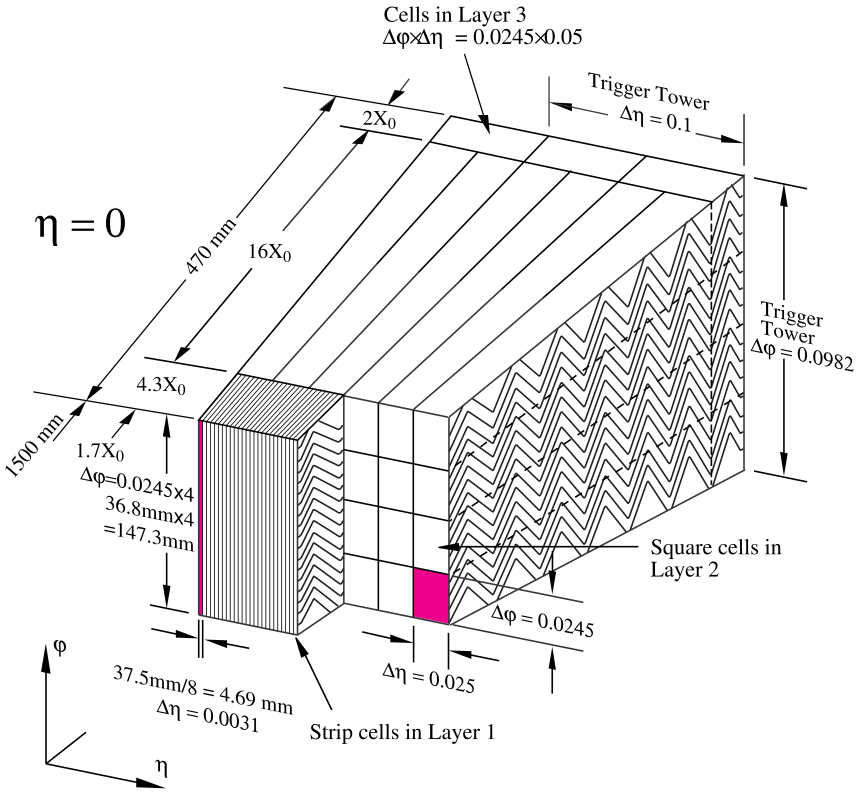

Figure 3.10. | Longitudinal and lateral segmentation of the EM calorimeter. Taken from Reference [126].

The EM calorimeter is segmented both laterally and longitudinally, which allows the determination of the shape of electromagnetic showers. This segmentation is shown schematically in Figure 3.10. In the region $0 < |\eta| < 2.5$, the EM calorimeter comprises three longitudinal layers, while it has two layers in the more forward region $2.5 < |\eta| < 3.2$. Each longitudinal layer has a different lateral segmentation granularity. The material distributions in each of these layers is shown in Figure 3.11. The cumulative amount of material typically is of the order $30\,X_0$. The innermost layer, called the *strip layer*, has a fine segmentation in η-direction in the central region of about 0.5 cm. This high granularity is essential for the discrimination between collimated pairs of photons created by the decay of neutral mesons such as π^0 and single photons or electrons. The granularity is significantly reduced in the more forward region $|\eta| > 2.4$. Below $|\eta| < 2.5$, the first EM calorimeter layer contributes about $5\,X_0$ of stopping material and correspondingly absorbs a sizable fraction of the energy of photons and electrons. The second layer has a finer granularity in ϕ, but a reduced granularity in η-direction, compared to the strip layer. In both

lateral directions its cell size is about 4 cm. It is the thickest layer below a pseudorapidity of $|\eta| < 2.5$; therefore, it contributes significantly to the stopping power of the EM calorimeter. In the region $|\eta| < 2.5$, a third layer with reduced granularity in η-direction is installed in order to capture the outermost part of very energetic showers. In η direction, the cell size is about 10 cm, whereas in ϕ-direction it is about 5 cm.

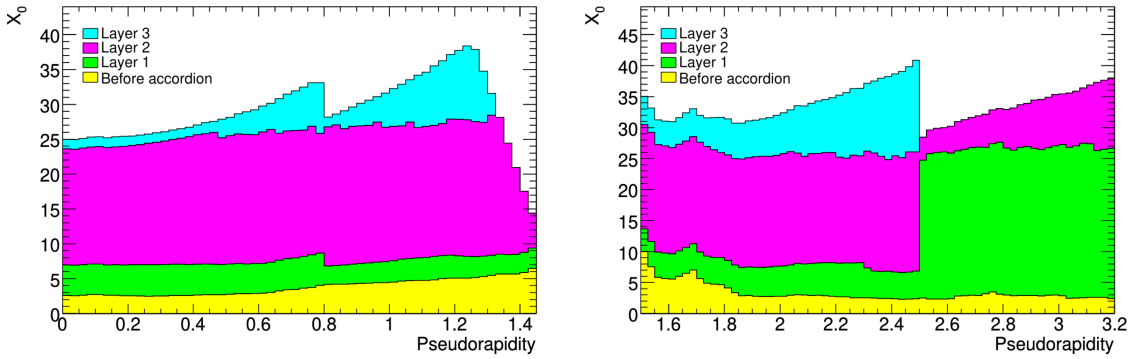

Figure 3.11. | Material distribution of the EM calorimeter in terms of the radiation length X_0 as a function of pseudorapidity. The left plot shows the distribution for the barrel region, while the right plot shows the distribution for the endcap region. Taken from Reference [126].

An additional detector called *presampler* is installed between the inner detector and the EM calorimeter in the range $|\eta| < 1.8$. It is used to correct for energy losses of particle due to showering in the material of the cryostat and the supporting structures.

Hadronic Showers and the Hadronic Calorimeter

Hadrons, which interact via the strong interaction and depending on the type also via the electromagnetic interaction with the detector material, lead to showers that tend to be more wide-spread and less regular than purely electromagnetic showers. Due to the frequent emission of gluons which subsequentially hadronize, hadrons from energetic proton-proton collisions form more or less collimated sprays of hadronic particles, called *jets*. The initial composition of these jets entering the calorimeter has influence on the fraction of energy that is deposited in the EM calorimeter: neutral mesons such as π^0 are abundant in showers of hadronic particles, and they decay most frequently to a pair of photons, which can be efficiently absorbed in the material of the EM calorimeter; the fraction of jet energy that is deposited in the hadronic calorimeter is correspondingly reduced. An additional complication consists in the ability of

strongly interacting particles to deposit energy in nuclei of the detector material, which is released sometimes only with significant delay. All this makes the modeling of hadronic showers and their energy measurement challenging, which is why the energy resolution for hadronic particles typically is worse than that for electrons or photons.

The two main purposes of the hadronic calorimeter are to measure the energy of jets, and to discriminate between hadrons and electromagnetic objects, such as photons and electrons, by determining the fraction of particle energy that is deposited in the hadronic calorimeter.

The granularity of the hadronic calorimeter subdetectors is generally coarser than that of the EM calorimeter. Three different combinations of active and passive material are used. The *tile calorimeter* covers the range $|\eta| < 1.7$. Its radial depth amounts to about 7 interaction lengths λ, defined as the mean distance a hadronic particle travels before it interacts with the material via the strong interaction. The passive material used in the tile calorimeter is steel, and scintillators are used as active material. The light emitted by the scintillators that are excited by the shower particles is shifted from UV light to a wavelength that efficiently activates the photon multiplier tubes into which the light is fed via readout fibers. The *hadronic endcap calorimeter* covers the range $1.5 < |\eta| < 3.2$ and uses LAr as active material. Copper was chosen for the passive absorber elements. The *forward calorimeter* spans from $|\eta| = 3.1$ to $|\eta| = 4.9$. It consists of three modules, the first of which employs copper as passive material. For reasons of shower containment, tungsten is used as absorber material in the two following modules. The active material was chosen to be LAr. The structure of the forward calorimeter modules corresponds to massive blocks of metal interspersed with thin tunnels containing LAr and electrodes.

In Figure 3.12 the material distribution of the various components of the ATLAS detector, excluding the muon spectrometer, is shown in terms of the interaction length λ. The hadronic calorimeter contributes most to the calorimeter's ability to absorb the energy of hadronic particles. Typical values for the stopping power are $10\,\lambda$, which is a relatively small value when compared to the electromagnetic stopping power of the calorimeter.

3.2.5. The Muon Spectrometer

Muons result in a very distinct signature in the ATLAS detector. Due to their electric charge they leave tracks in the inner detector. Unlike electrons, however, they are not stopped in the

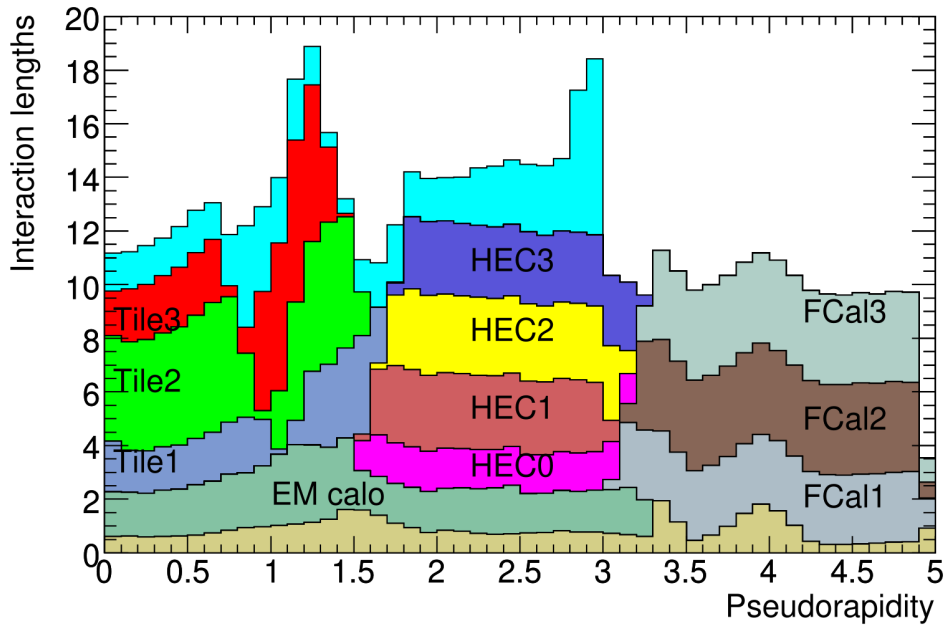

Figure 3.12. | Material distribution of the ATLAS detector excluding the muon spectrometer in terms of the interaction length λ as a function of pseudorapidity. The ocher-colored distribution corresponds to the material in front of the EM calorimeter. The distribution that is colored light-blue corresponds to the material between the hadronic calorimeter and the first sensitive layer of the muon spectrometer. Taken from Reference [126].

calorimeter. This is due to their relatively large mass which leads to less energy losses via photon emissions in presence of the detector material. Hence, they traverse the calorimeter relatively undisturbedly. In order to accurately measure the momentum of muons and to distinguish muons from other particles such as electrons, a dedicated detector for the reconstruction of muon tracks was installed, called the *muon spectrometer*. The muon spectrometer surrounds the hadronic calorimeter and is immersed in a magnetic field, which allows a momentum measurement through the curvature of the muon's path within the muon spectrometer, improving on the momentum measurement by the inner detector. Below a muon transverse momentum of 30 GeV, the inner detector provides the most accurate measurement of the transverse momentum, while above that value the muon spectrometer dominates the measurement [126]. The magnetic field is created by superconducting toroidal magnets. In order to achieve an optimal momentum resolution, the segmentation of the muon spectrometer is finest in the direction parallel to the direction into which the toroidal magnetic field bends the muons.

All muon spectrometers sensors operate on the principle of gaseous ionization detectors [126].

The muon spectrometer spans a pseudorapidity range of $|\eta| < 2.7$. Triggering is performed using three layers of *resistive-plate chambers* in the region $|\eta| < 1.05$ and three layers of *thin-gap chambers* in the region of $1.05 < |\eta| < 2.4$. These two types of subdetectors also provide information about the η- and ϕ-components of muon tracks. Two additional types of sensors are responsible for an accurate measurement of the muons' tracks in the bending plane. In the central region, *monitored drift tubes* are used for this. In order to be able to cope with the high particle rates in the endcaps, the muon spectrometer is equipped with *cathode strip chambers* in the region of $2.0 < |\eta| < 2.7$ in the innermost layer. The two other layers in the endcaps are equipped with monitored drift tubes.

3.3. Definition of Analysis Objects

3.3.1. Introduction

For the analyses presented in this work, the reconstructed physics objects of central importance are photons; also electrons, hadronic jets and muons are relevant. All these particles have different typical signatures in the detector. Based on features such as tracks in the inner detector and muon spectrometer, as well as clusters of energy depositions in the calorimeter, the reconstruction of corresponding physics objects is performed. Figure 3.13 schematically shows the ATLAS detector response to common SM particles. Charged particles, such as electrons, muons, and charged hadrons create tracks in the inner detector. Hadrons are typically found in jets, more or less collimated sprays of hadronic particles. Neutral particles do not create tracks in the inner detector. However, if a photon converts into an electron-positron pair in the presence of the inner-detector material, photons can result in tracks.

Energetic electrons and photons lead to clusters of energy deposition in the calorimeter, predominantly in the EM calorimeter. Hadronic jets also result in clusters of energy depositions in the calorimeters, but those clusters easily reach into the hadronic calorimeter. Based on the shape of the energy deposition clusters in the calorimeter, it is possible to discriminate photons and electrons against hadronic jets.

Over a wide energy range of about 1 GeV to several hundred GeV, muons can be approximated as *minimally ionizing particles* [133]. For that reason, muons can traverse the calorimeter without

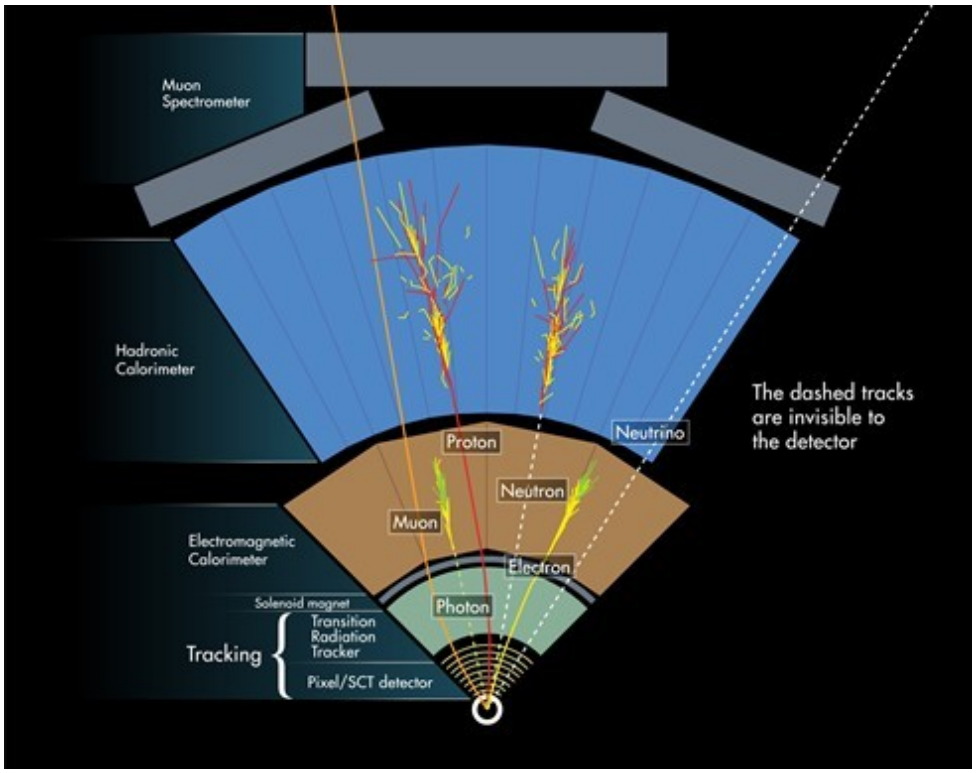

Figure 3.13. | Illustration of signatures in the ATLAS detector in a cross-sectional view as generated by different particle types. Taken from Reference [135].

loosing much of their energy. The muon spectrometer, which surrounds the calorimeters, allows a measurement of their momenta.

In the following sections, the reconstruction and identification of photons, electrons, muons and jets will be described. This includes an overview of the reconstruction of trajectories of charged particles in the inner detector, as well as of the reconstruction of primary vertices. Calorimeter information is condensed into a collection of clusters of energy depositions. Based on a combination of inner-detector information and such energy clusters, photon and electron candidates are build. The most common particles emerging from pp collisions at the LHC are hadrons, which is why most of the photon and electron candidates correspond to hadronic jets. However, by applying identification algorithms based on the shape of clusters in the calorimeter and, in the case of electrons, also based on tracking information, the purity of photon and electron candidate samples can be markedly increased. Additionally, isolation requirements are imposed that veto objects which are surrounded by relatively large amounts of additional activity, a typical signature of hadronic particles.

3.3.2. Tracks and Vertices

Tracks

Energetic charged particles produce a signal in the active detector components of the inner detector, which can be read out and analyzed. Based on these signals in the highly granular inner-detector modules, it is possible to reconstruct the trajectories of particles, commonly called *tracks*. By determining the curvature of a track in the solenoid magnetic field, the transverse momentum of the corresponding particle can be measured as described in Section 3.3.3 and in more detail in Chapter 4. The momentum resolution deteriorates with increasing transverse momentum as the track in that case approximates more and more a straight line. The inner detector allows a momentum resolution of $\sigma_p/p = 5 \cdot 10^{-4}\,\mathrm{GeV}^{-1} \cdot p_\mathrm{T}$ [126][1].

In Figure 3.14 an event display with a focus on reconstructed tracks and the corresponding energy depositions is shown. Tracks can be reconstructed within a pseudorapidity range of

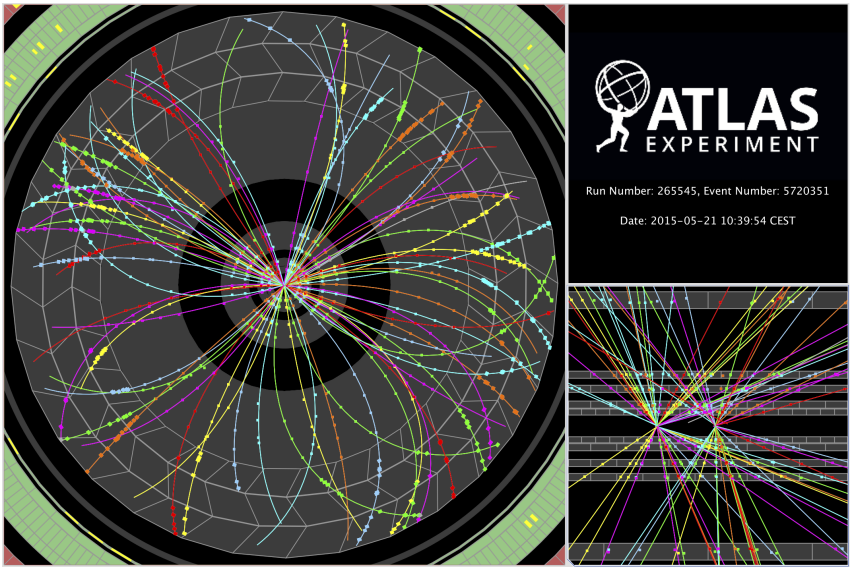

Figure 3.14. | Reconstructed tracks in the inner detector. The blobs represent energy deposits in the tracking devices. As one can see in the bottom right panel, the reconstructed tracks originate in two distinct vertices. Taken from Reference [137].

$|\eta| < 2.5$, corresponding to the acceptance of the inner detector. *Space-points*, 3-dimensional coordinates of energy depositions, are constructed based on clusters of energy depositions (*hits*)

[1] The determination of this particular resolution value does not include the information from the *Insertable B-Layer* (IBL), which has been added only in 2014 [136]. However, this most recently added innermost layer of the pixel detector does not change the momentum resolution significantly because the length of the track is not substantially increased by the IBL [130].

in the silicon detectors. In the barrel region, a charged particle emerging from the pp interaction region deposits energy in typically all four pixel layers, resulting in an equal number of space points. In the SCT barrel, four space points per track can be expected: four pairs of microstrip modules can register eight measurable clusters of energy depositions; however, the information from both modules of a pair needs to be combined to obtain all three spatial coordinates of the location of the particle transition through the module pair. A track's passage through the TRT results on average in more than 30 hits [132].

Based on the set of reconstructed space points in the pixel detector and the SCT, *track seeds* consisting of three space-points are generated [138]. This number corresponds to the minimal number of points necessary for a first estimate of the particle transverse momentum. Many of those track seeds are combinatorial artifacts that do not correspond to actual particle trajectories. In order to reduce the amount of those spurious track seeds, basic requirements on the transverse momentum and the estimated minimal distance of the trajectory to the interaction point are applied. At least one additional space-point must be consistent with having resulted from the same particle. Using a Kalman filter algorithm [139], further space-points from pixel detector and SCT that are consistent with the estimated trajectory are iteratively added. If in this way it is not possible to extend a seed with a transverse momentum of at least 1 GeV to a track with at least 7 space-points, a second attempt is made, allowing up to 30 % energy loss at each intersection of the trajectory with the detector material. This can recover tracks resulting from electrons, which have a relatively low mass and accordingly tend to lose considerable amounts of energy in form of bremsstrahlung. Such modified pattern recognition is also performed for seeds that are within a *region of interest* as defined by loosely selected energy clusters in the calorimeter.

The resulting sample of realistic track candidates contains track candidates which share space-points with other candidates – an indication that some space-points are wrongly assigned. For that reason, an ambiguity-solving algorithm is applied. Each track is assigned a score quantifying its quality. It takes into account the properties of the relevant clusters of energy depositions, missing space-points in sensor positions in which one would expect hits (*holes*), as well as the χ^2 of the initial track fit. In order to favor tracks with higher momentum against track candidates with relatively low momentum, which relatively often correspond to track candidates that include incorrectly assigned space-points, also the logarithm of the track momentum is taken

into account. Tracks with an insufficient score are removed. The remaining track candidates are fitted. Subsequently, they are subject to selection criteria based on the number of hits shared with other candidates, the number of holes, the number of assigned and shared space-points, and kinematic properties. Space-points can be removed from a track candidate if it is responsible for a too large number of shared space-points of either track candidate or an already accepted track candidate; after that, the pruned track candidate is re-evaluated. Accepted track candidates are fitted using all available information. Accepted tracks are then extrapolated into the TRT segment of the inner detector by finding hits in the TRT that are consistent with having resulted from the same particle as the track in the silicon detectors. A subsequent fit of the track candidates using all available information allows extracting precise kinematic properties of the tracks [140].

If a track with at least three silicon space-points is loosely matched to a cluster of energy depositions in the calorimeter, a *Gaussian-sum filter* (GSF) [141] is applied. This is a generalization of the Kalman filter algorithm, and it allows a more accurate track parameter estimation when non-linear effects due to bremsstrahlung energy losses are relevant.

In order to recognize tracks from e.g. electron-positron pair production from photon conversions in the material of the inner detector, it may be insufficient to rely on the outward extension of track seeds found in the silicon layers. Therefore, a pattern recognition based on TRT hits is performed [138] in regions close to the positions of loosely selected clusters in the EM calorimeter. More details on photon conversion reconstruction are given in Section 3.3.3.

Primary Vertices

Primary vertices are the points in which colliding protons interact with each other inelastically, resulting in the emergence of particles corresponding to the products of the proton-proton interactions. Typically, multiple of such vertices result from proton bunch crossings at the LHC. In Figure 3.14, an event with a relatively low number of primary vertices is shown. On average, a proton-proton interaction results in about 15 reconstructed tracks satisfying loose selection criteria [142]. The positions of the primary vertices are relevant for the determination of kinematic properties of particles, such as their transverse momentum as well as for associating particles that emerged from the same proton-proton interaction. Also, the reconstruction of primary vertices is relevant for the measurement of the amount of pileup on an event-by-event

basis.

Primary vertices can be determined by extending reconstructed tracks into the region in which the two proton beams cross each other and by subsequent analysis of the trajectories in the luminous region. The reconstruction of primary vertices based on these trajectories is an iterative process that involves the fitting of vertex positions based on tracks and a procedure of assigning individual tracks to vertices [143]. In order to reconstruct the primary vertices in a given collision event, the distribution of z-coordinates (z_{track}) of all considered tracks at the point of the closest approach to the beam line is considered. The z-coordinate at which the distribution of z_{track} has its global maximum is taken as seed for the position of the first reconstructed primary vertex. This seed and the track collection are then used to compute the best-fit vertex position iteratively by means of a χ^2 minimization procedure, reducing the influence of less compatible tracks on the fit result and a subsequent recomputation of the best-fit vertex position. Once this iterative process of determining the vertex position is completed, the tracks that are deemed incompatible with the reconstructed primary vertex in consideration are used to repeat the procedure in order to find further primary vertices. Incompatibility of a track with a vertex candidate is assumed if the contribution of the track to the χ^2 of the vertex fit exceeds 49. Only primary vertex candidates with at least two assigned tracks are considered as reconstructed primary vertex.

Determination of the Hard-Interaction Vertex

For the determination of particle four-momentum and, connected to that, for the calibration of the transverse-energy measurement, it is relevant to know the location of the primary vertex from which a given particle emerged. In ATLAS physics analyses, the studied processes often involves large momentum transfers, which is connected with relatively large transverse momenta of final-state particles. Therefore, it is standard procedure to choose the vertex for which the sum of transverse energies of its associated particles, $\sum_i p_{\text{T},i}^2$, is largest to be the *hard-interaction vertex*. For energetic photons from Higgs boson decays, however, this approach leads to sub-optimal results. A large fraction of the energy in these events is carried away by photons, which typically do not leave tracks that can be used to precisely point at the primary vertex in which they originated. Since the photons carry away a large fraction of the transverse momentum, the sum of the transverse momenta of the remaining particles from the interaction tends to be relatively

small. Accordingly, it can easily occur that another primary vertex, which is not related to the Higgs boson production but whose associated tracks can nevertheless have a considerable value for $\sum_i p_{\mathrm{T},i}^2$, is selected as hard-interaction vertex. In this case, the selected hard-interaction vertex would be not the true vertex of photon origin, and the calibration of the photon would be less precise. In addition, the measurement of quantities like the number of associated jets in Higgs events or the momentum of the leading jet would be less reliable.

In order to improve the selection of the primary vertex for events in which a Higgs boson decays to two photons, a more sophisticated vertex selection algorithm was created: a neural network was trained to select the Higgs boson production vertex in $H \to \gamma\gamma$ events by considering the following inputs:

- The summed squared and scalar transverse momenta of tracks assigned to the vertex, $\sum_i p_{\mathrm{T},i}^2$ and $\sum_i p_{\mathrm{T},i}$.
- The longitudinal segmentation of the calorimeter allows a pointing of the two photon-candidate showers back to the primary vertex, yielding an estimate of the z-position of the Higgs boson production vertex. Additionally, a constraint based on the average pp collision point location is used. If a conversion vertex, see Section 3.3.3, is reconstructed and matched to a photon, the conversion vertex enters the estimation of the primary vertex position as well, provided that the tracks belonging to the conversion vertex have hits in the silicon detectors.
- Due to conservation of momentum, the difference in azimuthal angle between the vectorial sum of tracks assigned to the primary vertex and the diphoton system tend to be close to 180 °. This difference in azimuthal angle is used as input for the neural network.

The selection efficiency in $H \to \gamma\gamma$ events for selecting the correct Higgs boson production vertex, defined as the fraction in which the algorithm determines the vertex position correctly to within 0.3 mm, depends on the Higgs boson production mode and on the amount of pileup. As can be seen in Figure 3.15, the efficiency is about 75 % for the dominant Higgs boson production mode, gluon fusion. In addition to the vertex selection efficiency for gluon fusion $H \to \gamma\gamma$ events, the efficiency is also shown for $Z \to e^+e^-$ events in which the tracking information for the two electrons is removed in order to emulate events with two photons while still having reliable information about the correct vertex position. On basis of such events, an uncertainty on the efficiency is estimated by computing the difference between the efficiency in simulation

and in data. The difference between the efficiency for $H \to \gamma\gamma$ events and $Z \to e^+e^-$ events is related to the different recoil characteristics in $H \to \gamma\gamma$ and $Z \to e^+e^-$ events. When the $Z \to e^+e^-$ events are reweighted such that the p_{T} distribution of the di-electron system is equal to that of the diphoton system in $H \to \gamma\gamma$ events, both vertex selection efficiencies are in good agreement [144].

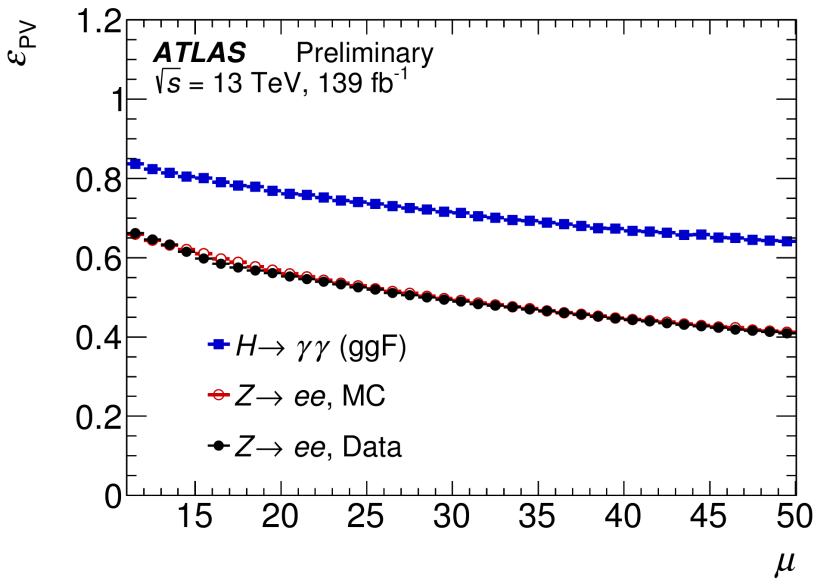

Figure 3.15. | Fraction of $H \to \gamma\gamma$ and $Z \to e^+e^-$ events in which the primary vertex chosen by the neural network has a distance of less than 0.3 mm to the correct production vertex position. The performance of this efficiency determination for $H \to \gamma\gamma$ events is cross-checked using $Z \to e^+e^-$ events in which the electron tracks have been removed before the vertex selection algorithm is applied. Taken from Reference [145].

3.3.3. Photons and Electrons

Introduction

As photons and electrons lead to quite similar signatures in the detector, the process of their reconstruction and calibration will be described in parallel. Both photons and electrons lead to narrow electromagnetic showers in the calorimeter, with most of the energy deposited in the EM calorimeter. Electrons create tracks in the inner detector due to their electric charge. Photons can indirectly lead to tracks in the inner detector; this happens by electron-positron pair production in interaction with the inner-detector material. The charged particles emerging from that interaction are able to create tracks. Photons which create such a pair of an electron and

positron are called *converted photons*. If no such pair production process occurs in the inner detector, a photon is called correspondingly *unconverted*. Converted photons and electrons tend to have wider showers than unconverted photons due to the radiation (bremsstrahlung) from electrically charged particles in the presence of the material of the inner detector.

Electron and photon showers correspond to clusters of energy depositions in the calorimeter cells. The reconstruction of these clusters is based on topologically connected calorimeter cells and is seeded by cells containing significant energy depositions. The resulting objects are called *topo-clusters* [146]. In order to improve the resolution of the determination of cluster energies in cases of interactions of electrons or photons with the inner-detector material that lead to a clear separation between the products of the interactions, different topo-clusters can be connected, resulting in *super-clusters*.

Topo-Cluster Reconstruction

Cluster building relies on the cell signal-to-noise ratio $\zeta_{\text{cell}} = \frac{E_{\text{cell}}}{\sigma_{\text{noise,cell}}}$, where E_{cell} is the energy deposited in a given cell of the calorimeter and $\sigma_{\text{noise,cell}}$ is the expected noise in that cell, including electronic noise and pileup effects. The cluster building is seeded by calorimeter cells that exceed a threshold of $|\zeta_{\text{cell}}| \geq 4$. The proto-cluster is padded in two iterations with adjacent cells with $|\zeta_{\text{cell}}| \geq 2$. Two clusters are merged if they contain the same cell. Finally, all directly neighboring cells are added to the cluster, irrespective of their energy. The result of this algorithm is called a topo-cluster, as it consists of a cluster of topologically connected calorimeter cells. For the determination of the *EM energy* of photon and electron topo-clusters, only cells of the EM calorimeter are used in most parts. In the region $1.37 < |\eta| < 1.63$, also the energy measurements from the presampler and scintillators between the calorimeter cryostats are taken into account in order to mitigate effects from energy losses in the upstream material. The fraction of the total topo-cluster energy that is deposited in the EM calorimeter cells is denoted f_{EM}. A preselection of $f_{\text{EM}} > 0.5$ is used to remove about 60 % of pileup clusters, effectively without removing clusters created by electrons or photons [147].

Given the energy of an electromagnetic cluster, the corresponding transverse energy commonly is computed via

$$E_{\text{T}} = \frac{E}{\cosh \eta_2}, \tag{3.4}$$

where η_2 denotes the pseudorapidity of the cluster barycenter in the second longitudinal layer of the EM calorimeter.

Matching of Tracks and Conversion Vertices

The tracks that are loosely matched to a cluster in the calorimeter and refitted with the GSF are extrapolated into the second layer of the EM calorimeter. In order to improve the matching efficiency of tracks that correspond to electrons with considerable energy losses in the inner-detector material, the track momentum that is used in this extrapolation can be scaled such that it matches the energy of the cluster. Matching of tracks and clusters is performed based on the angular distance, defined by $\Delta\phi$ and $\Delta\eta$, between cluster center and extrapolated track. If more than one track fulfills the matching criteria, a ranking system is used to select the track based on which the properties of the electron candidate are determined. Tracks with hits in the pixel detector rank higher than tracks without such hits. Within each of these categories, tracks with smaller $\Delta R = \sqrt{\Delta^2\eta + \Delta^2\phi}$ between track and cluster are preferred.

The probability for a photon conversion to occur depends on the material distribution in the inner detector. At low pseudorapidities, where relatively small amounts of material are encountered by particles, about 20 % of photons undergo conversion, while at $|\eta| \approx 2.3$ this fraction is about 65 %. For the reconstruction of photon conversion vertices, both tracks having silicon hits and tracks with only hits in the TRT are used [147]. The tracks need to be loosely matched to fixed-size calorimeter clusters and must have been assigned a high probability of being electron tracks by the TRT. One defines both two-track and single-track conversion vertices. The former type can be reconstructed based on two opposite-charge tracks that are consistent with emerging from a pair production process resulting from a massless particle. Single-track conversion vertices are based on single tracks without hits in the innermost sensitive layers of the inner detector.

The matching of reconstructed conversion vertices to calorimeter topo-clusters is performed based on the angular distance between the cluster and the track(s) constituting the conversion vertices. In case of more than one conversion vertex matching a topo-cluster, vertices with two tracks containing silicon hits are preferred over vertices with two tracks, which in turn are preferred over single-track conversion vertices. If more than one vertex exists for a given

category, the vertex with the smallest conversion radius is preferred.

Super-Clusters

Photons and electrons that originate in energetic pp-collisions can lead to more than one cluster of energy depositions in the calorimeter. In the case of electrons, considerable amounts of their energy can be radiated as bremsstrahlung photons, which can result in additional clusters in the vicinity of the cluster resulting from the electron. Photons, on the other hand, can convert in the presence of the material of the inner detector into a pair of electrons, which in turn can result in several distinct clusters. In case these distinct clusters are reconstructed as individual topo-clusters, it is possible to combine them, based on tracking information, into a *super-cluster*. A measurement based on such a supercluster results in a better energy resolution than a measurement that can take into account only individual topo-clusters. The reconstruction of super-clusters is performed independently for photon candidates and electron candidates. This way, energy depositions in the calorimeter can be treated both under the electron and photon hypothesis, enabling an ambiguity solving at a later stage.

Starting with topo-clusters with the largest transverse energy E_{T} and proceeding in order of descending E_{T}, topo-clusters are considered as a seed for a super-cluster if their E_{T} surpasses a given threshold. In the case of electrons this threshold is given by 1.0 GeV, and in the case of photons by 1.5 GeV. An electron seed cluster candidate must be matched to a track that has at least four hits in the silicon layers. A topo-cluster cannot be a seed cluster if it is already associated as a *satellite cluster* to another seed cluster.

Given a seed cluster, a topo-cluster is added to it if its angular distance $\Delta\eta \times \Delta\phi$ to the barycenter of the seed cluster is smaller than 0.075×0.125. This clustering is more permissive in ϕ-direction since this is the direction in which the magnetic field in the inner detector bends charged particles, resulting in a wider spread of energy depositions in ϕ-direction. Additionally, in case of supercluster building under the electron hypothesis, a topo-cluster is added as satellite cluster if its best-matched track is also the best-matched track of the seed cluster and if the angular distance $\Delta\eta \times \Delta\phi$ is less than 0.125×0.300. When building photon candidate super-clusters based on seed clusters that are matched to a conversion vertex with two silicon tracks, the basic satellite-cluster requirement is extended by adding topo-clusters whose best-matched track is

part of the conversion vertex. Moreover, a topo-cluster is added as a satellite if the considered conversion vertex, extrapolated as a neutral particle, matches that cluster. In order to reduce the impact of pileup on the super-clusters, their maximal width in η is chosen to be 0.075 in the barrel region and 0.125 in the endcaps. No such restriction is placed in ϕ-direction.

The energy of super-clusters is computed based on the three layers of the EM calorimeter and the presampler in front of it. In the transition region between the barrel and endcaps, $1.4 < |\eta| < 1.6$, also the energy measurement based on the scintillators between the cryostats of the calorimeter is used. Super-clusters are subject to an initial energy calibration and position correction. They are matched to tracks and conversion vertices, as described in Section 3.3.3, with the difference that this time super-clusters instead of topo-clusters are used.

As described above, a given seed cluster can be the basis of a photon and electron super-cluster at the same time. Based on tracking information, it is attempted to resolve this ambiguity and to classify a given super-cluster as either photon or electron. In Figure 3.16, the corresponding algorithm, which is based on matching electron tracks and conversion vertices to the super-cluster, is illustrated. If such classification is not possible with the necessary confidence, the

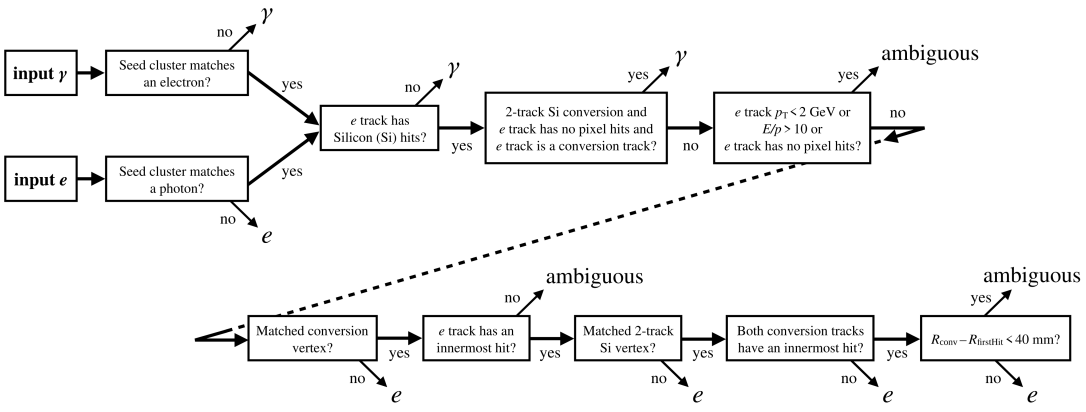

Figure 3.16. | Description of the algorithm for solving the ambiguity between photon and electron hypothesis for super-clusters. Taken from Reference [147].

super-cluster is labeled *ambiguous*. These ambiguous clusters can be dealt with differently by different analyses. After the stage of ambiguity resolution, an additional calibration of the photon and electron candidates is performed, taking into account tracks and conversion vertices.

Energy Calibration

After the super-clusters are built, their energy is calibrated in several steps [147, 148]. The cluster energy is corrected for energy losses due to upstream material, lateral leakage out of the cluster region, and leakage into the hadronic calorimeter. These corrections are taken into account by a multi-variate regression algorithm, derived from simulated events, which yields a combined correction for each region in η and E_{T}. The correction is derived separately for electrons, unconverted photons and converted photons, and applied both to cluster energies in simulated and data events. Before cluster energies in data are computed, several corrections are applied to the cell energies: cluster cell energies in data events are corrected with an intercalibration of the first and second layer of the EM calorimeter. This correction is derived from energy depositions of muons in the calorimeter in simulation and in data, and is computed in bins of η. Cluster energies in data events are also corrected for out-of-time-related pileup effects resulting from variations of the per-bunch luminosity and from simplifying assumptions about the bunch-train structure.

The uniformity of the energy response in data is improved by correcting for non-uniform energy losses between calorimeter modules in the barrel due to a variation in the gap width between absorber elements. Moreover, some sectors of the EM calorimeter are supplied with non-nominal values for the high-voltage; these inhomogeneities are corrected for as well.

Finally, $Z \to e^+e^-$ events are used to determine the difference in energy scale and resolution between data and simulated events. This is done by means of di-electron invariant-mass distributions in data and simulation. The differences in energy scale and resolution are extracted by performing a χ^2 fit of the corresponding mass templates. Based on these differences, corrections are derived and applied in order to improve the agreement between data and simulation. The resulting corrections on the energy scale are applied to data events. Corrections of the energy resolution, on the other hand, are applied to simulated events.

The resolution for a sampling calorimeter can be expressed as [149]

$$\frac{\Delta E}{E} = \frac{a}{\sqrt{E}} \oplus \frac{b}{E} \oplus c\,. \tag{3.5}$$

Here, a is the *sampling term*, which quantifies how large the impact of statistical fluctuations in the energy depositions in the active layers of the calorimeter on the energy measurement is.

The noise term b corresponds to influences to the measured shower energy which do not depend on the energy of the incoming particle; electronic noise has such effect. Lastly, the *constant term c* accounts for limitations on the accuracy of the energy measurement that result from a less than perfect calibration or from inhomogeneities in the detector. The constant term is relevant particularly at large energies, as its influence on the relative uncertainty does not decrease with increasing energy, as it is the case for the other terms.

Photon Identification

The collection of photon candidates from the reconstruction of electromagnetic clusters as described in the previous sections contains many QCD jets, which in the context of collecting samples of photon candidates can be called *fake photons*. In order to increase the purity in photons, selection criteria based on the *shower shape* in the calorimeter of the photon candidates are applied. These selection criteria are based on *shower shape variables*, which parametrize the shower shape and are designed to have discriminative power against QCD jets. Real photons have rather narrow showers that are to a good approximation confined to the EM calorimeter. QCD jets, on the other hand, tend to result in rather broad showers and a non-negligible fraction of their energy tends to be deposited in the hadronic calorimeter. Accordingly, the width and the depth of the shower are quantified in several shower shape variables.

A major source of fake photons are decays of energetic neutral mesons such as π^0 mesons into a collimated pair of photons. For this reason, photon identification involves the requirement of a lack of substantial substructure in lateral direction. The first layer of the EM calorimeter with its fine segmentation in η-direction is designed to allow the precise determination of the shower substructure in one lateral direction. In total, there are 11 shower-shape variables that are used for the photon identification. The selection consists in simple rectangular cuts on each of these variables. The selection values for each variable are optimized individually for different regions in photon transverse momentum[2] p_{T} and pseudorapidity $|\eta|$. Because the shower development of photons that underwent a conversion in the inner-detector material is different from that of unconverted photons, selection criteria are optimized for both types of photon signatures separately. In addition, the identification is optimized in bins of $|\eta|$ and p_{T}. Converted photons

[2]For massless particles the transverse momentum is identical to the transverse energy as defined in Eq.(eq:et). For energetic electrons, the numeric difference between transverse energy and transverse momentum is negligible.

tend to have wider showers due to interactions of the electrons and positrons with the detector before entering the calorimeter. The photon identification procedure and the measurement of the corresponding efficiency is described in more detail in Chapter 4. Generally, the efficiency of the *tight* photon identification for photons that pass isolation requirements (see Section 3.3.3)ranges from about 50 % to 70 % at a photon p_{T} of 10 GeV to more than 90 % above a p_{T} of about 60 GeV.

Electron Identification

The process of electron reconstruction leads to a sample which contains not only electron candidates from true electrons but also numerous QCD jets. In order to reduce the fraction of electron-faking QCD jets, an identification procedure is applied. It takes into account the shower shape in the calorimeter, the track matched to the cluster, and the spatial compatibility between the track and the cluster [147]. Electron candidates are required to meet basic quality criteria such as a sufficient number of hits in the silicon layers of the inner detector and to pass the TRT electron identification. The compatibility of the track with the reconstructed shower is determined using the differences in pseudorapidity and in azimuthal angle. The electron identification procedure involves both rectangular selection cuts as in the case of photon identification on a subset of variables and a likelihood-based method that takes into account the other variables. For the latter, probability density functions P_S, P_B for electrons and for background, respectively, are used. Given an electron candidate, the likelihood L_S or L_B of the observed properties under the hypothesis that the electron candidate results from a true electron or from background is given by

$$L_{S,B}(\mathbf{x}) = \prod_i P^i_{S,B}(x_i)\,, \tag{3.6}$$

where the discriminating variables are denoted by x_i. The likelihood discriminant used for the electron identification is given by the logarithm of the ratio of L_S and L_B. Most of the shower shape variables, impact parameter variables, the TRT electron identification variable, and variables related to the matching of track positions with cluster positions are taken into account in the likelihood discriminant. Simple selection cuts are imposed on the other considered variables, including the number of track hits in different parts of the inner detector and the ratio of track

momentum to the cluster energy [150].

The optimization of the electron identification is performed in bins of electron p_{T} and η [150]. The *tight* identification operating point, which is used in the context of this thesis, has an efficiency of approximately 80 % for electrons with a p_{T} larger than 30 GeV [147].

Isolation Requirements

Photon and electron candidates resulting from QCD jets tend to be surrounded by rather large amounts of additional activity, unlike photon or electron candidates from real photons and electrons, respectively. Therefore, the purity of electron and photon candidate samples can be improved by vetoing photon and electron candidates that are surrounded by considerable radiation. The amount of this radiation is quantified by *isolation* variables. Two types of such variables are used to discriminate against photon- and electron-faking jets:

- *Isolation based on calorimeter information*: $E_{\mathrm{T}}^{\mathrm{iso}}|_{\Delta R<r}$, is determined by summing the E_{T} of uncalibrated, positive-energy topo-clusters within a cone with radius r and subtracting the energy deposited in the EM calorimeter within $\Delta\eta \times \Delta\phi = 5 \times 7$ cells, in units of middle-layer cells, around the barycenter of the candidate. See Figure 3.17 for a schematic illustration of the isolation determination. The cone radius for the *loose* isolation selection, which is used in the analyses in this thesis, is $r = 0.2$. An estimate of the leakage of the photon or electron energy outside this central region is subtracted. Moreover, a correction for pileup effects is applied.
- *Isolation based on tracking information*: $p_{\mathrm{T}}^{\mathrm{iso}}|_{\Delta R<r}$, the summed transverse momenta of tracks within a cone with radius r. For the *loose* isolation selection, this radius is chosen to be $r = 0.2$. Tracks that are matched to conversion vertices of the photon candidate or the electron candidate are excluded from the computation of this quantity, as are tracks that are not associated with the hard-interaction vertex. Further requirements on the considered tracks are a p_{T} of larger than 1 GeV and a good track quality, assessed based on the number of hits and number of missing hits in the silicon layers of the inner detector.

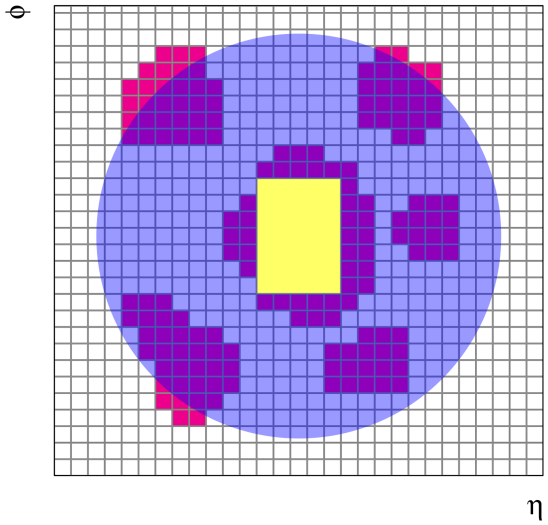

Figure 3.17. | Illustration of the definition of calorimeter isolation. The filled circle around the photon or electron candidate corresponds to the radius of the cone in which the topo-cluster-based calorimeter isolation variable is defined. Topo-clusters with a barycenter which lie within the cone radius and therefore are considered for the computation of the isolation are colored red. The yellow rectangle corresponds to the area assigned to the photon or electron candidate. Energy depositions in this area are not included in the calculation of the isolation. The grid represents cells from the second EM calorimeter layer. Taken from [150].

3.3.4. Jets

When energetic quarks and gluons emerge from the interaction point, they undergo showering and hadronization, resulting in a spray of hadrons, which can be detected by the inner detector in the form of tracks and in the calorimeter as clusters of energy depositions. A jet reconstruction based on these tracks in the inner detector, clusters in the calorimeter or four-momenta of simulated particles allows the determination of the kinematic properties of the original parton that emerged from the hard interaction.

Jet Definition

Jets are reconstructed following an algorithm which groups nearby *entities* such as tracks, calorimeter clusters, and particle four-momenta, leading to a set of reconstructed jets. Generally, such an algorithm must be *infrared-safe* and *collinear-safe*. An infrared-safe jet reconstruction algorithm is not sensitive on the emission of a soft parton, and a collinear-safe algorithm is not sensitive to a collinear splitting of a parton.

In the context of this thesis, the *anti-*k_t jet-reconstruction algorithm is used [151]. It takes a

collection of entities defined by rapidity y_i, azimuthal angle ϕ_i, and transverse momentum k_{ti}, as input and returns a collection of jets. Jets are built by comparing distances between these entities, using the following distance measures:

$$d_{ij} = \min(k_{ti}^{-2}, k_{tj}^{-2}) \cdot \frac{\Delta_{ij}^2}{R^2},$$
$$d_{iB} = k_{ti}^{-2}, \tag{3.7}$$

where Δ_{ij} is defined as $\Delta_{ij} = \sqrt{(y_i - y_j)^2 + (\phi_i - \phi_j)^2}$. The radius parameter R, which controls the lateral size of the reconstructed jets, is commonly chosen to be 0.4 in the ATLAS collaboration. The quantity d_{ij} is a measure of how big the separation between two entities is relative to the chosen jet radius, with a modifying factor that takes into account the larger of the two considered transverse momenta.

The jet reconstruction algorithm consists in the repeated application of the following steps: The smallest of all distances d_{ij}, d_{iB} is determined, where $i \in \{1, \ldots, N_{\text{elements}}\}$ and $j \in \{1, \ldots, N_{\text{elements}}, \text{ excluding } i\}$.

- If this smallest distance is a member of the d_{ij} set, entities i and j are combined and the resulting combination of four-momenta enters the collection of entities. The distances d_{ij}, d_{iB} are recomputed based on the updated collection.
- If the smallest distance is of the type d_{iB}, the corresponding entity with index i is declared a jet and removed from the set of distances.

This iteration stops as soon as no further entities remain in the set. In this way, all initial entities are either declared as a jet directly, or first combined with other entities and then as combined entity declared as a jet.

The distance measure between an entity with large k_t and an entity with low k_t is fully determined by the transverse momentum of the former and the angular distance between them. Such a particle with large k_t will be combined with all soft particles within a radius R if no other hard particle lies within a distance of $2R$. If another entity with large k_t is present within a range $R < \Delta_{ij} < 2R$, two hard jets will be constructed as a result. If the distance Δ_{ij} between the two entities with large k_t is smaller than R, they will be combined to a single jet. In the case that both of the considered entities have low k_t and a similar angular separation as the large-k_t and low-k_t

entities in the previous example, the distance measure will be much larger, rendering it unlikely that two soft entities are combined.

Jet Energy Calibration

Jets that are build using a clustering algorithm as described above initially have a cluster energy at the *EM scale*. Several consecutive steps are performed in order to calibrate jets [152, 153]. Some of these steps rely on MC simulation, while others are in-situ methods. The latter result in corrections that are exclusively applied to events in data. The calibration is aimed at bringing the measured energy at reconstruction level to the jet energy at truth level. Correcting the jet origin to the actual primary vertex position constitutes the first step; this has effect on the η of the jet, while the jet energy is unchanged. The next step corrects for pileup influences. One part of this correction consists in subtracting a jet-area-based estimate of the pileup contribution from the jet p_{T}. The area A of the jet is determined by a method called *ghost association* [154]. The energy density ρ of the event corresponds to the median of the p_{T} distribution of a collection of jets as reconstructed using a k_t jet clustering algorithm [155]. Residual dependencies on the number of reconstructed vertices, quantified by the parameter α, and on the average number of pp interactions μ, quantified by the parameter β, are taken into account as well. The corrected p_{T} of a jet is then given by

$$p_{\mathrm{T}}^{\mathrm{corr}} = p_{\mathrm{T}}^{\mathrm{reco}} - \rho \cdot A - \alpha \cdot (N_{\mathrm{PV}} - 1) - \beta \cdot \mu \,. \tag{3.8}$$

Next, the absolute jet energy scale and η calibration is performed, with the purpose to match the energy of jets with the particle-level energy. The calibration is derived from jets in simulated events, and is based on the jet energy response given by the ratio of the energy of jets at reconstruction and at truth level.

The jet response is not identical for gluon- and quark-initiated jets, which is why a residual dependency on variables that are correlated to the jet type is corrected for in the *global sequential calibration* [156]. This is performed based on five variables that quantify the lateral and longitudinal features of jets and which are related to the particle composition of the jet.

Finally, *in situ* calibrations methods are applied to data events, in order to correct for residual differences between data and simulation using well-calibrated objects such as photons or electron-

positron pairs from Z-boson decays to determine the jet energy response in data and in simulation. Such differences result from an imperfect modeling of the detector material distribution, the detector response, pileup effects, and of interactions of particles with detector material.

3.3.5. Muons

The signature of a muon traversing the ATLAS detector consists in a track in the inner detector, only modest energy depositions in the calorimeter consistent with resulting from a minimally-ionizing particle, and a track in the muon spectrometer. Muons are reconstructed using primarily information from the muon spectrometer and the inner detector [157]. Four types of muon reconstructions are available, differing in what detector information is used for the reconstruction. *Combined* muons are based on tracks that have been reconstructed independently in the inner detector and in the muon spectrometer and in a later step combined to a single muon track, performing a re-fit using hits both in the inner detector and the muon spectrometer. *Segment-tagged* muons result from tracks in the inner detector which, if extrapolated to the muon spectrometer, match a track segment in either monitored drift tubes or cathode strip chambers. This way, muons can be recovered which did not leave sufficient hits in the muon spectrometer due to limited acceptance or due to an insufficient transverse momentum. *Calorimeter-tagged* muons do not incorporate tracking information from the muon spectrometer; instead, they correspond to tracks from the inner detector which are matched to energy depositions in the calorimeter that are consistent with resulting from a minimally-ionizing particle. This definition allows the recovery of muons in the detector region at $|\eta| \approx 0$, in which the muon spectrometer has a limited functionality in order to allow for the deployment of services for other detector components. *Extrapolated* muons are based solely on track segments from the muon spectrometer which are consistent with originating in the interaction point. This reconstruction method is helpful to recover muons in the region $2.5 < |\eta| < 2.7$, where the muon spectrometer has tracking ability but the inner detector has not.

The sample of muons for physics analyses is based on a combination of the muon candidates from these four reconstruction methods. For this combination, overlaps between candidates need to be removed: if two reconstructed muons from two different methods are associated with the same track in the inner detector, combined muons are prioritized over segment-tagged muons,

which in turn are prioritized over calorimeter-tagged muons. The overlap of extrapolated muons with other types is resolved by selecting the track based on the goodness of fit and the number of hits.

The muon momentum is determined based on the curvature of the reconstructed track and is corrected for the energy loss in the calorimeter. In order to ensure the robustness of the muon momentum determination, track quality requirements regarding the number of hits in the inner detector and muon spectrometer are imposed. Decays of hadrons to a final state containing a muon are considered background. In such events, there are often missing hits in the innermost layers in the case of electrically neutral hadrons, or there can be a kink in the reconstructed track in the case of charged hadrons. In order to reduce the contribution of such events to the muon collection, the consistency of the individual momentum measurements in the inner detector and muon spectrometer and the fit quality is used as a discriminant.

3.4. The Trigger

With current technology, it is not possible to write and fully reconstruct all the proton-proton collision events that occur during LHC operation. However, for the physics goals of the ATLAS experiment this is also not necessary: most of the occurring collisions only involve QCD interactions with small momentum transfers, and these are not the focus of the ATLAS physics program. Instead, rarer processes with larger momentum transfers are of greater value for most ATLAS physics analyses.

Proton-proton collisions are occurring at the LHC with a frequency of up to 40 MHz. At the same time, events can be written with a frequency of 1 kHz [158]. This means that only one in 40.000 events can be written to disk and accordingly be subject to detailed analysis. The *trigger* is the system that decides whether a given collision event is worth being written to disk and fully reconstructed. In order to be able to make quick decisions, the trigger algorithm is based on less than fully detailed event representations. These include calorimeter regions with large transverse energy, information about missing transverse energy, hits in the muon spectrometer, and inner-detector information. The trigger algorithm has two stages. While the first is a hardware-based trigger (L1), the second is software-based and is called *high-level trigger* (HLT). If an event passes the requirements of the L1 trigger, it is forwarded to the HLT, where a

trigger decision based on more detailed event information is made. Only information from the calorimeter and the muon spectrometer is considered for the L1 decision. The L1 trigger defines *regions of interest*, which are taken into consideration by the HLT. The HLT, which deals with a significantly reduced frequency of event processing compared to the L1 trigger, has access to more detailed event information, including calorimeter information with finer granularity and information from the inner detector. If both trigger stages are passed by the event, the event is written to disk. Due to the limited readout capacity of the ATLAS detector, the maximum trigger rate for the L1 system is constrained to a rate of 100 kHz. The output rate of the HLT is about 1 kHz.

3.5. Luminosity Measurement

The measurement of cross sections directly depends on the accurate knowledge of the integrated luminosity via Eq. (2.19). The luminosity is measured as laid out in Reference [159]. Besides a dedicated luminometer called *LUCID* [126] also the inner detector and calorimeter of ATLAS are used to measure the luminosity. Having multiple detectors and measurement algorithms to measure the luminosity results in a more robust measurement and assessment of systematic uncertainties. LUCID is used to determine the central value of the measured integrated luminosity and correspondingly is of central importance. It is a detector based on Cherenkov-radiation-sensors and is sensitive to the number of proton-proton interactions per bunch crossing. Its location is close to the beampipe in a distance of ±17 m to the interaction point. Alternative ways of determining the bunch-by-bunch luminosity include the counting of tracks from charged particles in the inner detector.

The instantaneous bunch luminosity L_b, which is related to the overall instantaneous luminosity via $L = n_\mathrm{b} L_\mathrm{b}$, can be expressed as

$$L_\mathrm{b} = \frac{f_\mathrm{r} \cdot \mu}{\sigma_\mathrm{inel}}, \tag{3.9}$$

Here, n_b denotes the number of proton bunches per beam, f_r the rotation frequency of the bunches, μ the average number of inelastic proton-proton interactions per bunch crossing, and σ_inel the cross section for inelastic proton-proton interactions. Considering the limited acceptance of the

detectors responsible for the bunch-by-bunch luminosity measurement, this translates into

$$L_{\mathrm{b}} = \frac{f_{\mathrm{r}} \cdot \mu_{\mathrm{vis}}}{\sigma_{\mathrm{vis}}}, \tag{3.10}$$

where μ_{vis} denotes the *observed* number of inelastic proton-proton interactions, and σ_{vis} denotes the corresponding cross section. The quantity μ_{vis} can be measured for a given bunch crossing by the counting of primary vertices. Thus, in order to be able to calculate the bunch luminosity L_{b} with a given measurement method based on μ_{vis}, one needs to determine σ_{vis}, which acts as a calibration constant. The determination of σ_{vis} is achieved using a special LHC running condition, called *van-der-Meer* scan. In such a scan, the two proton beams are intersected with different overlap by lateral shifts in x- and y-direction. As a result, one obtains the convolved beam sizes [160] in horizontal and vertical scan direction, Σ_x and Σ_y, respectively, using following relation:

$$\Sigma_{x(y)} = \frac{1}{\sqrt{2}} \frac{\int R_{x(y)}(\delta) \mathrm{d}\delta}{R_{x(y)}(0)}, \tag{3.11}$$

where $R(\delta)$ denotes the measured luminosity in arbitrary units as a function of the beam separation δ. Then the bunch luminosity in the van-der-Meer scan $L_{\mathrm{b}}^{\mathrm{vdM}}$ can be determined as follows:

$$L_{\mathrm{b}}^{\mathrm{vdM}} = \frac{f_{\mathrm{r}} n_1 n_2}{2\pi \Sigma_x \Sigma_y}. \tag{3.12}$$

Applying Eq. (3.10), the calibration constant σ_{vis} can be extracted from the van-der-Meer scan by relating the luminosity from Eq. 3.12 to the simultaneously measured visible interaction rate, μ_{vis}:

$$\sigma_{\mathrm{vis}} = \mu_{\mathrm{vis}}^{\mathrm{max}} \frac{2\pi \Sigma_x \Sigma_y}{n_1 n_2}, \tag{3.13}$$

where $\mu_{\mathrm{vis}}^{\mathrm{max}}$ is the maximal visible interaction rate in the scan. The measurement of the visible interaction rate is performed using a variety of different detector systems and with different algorithms.

Van-der-Meer scans have been performed once per year under beam conditions with low beam intensities, corresponding to an average number of proton-proton interactions of approximately 0.5. The calibration constant σ_{vis} can be used in runs with larger luminosities in combination with the determination of the corresponding μ_{vis} to measure the instantaneous luminosity.

The LUCID detector suffers to some degree from a non-linear response to μ_{vis}. An alternative, tracking-based method of measuring the luminosity, however, has an approximately linear response; therefore, it can be used to correct for the non-linearity in the LUCID measurement. The uncertainty on this correction, assessed by a further method of luminosity measurement that is based on the tile calorimeter, which has also an approximately linear response, is propagated to the corrected LUCID measurement. This calibration-transfer uncertainty is the dominant uncertainty on the measured integrated luminosity in most data-taking periods, ranging from 1.3 % to 1.6 %. The relative uncertainty on the measured integrated luminosity of the 2015 to 2017 dataset is 2.03 %.

Instantaneous luminosities are averaged over time periods called *luminosity blocks*, which typically amount to 60 s. For each luminosity block, an entry in a database is created in which the instantaneous luminosity, its duration and other detector quality information are written. The integrated luminosity is obtained by adding up the products of the duration of the luminosity block with the corresponding averaged instantaneous luminosity for all blocks that are used in a given analysis.

3.6. Summary

The LHC was built and equipped with four major detector experiments at each of the beam crossing points in order to study fundamental interactions using proton-proton collisions at a high center-of-mass energy. One of the four detectors is the ATLAS detector. Being a multi-purpose detector, it can be used to record and analyze proton-proton interaction events with many different signatures. The ATLAS detector consists of three major subdetectors: the inner detector, which tracks the trajectories of charged particles; the calorimeter, which enables the accurate measurement of the energy of both charged and neutral particles; the muon spectrometer, which is used to detect muons and determine their momenta.

The detector readout results in event representations that consist of information about localized energy depositions in the various detector components. Based on these energy depositions, candidates for various particles can be constructed, including photons, electrons, hadronic jets, and muons. Events can be selected based on the presence and kinematic properties of such particles. Identification algorithms are used to enhance the purity of the corresponding samples.

A fast, two-staged trigger system makes an efficient filtering of the large number of occurring proton-proton collision events feasible, with the aim of selecting only events that are of interest for ATLAS physics analyses. The measurement of the integrated luminosity is performed by means of a dedicated luminometer LUCID, which is close to the beamline, and ATLAS components such as the inner detector and calorimeter, which are sensitive to the visible interaction rate. The integrated luminosity is known with an accuracy of approximately 2 %.

4. Measurement of the Photon Identification Efficiency Using the Electron-Extrapolation Method

4.1. Introduction

Photons, the quanta of the electromagnetic interaction, can be produced in collisions at the LHC in various ways. Since quarks are electrically charged, they can couple to photons. As a consequence, the detection of photons emitted in hard QCD interactions can be used to study the dynamics of the strong interaction. Photons can also be produced in decays of the Higgs boson via an intermediate loop of charged, massive particles. Besides SM processes as described above, photons possibly could be produced in non-SM interactions, in which case photons would be a window to physics beyond the SM. Typical examples for this would be additional resonances decaying to a pair of photons or the relaxation of excited quarks, in which the excitation energy is carried away by a photon. Thus, the photon is an important tool for studying SM processes and searches for new phenomena.

Given an ATLAS physics analysis in which final-state photons are relevant, events are selected based on reconstructed and identified photon candidates. The reconstruction of photon candidates from clusters of energy depositions in the EM calorimeter and from inner-detector information has been described in Chapter 3. Jets from hadrons are by far the most common particle signatures in LHC collisions and constitute the majority of photon candidates from photon reconstruction. Decays of hadrons within a jet often result in photons. However, such jets containing photons produced in hadron decays are considered to be background as well, since the corresponding

photons do not contain information about photons that emerged in the proton-proton interaction.

In order to increase the purity in the sample of photon candidates, i.e. to veto QCD jets from being considered as photons in analyses, selection criteria are imposed on the photon candidates: criteria regarding the isolation of photon candidates, see Section 3.3.3, and criteria regarding their shower shape in the calorimeter. The latter selection is called photon identification and has been briefly introduced in Section 3.3.3.

Many ATLAS analyses require an efficient identification of photons and a good rejection of jets faking photons, also known as fake photons. One of those analyses is the measurement of Higgs boson production cross sections in the $H \to \gamma\gamma$ decay channel, which is presented in Chapter 5. For that measurement, the efficiency of the photon identification should be high in order to keep as many diphoton signal events as possible. At the same time, the background from fake photons to the signal events should be as small as possible in order to maximize the significance $S/\sqrt{B}$ of the measurement, where S and B correspond to the number of signal and background events. The photon identification efficiency is in this context defined as the fraction of true, isolated photons that pass the photon identification selection:

$$\varepsilon_{\mathrm{ID}} = \frac{N^{\gamma}_{\text{pass ID, isol.}}}{N^{\gamma}_{\text{isol.}}} \,. \tag{4.1}$$

Here, $N^{\gamma}_{\text{isol.}}$ denotes the number of photons that pass the isolation selection, and $N^{\gamma}_{\text{pass ID, isol.}}$ denotes the number of photons that pass both isolation and identification selections. The isolation requirement that is imposed for this definition is based on reconstruction-level information. The combined requirements of isolation and identification lead to a significant reduction of fake photons in the sample of photon candidates. Photon candidates that are used in the analyses of this thesis are required to have $E_{\mathrm{T}}^{\mathrm{iso}}|_{\Delta R<0.2} < 0.065 \times E_{\mathrm{T}}$, and $p_{\mathrm{T}}^{\mathrm{iso}}|_{\Delta R<0.2} < 0.05 \times E_{\mathrm{T}}$, corresponding to the isolation working point called *FixedCutLoose*.

Photon identification in ATLAS is performed using the application of simple rectangular selection criteria, called *cuts*, on the shower-shape variables of photon candidates, which parametrize the shape of the showers in the detector. The shower-shape variables that are used to perform the photon identification are briefly described in Table 4.1.

Candidates which have a large shower width or depth are rejected, as such signatures are typical of QCD jets. Showers of photons typically are narrow. For electromagnetic showers

one defines the *Molière radius* $R_{\mathrm{M}} = X_0/E_c \cdot 21\,\mathrm{MeV}$, where E_c is the *critical energy*, at which the ionization loss of an electron equals the electron's energy given in units of MeV [133]. On average, only 10 % of the energy of an electromagnetic shower is deposited outside the Molière radius. For lead, which is used in the EM calorimeter as absorber material, the Molière radius is given by 16 mm [149]. The shower width is quantified with the following variables: R_η, R_ϕ, w_{η_2}, w_{s3}, $w_{s\,\mathrm{tot}}$, and F_{side}. Because Photons (and electrons) tend to deposit only small fractions of their energy in the hadronic calorimeter, it is possible to discriminate between photons and jets using the *hadronic leakage*, which corresponds to the fraction of shower energy that is deposited in the hadronic calorimeter. Depending on the considered pseudorapidity region, either R_{had1} or R_{had} is used. In addition to the shower width and depth, the substructure of the energy depositions in the finely segmented first layer of the EM calorimeter is analyzed. A single photon is unlikely to produce a substructure in lateral direction consisting of more than one distinct local maximum. If such a substructure is found, it is likely that it resulted from more than one particle. In particular, collimated pairs of photons from decays of energetic neutral mesons such as the π^0 meson can cause a lateral substructure. The fine segmentation of the first layer of the EM calorimeter was designed for the purpose of rejecting such collimated pairs of photons from meson decays. Both ΔE_s and E_{ratio} quantify the presence of additional local maxima in lateral direction. The ratio of the cluster energy that is deposited in the first calorimeter layer, f_1, is commonly used to ensure that in the course of the shower development a sufficient amount of energy has been deposited in the first layer, which is required for a reliable computation of the first-layer variables.

The identification criteria for converted and unconverted photons, see Section 3.3.3, are not identical. The reason for this is that converted photons tend to have wider showers. One reason for this is that electrons and positrons from photon conversions tend to radiate when scattering in the upstream material and correspondingly tend to start showering at lower radii. Moreover, the magnetic field bends the trajectories of electrons and positrons in opposite azimuthal directions, which increases the shower width in ϕ-direction.

The selection criteria are optimized for different regions of photon p_{T} and $|\eta|$, as the shower development in different kinematic regions can differ considerably. The amount of upstream material in front of the calorimeter depends on the pseudorapidity. More upstream material leads to an earlier start of the shower development, resulting in more wide-spread showers in the

Category	Description	Shower-shape variable
Hadronic leakage	Ratio of E_{T} in the first sampling of the hadronic calorimeter to E_{T} of the EM cluster (used over the ranges $\lvert\eta\rvert < 0.8$ and $\lvert\eta\rvert > 1.37$)	R_{had1}
	Ratio of E_{T} in the hadronic calorimeter to E_{T} of the EM cluster (used over the range $0.8 < \lvert\eta\rvert < 1.37$)	R_{had}
EM middle layer	Ratio of the energy in 3×7 $\eta\times\phi$ cells over the energy in 7×7 cells centered around the photon cluster position	R_{η}
	Lateral shower width, $\sqrt{(\sum E_i\eta_i^2)/(\sum E_i) - ((\sum E_i\eta_i)/(\sum E_i))^2}$, where E_i is the energy and η_i is the pseudorapidity of cell i and the sum is calculated within a window of 3×5 cells	w_{η_2}
	Ratio of the energy in 3×3 $\eta\times\phi$ cells over the energy in 3×7 cells centered around the photon cluster position	R_{ϕ}
EM Strip layer	Lateral shower width, $(E_i(i-i_{\mathrm{max}})^2)/(\sum E_i)$, where i runs over all strips in a window of 3×2 $\eta\times\phi$ strips, and i_{max} is the index of the highest-energy strip calculated from three strips around the strip with maximum energy deposit	w_{s3}
	Lateral shower width, $(E_i(i-i_{\mathrm{max}})^2)/(\sum E_i)$, where i runs over all strips in a window of 20×2 $\eta\times\phi$ strips, and i_{max} is the index of the highest-energy strip calculated from three strips around the strip with maximum energy deposit	$w_{s\,\mathrm{tot}}$
	Energy outside the core of the three central strips but within seven strips divided by energy within the three central strips	F_{side}
	Difference between the energy associated with the second maximum in the strip layer and the energy reconstructed in the strip with the minimum value found between the first and second maxima	ΔE_s
	Ratio of the energy difference between the maximum energy deposit and the energy deposit in the secondary maximum in the cluster to the sum of these energies	E_{ratio}
	Ratio of the energy in the first layer to the total energy of the EM cluster	f_1

Table 4.1. | Discriminating variables used for the *tight* photon identification. E^{S2} denotes energy deposited in the second layer of the calorimeter. E_{T} denotes the transverse energy of the photon candidate. In general, the shower-shape variables can be divided into three categories: the variables R_{ϕ}, R_{η}, w_{η_2}, w_{s3}, $w_{s\,\mathrm{tot}}$, and F_{side} quantify the lateral width of the shower. R_{had1} and R_{had} are used to measure the hadronic leakage, i.e. the longitudinal extent of the shower. The variables E_{ratio} and ΔE_s can be used to put constraints on the substructure of showers. Adapted from Table 1 in Reference [161].

first calorimeter layers relative to regions in which only a small amount of upstream material is encountered. The distribution of energy depositions in the calorimeter material also depends on the energy of the incident particle, which means that the lateral shower widths in different depths depends to some degree on the energy. In addition, backgrounds from photon-faking QCD jets are not identical for different photon energies. The values for the selection criteria used in this study of the photon identification efficiency correspond to what is called the *tight* photon identification, which is used by most physics analyses for their photon selection.

The binning, i.e. the set of separately considered kinematic regions for the measurement of the photon identification measurement, is shown for p_{T} and $|\eta|$ in Tables 4.2 and 4.3, respectively. For the method of measuring the photon identification efficiency described in this thesis, the p_{T} range from 25 GeV to 250 GeV is considered. Pseudorapidities of up to 2.37 are taken into account, excluding the barrel-to-endcap transition region $1.37 < |\eta| < 1.52$, in which the first EM calorimeter layer has too coarse a granularity to allow a reliable photon identification and in which a relatively large amount of upstream material in front of the calorimeter is encountered by particles.

Bin limits [GeV]: 25 – 30 – 35 – 40 – 45 – 50 – 60 – 80 – 100 – 125 – 150 – 175 – 250

Table 4.2. | The boundaries of the 12 p_{T} bins in which the photon identification efficiency is measured.

$\lvert\eta\rvert$ bin number	1	2	3	4
Lower boundary	0	0.6	1.52	1.81
Upper boundary	0.6	1.37	1.81	2.37

Table 4.3. | The upper and lower boundaries of the four $|\eta|$ bins in which the photon identification efficiency is measured.

The shower development and the resulting signal in the detector generally is not identical in simulated events and events from data-taking. Mismodeling of the shower, and correspondingly also the distributions of shower-shape variables, in simulation has several causes. A less than perfect description of the detector material in simulation and a mismodeling of particle interactions with that material will result in shower differences between data and simulation. Another

source of data-simulation differences is the modeling of the detector readout in simulation: in the readout of calorimeter information, capacitive *cross-talk* effects play a role. In particular, the finely-segmented first layer of the electromagnetic calorimeter, which the photon identification relies on heavily for photon identification, is subject to cross-talk effects. The simulation of the detector readout characteristics is not necessarily identical to those in the actual detector. In order to mitigate the effects of these types of mismodeling, the shower-shape variables are corrected using additive corrections on the majority of the distributions listed in Table 4.1, depending on the p_{T} and $|\eta|$ of the photon. Similarly, electron shower-shape distributions are corrected in simulation within the context of the measurement described in this chapter. The corrections result in a better agreement in the bulk region of the shower-shape variable distributions between data and simulation; however, residual differences persist due to differences in the shapes of distributions, particularly in tail regions of the distributions. See Figure 4.1 for an illustration of the mitigation of disagreement between a shower-shape variable distribution in simulation and data. So while the disagreement of identification efficiencies in simulation and data is reduced

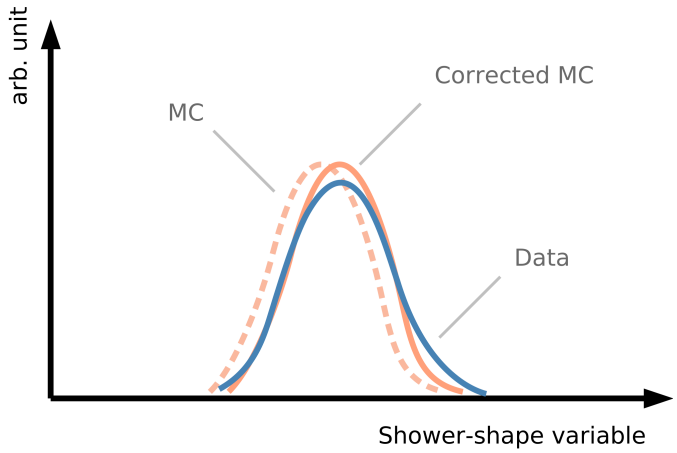

Figure 4.1. | Illustration of the correction of data-simulation differences in shower-shape variable distributions. A comparison of the distributions in simulation and in data is shown. The original distribution in simulation (dashed orange line) has a different mean than the distribution in data (blue line). This disagreement can be alleviated by applying a simple shift to the distribution in simulation, resulting in a distribution (solid orange line), whose mean now is in good agreement with the distribution in data, but may still have residual differences due to differing distribution shapes.

by applying corrections on shower-shape variable distributions, a residual difference persists. This difference in identification efficiency can be captured by a *scale factor*

$$c_{\mathrm{SF}} = \frac{\varepsilon_{\mathrm{ID}}^{\mathrm{data}}}{\varepsilon_{\mathrm{ID}}^{\mathrm{MC}}}, \tag{4.2}$$

which can be applied as additional weight on simulated photons, leading to an improved agreement between simulated events and events in data in terms of identification efficiency. The measurement of the photon identification efficiency in data events is thus important in order to render simulated event samples comparable with data event samples by means of scale factors. There are currently three methods in use for the measurement of this efficiency and corresponding scale factors, which are combined before being used in physics analyses.

4.2. The Electron-Extrapolation Method

In this work, photon identification efficiencies have been measured using the *electron-extrapolation* method. It makes use of the similarity of shower shapes of electrons and photons. One can derive transformations that transform the shower shape of electrons such that the resulting objects have distributions of shower-shape variables that resemble closely those of photons. These shower-shape transformations are based on *Smirnov transformations* [162]. By applying the shower-shape transformations to electrons in data, which can be selected from $Z \to e^+e^-$ events using a tag-and-probe method as described in Section 4.5.2, one obtains a sample of *pseudo-photons*, which can be used to determine the photon identification efficiency in data.

It is possible to collect a pure and unbiased sample of photons from $Z \to \ell^+\ell^-\gamma$ events, using a method that is briefly described in Section 4.3. Therefore, it is warranted to ask why such a detour over electrons and shower-shape transformations should be made. The answer is that the method of collecting photons from $Z \to \ell^+\ell^-\gamma$ events results in a sample of photons with relatively low p_{T}, as these photons correspond to emissions from one of the leptons from the Z-boson decay. Electrons in $Z \to e^+e^-$ events, on the other hand, tend to have comparatively large p_{T}. Therefore, by transforming these electrons to pseudo-photons, one obtains a collection of photon-like objects with higher p_{T} than is the case in the method based on $Z \to \ell^+\ell^-\gamma$ events. The statistical uncertainty of the measured photon identification efficiency is therefore lower at intermediate to high p_{T} in the electron-extrapolation method than in the method based on $Z \to \ell^+\ell^-\gamma$ events.

The transformations used to transform electrons to photon-like objects are based on samples of simulated $Z \to e^+e^-$ events electrons and on samples of inclusive-photon events, see Section 4.4.2. For each of the considered shower-shape variables and for converted and unconverted photons

separately, the transformations are derived in 7 $|\eta|$ bins $\times$ 12 p_{T} bins, see Tables 4.4 and 4.2, respectively. The relatively fine binning in $|\eta|$ is used because shower-shape variable distributions can vary significantly in different regions of $|\eta|$. The principle of the shower-shape transformations

$\lvert\eta\rvert$ bin number	1	2	3	4	5	6	7
lower boundary	0	0.6	0.80	1.15	1.52	1.81	2.01
upper boundary	0.6	0.8	1.15	1.37	1.81	2.01	2.37

Table 4.4. | The upper and lower boundaries of the seven $|\eta|$ bins for which the electron transformations are derived.

is illustrated in Figure 4.2. An example based on simulation is shown in Figure 4.3. A description

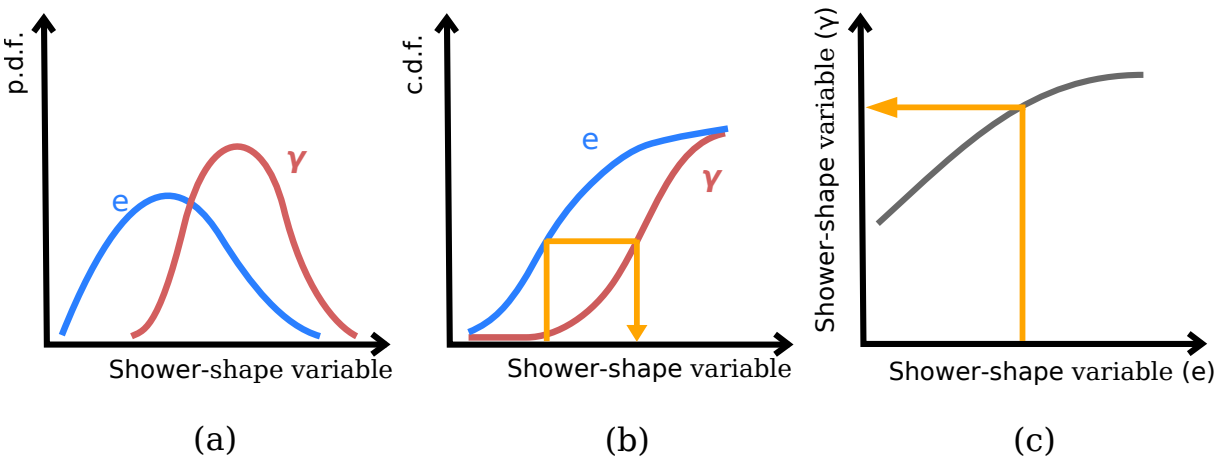

Figure 4.2. | Illustration of the electron-extrapolation method. In (a), the distribution of a shower-shape variable is shown for both photons and electrons. In (b), the corresponding c.d.f.s are shown. The orange arrow illustrates the transformation procedure based on the c.d.f.s. The corresponding mapping from electron values for the shower-shape variable to the corresponding values for photons, $(\mathrm{F}_\gamma)^{-1}(\mathrm{F}_\mathrm{e}(x_e))$, is shown in (c).

of the principle is given below for a shower-shape variable denoted by x and for a p_{T} bin i and a $|\eta|$ bin j:

1. Based on simulated samples of electrons and photons, normalized shower-shape variable distributions, i.e. probability density functions (p.d.f.s),
   - $\mathrm{f}_e\,(\,x \mid p_{\mathrm{T}}$ bin $i;\, |\eta|$ bin $j\,)$
   - $\mathrm{f}_\gamma^{(\mathrm{un})\mathrm{conv}}\,(\,x \mid p_{\mathrm{T}}$ bin $i;\, |\eta|$ bin $j\,)$

   are determined for electrons and converted (unconverted) photons. See Figure 4.2 (a).

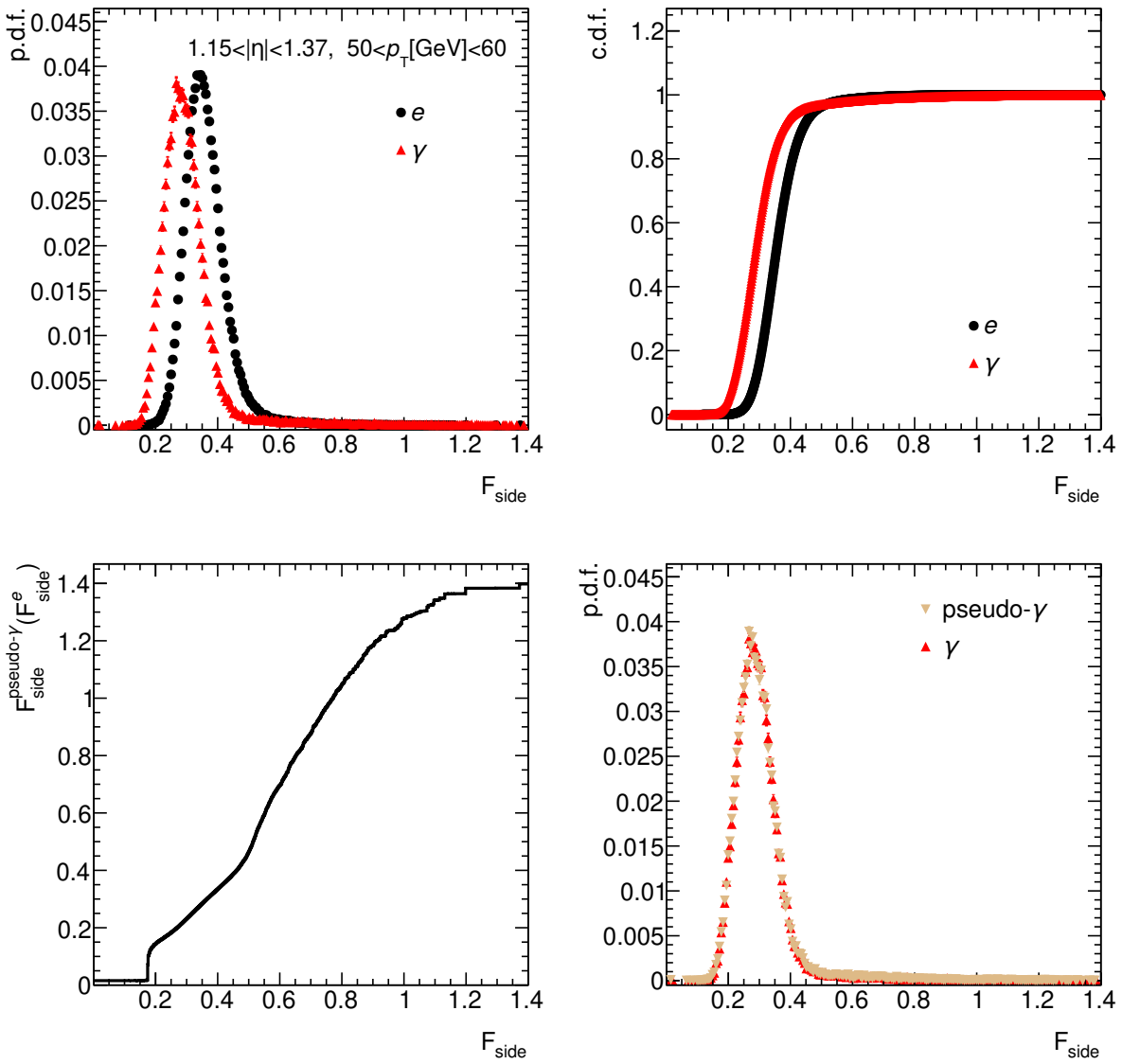

Figure 4.3. | Example of the derivation and application of a shower-shape transformation. The shower-shape variable in this example is chosen to be F_{side}. The red and black markers correspond to distributions of photons and electrons in simulation, respectively. In the top-left plot, the p.d.f.s, and in the top-right plot, the corresponding c.d.f.s are shown. The mapping from electron values for the F_{side} variable to corresponding pseudo-photon values is shown in the bottom-left plot. The result of the application of this transformation on a sample of electrons and a comparison with the original photon p.d.f. is shown in the bottom-right plot.

2. These distributions are the basis for the computation of *cumulative distribution functions* (c.d.f.s) of the shower-shape variable distributions [163], see Figure 4.2 (b). A c.d.f. is defined as

$$\mathrm{F}_e\,(\,x \mid p_\mathrm{T}\text{ bin }i;\,|\eta|\text{ bin }j\,) = \int_{-\infty}^{x} \mathrm{f}_e\,(\,x' \mid p_\mathrm{T}\text{ bin }i;\,|\eta|\text{ bin }j\,)\,\mathrm{d}x' \tag{4.3}$$

for electrons and similarly for converted (unconverted) photons:

$$\mathrm{F}_\gamma^{(\mathrm{un})\mathrm{conv}}\,(\,x \mid p_\mathrm{T}\text{ bin }i;\,|\eta|\text{ bin }j\,) = \int_{-\infty}^{x} \mathrm{f}_\gamma^{(\mathrm{un})\mathrm{conv}}\,(\,x' \mid p_\mathrm{T}\text{ bin }i;\,|\eta|\text{ bin }j\,)\,\mathrm{d}x'\,. \tag{4.4}$$

Given the electron and photon c.d.f.s for the shower-shape variable, a given electron can now be transformed to a pseudo-photon by applying the following operations, summarized also in Figure 4.2 (b) and (c) in form of an arrow:

1. For a given electron, the value x_meas of the shower-shape variable x is determined.

2. In order to obtain the shower-shape variable value of the to-be-created pseudo-photon, the inverted photon c.d.f. is evaluated at the value of the electron c.d.f. at the measured shower-shape variable value x_meas:

$$x_\gamma^{(\mathrm{un})\mathrm{conv}} = (\mathrm{F}_\gamma^{(\mathrm{un})\mathrm{conv}})^{-1}\,(\,\mathrm{F}_e(x_\mathrm{meas})\,)\,, \tag{4.5}$$

where the dependence of the c.d.f.s on the p_T and $|\eta|$ of the electron is implicit.

While the transformations reproduce the one-dimensional photon shower-shape distributions, the transformations preserve the electron-like correlations between shower-shape variables. A correction for this bias is applied to the measured efficiency.

The transformation procedure is applied to electrons from $Z \to e^+e^-$ events collected with a tag-and-probe method in data, see Section 4.5.2. Given an electron to be transformed, the transformations for the various shower-shape variables are selected based on the p_T and $|\eta|$ of that electrons. The photon identification efficiency measurement is based on the invariant-mass spectrum of the tagged electron and transformed electron-candidate probe. Based on this mass spectrum, a signal-plus-background fit is performed in order to extract signal yields for both probe selections relevant for the efficiency determination, following Eq. (4.1). The efficiency

then is given by the ratio of the signal yield when applying the photon identification selection to the probe pseudo-photons and the signal yield when no identification selection is applied. Since the efficiency measurement is performed for isolated photons, the isolation criteria are part of both numerator and denominator selections applied to the probe pseudo-photon. Separate invariant-mass distributions are defined for $N_{\text{bins}}^{p_{\text{T}}} \times N_{\text{bins}}^{|\eta|} = 12 \times 4$ kinematic regions of the probe.

The electron-extrapolation method relies on electrons from Z decays in sufficient numbers; therefore, it is currently constrained to values of transverse momentum below about 250 GeV. There is, however, no fundamental reason against expanding this upper limit once more data is taken. A lower p_{T} boundary of 25 GeV is used since the level of background events increases towards low p_{T}.

In Appendix C, the distributions of the various shower-shape variables for photons and electrons are shown for a representative selection of kinematic regions. Additionally, the effect of the shower-shape transformation is shown in terms of the difference between the variable value after and before the transformation was applied.

4.3. Complementary Methods of Efficiency Measurement

Besides the electron-extrapolation method, there are presently two additional and complementary methods used to measure the photon identification efficiency:

- *Radiative Z Decays*, in the p_{T} range of 10 GeV to 100 GeV
- *Matrix method*, in the p_{T} range of 25 GeV to 1500 GeV

While the measurement described in this work is performed using the electron-extrapolation method, the two other methods will be briefly explained as well in order to give a more complete picture of the determination of photon identification efficiencies. The final efficiency scale factors that are used in photon-based physics analyses are determined using a combined fit of all three methods, the result of which is shown in Section 4.8.

4.3.1. Radiative *Z*-Boson Decays

As mentioned in Section 4.2, it is possible to collect a photon sample from $Z \to \ell^+\ell^-\gamma$ events with lepton-antilepton pairs from a Z-boson decay in association with a photon [161], where the

lepton flavor can be either electron or muon. This selection method is similar to the tag-and-probe method for the selection of electron-positron pairs from $Z \to e^+e^-$ events which is described in Section 4.5.2. Since electrons and muons are electrically charged, they have the chance to emit photons. The event selection for this method consists in requiring an e^+e^- or $\mu^+\mu^-$ candidate pair in combination with a photon candidate. If the photon candidate in consideration indeed corresponds to final-state radiation from one of the two leptons from a Z-boson decay, the invariant mass of the three-body system $\ell^+\ell^-\gamma$ is close to the Z-boson mass. If, however, the photon candidate corresponds to initial-state radiation or to a QCD jet, the invariant mass of the two leptons will be closer to the Z-boson mass than the three-body $\ell^+\ell^-\gamma$ mass. By constraining the event selection such that predominantly events with final-state radiation are selected, i.e. events with photons emitted from one of the two leptons from a Z-boson decay, the purity of the photon sample can be greatly increased. This is achieved by a kinematic selection based on the invariant mass of the $\ell^+\ell^-\gamma$ and of the $\ell^+\ell^-$ system. While lepton identification cuts are applied to the two leptons in the process of event selection, the photon candidate is not subject to any identification cuts within the context of event selection, leading to an unbiased sample of photons. After performing a background subtraction that reduces the influence of event signatures such as Z + jets, which can have a very similar detector signature as $Z \to \ell^+\ell^-\gamma$ events, the photon identification efficiency can be determined based on the photon candidate sample.

Due to the low probability of final-state radiation with large transverse momentum, this method is at the time of this measurement used in the region of $p_{\mathrm{T}} < 100\,\mathrm{GeV}$. This method is one of the cleanest ways of measuring the photon identification efficiency, as it involves only small backgrounds and relies on only few basic assumptions.

4.3.2. Matrix Method

The matrix method is based on the analysis of an inclusive-photon sample collected with single-photon triggers, and relies on a track isolation variable (see Section 3.3.3) as an auxiliary discriminating variable. Because even at large p_{T} many photon candidates can be collected using single-photon triggers, this method provides a measurement of the photon identification efficiency up to transverse momenta of the order TeV.

Based on the track isolation efficiencies for real photons and for photon-faking jets, the purity

of real photons in a sample of photon candidates that pass the identification, $P^{\text{pass ID}}$, can be determined, as well as the purity of real photons in an inclusive sample of photon candidates, P^{incl} [161]. In combination with the number of photon candidates that pass identification, $N^{\text{pass ID}}$, and the number of photon candidates in the inclusive sample, N^{incl}, the identification efficiency can be computed:

$$\varepsilon_{\text{ID}} = \frac{P^{\text{pass ID}} \cdot N^{\text{pass ID}}}{P^{\text{incl}} \cdot N^{\text{incl}}} \tag{4.6}$$

The required purities can be determined based on efficiencies of a track-based isolation selection. This efficiency must be known for photon-faking jets, for true photons, as well as for the inclusive sample containing both fake photons and true photons. The efficiency for true photons is estimated based on a simulated photon sample. For photon-faking jets, efficiencies are determined based on data: by inverting selection cuts on all or some of the shower-shape variables, exploiting the fact that some shower-shape variables are approximately uncorrelated to the track isolation, track isolation efficiencies are estimated.

4.4. Data Samples and Simulation

4.4.1. Dataset and Single-Electron Trigger

The dataset used in the electron-extrapolation method consists of data collected in the years 2015 to 2017, corresponding to an integrated luminosity of 79.8/fb. In order to obtain an unbiased sample of electrons to which shower-shape transformations can be applied, a single-electron trigger is used. For this tag-and-probe method, it is important to not use di-electron triggers, since the requirement that two electrons pass the trigger selection would prevent the selection of an unbiased sample of electrons. Table 4.5 gives an overview over the single-electron triggers that were used in the various data-taking periods.

The triggers given in Table 4.5 fire if an electron candidate satisfies certain requirements, which will be detailed below. Generally, a single-electron trigger requires the transverse energy of a candidate to surpass a given threshold in the context of the high-level trigger (“HLT”). In some cases, high-level triggers need to be seeded by a sufficiently large transverse energy at level-1 (“L1”). If “V” is part of the L1 trigger name, the threshold changes with pseudorapidity in order to account for varying energy losses in the upstream material. If a “H” is added, an additional

	2015	2016	2017
HLT_e24_lhmedium_L1EM18VH	✓		
HLT_e24_lhmedium_L1EM20VH	✓		
HLT_e26_lhtight_nod0_ivarloose		✓	✓
HLT_e60_lhmedium	✓		
HLT_e60_medium		✓	✓
HLT_e120_lhloose	✓		
HLT_e140_lhloose_nod0		✓	✓
HLT_e300_etcut		✓	✓

Table 4.5. | A summary of the single-electron triggers used in the electron-extrapolation measurement for different data-taking periods.

isolation requirement is used that is based on information from the hadronic calorimeter. In order to reduce the trigger rate and background contamination, an electron identification selection can be applied to the candidate. The identification selection can be adjusted in its restrictivity. The strictness of the electron identification is indicated by the "lhloose", "medium", "lhmedium", and "lhtight" keywords. Triggers that have the keyword "etcut" in their name do not apply any identification selection. By applying an isolation selection, the trigger rate can be further reduced. The keyword "ivarloose" indicates the use of an isolation selection based on a variable-sized cone around the candidate. Some trigger names contain the keyword "nod0", which means that in these trigger selections no restrictions on the transverse impact parameter of the candidate are imposed.

4.4.2. Simulation

Simulated samples of single-photon and $Z \to e^+e^-$ events are used to extract the shower-shape transformations that are applied to electrons collected in data events. The simulated photon samples contain two types of $2 \to 2$ scattering processes.

- Events, in which the photon production is described by the hard-scattering matrix element, corresponding to the processes $qg \to q\gamma$ and $q\bar{q} \to g\gamma$.
- Events, in which photons are generated in the fragmentation process of the final state partons. Such photons are called *fragmentation photons*; the relevant scattering processes

at matrix-element level are $gg \to q\bar{q}$, $qg \to qg$, $qq \to qq$, and $q\bar{q} \to q\bar{q}$.

The MC simulations that have been used are listed in Table 4.6. Both events with fragmentation

MCID	Process	σ [fb]	p_{T} slice [GeV]	Filter efficiency	Events in sample	Generator
423100	Incl. γ	1.67e+13	17 to 35	2.9e−05	2.23e+06	Pythia8
423101	Incl. γ	1.40e+12	35 to 50	2.5e−05	2.25e+06	Pythia8
423102	Incl. γ	3.80e+11	50 to 70	2.3e−05	3.00e+06	Pythia8
423103	Incl. γ	1.06e+11	70 to 140	3.9e−05	2.89e+06	Pythia8
423104	Incl. γ	6.70e+9	140 to 280	5.0e−05	0.34e+06	Pythia8
361106	$Z \to e^+e^-$	1.90e+6	n.a.	1.0	79.94e+06	Powheg-Box+Pythia8

Table 4.6. | A summary of the MC samples used in the electron-extrapolation measurement.

photons and events with photons from the hard interaction are generated using Pythia8 [77]. The matrix element is computed at leading order in perturbation series, and the Pythia8-internal showering is used to describe the QCD emissions beyond the considered order in the matrix element as well as to describe non-perturbative effects. Simulated $Z \to e^+e^-$ events are generated at NLO with Powheg-Box [164] interfaced to Pythia8.

The weight for a given simulated event is a product of several factors, namely the initial event weight from the generator w_{evt}, a pileup weight w_{pileup}, a cross section σ, a filter efficiency $\varepsilon_{\mathrm{filter}}$, and a vertex weight w_{vtx}:

$$w = w_{\mathrm{evt}} \cdot w_{\mathrm{pileup}} \cdot w_{\mathrm{vtx}} \cdot \varepsilon_{\mathrm{filter}} \cdot \sigma \cdot \frac{1}{\sum_i w_i}. \tag{4.7}$$

The pileup weight is chosen such that the simulated sample has a distribution of the number of pileup interaction closely resembling that in data. A vertex-position-based reweighting is performed in order to match the distribution of vertex z-coordinates as observed in data. The inclusive cross section σ of the process, i.e. inclusive photon production in a given range in photon p_{T} or $pp \to Z \to e^+e^-$, is relevant when events from different samples are combined as in the case of photon events. In order to account for the application of a generator-level filter that is used obtain a sample of events containing events with at least one photon with $|\eta| < 2.5$ and a transverse momentum within a specified range, the corresponding efficiency $\varepsilon_{\mathrm{filter}}$ needs to be included. The inverse of the sum of weights of all simulated events, running over all events of

the event sample of which the event in question is part of, serves as normalization.

4.5. Event Selection

4.5.1. Photon Selection

The selection criteria for simulated photons that are used for the derivation of the shower-shape transformations and for the determination of photon identification efficiencies in simulation include cuts on the photon kinematics as well as an isolation-based selection. If more than one photon in an event passes the following requirements, the photon with the highest p_{T} is selected.

- The photon candidate must have a $p_{\mathrm{T}} > 25\,\mathrm{GeV}$ and fall within the pseudorapidity range $0 < |\eta| < 2.37$, excluding the region $1.37 < |\eta| < 1.52$.
- The photon must pass loose selections on the calorimeter- and track-based isolation variables, corresponding to $E_{\mathrm{T}}^{\mathrm{iso}}|_{\Delta R<0.2} < 0.065 \cdot E_{\mathrm{T}}$ and $p_{\mathrm{T}}^{\mathrm{iso}}|_{\Delta R<0.2} < 0.05 \cdot E_{\mathrm{T}}$. See Section 3.3.3 for details on the isolation variables.
- The reconstructed photon must be matched to a truth-level photon, accessing truth-level simulation information in simulation. This prevents non-photon signatures such as particles from hadron decays to be taken into account in the creation of transformations and in the determination of identification efficiencies.

These selection criteria are applied before the identification efficiency is determined. An additional requirement is imposed for photons that are used in the context of the derivation of shower-shape transformations: a minimal fraction of the photon cluster energy must be deposited in the first layer of the EM calorimeter, $\mathrm{f}_1 > 0.005$. This pre-selection on the basis of f_1 is applied in order to ensure a robust determination of the shower-shape variables in the first EM calorimeter layer. By imposing this pre-selection, the other shower-shape variable distributions are slightly biased, which is also reflected in the resulting transformations and consequently in the measured efficiencies from data. By multiplying the measured efficiency with the ratio $\varepsilon_{\mathrm{ID,MC}}/\varepsilon_{\mathrm{ID,MC}}^{\mathrm{f_1-pre-sel.\,applied}}$ as obtained in simulation and corresponding to the efficiency of the f_1 selection, the bias is corrected; $\varepsilon_{\mathrm{ID,MC}}$ denotes the nominal photon identification efficiency in simulation, and $\varepsilon_{\mathrm{ID,MC}}^{\mathrm{f_1-pre-sel.\,applied}}$ corresponds to the photon identification efficiency of a sample

of photons that pass the pre-selection for f_1. The corrected efficiency is then given by:

$$\varepsilon_{\mathrm{ID,data}} = \varepsilon^{\mathrm{uncorr.}}_{\mathrm{ID,data}} \cdot \frac{\varepsilon_{\mathrm{ID,MC}}}{\varepsilon^{f_1-\mathrm{pre-sel.\,applied}}_{\mathrm{ID,MC}}}, \tag{4.8}$$

where $\varepsilon_{\mathrm{ID,data}}$ ($\varepsilon^{\mathrm{uncorr.}}_{\mathrm{ID,data}}$) corresponds to the corrected (uncorrected) measured efficiency. In Figure 4.4 the correction is shown for converted and unconverted photons as a function of p_{T} and in four different $|\eta|$ regions. In the case of converted photons, the f_1 selection efficiency is very close to 100 %, while for unconverted photons it can be as low as 98 % at large values of $|\eta|$. This difference is due to the fact that unconverted photons tend to initiate shower development at larger radii, which leads to a slight reduction of the average of the energy deposited in the first calorimeter layer.

4.5.2. Electron Selection with a Tag-and-Probe Method

In order to obtain a sample of pseudo-photons, i.e. of transformed electrons, that can be used to measure the photon identification efficiency, it is necessary to have a pure and unbiased electron sample to which the shower-shape transformations can be applied. Such a sample can be obtained by selecting electrons from Z-boson decays using a tag-and-probe method. In this method, events are selected which fire at least one of the single-electron triggers mentioned in Section 4.4 and which contain at least one electron and one positron candidate. For the sake of simplicity, both electrons and positrons will be called electrons henceforth.

For all possible combinations of two electron candidates with opposite charge in a given event, it is checked whether one of them satisfies the following requirements:

- The electron candidate has a p_{T} larger than 25 GeV and lies in a detector region allowing a reliable electron identification, that is, $|\eta| < 2.47$ and excluding $1.37 < |\eta| < 1.52$.
- The electron candidate matches to the object that fired the trigger, i.e. its angular distance ΔR to the fired trigger is sufficiently small. In this analysis, the threshold is chosen to be $\Delta R < 0.1$.
- The electron candidate passes tight electron identification criteria, see Section 3.3.3.

If the considered electron candidate fulfills these requirements, and the invariant mass of the system of the two electron candidates is close to the Z-boson mass of 91.2 GeV [6], it is likely

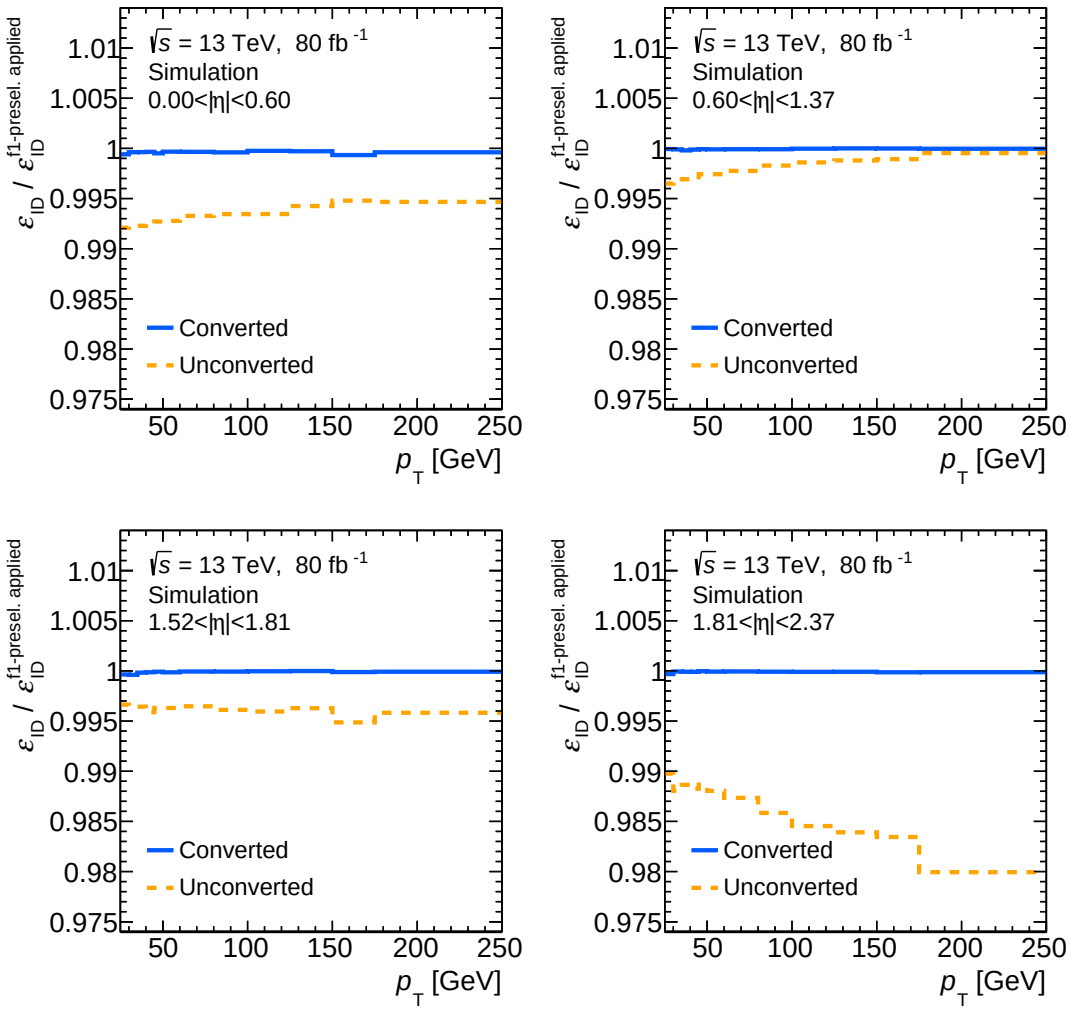

Figure 4.4. | Efficiency corrections for a bias due to a pre-selection based on f_1. The correction is shown for converted and unconverted photons as a function of p_T and in four different $|\eta|$ regions.

that the electron candidate is indeed one of the two electrons from a $Z \to e^+e^-$ decay. As a consequence, this electron can be used as a *tag* for the other electron candidate, which is called the *probe*. Since all selection criteria so far have been applied to the tag electron candidate, the corresponding selection of probe electron candidates remains unbiased. Therefore, the probes can be used to determine identification efficiencies. An electron candidate that is used as a probe in a given pairing of electron candidates can also be used as a tag itself in the same pairing if it passes the corresponding tag selection criteria. Generally, all possible combinations of electron candidates are considered.

To a large degree, the electron-extrapolation method of measuring photon identification efficiencies follows that of the electron identification efficiency measurement [150], which is outlined below. The major difference is that the selected probe electrons are transformed to pseudo-photons, which allows measuring the efficiency of the photon identification algorithm.

The measurement of the electron identification efficiency is based on invariant-mass distributions for two different probe selections, corresponding to the numerator (identification selection applied) and denominator (no identification selection applied) of the efficiency. After subtracting the background in the invariant-mass spectrum, stemming predominantly from $W^\pm$ + jets events with a leptonically decaying $W^\pm$ boson and from multi-jet events, the ratio of the integrals of the numerator and the denominator distributions around the Z-boson mass peak corresponds to the electron identification efficiency, as illustrated in Figure 4.5.

The background subtraction is performed in a simple signal-plus-background fit, considering electron-candidate pairs with an invariant mass m_{ee} within $65\,\text{GeV} \leq m_{ee} \leq 250\,\text{GeV}$. The shape of the $Z \to e^+e^-$ signal mass distribution is based on simulation. A template for the background shape is taken from data, using inverted isolation and identification criteria in order to obtain a sample enriched in background events. Basic track quality selection criteria are applied to all candidates. In order to contribute to the background sample, a candidate must fail at least two rectangular selection requirements on shower and track properties. Additionally, if the candidate's transverse energy is below 30 GeV, the calorimeter-based isolation variable defined in a cone of radius 0.3, topo-$E_\text{T}^{\text{cone}\,30}$, must exceed 2 % of the candidate's transverse momentum. The background template is sketched in Figure 4.5 as gray area. The numerator and denominator in the efficiency measurement are computed in a mass region close to the Z-boson mass in order to be less sensitive to mismodeling of the background template and because only a small fraction

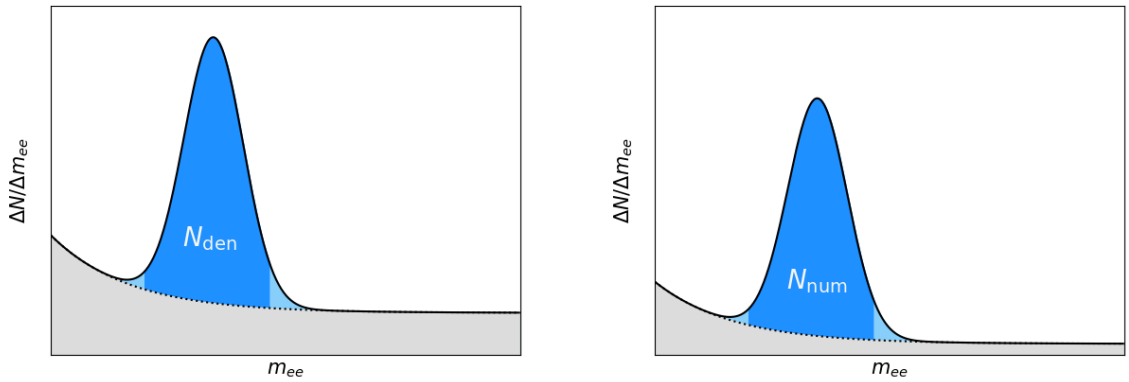

(a) *(b)*

Figure 4.5. | Sketch of the determination of the identification efficiency with a tag-and-probe method. Shown are two invariant-mass distributions of di-electron candidates. In each of these, the $Z \to e^+e^-$ signal, colored blue (dark and light), is stacked on the background, colored gray. The black line corresponds to the sum of both distributions. No identification selection is applied in the right distribution *(b)*, while in the invariant-mass distribution in *(a)*, the probe must pass the identification selection. In order to be less sensitive to background effects, the efficiency is determined in a small mass range around the Z-boson mass peak. The signal that is used for the numerator and denominator computation (N_{num}, N_{den}) is colored dark-blue, while the signal that is disregarded for the efficiency determination is colored light-blue. The ratio of the dark-blue areas of the right and left plot correspondingly corresponds to the efficiency.

of electron-positron pairs from $Z \to e^+e^-$ events have a mass that differs considerably from m_Z. Nominally, the mass range for the computation of the numerator and denominator signal yield is $70\,\text{GeV} \leq m_{ee} \leq 110\,\text{GeV}$.

This description of the determination of electron identification efficiencies translates easily to the determination of photon identification efficiencies, with the difference that the photon identification selection is applied to pseudo-photons which correspond to transformed probe electrons. Transformations have been derived for several kinematic regions of the probe electron. Another modification with respect to the measurement of electron identification efficiencies as described above is that an isolation requirement is imposed on both the denominator and the numerator level in the case of the determination of photon identification efficiencies, i.e. the probe pseudo-photons must be isolated.

In Figures 4.6 and 4.7, examples of measured invariant-mass distributions for the numerator and denominator probe selection are shown. As explained in Section 4.2, sets of electron shower-shape transformations are derived to map electron shower shapes to those of converted and unconverted photons individually. For Figures 4.6 and 4.7, the mappings to shower shapes of un-

converted photons are applied to probe electrons, allowing the measurement of the identification efficiency for unconverted photons.

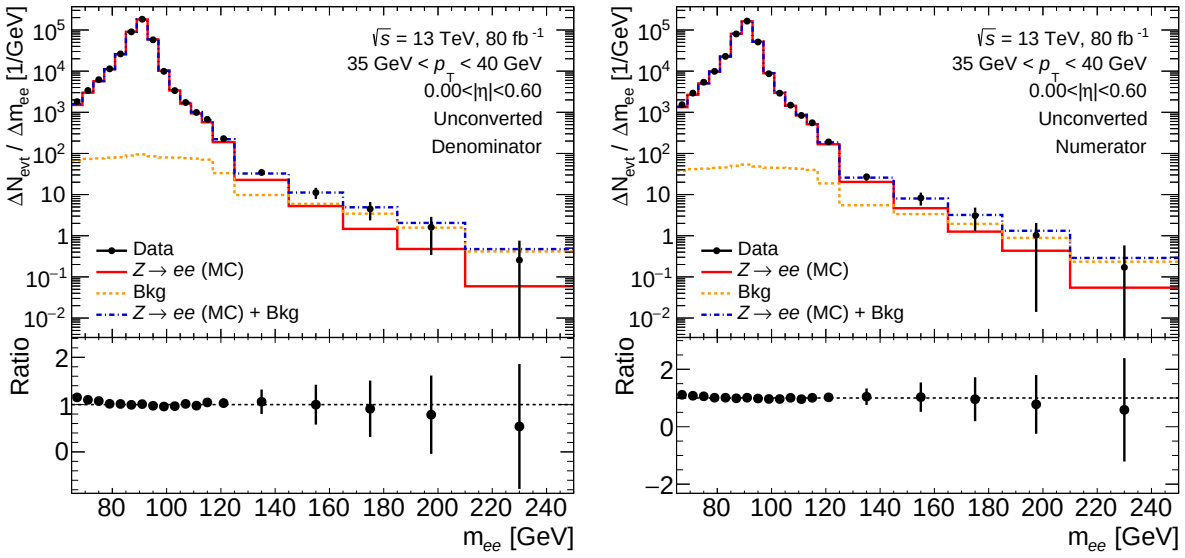

(a) *(b)*

Figure 4.6. | Examples of m_{ee} distributions for unconverted pseudo-photon probes with $35\,\text{GeV} < p_\text{T} < 40\,\text{GeV}$ and $|\eta| < 0.6$. In *(a)* the denominator selection consisting of an isolation requirement is applied, while in the numerator selection in *(b)* also the photon identification requirement is applied. The ratio in the lower panel shows the agreement between the distribution observed in data with the fitted signal-plus-background distribution.

In the low-p_T region, e.g. $25\,\text{GeV} < p_\text{T}^\text{probe} < 30\,\text{GeV}$ (see Figure 4.6) the only distinct accumulation of events is the peak at m_Z. An additional feature of the distribution occurs at larger p_T, e.g. $100\,\text{GeV} < p_\text{T}^\text{probe} < 125\,\text{GeV}$ (see Figure 4.7): At a mass of roughly $m_{ee} = 2p_\text{T}^\text{probe}$ a second, smaller and broader maximum is visible, resulting from non-resonant Drell-Yan events, i.e. $q\bar{q} \to \gamma^*/Z^* \to e^+e^-$. While in the case of resonant production with $m_{ee} \approx m_Z$, the invariant mass of the final-state electrons for generic Drell-Yan di-electron production is given by

$$m_{ee}^2 = 2\,p_\text{T}^\text{tag}\,p_\text{T}^\text{probe}\left[\cosh(\eta_\text{tag} - \eta_\text{probe}) - \cos(\phi_\text{tag} - \phi_\text{probe})\right], \tag{4.9}$$

where p_T^i, η_i, and ϕ_i correspond to the transverse momentum, the pseudorapidity and the azimuthal angle of the tag and the probe electrons. The mean value of the difference $(\eta_\text{tag} - \eta_\text{probe})$ is zero, while for $(\phi_\text{tag} - \phi_\text{probe})$ it is 180^o. Hence, the mean value for the invariant mass of electron-positron pairs from non-resonant Drell-Yan production amounts to about $m_{ee} \approx 2\,p_\text{T}^\text{probe}$ in the case of unboosted di-electron systems, i.e. $p_\text{T}(e^+e^-) \approx 0$. As can be seen in Figure 4.7,

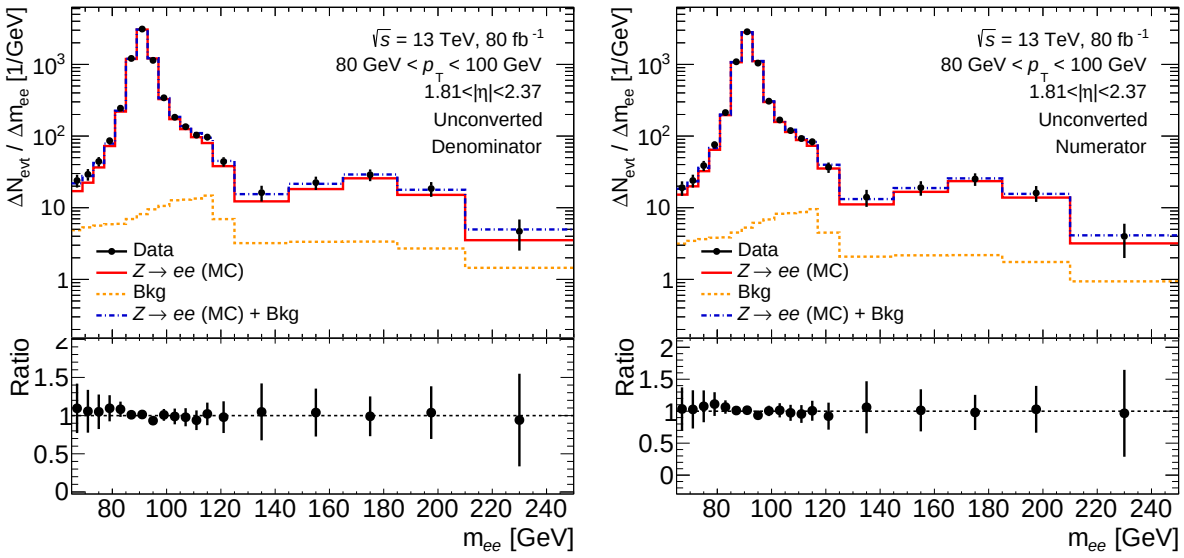

(a) *(b)*

Figure 4.7. | Examples of m_{ee} distributions for unconverted pseudo-photon probes with 80 GeV $< p_{\mathrm{T}} <$ 100 GeV and $1.81 < |\eta| < 2.37$. In *(a)*the denominator selection consisting of an isolation requirement is applied, while in the numerator selection in *(b)* also the photon identification requirement is applied. The ratio in the lower panel shows the agreement between the distribution observed in data with the fitted signal-plus-background distribution.

this corresponds to the mass value at which the second peak is centered.

4.6. Uncertainties

The uncertainty of the photon identification efficiency as measured with the electron-extrapolation method has both a systematic and statistical component. Thanks to the large number of $pp \to Z \to e^+e^-$ events in LHC collisions, the statistical uncertainty is small. The clearly dominant systematic component of the uncertainty is consists of a number of different uncertainty contributions which are added in quadrature. Broadly speaking, the systematic uncertainty contributions can be divided into the following types, which will be described in more detail in the following sections:

- Intrinsic bias of the method due to the procedure of transforming shower-shape variables, corresponding to a *non-closure* of the method.
- Background subtraction uncertainty.
- Uncertainty due to mismodeling in MC simulations.
- Uncertainty due to a limited number of simulated events.

4.6.1. Non-Closure of the Electron-Extrapolation Method

The electron-extrapolation method does not account for differences in shower-shape variable correlations between electrons and photons. The individual application of one-dimensional transformations for each shower-shape variable does not change the correlations between the various shower-shape variables. This leads to objects whose shower-shape variable distributions individually are very similar to those of photons, but whose inter-variable correlations are those of the original electrons. Because the photon identification is to some extent sensitive to these correlations, deviating correlations have an influence on the identification efficiency.

The resulting bias can be estimated using the simulated photon and electron samples. The transformations are applied to the electrons of the simulated $Z \to e^+e^-$ sample from which these transformations were derived in the first place. If the correlations between the shower-shape variables of photons and electrons would be identical, the photon identification efficiencies of those pseudo-photons from simulation would be the same as the efficiencies of the simulated photons. Generally, however, that difference in efficiency is non-zero, as can be seen in Figure 4.8, where the relative difference in efficiency is given in bins of p_{T} and in four separate $|\eta|$ regions. The non-closure is largest for unconverted photons, for which the relative difference ranges from

−1 % to almost 4 %. In the case of converted photons, the relative difference is typically in the range from −1 % to 1 %. Such smaller differences can be expected, since the shower development of converted photons is more similar to that of electrons than the shower development of unconverted photons is.

The values $\Delta\varepsilon/\varepsilon$ for the intrinsic non-closure of the method as shown in Figure 4.8 are used to correct the central value of the measured photon identification efficiency $\varepsilon_{\text{data}}$,

$$\varepsilon_{\text{data}}^{\text{corr.}} = \varepsilon_{\text{data}} \cdot \left(1 + \frac{\Delta\varepsilon}{\varepsilon}\right). \tag{4.10}$$

While the transformations are derived and applied in 7 bins of $|\eta|$, the identification efficiency is measured in 4 $|\eta|$ bins. Correspondingly, non-closure corrections to the efficiency must be provided in 4 bins of $|\eta|$. In addition to the correction of measured efficiencies, 100 % of the absolute value of the estimated non-closure is added as an uncertainty in order to have a conservative estimate of the identification efficiency uncertainty.

4.6.2. Background Contamination

A part of the selected electron candidate sample originates in background events rather than in $Z \to e^+e^-$ decays, as described in Section 4.5.2. In order to compute identification efficiencies, these events need to be subtracted from the invariant-mass distributions before the denominator and numerator of the efficiency calculation are determined. After that subtraction, a mass region around the Z-boson mass of 70 GeV to 110 GeV is used to compute signal yields of pseudo-photons passing the denominator and numerator selection. The accuracy of the background subtraction is not perfect; in order to assess the uncertainty due to imperfections in the background subtraction, the mass range from which the numerator and denominator are computed is varied to 80 GeV to 100 GeV. The difference between the nominal identification efficiency and the efficiency determined using the smaller mass range serves as an estimate of the background subtraction uncertainty; see Figure 4.9 for the result. At low p_{T}, the uncertainty is highest, with up to about 1 %. In most other kinematic regions, however, the uncertainty is well below this.

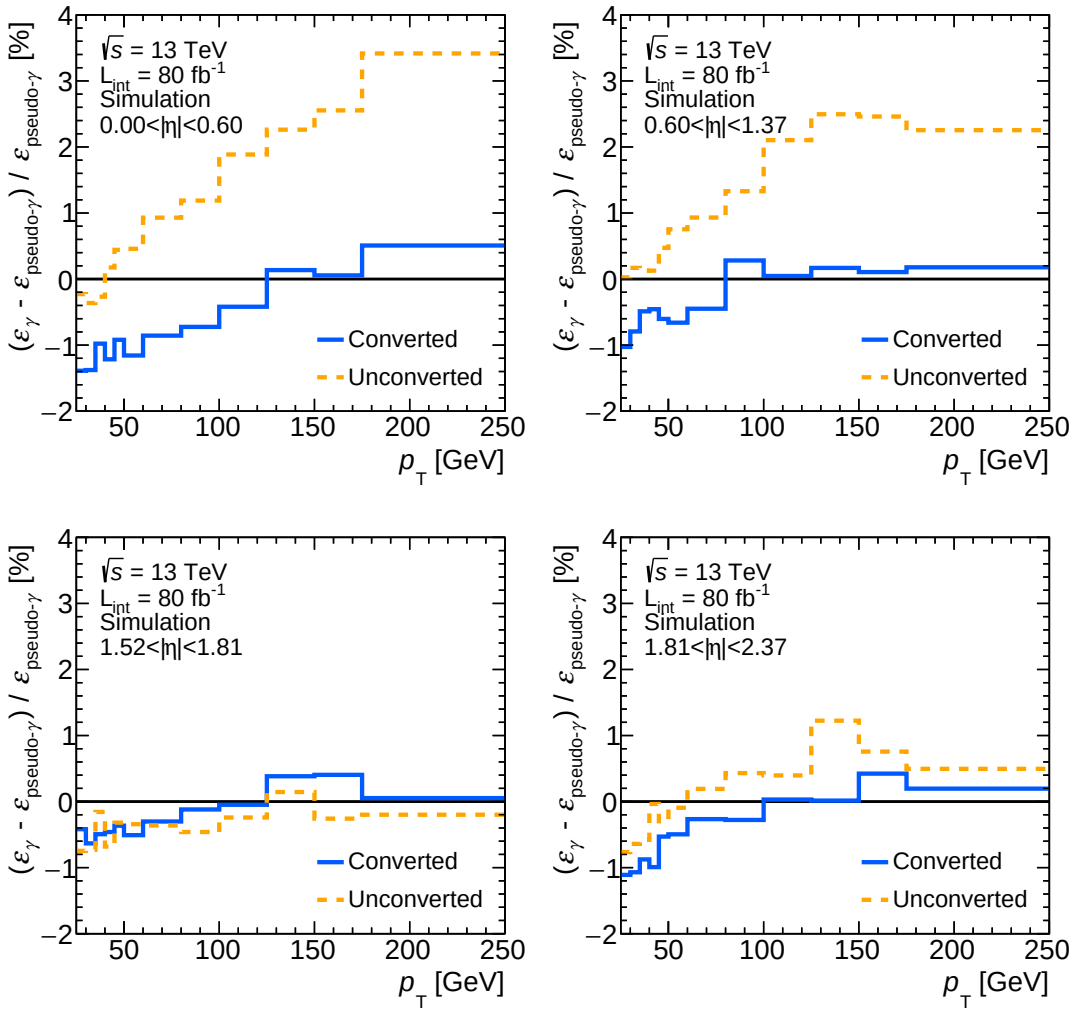

Figure 4.8. | Non-closure corrections as applied to measured photon identification efficiencies, with $\varepsilon_{\text{data}}^{\text{corr.}} = \varepsilon_{\text{data}} \cdot \left(1 + \frac{\Delta\varepsilon}{\varepsilon}\right)$. Values are given as a function of p_{T} and in four separate regions of absolute pseudorapidity $|\eta|$.

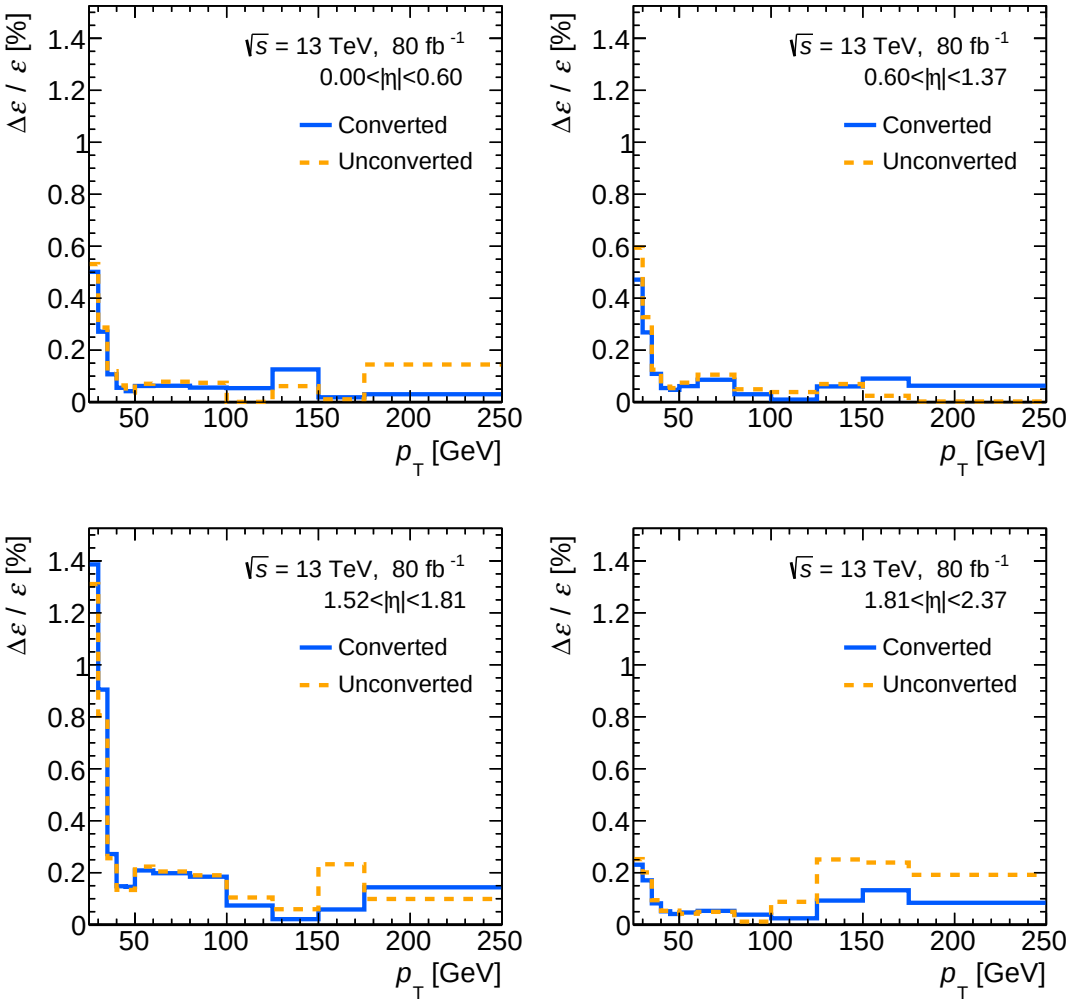

Figure 4.9. | Uncertainty contribution from the background subtraction procedure as a function of p_{T} for converted and unconverted photons, relative to the measured efficiencies. Each plot represents a different $|\eta|$ region.

4.6.3. Photon Conversion Misreconstruction

As described in Section 4.2, shower-shape transformations are derived separately for converted and unconverted photons, where the distinction between converted and unconverted photons is made at reconstruction level. The classification of photons into the converted and unconverted categories is not perfect, resulting in a certain fraction of actually converted photons that are reconstructed as unconverted photons and vice versa[1]. The figure of merit is the purity of photons within a given conversion category, e.g. in the sample of converted photons it is the fraction of photons that are indeed converted at truth level. Based on the nomenclature as given in Table 4.7, the purities for converted and unconverted photons are defined as follows:

$$
\begin{aligned}
f_{\text{reco conv}}^{\text{truth conv}} &= \frac{N_{\text{reco conv}}^{\text{truth conv}}}{N_{\text{reco conv}}^{\text{truth conv}} + N_{\text{reco conv}}^{\text{truth unconv}}} \\
f_{\text{reco unconv}}^{\text{truth unconv}} &= \frac{N_{\text{reco unconv}}^{\text{truth unconv}}}{N_{\text{reco unconv}}^{\text{truth unconv}} + N_{\text{reco unconv}}^{\text{truth conv}}},
\end{aligned}
\tag{4.11}
$$

Given a photon that is reconstructed to be converted or unconverted, the identification efficiency

	Reconstructed: converted	Reconstructed: unconverted
Truth: converted	$N_{\text{reco}-\text{conv}}^{\text{truth}-\text{conv}}$	$N_{\text{reco}-\text{unconv}}^{\text{truth}-\text{conv}}$
Truth: unconverted	$N_{\text{reco}-\text{conv}}^{\text{truth}-\text{unconv}}$	$N_{\text{reco}-\text{unconv}}^{\text{truth}-\text{unconv}}$

Table 4.7. | Possible cases of conversion reconstruction of photons that are either converted or unconverted at truth level.

of it depends on whether it is converted or unconverted at truth level. The identification efficiencies for photons that are reconstructed as converted and unconverted, respectively, are given by the following equations:

$$
\begin{aligned}
\varepsilon_{\text{ID, reco conv}} &= f_{\text{reco conv}}^{\text{truth conv}}\, \varepsilon_{\text{reco conv}}^{\text{truth conv}} + (1 - f_{\text{reco conv}}^{\text{truth conv}}) \varepsilon_{\text{reco conv}}^{\text{truth unconv}} \\
&= \varepsilon_{\text{reco conv}}^{\text{truth conv}} - \Delta\varepsilon_{\text{ID}}^{\text{reco conv}} \cdot (1 - f_{\text{reco conv}}^{\text{truth conv}}) \\
\varepsilon_{\text{ID, reco unconv}} &= f_{\text{reco unconv}}^{\text{truth unconv}}\, \varepsilon_{\text{reco unconv}}^{\text{truth unconv}} + (1 - f_{\text{reco unconv}}^{\text{truth unconv}})\, \varepsilon_{\text{reco unconv}}^{\text{truth conv}} \\
&= \varepsilon_{\text{reco unconv}}^{\text{truth unconv}} - \Delta\varepsilon_{\text{ID}}^{\text{reco unconv}} \cdot (1 - f_{\text{reco unconv}}^{\text{truth unconv}}),
\end{aligned}
\tag{4.12}
$$

[1] If not otherwise specified, the phrases *converted photons* and *unconverted photons* refer to photons that are *reconstructed* as converted and unconverted, respectively.

where with $\Delta\varepsilon_{\mathrm{ID}}^{\mathrm{reco\,conv}} = \varepsilon_{\mathrm{reco\,conv}}^{\mathrm{truth\,conv}} - \varepsilon_{\mathrm{reco\,conv}}^{\mathrm{truth\,unconv}}$ and $\Delta\varepsilon_{\mathrm{ID}}^{\mathrm{reco\,unconv}} = \varepsilon_{\mathrm{reco\,unconv}}^{\mathrm{truth\,unconv}} - \varepsilon_{\mathrm{reco\,unconv}}^{\mathrm{truth\,conv}}$. As one can see, the identification efficiencies for photons that are reconstructed as converted (unconverted) depend on the purities $f_{\mathrm{reco\,conv}}^{\mathrm{truth\,conv}}$ ($f_{\mathrm{reco\,unconv}}^{\mathrm{truth\,unconv}}$). These purities are modeled in MC simulation with limited accuracy. In order to assess the systematic uncertainty that results from the mismodeling of the conversion reconstruction, the purities are varied and the resulting shower-shape transformations are used to compute alternative photon identification efficiencies. The purities are varied by increasing and decreasing the fraction of truly converted photons among the photon sample. This is done by weighting events in which the considered photon is truly converted up and down by a factor 1.1 and 0.9, respectively. The relative difference between the efficiencies from the up- and down-variations of the conversion fractions at truth level, divided by 2, is shown in Figures 4.10. This systematic uncertainty is relatively small, being less than 0.3 % in all kinematic regions.

For unconverted photons, the uncertainty tends to be largest at low p_{T}, except in the pseudo-rapidity region of $1.81 < |\eta| < 2.37$. In order to understand this, it is helpful to consider again Eq. (4.12). The identification efficiency of photons that are reconstructed as unconverted depends on the purity $f_{\mathrm{reco\,unconv}}^{\mathrm{truth\,unconv}}$ as well as on the difference in efficiency $\Delta\varepsilon_{\mathrm{ID}}^{\mathrm{reco\,unconv}} = \varepsilon_{\mathrm{reco\,unconv}}^{\mathrm{truth\,unconv}} - \varepsilon_{\mathrm{reco\,unconv}}^{\mathrm{truth\,conv}}$ of the identification selection for unconverted photons between photons that are unconverted at truth level and photons that are converted at truth level. These efficiencies as well as the purity are shown in Figure 4.11. The purity is approximately constant over the considered p_{T} range. Except for the $|\eta|$ region above 1.81, where the purity is about 70 %, the purity is of the order 90 %. The difference in efficiency, which determines how large the effect of purity variations is, is largest for low p_{T} and considerable for high p_{T}. At intermediate p_{T} values, the two efficiency curves intersect; differences between the two efficiencies are small. As a consequence, purity variations for unconverted photons tend to have the largest effects at low p_{T}, small effects at intermediate p_{T}, and sizable effects at high p_{T}.

In most kinematic regions, the uncertainty is smaller for converted photons than for unconverted photons. In Figure 4.12, the relevant efficiencies and purities are shown. The difference in efficiency between truth-converted and truth-unconverted photons that have been reconstructed as converted is relatively small, except in the $|\eta|$ region above 1.81, where the efficiency difference is large in most p_{T} bins. However, the purity tends to be close to 100 %, with a minimum value of about 80 % at low $|\eta|$ and low p_{T}. Therefore, changes in weights depending on the truth-

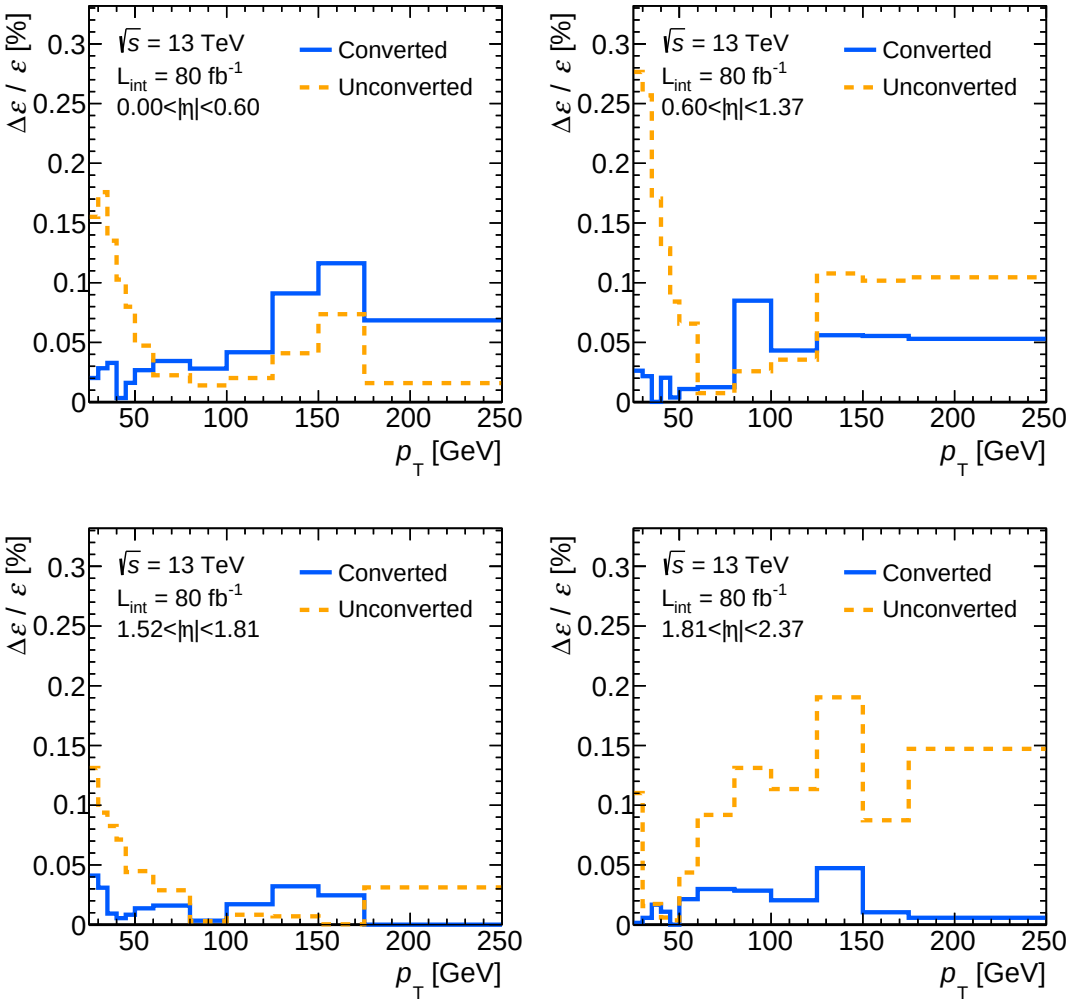

Figure 4.10. | Uncertainty contribution from the modeling of conversion reconstruction as a function of p_{T} for converted and unconverted photons, relative to the measured efficiencies. Each plot represents a different $|\eta|$ region.

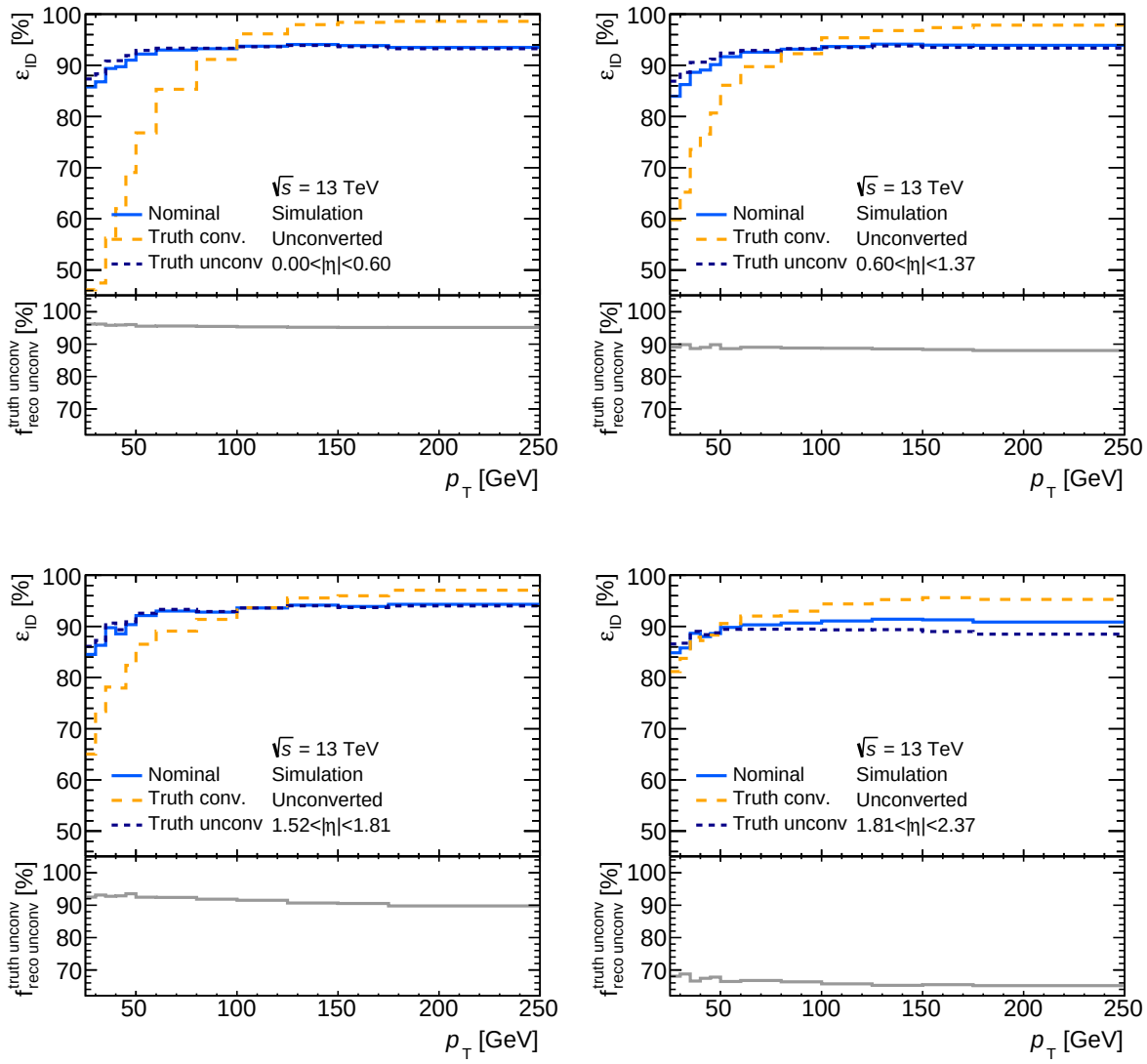

Figure 4.11. | Identification efficiencies for photons that are reconstructed as unconverted, based on MC simulation. Efficiencies are computed for photons that are unconverted at truth level as well as for photons that are converted at truth level. Moreover, the nominal efficiency is shown, based on the nominal sample of photons that are reconstructed as unconverted, consisting predominantly of photons that are unconverted at truth level. The fraction of truly unconverted photons that are reconstructed as unconverted corresponds to the purity, $f^{\text{truth unconv}}_{\text{reco unconv}}$, and is shown in the lower panels.

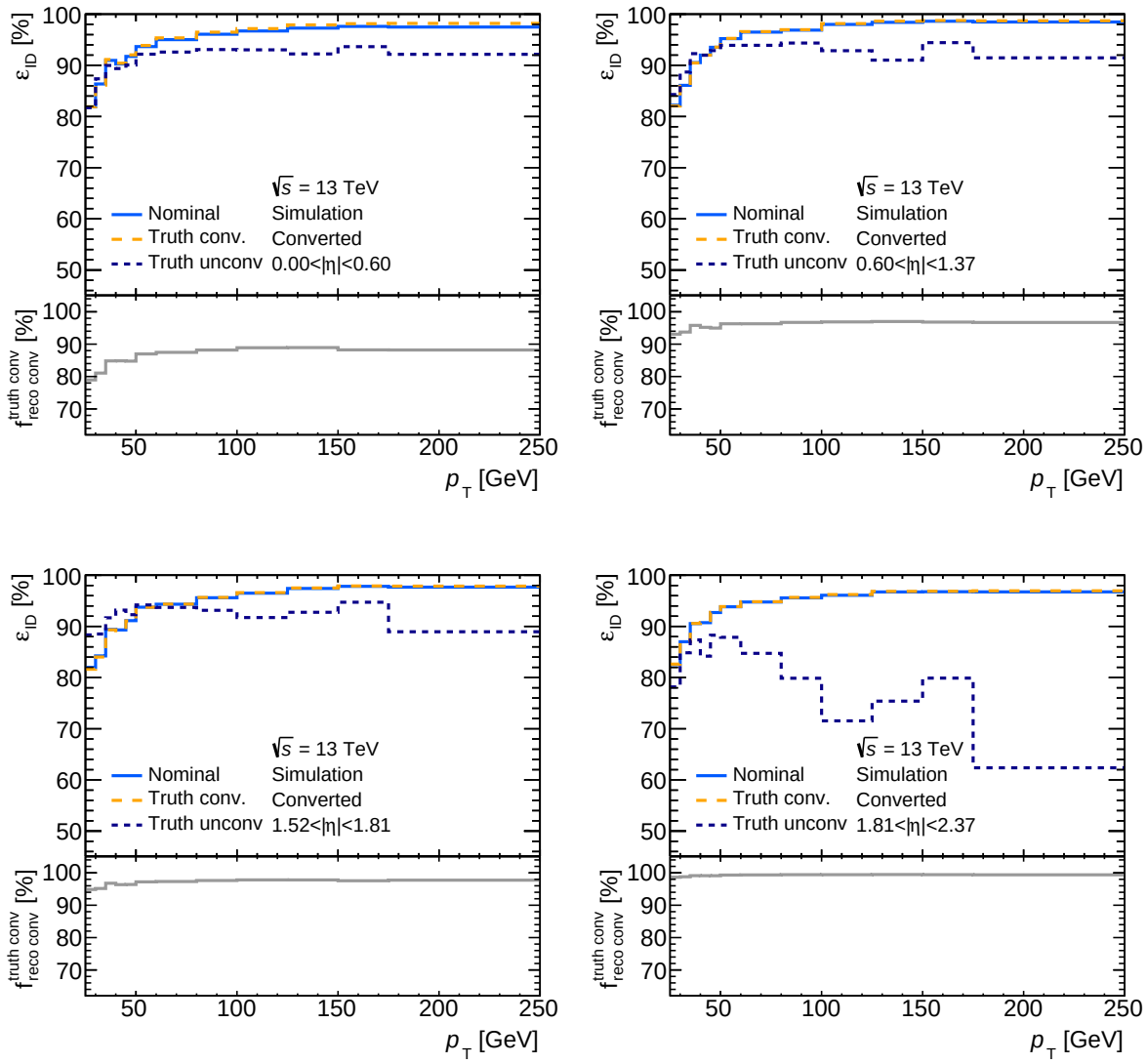

Figure 4.12. | Identification efficiencies for photons that are reconstructed as converted, based on MC simulation. Efficiencies are computed for photons that are converted at truth level as well as for photons that are converted at truth level. Moreover, the nominal efficiency is shown, based on the nominal sample of photons that are reconstructed as converted, consisting predominantly of photons that are converted at truth level. The fraction of truly converted photons that are reconstructed as converted corresponds to the purity, $f^{\text{truth conv}}_{\text{reco conv}}$, and is shown in the lower panel.

conversion information have little effects on the purity, leading to relatively low uncertainties from mismodeling of photon conversion reconstruction.

4.6.4. Fragmentation Photons

The sample of simulated photon events contains on the one hand events in which the photon is created in the hard-scattering process; see Section 4.4. On the other hand, the sample also includes events in which photons are emitted by final-state quarks, i.e. fragmentation photons. These different types of photon events cannot be expected to have identical kinematic and isolation-related properties. Photons from fragmentation processes tend to be less isolated than photons from the hard scattering. Therefore, the photon identification efficiency of these two kinds of photons can differ. The relative contributions of these two types of photon events to the photon sample used to extract electron-extrapolation efficiencies not necessarily corresponds to those in data event samples. In the simulated samples of photons that have been used for this measurement, the fraction of fragmentation photons in simulation is about 60 % at low p_{T}, while at transverse momenta above 100 GeV, it is about 45 %. This fraction to some extent depends on the specifications of a given physics analysis. Therefore, it is necessary to estimate the effect of variations in the composition of photon samples on the photon identification efficiency. The difference between efficiencies based on correspondingly varied photon samples is taken into account in the determination of the systematic uncertainty on the measured photon identification efficiencies.

In Figures 4.13 and 4.13 the efficiencies of the two types of photons are shown in combination with their relative contributions in the simulated photon samples. As one can see, the difference in efficiency tends to be largest at high p_{T}. The composition of the simulated photon sample is varied by an up- and down-variation of weights by factors of 1.5 and 0.5, respectively, of events in which the photon is produced in the hard scattering process. Corresponding varied sets of shower-shape transformations are derived, which in turn are applied to electrons in data. The difference between the resulting identification efficiencies, divided by 2, serves as uncertainty related to the imperfect knowledge of the relative fraction of fragmentation photons in data events.

The resulting uncertainties for unconverted and converted photons are shown in Figure 4.15.

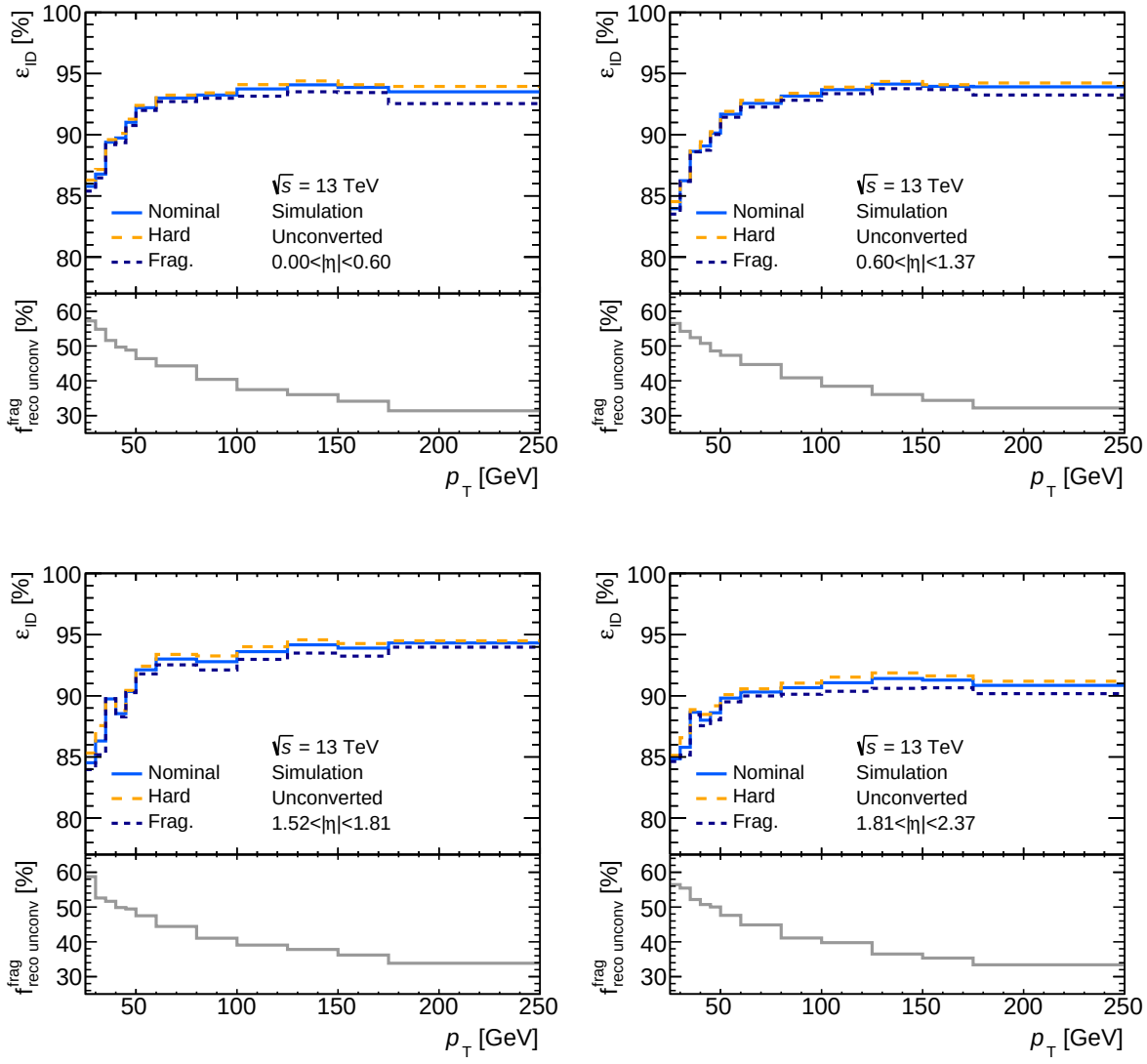

Figure 4.13. | Comparison of identification efficiencies for unconverted photons produced either in the hard interaction or in parton fragmentation. Additionally, the efficiency resulting from the nominal mixture of these two types in the simulated sample is shown. The fraction of photons that are fragmentation photons, defined as $f^{\text{frag}}_{\text{reco unconv}}$, is shown in the lower panel of each plot.

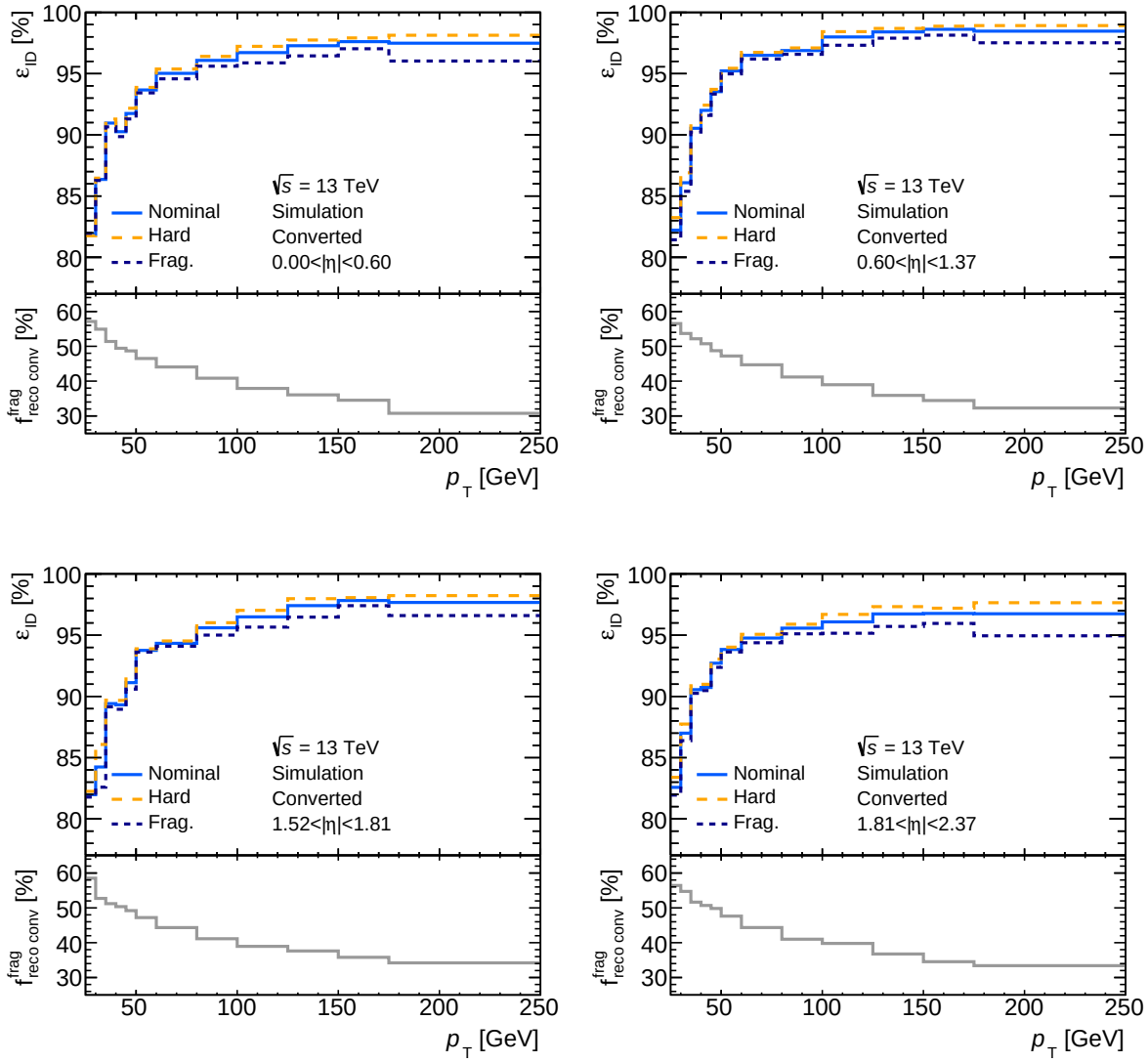

Figure 4.14. | Comparison of identification efficiencies for converted photons produced either in the hard interaction or in parton fragmentation. Additionally, the efficiency resulting from the nominal mixture of these two types in the simulated sample is shown. The fraction of photons that are fragmentation photons, defined as $f^{\text{frag}}_{\text{reco unconv}}$, is shown in the lower panel of each plot.

For unconverted and converted photons, this uncertainty is typically of the order 0.25 % and 0.5 %, respectively. While for the shown results, a reweighting of photons from the hard

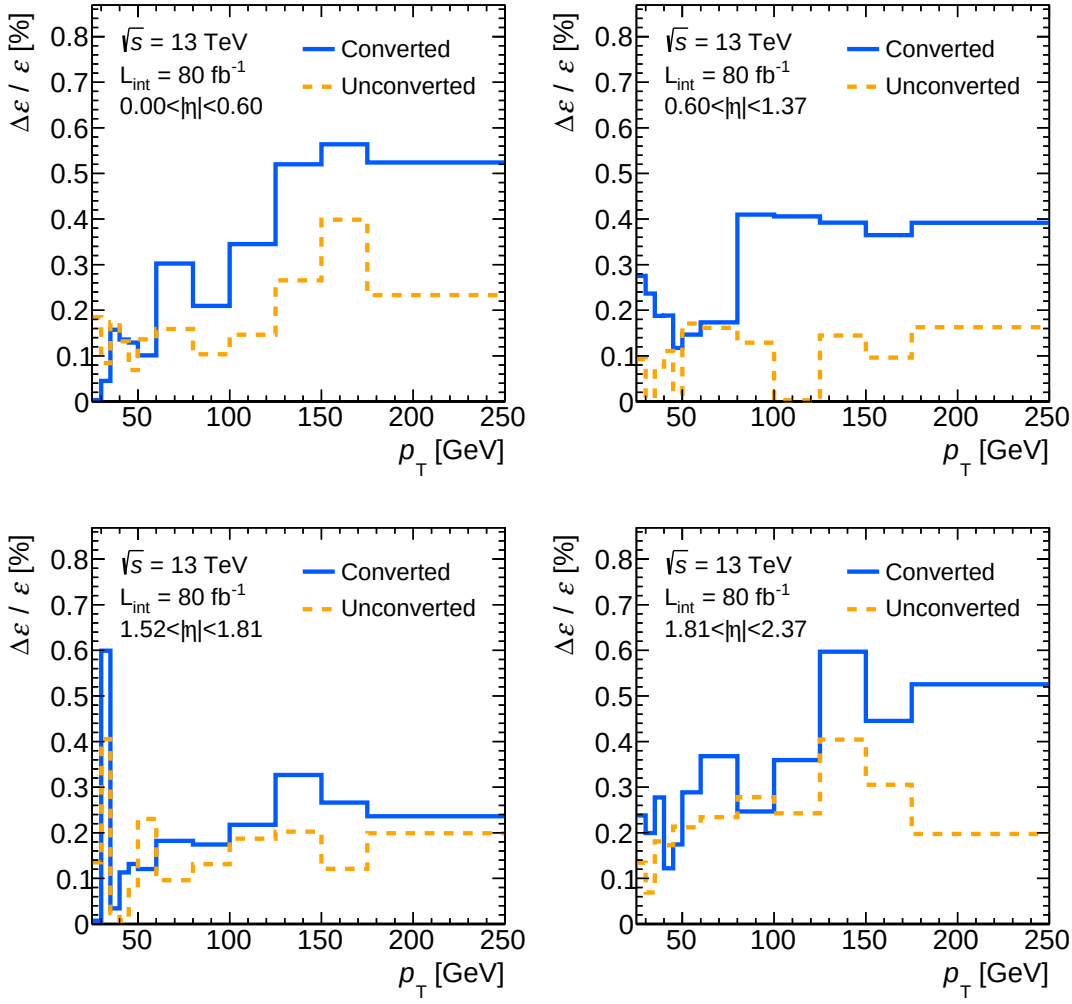

Figure 4.15. | Uncertainty contribution from the modeling of fraction of fragmentation photons as a function of p_{T} for converted and unconverted photons, relative to the measured efficiencies. Each plot represents a different $|\eta|$ region.

interaction was performed in order to extract related uncertainties, for future measurements it is planned to reweight fragmentation-photon events instead. That way, a more conservative estimate of the uncertainty can be achieved: If the fraction of fragmentation photons in simulation is lower than 50 %, the impact of a reweighting of fragmentation-photon events on the efficiency is larger than that of a reweighting of photons from the hard interaction. As can be seen in Figures 4.13 and 4.13, the fragmentation-photon fraction in most kinematic regions is below 50 %.

4.6.5. Shower-Shape Mismodeling

The shower-shape variable distributions of photons in data and simulation do not agree perfectly; the same is true for electrons. In order to mitigate the disagreement, corrections are applied to the simulation; see Section 4.1. These corrections consist of simple shifts (*fudge factors*) on most of the shower-shape variables. As a consequence, the mean values of the shower-shape variable distributions in data and simulation can be brought to good agreement. However, this simple correction cannot account for differences in the shape of the distributions, leading to residual differences between shower-shape variable distributions in data and simulation, see Figure 4.1. Since shower-shape variable distributions of photons and electrons in simulation are the basic ingredients of the shower-shape transformations, a mismodeling of these distributions directly affects the reliability of the method. Accordingly, the effect of such mismodeling must be assessed and included as uncertainty.

The corrections for shower-shape variable distributions are computed using comparisons of shower-shape variable distributions in data and in simulation based on minimizing a χ^2 statistic. In the nominal case, the whole range of the shower-shape variable distribution is considered. The fit result is dominated by the region in which the distribution peaks; the tails of the distribution have relatively little impact on the resulting correction. However, especially the tail on the side of the distribution in which the selection cut is applied tends to be subject to mismodeling in simulation. This results in a shape difference that cannot be resolved by applying a simple shift of the shower-shape variable distribution. In order to assess the impact of this mismodeling on the identification efficiency, an alternative set of shower-shape corrections is derived in which only the tail region is considered in the corresponding χ^2 fit. This procedure of deriving alternative corrections is performed both for photons and for electrons. Based on these alternative corrections, alternative sets of shower-shape transformations are created and applied to electrons in data. The uncertainty on the efficiency is then determined by comparing the resulting identification efficiencies to the nominal efficiencies, which are based on the application of nominal corrections to the shower-shape variable distributions.

Correlations between the various shower-shape variables should be taken into account in this procedure. Because some variables are correlated with each other, one should neither vary shifts on each shower-shape variable at a time and then add the resulting differences from the

nominal efficiency in quadrature, nor should one vary all shower-shape variables at once. Instead, a more sensible approach is to group the shower-shape variables according to their degree of correlation and perform variations of the shower-shape corrections for each of the resulting sets of shower-shape variables individually. For this measurement, the following grouping of variables was chosen:

- Variables sensitive to leakage into the hadronic calorimeter: R_{had}
- Variables sensitive to width in ϕ-direction in the second layer of the EM calorimeter: R_{ϕ}
- Variables sensitive to width in η-direction in the second layer of the EM calorimeter: R_{η} and w_{η_2}
- Variables sensitive to width in η-direction in the first layer of the EM calorimeter: $w_{s\,3}$, F_{side} and $w_{s\,\mathrm{tot}}$

The variables ΔE or E_{ratio} are not considered since the shape differences of the corresponding distribution in data and simulation are small.

As a result, one obtains four differences $\varepsilon_{\mathrm{ID}}(\text{nominal corrections}) - \varepsilon_{\mathrm{ID}}(\text{variation}_i)$ which are added in quadrature. The resulting uncertainty, relative to the nominal efficiencies, is shown in Figure 4.16. For both converted and unconverted photons, this uncertainty is typically of the order 1 % to 3 %, and tends to be largest at low p_{T}.

4.6.6. Size of the Simulation Samples

The precise knowledge of the shower-shape transformations is limited by the finite number of simulated events in the samples of photons and electrons that are used to derive these transformations. The larger the simulated samples are, the smoother are the shower-shape variable distributions and the closer the resulting transformations will be to their "true" shape.

The influence of statistical fluctuations in the shower-shape variable distributions in simulation is assessed by a pseudo-experiment-based method, referred to as the *bootstrap method* [165]: for each shower-shape variable, a set of pseudo-experiments is created, based on the original simulated samples of photons or electrons by multiplying each event weight with an additional weight drawn from a Poisson distribution with mean one. A set of transformations is extracted from each of the resulting pseudo-experiment distributions of shower-shape variables. Each of these sets is then applied to electrons in data, leading to individual photon identification

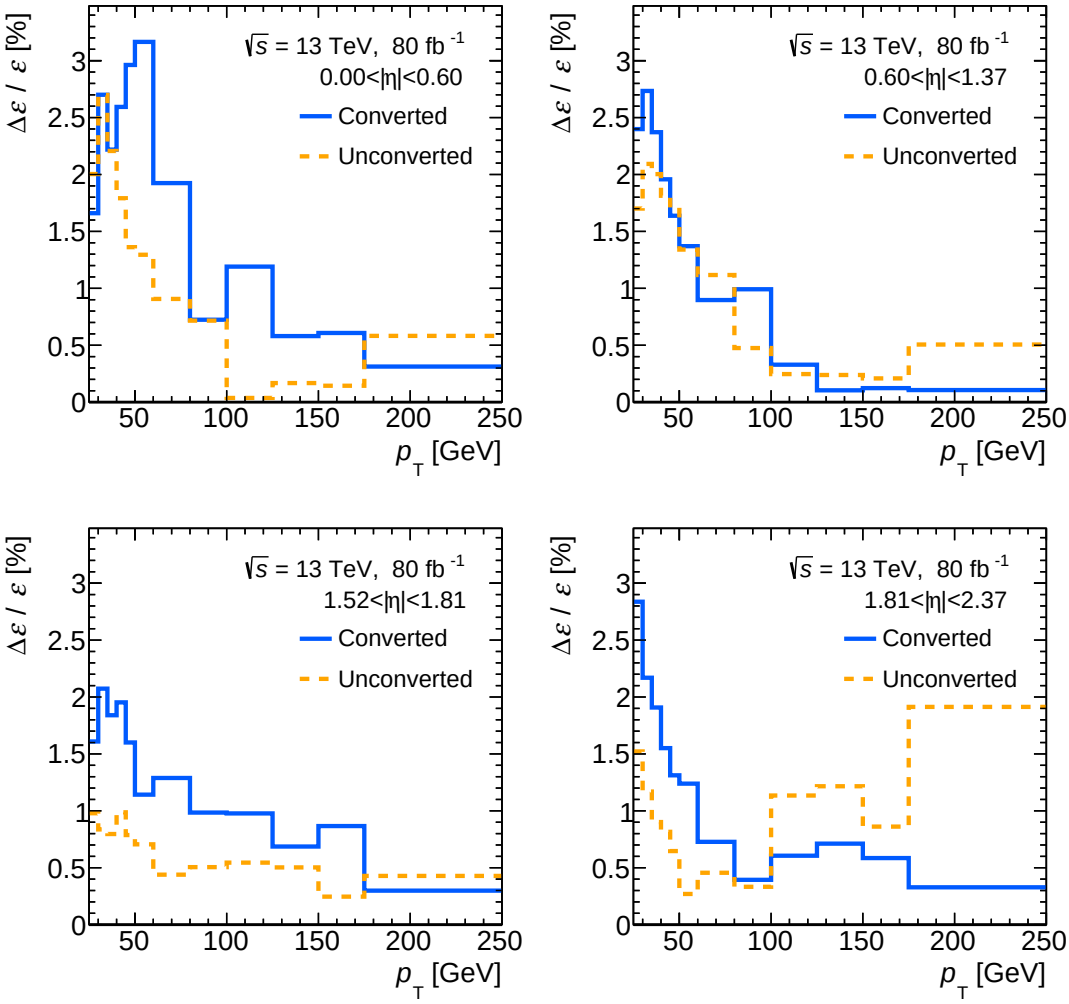

Figure 4.16. | Relative efficiency uncertainty converted and unconverted photons from residual differences in shower-shape variable distributions between MC simulation and data as a function of p_{T}. Each plot represents a different $|\eta|$ region.

efficiencies for each pseudo-experiment. The standard deviation of this distribution of efficiencies, defined as

$$\sigma_{\varepsilon_{\mathrm{ID}}} = \sqrt{\frac{1}{N}\sum_{1}^{N}(\varepsilon_{\mathrm{ID},i} - \varepsilon_{\mathrm{ID,mean}})^2}\,, \tag{4.13}$$

is used as the uncertainty on the photon identification efficiency due to the statistical limitation of the simulated samples. This contribution can be seen in Figure 4.17, for which 150 pseudo-experiments have been used. It is typically less than 0.5 %, and tends to be lowest at intermediate p_{T}. This is related to the fact that most electrons from $Z \to e^+e^-$ decays have a p_{T} of the order $m_Z/2 \approx 45\,\mathrm{GeV}$; additionally, the number of simulated photon events is lower for high-p_{T} samples, as can be seen in Table 4.6.

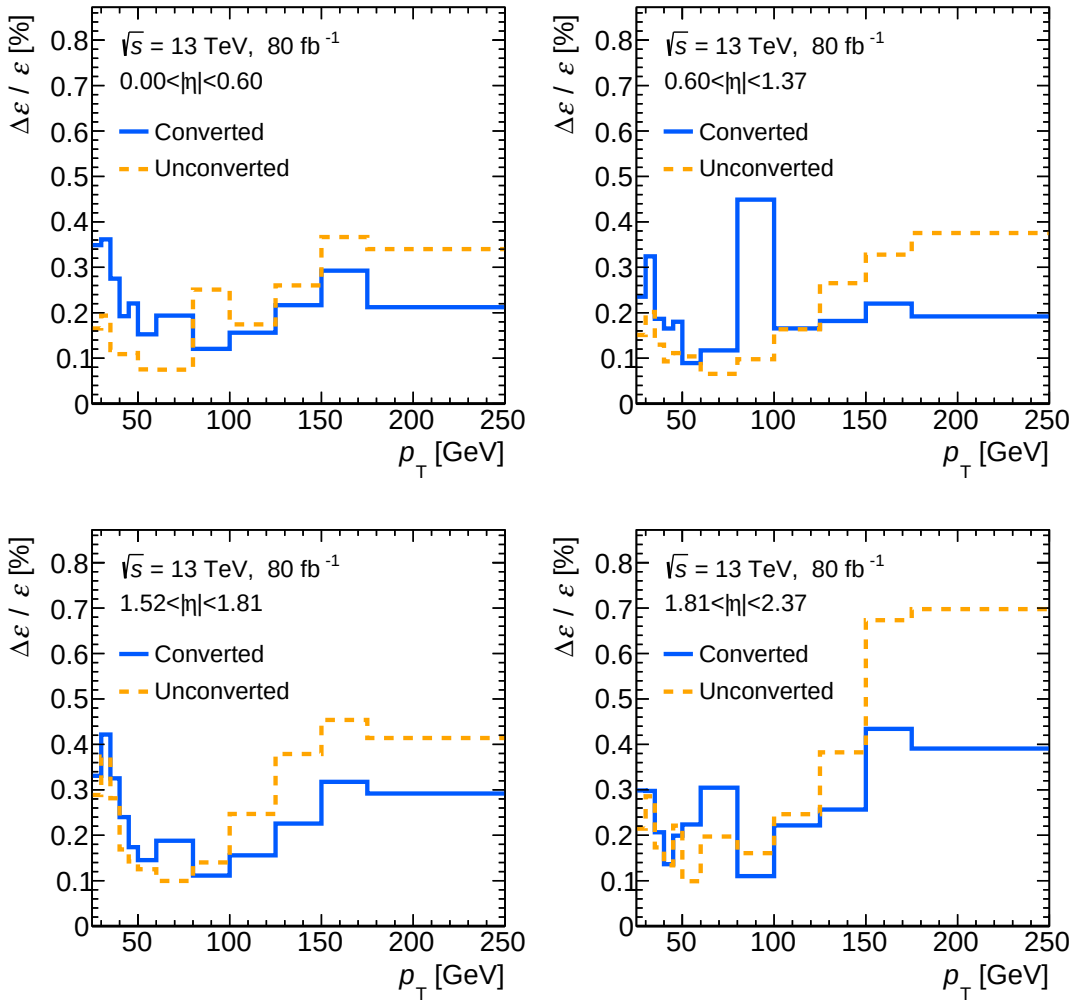

Figure 4.17. | Uncertainty contribution from the limited size of MC simulation samples as a function of p_{T} for converted and unconverted photons, relative to the measured efficiencies. Each plot represents a different $|\eta|$ region.

4.6.7. Statistical Uncertainty

The statistical uncertainty due to a limited data sample is evaluated based on the signal-plus-background fit as follows [166]:

$$\Delta\varepsilon = \frac{1}{N_{\text{den}}} \cdot \sqrt{(1-2\varepsilon)\cdot \Delta N_{\text{num}}^2 + \varepsilon^2 \cdot \Delta N_{\text{den}}^2}, \tag{4.14}$$

where N_{den} and N_{num} denote the extracted number of $Z \to e^+e^-$ signal events for the denominator and numerator probe selection. The identification efficiency is given by $\varepsilon = N_{\text{num}}/N_{\text{den}}$. The uncertainties ΔN_{num} and ΔN_{num} on the extracted number of signal events for the two probe selections is evaluated using the equation

$$\begin{aligned} \Delta N_{\text{num}} &= \sqrt{\left(\Delta f_{\text{num}}^{\text{signal}} \cdot N_{\text{num}}^{\text{total}}\right)^2 + \left(f_{\text{num}}^{\text{signal}} \cdot \sqrt{N_{\text{num}}^{\text{total}}}\right)^2} \\ \Delta N_{\text{den}} &= \sqrt{\left(\Delta f_{\text{den}}^{\text{signal}} \cdot N_{\text{den}}^{\text{total}}\right)^2 + \left(f_{\text{den}}^{\text{signal}} \cdot \sqrt{N_{\text{den}}^{\text{total}}}\right)^2}, \end{aligned} \tag{4.15}$$

where $f_{\text{num}}^{\text{signal}}$ ($f_{\text{den}}^{\text{signal}}$) is the fraction of signal events as extracted in the fit of the mass spectrum resulting from the numerator (denominator) probe selection; $N_{\text{num}}^{\text{total}}$ ($N_{\text{den}}^{\text{total}}$) corresponds to the total number of events in the considered range of the mass spectrum for the numerator (denominator) probe selection.

In Figure 4.18 the statistical uncertainties on the measured photon identification efficiencies are shown for both converted and unconverted photons. This uncertainty generally is very small. It is largest at high p_{T}, as electrons from Z-boson decays tend to have transverse momenta of the order $m_Z/2$.

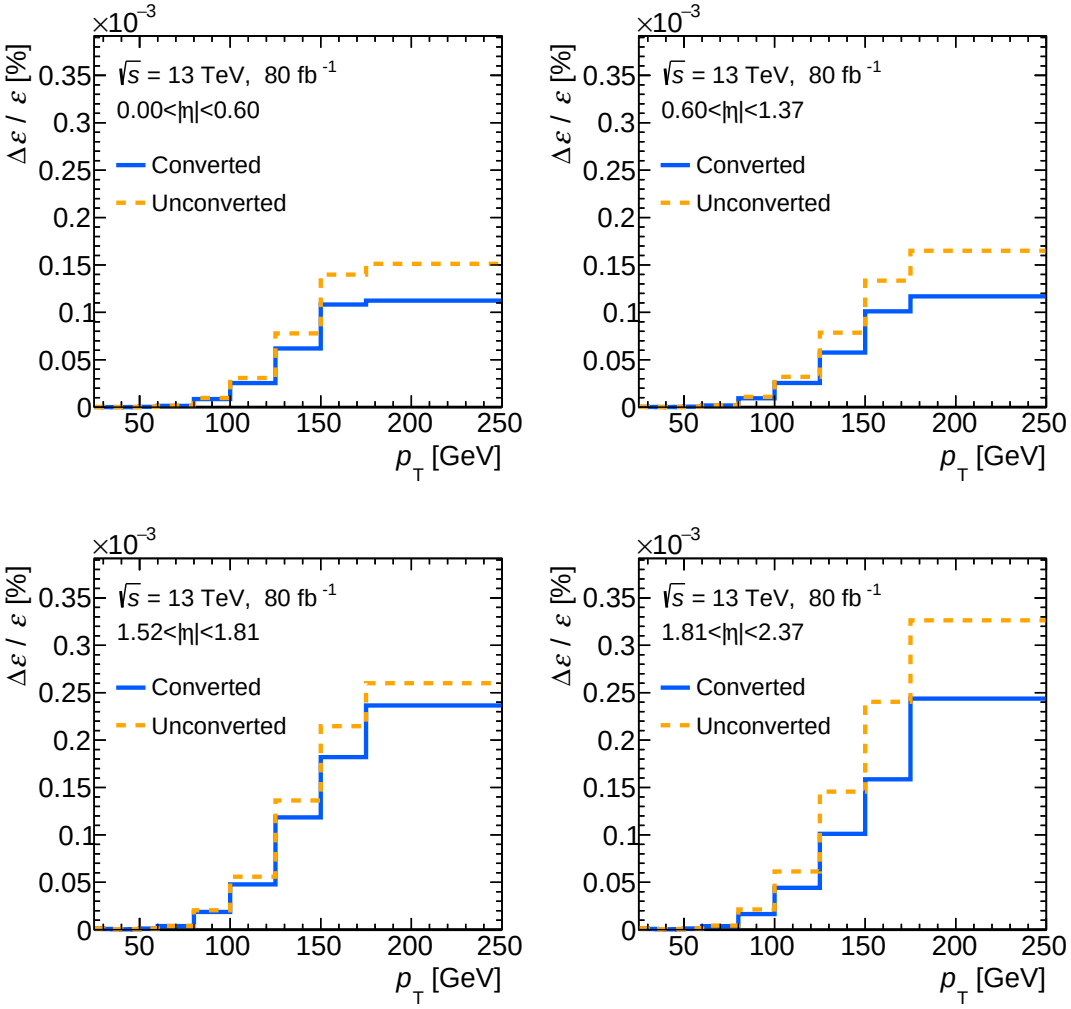

Figure 4.18. | Uncertainty contribution due to a limited number of events in the data sample as a function of p_{T} for converted and unconverted photons, relative to the measured efficiencies. Each plot represents a different $|\eta|$ region.

4.7. Results

The measured photon identification efficiencies and the uncertainties are shown in Figures 4.19 and 4.20 for unconverted and converted photons, respectively. Additionally, the identification efficiencies in MC simulation are shown. The result of the efficiency measurement is also detailed in Tables B.2 and B.1 in Appendix B.

At low photon p_{T} the efficiency is generally lower than at higher p_{T}, reaching a plateau at about 70 GeV and 90 GeV for unconverted and converted photons, respectively. Depending on the region in pseudorapidity, the plateau value for the efficiency lies between 95 % and 100 % for converted photons, and between 90 % and 95 % for unconverted photons. At a p_{T} of roughly 25 GeV, the identification efficiency is about 80 % to 85 % for both converted and unconverted photons. The agreement between data and simulation after applying corrections to shower-shape variables is good, resulting in scale factors $\varepsilon_{\mathrm{ID,data}}/\varepsilon_{\mathrm{ID,MC}}$ close to 1. The scale factors and their uncertainty are shown in Figures 4.21 and 4.22 as a function of p_{T} and in the four distinct regions of pseudorapidity for unconverted and converted photons, respectively.

A summary of the relative uncertainties that have been evaluated for the measurement of the photon identification efficiencies using the electron-extrapolation method is shown in Figures 4.23 and 4.24 for unconverted and converted photons, respectively. Typical ranges of values for the various uncertainty contributions are given in Table 4.8. In general, combined uncertainties for both unconverted and converted photons typically are in the range 1 % to 3 %. The uncertainty for unconverted photons tends to be largest at high p_{T}, while for converted photons uncertainties are largest in the low-p_{T} region. Uncertainties due to shower mismodeling and the uncertainty due to non-closure are the dominant contributions for both converted and unconverted photons. For unconverted photons, non-closure uncertainties are particularly important in the region of high p_{T} and $|\eta| < 1.37$; for converted photons, on the other hand, the shower-modeling uncertainty is clearly dominant at low p_{T} for all $|\eta|$ regions. In the high-p_{T} region, the uncertainty due to possible mismodeling of the fragmentation-fraction photons can be relevant for converted photons. The background-subtraction uncertainty is relatively small in most kinematic regions, except in the low-p_{T} region within $1.52 < |\eta| < 1.81$, where it is one of the dominant uncertainty contributions. In the more forward region $|\eta| > 1.52$ and at high p_{T}, the uncertainty due to a limited amount of simulated photon- and electron events can be relevant. The conversion-

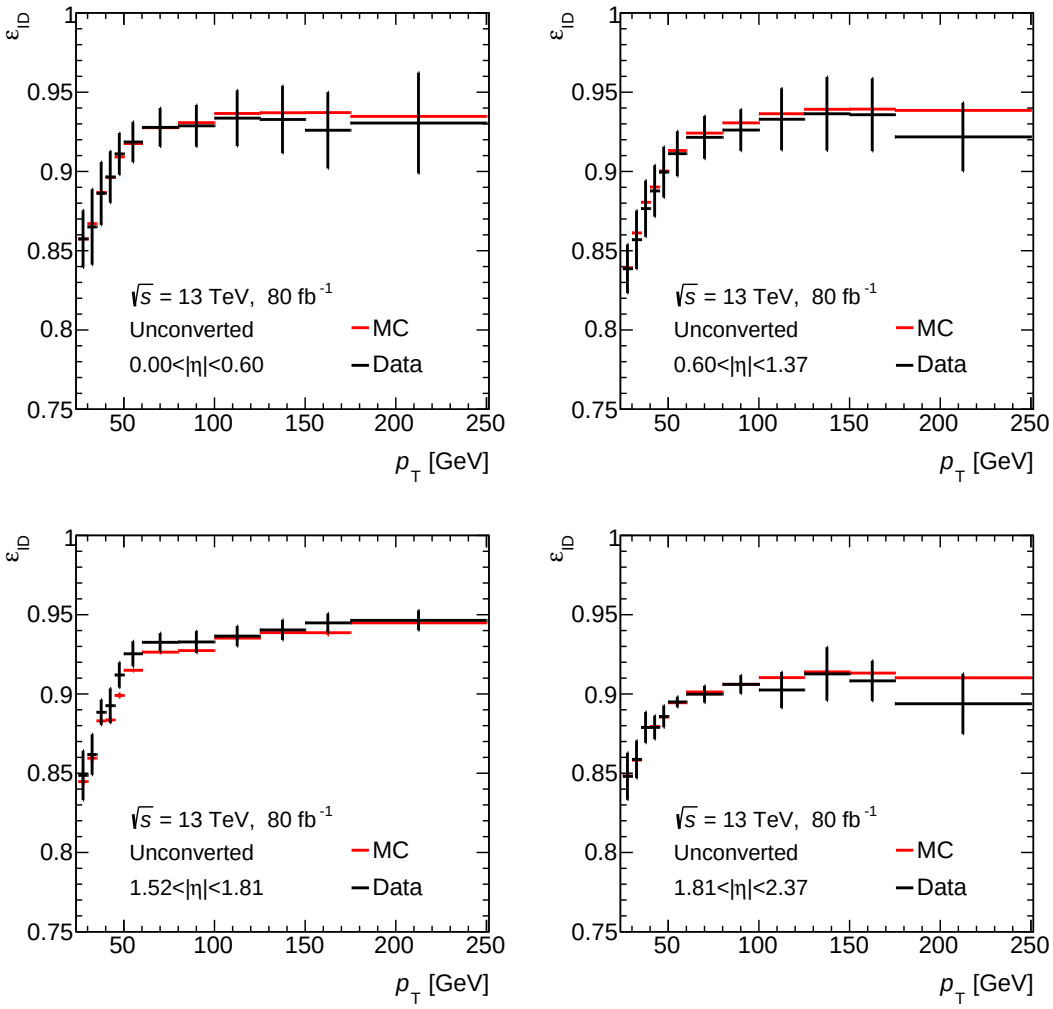

Figure 4.19. | Comparison of photon identification efficiencies for unconverted photons in simulation and data, including uncertainties. Each plot represents a different $|\eta|$ region.

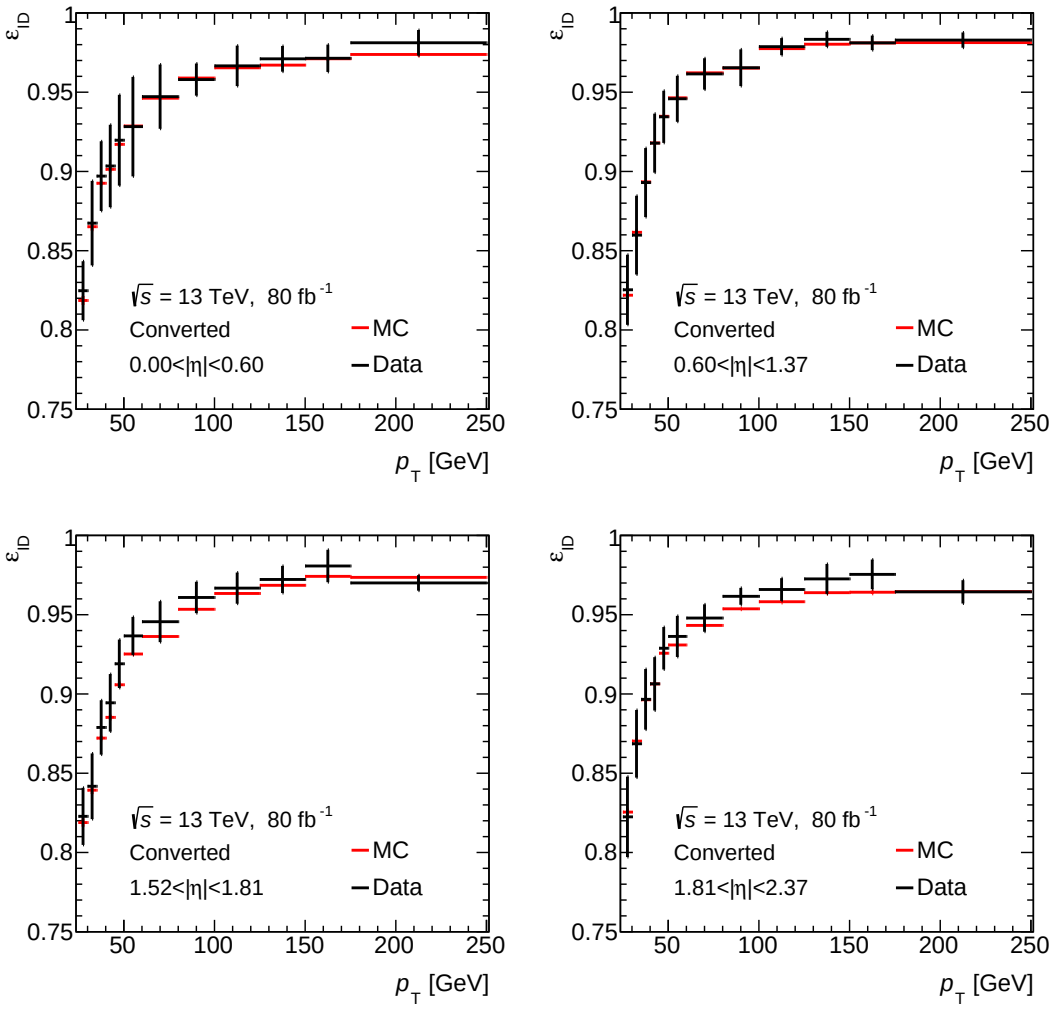

Figure 4.20. | Comparison of photon identification efficiencies for converted photons in simulation and data, including uncertainties. Each plot represents a different $|\eta|$ region.

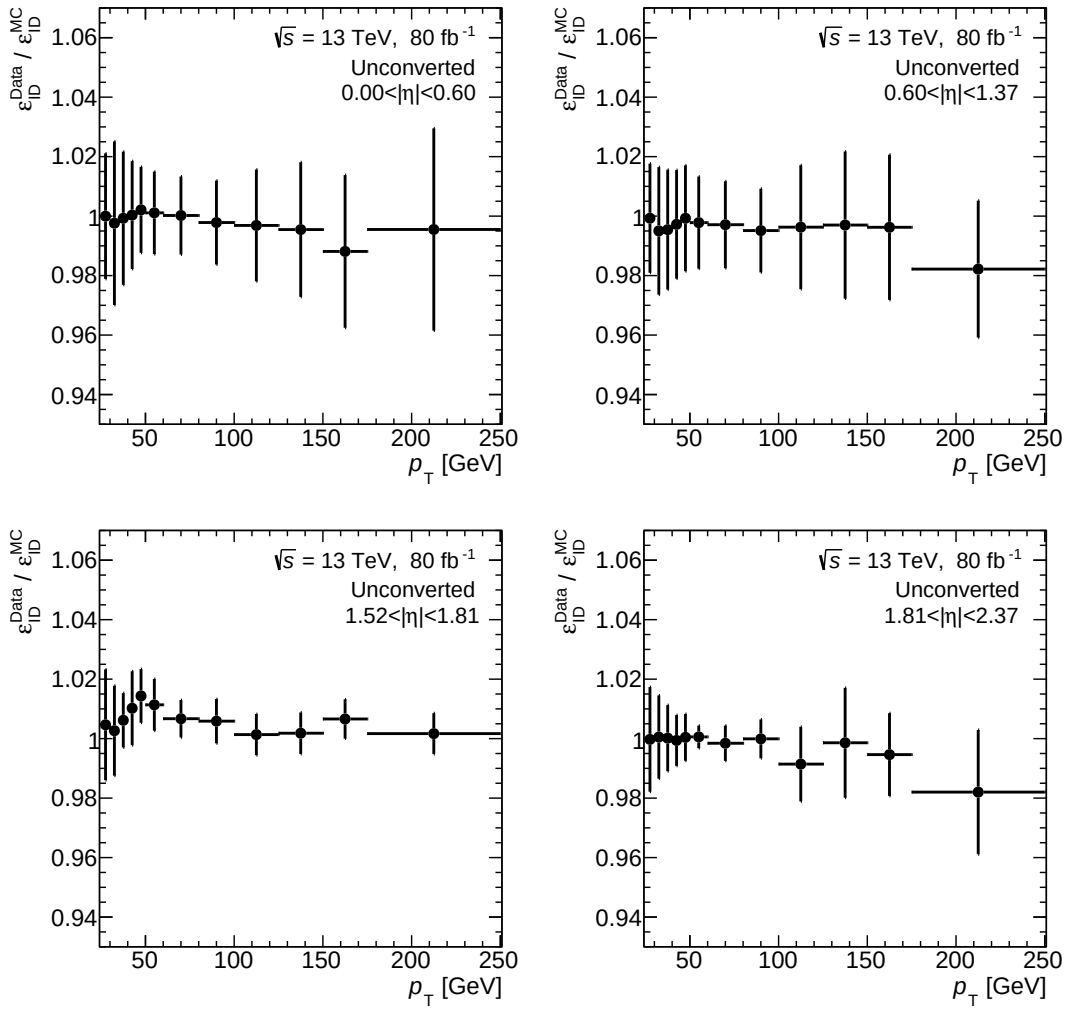

Figure 4.21. | Scale factors $\varepsilon_{\mathrm{ID,data}}/\varepsilon_{\mathrm{ID,MC}}$ with uncertainties for unconverted photons as a function of p_{T}. Each plot represents a different $|\eta|$ region.

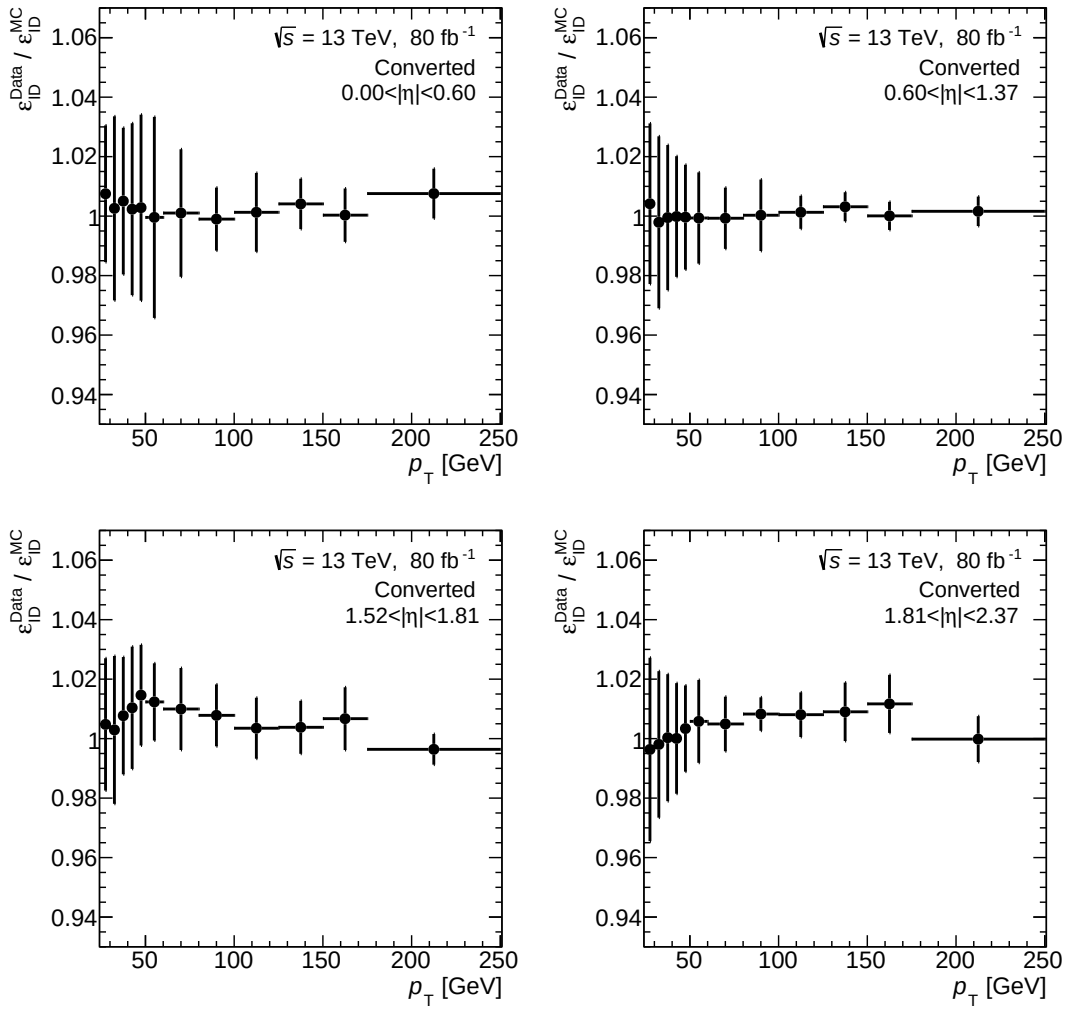

Figure 4.22. | Scale factors $\varepsilon_{\mathrm{ID,data}}/\varepsilon_{\mathrm{ID,MC}}$ with uncertainties for converted photons as a function of p_{T}. Each plot represents a different $|\eta|$ region.

reconstructed-related uncertainty and the statistical uncertainty are generally small.

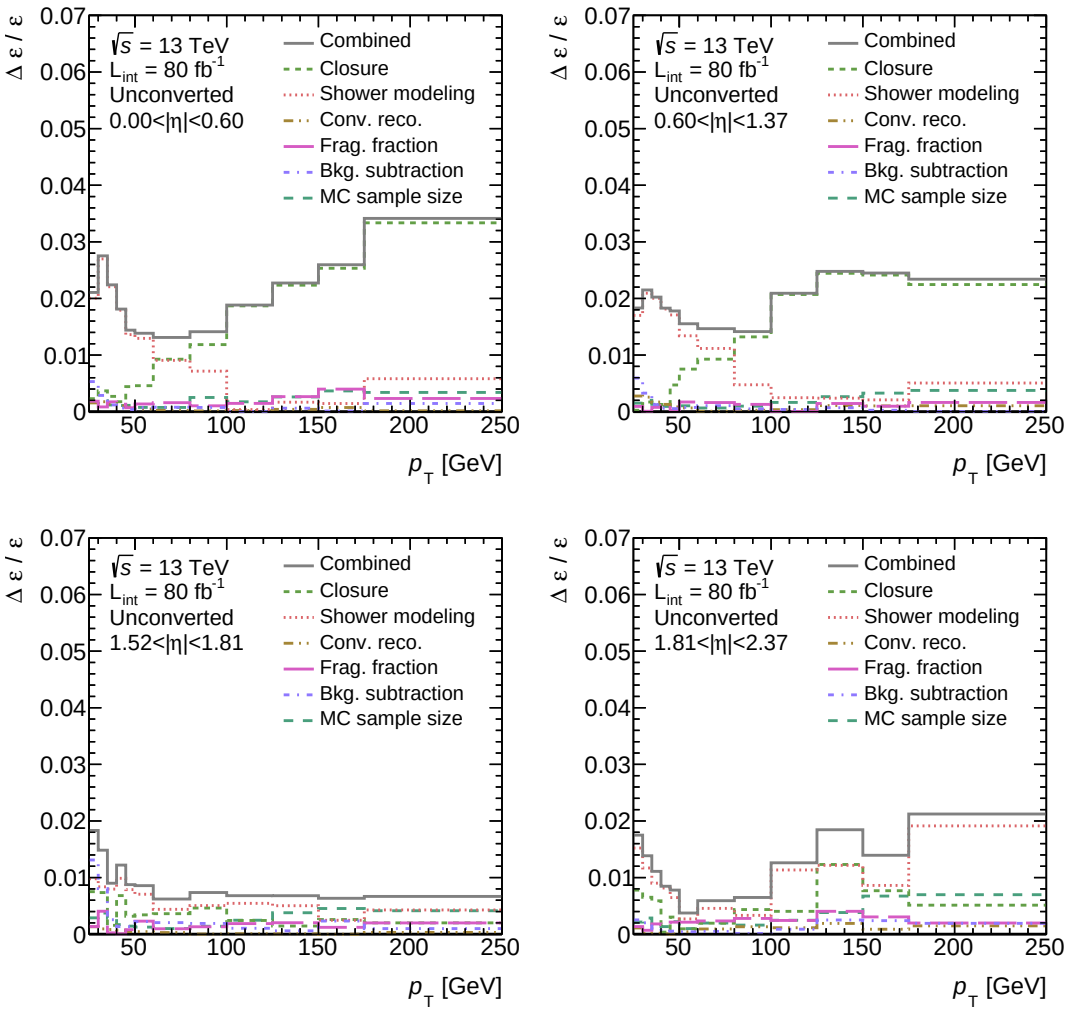

Figure 4.23. | Comparison of contributions to the relative uncertainties for unconverted photons. Shown are the various uncertainty contributions and total uncertainty on the photon-identification efficiency scale factor for unconverted photons as a function of p_{T}. Each plot represents a different $|\eta|$ region.

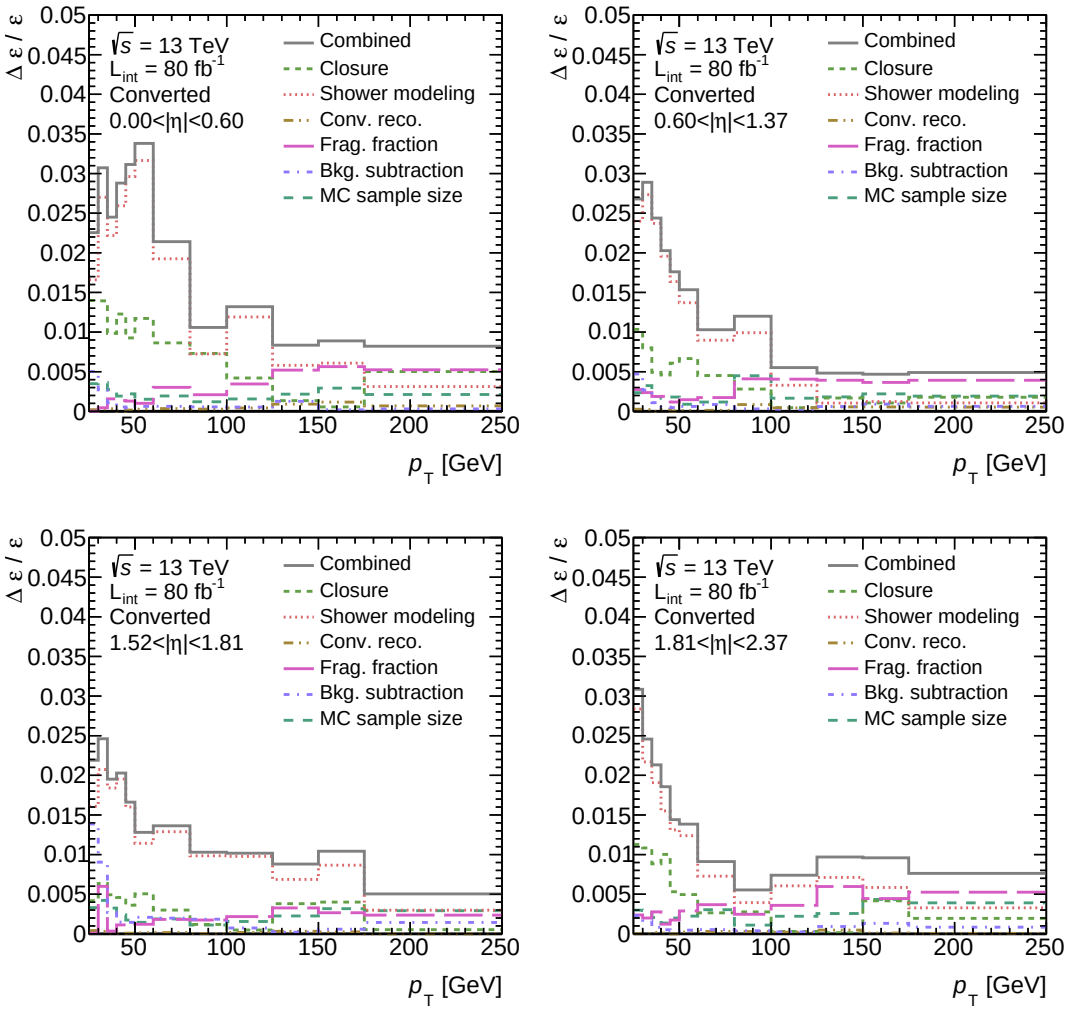

Figure 4.24. | Comparison of contributions to the relative uncertainties for converted photons. Shown are the various uncertainty contributions and total uncertainty on the photon-identification efficiency scale factor for unconverted photons as a function of p_{T}. Each plot represents a different $|\eta|$ region.

Type of uncertainty	Converted photons	Unconverted photons
Closure	1.4 %	3.4 %
Background	1.4 %	1.3 %
Conversion reconstruction	0.1 %	0.3 %
Fragmentation-photon fraction	0.6 %	0.4 %
Shower-shape mismodeling	3.2 %	2.7 %
MC sample size	0.5 %	0.7 %
Statistical	< 0.1 %	< 0.1 %

Table 4.8. | Summary of maximal values for all considered uncertainties, relative to the measured efficiencies.

4.8. Combination of Scale Factors

The results from the three methods of measuring the photon identification efficiency, as described in Sections 4.3 and 4.2, can be combined in order to obtain a set of scale factors for a wider range of transverse momentum and higher accuracy than a single method could provide. The three methods use events with different event topologies with possibly different photon identification efficiencies. A combination of these efficiencies and a subsequent computation of a combined set of scale factors would therefore be problematic. A combination of scale factors from the individual methods alleviates this problem, because the dependency on the event topology can be assumed to be present in both data and simulation. As a consequence, the computation of scale factors for each measurement method by the division of $\varepsilon_{\mathrm{ID,data}}$ and $\varepsilon_{\mathrm{ID,MC}}$ reduces the impact of different event topologies on the result. The combination of scale factors from different measurement methods is described in Reference [147] and is based on the *BLUE* method [167, 168]; the coefficients of the linear combination depend on the respective statistical and systematic uncertainty. Both statistical and systematic uncertainties are treated as uncorrelated.

The efficiencies from the three different measurement methods, and the corresponding scale factors are shown in Figures 4.25 and 4.26 for unconverted photons and converted photons, respectively. Additionally, the scale factors based on a combination of the three individual scale factor measurements are shown.

The results of the electron-extrapolation method as shown in Figures 4.25 and 4.26 reflect an earlier analysis of the data. In that earlier analysis, the identification efficiencies for simulated unconverted photons were by mistake based on a pileup profile exclusively taken into account 2017 LHC running conditions, in which larger levels of pileup were present than in 2015 and 2016. However, this effective mismodeling of pileup affects both the numerator and the denominator of the scale factor determination. The numerator is proportional to the non-closure correction of the measured efficiency, which in turn is proportional to the photon identification efficiency in simulation after a pre-selection based on f_1, the fraction of EM cluster energy in the first EM-calorimeter layer. The denominator, on the other hand, corresponds to the nominal photon identification efficiency in simulation. Therefore, the effect of this partial mismodeling of the pileup distribution on the scale factor for unconverted photons is reduced considerably by a cancellation of corresponding biases in efficiencies in simulation. As a result, the scale

factors as shown in Section 4.7 are similar to those used in the combination of scale factors; the differences between them range from $1 \cdot 10^{-5}$ to 0.004. Since the non-closure of the method, which relies on the photon identification efficiency in simulation, is also taken into account as an uncertainty, the overall uncertainty in the earlier measurement was biased as well. Concretely, non-closure-related uncertainties were overestimated at low-p_{T} by up to 1.5 %; in few bins, an under-estimation of up to 0.5 % occurred. In the measurement described in this chapter, these biases were corrected. The present measurement includes another, unrelated change: in the earlier measurement, the uncertainties due to potential mismodeling of the fragmentation-photon fraction and of conversion reconstruction have been computed by taking the full difference between the efficiency resulting from the up- and down-variation of corresponding event weights. In the uncertainty estimated shown in Sections 4.6.3 and 4.6.4, this difference has been divided by a factor of 2, in order to avoid a double-counting of uncertainties.

The qualitative message, however, of the combination is not changed by these differences: the results from all three methods agree well within the overlapping ranges in p_{T}, and the uncertainty on the scale factor can be reduced substantially by taking into account the information from each of the three methods.

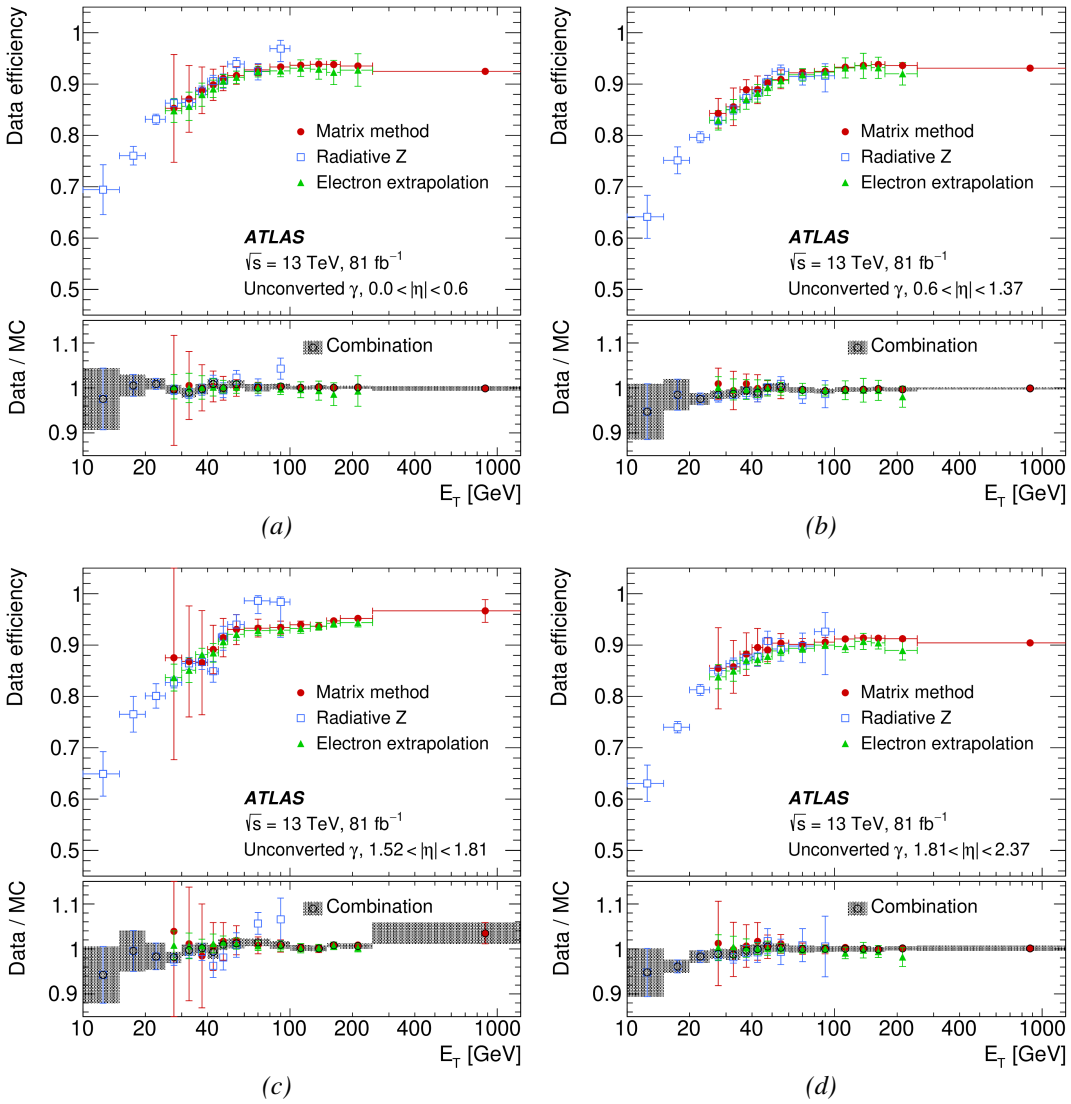

Figure 4.25. | Photon identification efficiencies for unconverted photons as measured by the three different methods in the upper panel and the combination of the corresponding scale factors in the lower panel. The gray band corresponds to the total uncertainty on the combined scale factors. The efficiencies and scale factors are measured in four different regions of $|\eta|$ and as a function of photon E_{T}. Taken from Reference [147].

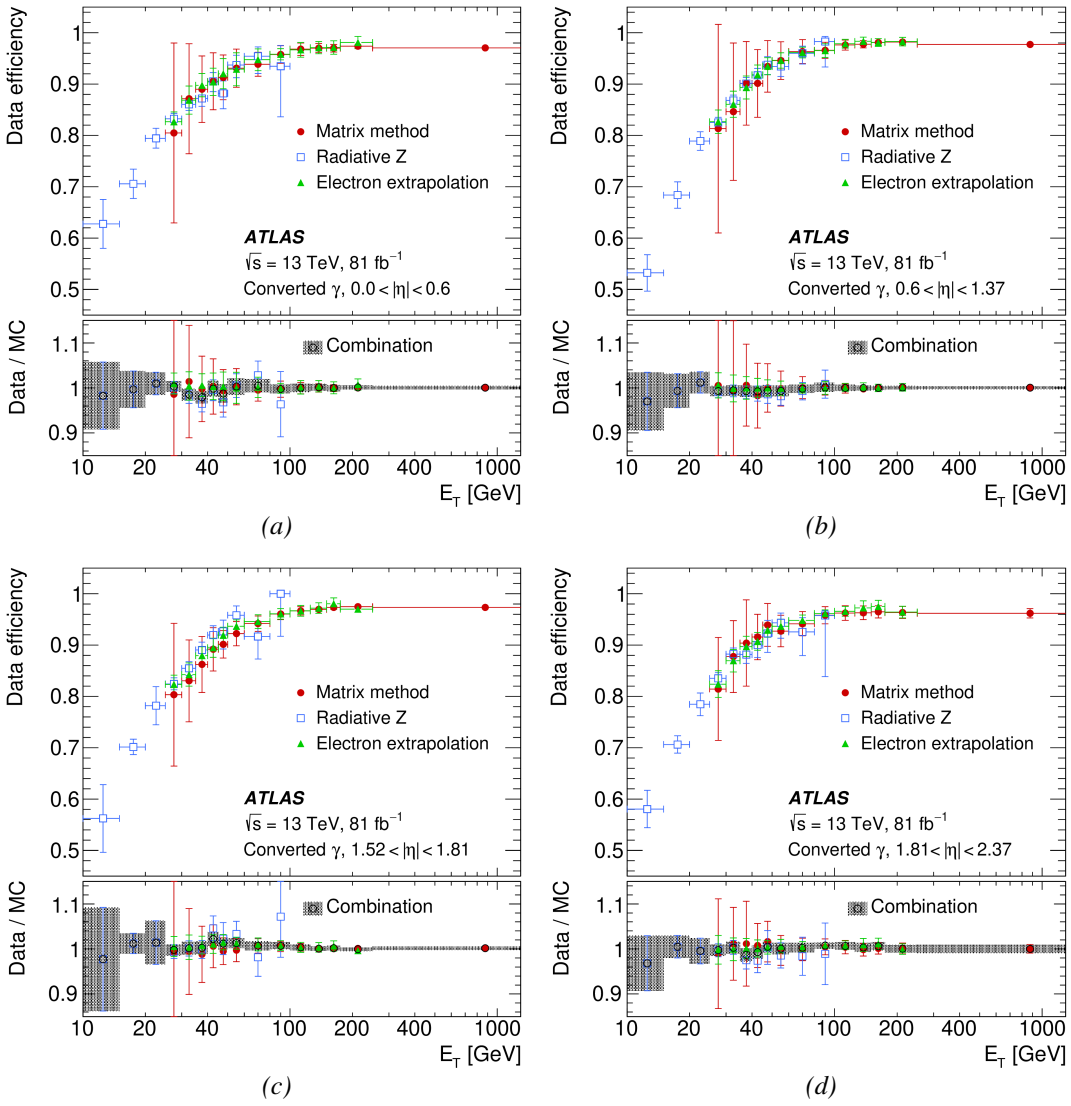

Figure 4.26. | Photon identification efficiencies for converted photons as measured by the three different methods in the upper panel and the combination of the corresponding scale factors in the lower panel. The efficiencies and scale factors are measured in four different regions of $|\eta|$ and as a function of photon E_{T}. Taken from Reference [147].

4.9. Summary

A good understanding of photons and their identification in the ATLAS experiment is crucial for photon-based physics analyses. Photon identification relies on simple cuts on shower-shape variables, which parametrize the shape of energy clusters in the calorimeter. The measurement of photon identification efficiencies is possible with currently three methods. One of these methods, the electron-extrapolation method, has been applied within the scope of this thesis. In addition to its application, efforts have been made to make the method more robust by improving the uncertainty estimation and by correcting for effects of a non-closure of the method on measured efficiencies.

The electron-extrapolation method is based on the transformation of a pure and unbiased electron sample from a tag-and-probe method into a sample of pseudo-photons, which have shower-shape variable distributions very similar to those of photons, and therefore can be used to measure the photon identification efficiency. This is done by means of fits to invariant-mass distributions for pairs of electrons, of which one (the probe) has been transformed to a pseudo-photon. The efficiency is measured in several bins of transverse momentum and pseudorapidity, and for converted and unconverted photons separately.

Above transverse momenta larger than approximately 50 GeV, the photon identification efficiencies have values between 90 % and 100 %, while at lower transverse momentum of about 25 GeV they typically are in the range of 80 % to 90 %. The statistical uncertainty on the measured efficiencies is negligible. There are several systematic uncertainty contributions that result in a combined uncertainty on the measured efficiency that lies typically within 1 % to 3 %.

The measured identification efficiencies are used in combination with identification efficiencies from Monte-Carlo simulation to determine efficiency scale factors. The resulting set of scale factors can be combined with scale factors from the other two methods of measuring the photon identification efficiency. These combined scale factors can be applied to simulated events containing photons in order to correct simulated events for differences in photon identification efficiency between data and simulation. In this way, the combined scale factors and their uncertainties find application in photon-based ATLAS physics analyses.

5. Measurement of Fiducial Inclusive and Differential Cross Sections for Higgs Boson Production in the Diphoton Decay Channel

5.1. Introduction

Given the mass of the Higgs boson, which has been measured by the CMS and ATLAS experiments to be (125.09 ± 0.24) GeV [7], the SM can be used to predict the inclusive Higgs boson production cross section. Furthermore, predictions are available for differential cross sections in various observables related to the kinematics of the Higgs events. The comparison of measured Higgs boson production cross sections with SM predictions is an important test of the SM. The diphoton decay channel $H \to \gamma\gamma$ is well suited to measure the Higgs boson production cross section, as the good mass resolution enables a robust subtraction of the background, which consists of non-resonant events with a diphoton, photon-jet or jet-jet final state. The diphoton event selection includes criteria such as photon identification, photon isolation and criteria based on the photon kinematics. Therefore, the measured cross section can not directly be compared to predictions in the full phase space. In order to allow such a comparison, the predictions to which the measured cross sections are compared can be provided in a *fiducial* region of phase space that is similar to the ATLAS detector acceptance and the event selection criteria, minimizing the model dependence: if the cross section as measured in the limited detector acceptance would have to be extrapolated to the full phase space in order to perform a comparison, the result would

rely to a large degree on the prediction used for the extrapolation. At the level of measured cross sections, inefficiencies and migrations between different considered regions of phase space, i.e. bins, due to a limited detector resolution need to be corrected for in order to enable a comparison with predictions. This process is called *unfolding*. The measured and corrected fiducial Higgs boson production cross sections in the $H \to \gamma\gamma$ decay channel, both inclusive and differential, are compared to predicted values for $\sigma_H^{\mathrm{SM}} \cdot \mathcal{B}_{\mathrm{SM}}(H \to \gamma\gamma)$ and $(\Delta\sigma_H^{\mathrm{SM}}/\Delta x) \cdot \mathcal{B}_{\mathrm{SM}}(H \to \gamma\gamma)$, respectively, where x represents the variable in which the differential cross section in measured and $\mathcal{B}_{\mathrm{SM}}(H \to \gamma\gamma)$ denotes the $H \to \gamma\gamma$ branching ratio of 0.0023 as predicted by the SM.

The differential cross sections contain information about the Higgs boson that is not available in the inclusive cross section. In this measurement, differential cross sections in four variables are measured, each of which is sensitive to a different set of aspects of the underlying theory:

- The *transverse momentum of the Higgs boson*, p_{T}^{H} (also denoted by $p_{\mathrm{T}}^{\gamma\gamma}$ in this context), distribution is sensitive to the QCD aspects of the Higgs boson production. Moreover, the Higgs boson coupling to quarks has an impact of the p_{T}^{H} distribution. It is also sensitive to the treatment of the t-quark mass in the calculation. See Figure 5.1 for an illustration of the corresponding impacts on the p_{T}^{H} spectrum: at low p_{T}^{H}, the spectrum is sensitive to the Yukawa coupling of quarks such as the c- or b-quarks to the Higgs boson. The high-p_{T}^{H} tail, on the other hand, is sensitive to t-quark-related effects and potential heavy non-SM particles in the gluon fusion loop. The comparison of predicted and measured differential cross sections in p_{T}^{H} can be used to set limits on the Yukawa couplings between quarks such as the b- or c-quark and the Higgs boson, as described in Chapter 6.
- The *transverse momentum of the leading jet*, $p_{\mathrm{T}}^{j_1}$, is correlated with p_{T}^{H} due to momentum conservation. Thus, the corresponding distribution is sensitive to the same features as the p_{T}^{H} distribution. Additionally, the $p_{\mathrm{T}}^{j_1}$ distribution depends on the relative contributions from the different Higgs boson production mechanisms. The p_{T} of jets from vector-boson-fusion Higgs boson production, for example, tend to be larger than the p_{T} of jets from gluon fusion Higgs boson production.
- The *rapidity of the Higgs boson*, y_H (also denoted by $y_{\gamma\gamma}$ in this context), distribution is sensitive to the proton PDFs.
- The measurement of the distribution of the *number of b-jets*, $N_{b-\mathrm{jets}}$, can be used to obtain an estimate for the corresponding background contribution for measurements involving

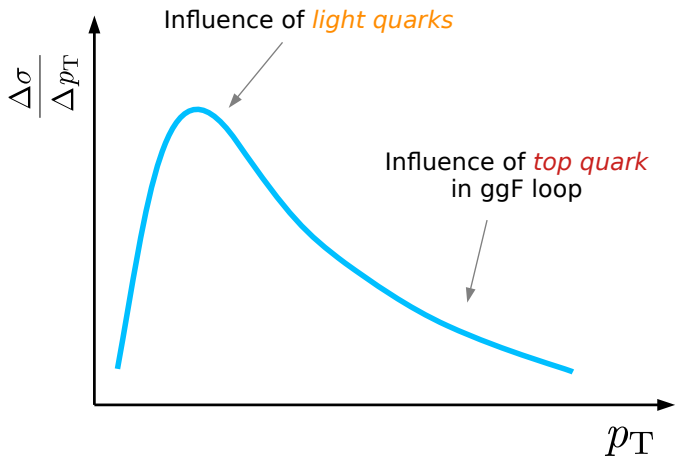

Figure 5.1. | Illustration of the differential cross section in Higgs boson transverse momentum and its sensitivity to Higgs boson couplings to particles of different masses.

$pp \to t\bar{t}H$ and $pp \to H(\to \gamma\gamma)H(\to b\bar{b})$ processes.

5.2. Dataset and MC Simulations

5.2.1. Data

The dataset used for the measurement of Higgs boson production cross sections as described in this thesis contains the data from the 2015 – 2017 data-taking periods, corresponding to 79.8/fb of integrated luminosity at a center-of-mass energy of $\sqrt{s} = 13\,\mathrm{TeV}$. Details on the diphoton trigger that is used to collect $H \to \gamma\gamma$ events are given in Section 5.3.1

5.2.2. MC Simulation

MC simulations are used for several purposes in particle physics, among them the prediction of cross sections, the modeling of parton showers, and the modeling of the detector response to energetic particles. As a consequence, they can also be used to model the shape of the invariant-mass distribution of $H \to \gamma\gamma$ and QCD background events with two photon candidates in the final state, which is crucial for the signal-plus-background fit of the invariant-mass spectrum of diphoton candidates. In the case of background events, the detector response is parametrized, the

parametrization being derived from detailed simulations of the interactions of energetic particles with the ATLAS detector [169]. Simulations can also be used to provide predictions for cross sections to which the measured spectrum can be compared. At the same time, the comparison of simulated $H \to \gamma\gamma$ events before and after their reconstruction in the detector and selection allows to correct the measured inclusive and differential cross sections for detector effects and thus to obtain particle-level cross sections.

The effect of pileup on the hard-interaction signature in the detector is modeled by adding a number of *minimum-bias* interactions, generated by Pythia8 with the *A3* parameter set [170], to the hard-interaction event. The number of pileup interactions is drawn event-by-event from a Poisson distribution with mean $\mu - 1$, where μ is the expected number of proton-proton interactions per bunch crossing. Eq. 3.10 in Section 3.5 can be used to compute μ:

$$\mu = L_{\mathrm{b}} \cdot \sigma_{\mathrm{inel}} / f_{\mathrm{r}} \,. \tag{5.1}$$

Here, σ_{inel} denotes the inelastic proton-proton scattering cross section, f_{r} the rotation frequency of the proton bunches, and L_{b} the per-bunch luminosity. The LHC running conditions, including the amount of pileup, are not uniform over time. Therefore, a range of different pileup conditions need to be considered for the event simulation. This is done by generating events for a sufficiently wide range of mean values $\mu - 1$ for the Poisson distribution from which the number of interaction is drawn on an event-by-event basis. The knowledge of the luminosity conditions of the considered dataset allows a reweighting of the simulated events such that the resulting pileup distribution resembles the distribution in data.

Process	Generator	Showering	$\sigma[pb]$	Order of σ calculation	Order on generator level
ggF	Powheg NNLOPS	Pythia8	48.52	N^3LO(QCD)+NLO(EW)	NNLL + effect. NNLO
VBF	Powheg-Box	Pythia8	3.78	approx. NNLO(QCD)+NLO(EW)	NLO
WH	Powheg-Box	Pythia8	1.37	NNLO(QCD)+NLO(EW)	NLO
$q\bar{q} \to ZH$	Powheg-Box	Pythia8	0.76	NNLO(QCD)+NLO(EW)	NLO
$gg \to ZH$	Powheg-Box	Pythia8	0.12	NLO(QCD)	LO
$t\bar{t}H$	Powheg-Box	Pythia8	0.51	NLO(QCD) + NLO(EW)	NLO
$b\bar{b}H$	Powheg-Box	Pythia8	0.49	5FS: NNLO(QCD)+NLO(EW), 4FS: NLO(QCD), NLO(EW)	4FS: NLO(QCD)
tHq	MadGraph5_aMC@NLO	Pythia8	0.07	5FS: NLO	LO
tHW	MadGraph5_aMC@NLO	Herwig++	0.02	5FS: NLO	LO

Table 5.1. | MC simulations that are used for the various considered Higgs production modes. Based on material in Reference [171]. See Section 2.4.3 for references on cross section computations for the individual production modes.

Generally, Higgs boson events are produced by MC simulations for each Higgs boson production mode separately. See Section 2.4.3 for an overview of the various Higgs boson production modes. Gluon fusion events are simulated using Powheg NNLOPS; see Section 2.6.4 for more details. The VBF, VH, $t\bar{t}H$ and $b\bar{b}H$ Higgs boson production modes are simulated using Powheg-Box [112, 172–174]. At generator level, the predictions for VBF [175], WH, $q\bar{q} \to ZH$ [176], $t\bar{t}H$ [177], $b\bar{b}H$ [112] are accurate to NNLO in QCD and include electroweak corrections to NLO. The $gg \to ZH$ is generated at LO in QCD [178]. In the case of associated single-t-quark and Higgs boson production, events are generated with LO precision in QCD using MadGraph5_aMC@NLO [113]. In Table 5.1, an overview of the MC simulation of each considered production mode is given.

Except for the simulation of the tHW production mode, for which Herwig++ [179, 180] is used, all simulations employ Pythia8 [77] as parton shower simulation; see Section 2.6.3. Pythia8 is run in most cases with the AZNLO parameter set [181], except for tHW, in which the A14 parameter set has been used [182]. For all processes except tHq and tHW, in which the CT10 PDF set was used [183], the simulated samples are reweighted such that the results correspond to the PDF4LHC15 PDF set [184].

The inclusive gluon fusion cross section to which the simulated sample is normalized is computed at N^{3}LO accuracy in QCD, with NLO electroweak corrections included; see Section 2.6.4. For these production modes, the inclusive cross sections are accurate to NNLO in QCD and include NLO electroweak corrections, except for $gg \to ZH$, whose cross section includes only QCD corrections up to NLO.

The sample of non-Higgs diphoton events has been generated with Sherpa 2.2.4 [185, 186] and the CT10 PDF set. The parton shower simulation is also implemented in Sherpa 2.2.4 [187].

In order to be able to directly compare simulated events with data events, it is necessary to model the detector response to the particles in simulation. For the $H \to \gamma\gamma$ samples, this is done using GEANT4 [188–190]; for QCD diphoton background events a parametrization of the ATLAS response has been used in order to reduce the computational effort [169].

5.3. Event Selection

Events in which a Higgs boson decays to a pair of photons are marked by the presence of two photons with an invariant mass close to the Higgs boson mass m_H and with transverse momenta of the order $m_H/2$. Correspondingly, the presence of at least two photons or photon candidates is a central selection criterion for the $H \to \gamma\gamma$ event selection at particle and reconstruction level, respectively. If more than two photon candidates are present, the two candidates with the largest p_{T}^{γ} are considered. The selection criteria at particle level, i.e. the fiducial phase-space definition, are designed to be similar to those at reconstruction level in order to reduce model dependence.

5.3.1. Reconstruction Level

The event selection at reconstruction level is applied to data and simulated events likewise. The baseline selection is constituted by a trigger selection, selections based on the kinematics of the photon candidates, as well as on identification and isolation requirements on the photon candidates. In addition, a selection based on the invariant mass of the system of the two photon candidates, $m_{\gamma\gamma}$, is performed.

Trigger Requirements

For an event to be recorded, it must pass a trigger selection. For this analysis, a diphoton trigger is used, with p_{T}^{γ} thresholds for the (sub-)leading photon candidate of 35 GeV (25 GeV). In addition to kinematic selection criteria, the trigger requirements involve identification algorithms: in the data-taking periods of 2015 and 2016, a loose identification selection was applied to the photon candidates, which takes into account the fraction of cluster energy deposited in the hadronic calorimeter and shower shape variables defined in the second, relatively coarse layer of the EM calorimeter. In 2017, the identification selection of the trigger algorithm has been tightened in order cope with an increase of the trigger rate due to the increased instantaneous luminosity. This tighter identification procedure takes into account also information from the finely-segmented first layer of the EM calorimeter. The diphoton trigger efficiency for $H \to \gamma\gamma$ events is close to

100 %. It can be determined using following equation:

$$\varepsilon_{\gamma\gamma}^{\text{trig}} = \iint \mathrm{d}p_{\mathrm{T}}^{\text{lead}} \mathrm{d}p_{\mathrm{T}}^{\text{sublead}} \varepsilon_{\gamma,35}^{\text{trig}}(p_{\mathrm{T}}^{\text{lead}}) \cdot \varepsilon_{\gamma,25}^{\text{trig}}(p_{\mathrm{T}}^{\text{sublead}}) \cdot f(p_{\mathrm{T}}^{\text{lead}}, p_{\mathrm{T}}^{\text{sublead}}). \tag{5.2}$$

Here, $f(p_{\mathrm{T}}^{\text{lead}}, p_{\mathrm{T}}^{\text{sublead}})$ denotes the two-dimensional p.d.f. of the p_{T} for the leading and subleading photon candidates. The trigger efficiency of the single-photon *trigger leg* of the diphoton trigger with a p_{T} threshold of 35 GeV (25 GeV) is denoted by $\varepsilon_{\gamma,35(25)}^{\text{trig}}$. These single-photon trigger efficiencies, defined relative to isolated photon candidates which pass offline identification requirements, were measured using $Z \to \ell^+\ell^-\gamma$ events [191], similar to the method outlined in Section 4.3.1. The systematic efficiency uncertainty is given by the difference between the measured trigger efficiency and the trigger efficiency as estimated in simulation, and is propagated to the diphoton efficiency determination following Eq. (5.2). The relative systematic diphoton trigger efficiency uncertainty amounts to 0.7 %.

Object-Level Selection

Both photons are required to have a p_{T}^{γ} of larger than 25 GeV. The p_{T}^{γ} of the leading (subleading) photon candidate must also be larger than 35 % (25 %) of $m_{\gamma\gamma}$. Photon candidates are disregarded if they are located within the barrel-endcap transition region, $1.37 < |\eta| < 1.52$. In order to ensure that the two considered photon candidates correspond to the objects that fired the diphoton trigger, a matching based on the angular distance between photon candidates and trigger-firing objects is performed. The photon candidates must pass the *tight* identification selection, consisting of selection criteria regarding variables that parametrize the shape of the shower in the calorimeter; see Chapter 4 for details on the identification procedure. In addition, requirements on the isolation of the photon candidates are imposed; see Section 3.3.3.

Event-Level Selection

At least one primary vertex must be reconstructed, and all ATLAS detector components at the time of the event recording must have been functional. The invariant mass of the diphoton candidate must lie within $105\,\text{GeV} < m_{\gamma\gamma} < 160\,\text{GeV}$. Choosing a range that is significantly larger than the typical range of $m_{\gamma\gamma}$ from $H \to \gamma\gamma$ events enables a robust subtraction of non-Higgs background.

Selection of Jets and Leptons

Some of the measured differential cross sections describe jet-related properties of Higgs events. In the measurements of differential cross sections for jet-related variables, jets are required to have a $p_{\mathrm{T}} > 30\,\mathrm{GeV}$ and an absolute rapidity of $|y_j| < 4.4$. In the region $|y_j| < 2.4$, $p_{\mathrm{T}} < 60\,\mathrm{GeV}$ an additional selection based on a multivariant discriminant called *jet vertex tag* is applied to jets, reducing the number of jets from pileup interactions [192, 193].

As described in Section 3.3.3, a given shower in the calorimeter can be reconstructed as both photon and electron candidate simultaneously if the inner-detector information does not allow a unique categorization. This ambiguity is resolved at the stage of the $H \to \gamma\gamma$ analysis by removing electron candidates that are close to a photon candidate: if an electron candidate has a distance $\Delta R = \sqrt{\Delta\phi^2 + \Delta y^2}$ to a photon candidate of less than 0.4, the electron candidate is disregarded. Similarly, if a jet overlaps with either one of the selected photon candidates ($\Delta R < 0.4$) or a remaining electron candidate ($\Delta R < 0.2$), it is removed. The reason for this is that electron candidates and photon candidates are also reconstructed as a jet by the jet reconstruction algorithm. By removing the corresponding jets, this ambiguity is resolved. Remaining electrons that are too close to a remaining jet ($\Delta R < 0.4$) are removed for reasons of consistency with the electron isolation efficiency measurement, and because it removes electrons from decays of heavy-flavor hadrons. Muons overlapping with either selected photons or jets ($\Delta R < 0.4$) are removed in the last step of the overlap removal.

Considered electrons must have a p_{T} of larger than 10 GeV and a pseudorapidity within the range of $0 < |\eta| < 1.37$ or $1.52 < |\eta| < 2.47$. Selected muons must satisfy $|\eta| < 2.7$, corresponding to the acceptance of the muon spectrometer, and $p_{\mathrm{T}}^{\mu} > 10\,\mathrm{GeV}$. In addition, they must be isolated and identified [157].

A b-jet is a jet originating in a hadron that contains a b-quark. In order to classify jets as b-jets at reconstruction level, a *b-tagging* algorithm with an efficiency of 70 % is used [194]. To qualify as a b-jet in this analysis, a jet also must be central, i.e. the rapidity of that jet has to satisfy $|y_j| < 2.5$.

5.3.2. Particle Level

The fiducial particle-level selection is based on final-state particles with a lifetime larger than 10 ps, called *stable*, and which do not result from the GEANT4 simulation of particle-detector interactions. Moreover, photons, electrons and muons are disregarded if they result from a hadron decay.

To a large extent, the particle-level selection mirrors the selection at reconstruction level. Photons must satisfy $p_{\mathrm{T}}^{\gamma} > 25\,\mathrm{GeV}$. Moreover, the p_{T}^{γ} of the leading (sub-leading) photon must exceed 35 % (25 %) of the invariant mass of the leading and sub-leading photons $m_{\gamma\gamma}$. The diphoton invariant-mass is required to be within the range $105\,\mathrm{GeV} < m_{\gamma\gamma} < 160\,\mathrm{GeV}$. The pseudorapidity of selected photons must lie within $0 < |\eta| < 1.37$ or $1.52 < |\eta| < 2.37$. A particle-level isolation selection is applied to photons; it is defined as the transverse energy of the summed four-momenta of all charged particles within a cone of radius $\Delta R < 0.2$ around the photon, considering only particles with a p_{T} of at least 1 GeV. If this quantity is larger than 5 % of a photon's transverse momentum, the photon is disregarded.

The four-momenta of electrons and muons include those of stable photons within a cone with radius $\Delta R < 0.1$ in order to recover the lepton energy lost by bremsstrahlung processes. Electrons with a pseudorapidity within $1.37 < |\eta| < 1.52$ or a p_{T} lower than 10 GeV are disregarded. Muons are required to have a pseudorapidity within $|\eta| < 2.7$ and a p_{T} larger than 10 GeV. The overlap between photons and electrons is removed by disregarding electrons that are closer than $\Delta R < 0.4$ to one of the two leading photons.

Jets at particle-level are reconstructed based on stable particles, excluding neutrinos and muons, because those do not deposit sizable amounts of energy in the calorimeter, and therefore are effectively not accounted for by reconstruction-level jets. The absolute rapidity of jets is required to be within $|y_j| < 4.4$, and their p_{T} to be larger than 30 GeV. In order to remove the overlap of jets with photons, a jet is removed if it is closer than $\Delta R < 0.4$ to a photon with a p_{T} of at least 25 GeV. Similarly, if the distance between a jet and an electron with a p_{T} of at least 10 GeV is smaller than $\Delta R < 0.2$, the jet is disregarded.

A jet that satisfies the requirements above and which contains a b-hadron with a p_{T} larger than 5 GeV and an angular distance to the jet direction smaller than $\Delta R < 0.4$ is considered to be a b-jet. Additionally, in order for a b-jet to be considered in the analyses, it must lie within

$|y_j| < 2.5$.

5.3.3. Dalitz Events

Not all photons from $H \to \gamma\gamma$ decays are stable; some photons from Higgs boson decays have high virtuality, i.e. they do not obey the energy-momentum relation, resulting in a quick decay to a pair of charged particles. The occurrence of such $H \to \gamma^*\gamma \to f\bar{f}\gamma$ events, called *Dalitz events*, needs to be considered in order to properly correct the extracted number of signal events for a comparison with $H \to \gamma\gamma$ predictions. About 6 % of the simulated events are Dalitz events. These events are not considered in the computation of the $H \to \gamma\gamma$ branching ratio. As they do not result in a stable diphoton final state, they are not part of the fiducial selection at particle level. The remaining 94 % are reweighted such that the predicted $H \to \gamma\gamma$ production cross section is matched again.

Because $H \to \gamma^*\gamma \to f\bar{f}\gamma$ events have a low efficiency of passing the diphoton selection as described in Section 5.3.1, Dalitz events constitute only about 0.4 % of the selected diphoton events at reconstruction level according to simulation; these selected Dalitz events are not removed. Therefore, the unfolding of the measured cross sections to particle level removes the expected impact of Dalitz events on the cross section.

5.4. Signal Extraction

5.4.1. Introduction

The measured number of $H \to \gamma\gamma$ events, called the *signal yield*, is extracted using an unbinned signal-plus-background fit of the invariant-mass spectrum of the selected diphoton candidate events using a *maximum profile-likelihood* method. The likelihood function is maximized by adjusting its parameters, namely the signal yield, background yield and a number of *nuisance parameters*. The combination of parameters for which the observation of the measured invariant-mass spectrum is most likely corresponds to the fit result. Nuisance parameters are parameters that are not of central interest in the fit, and which are known with limited accuracy or can be unconstrained. Within the fitting procedure, they are *profiled out*; this is explained in some detail in Section 6.3.1 of the next chapter. The set of nuisance parameters includes the parameters

that describe the shape of the background-modeling function, parameters that take into account uncertainties in the photon energy scale and resolution, as well as a parameter that allows a slight shift in the Higgs peak position in the mass spectrum. In the case of background-modeling parameters, no constraints on the nuisance parameters are imposed. For the other nuisance parameters, however, p.d.f.s are included into the likelihood fit that penalize deviations from the nominal parameter values.

In this way, signal yields can be determined in various phase-space regions, each of which corresponds to an individual invariant-mass distribution based on events that satisfy given phase-space requirements. The basic event selection as described in Section 5.3.1 is applied for each. Figure 5.2 shows the resulting invariant-mass spectrum and the best-fit signal-plus-background model. In addition to this basic selection, further phase-space specifications in terms of various

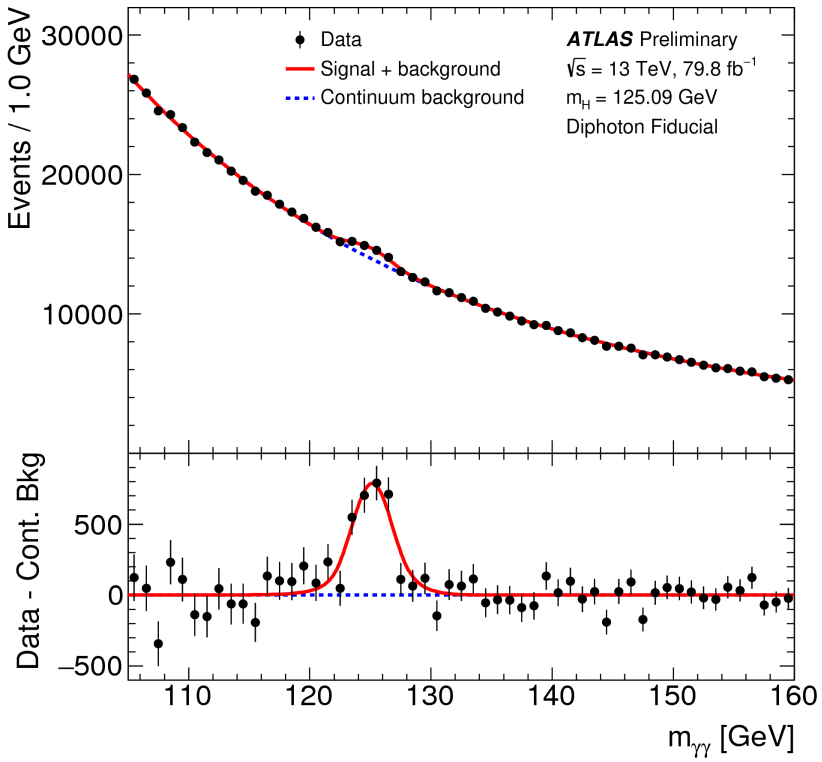

Figure 5.2. | Diphoton invariant-mass spectrum for the inclusive fiducial selection. While the maximum-likelihood fit is performed in an unbinned way, a binning has been used in this plot in order to enable a visualization of the spectrum. The measured number of events per $m_{\gamma\gamma}$ bin are shown as black markers, and the corresponding best-fit signal-plus-background function is shown in red. Shown in the lower panel is the difference between the spectrum and the fitted background function. Taken from Reference [171].

kinematic variables such as p_{T}^{H} can be imposed, resulting in invariant-mass spectra that can be

used to determine differential distributions. When extracting the signal yields for the differential cross section in a given kinematic variable, all bins are taken into account simultaneously by maximizing the product of the likelihood functions corresponding to each bin. This entails that the energy scale and resolution nuisance parameters are aligned over all bins.

The binning in the considered kinematic variables is given in Table 5.2. In the case of $p_{\mathrm{T}}^{j_1}$, the first bin, ranging from 0 GeV to 30 GeV, contains the events lacking any reconstructed jet satisfying the jet selection criteria as described in Section 5.3.1. In the case of the differential distribution in $N_{b-\mathrm{jets}}$, an additional pre-selection is applied for all bins, requiring at least one central jet ($|y_j| < 2.5$) and an absence of electrons and muons. The first bin of the $N_{b-\mathrm{jets}}$ distribution then contains events passing these selection criteria which do not contain a b-jet.

Variable	Binning	N_{bins}
p_{T}^{H} [GeV]	0 – 5 – 10 – 15 – 20 – 25 – 30 – 35 – 45 – 60 – 80 – 100 – 120 – 140 – 170 – 200 – 250 – 350	17
$p_{\mathrm{T}}^{j_1}$ [GeV]	0 – 30 – 55 – 75 – 120 – 350	5
$\lvert y_H \rvert$	0.00 – 0.15 – 0.30 – 0.45 – 0.60 – 0.75 – 0.90 – 1.20 – 1.60 – 2.40	9
$N_{b-\mathrm{jets}}$	0 – 1 – 2 – ∞	3

Table 5.2. | The binning for the differential cross section measurement in the four considered kinematic variables. The first $p_{\mathrm{T}}^{j_1}$ bin, from 0 GeV to 30 GeV contains events without at least one jet passing the selection. In the case of $N_{b-\mathrm{jets}}$, a pre-selection consisting of the requirements that at last one central jet and neither electron nor muon is present.

5.4.2. Modeling of the Invariant-Mass Spectrum

In order to perform a signal-plus-background fit to the diphoton invariant-mass spectrum, p.d.f.s for both signal and background needs to be provided. The Higgs signal consists of a peak centered at the Higgs boson mass, and the background corresponds to a smoothly falling function. In the two following sections it is discussed how appropriate p.d.f.s for signal and background are obtained.

Modeling of the Signal Peak

The $H \to \gamma\gamma$ diphoton invariant-mass spectrum at particle level is given by a narrow and symmetric Breit-Wigner curve, centered at the Higgs boson mass of 125.09 GeV and having

a width of 4 MeV [7, 13]. Due to the limited detector resolution, however, the peak width at reconstruction level is considerably larger than the intrinsic width of 4 MeV, and the shape is in general not perfectly symmetric around the peak. The signal distribution in reconstructed events can be well described by a double-sided Crystal-Ball function, which consists of a Gaussian core and power-law tails, each component normalized such that the transition from one part to the adjacent parts is continuous [195, 196]. The expression for the corresponding p.d.f. is given by

$$\mathcal{S}_{\mathrm{CB}}(m) = N \cdot \begin{cases} e^{-\frac{t^2}{2}} & \text{if } -\alpha_{\mathrm{low}} < t < \alpha_{\mathrm{high}} \\ \left(\frac{n_{\mathrm{low}}}{|\alpha_{\mathrm{low}}|}\right)^{n_{\mathrm{low}}} e^{-\frac{|\alpha_{\mathrm{low}}^2|}{2}} \cdot \left(\frac{n_{\mathrm{low}}}{|\alpha_{\mathrm{low}}|} - |\alpha_{\mathrm{low}}| - t\right)^{-n_{\mathrm{low}}} & \text{if } t < -\alpha_{\mathrm{low}} \\ \left(\frac{n_{\mathrm{high}}}{|\alpha_{\mathrm{high}}|}\right)^{n_{\mathrm{high}}} e^{-\frac{|\alpha_{\mathrm{high}}^2|}{2}} \cdot \left(\frac{n_{\mathrm{high}}}{|\alpha_{\mathrm{high}}|} - |\alpha_{\mathrm{high}}| - t\right)^{-n_{\mathrm{high}}} & \text{if } t > \alpha_{\mathrm{high}} \end{cases}, \quad (5.3)$$

where $t = \frac{m_{\gamma\gamma} - \overline{m}_{\gamma\gamma}}{\sigma}$, in which $\overline{m}_{\gamma\gamma}$ denotes the mass at which the distribution has its peak. The width of the Gaussian core is denoted by σ. Transition points between the Gaussian core and the power-law functions describing the lower and upper tails are given by α_{low} and α_{high}, respectively. The exponents of the power-law functions are denoted by n_{low}, n_{high}, and N is a normalization factor.

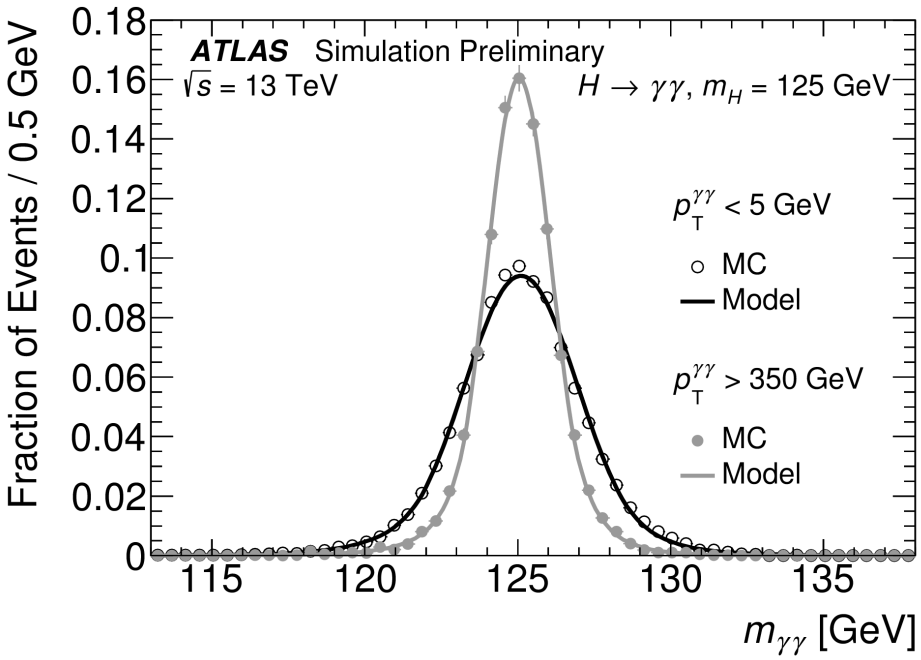

Figure 5.3. | Simulated $m_{\gamma\gamma}$ distributions of the Higgs resonance at reconstruction level for two regions of p_{T}^{H} (open and filled markers). The fitted Crystal-Ball functions for both distributions are shown as solid lines. Taken from Reference [145].

The best-fit parameters of this p.d.f. for each considered phase-space region individually are extracted based on MC simulation before the signal-plus-background fit is performed. In Figure 5.3, examples of fitted simulated $m_{\gamma\gamma}$ distributions at reconstruction level are shown for two different phase-space regions. As one can see, the width of the Crystal-Ball function can differ considerably between different phase-space regions. Since in the simulation a Higgs boson mass of 125.00 GeV is assumed, which is 90 MeV lower than the measured value, the fitted mean values of the Crystal-Ball functions in the various considered kinematic regions are shifted by that amount.

Modeling of the Background

The non-Higgs background dominates the $m_{\gamma\gamma}$ spectrum, as can be seen in Figure 5.2, and its parametrization is one of the largest sources of systematic uncertainty. There is no a-priori functional form that would follow from theoretical predictions, which is partly due to the influence of photon-jet and jet-jet events that pass the diphoton selection. Such events have an influence on the shape of the mass spectrum that is difficult to predict. Therefore, the function that is used to parametrize the background to the Higgs signal is chosen from a set of several smoothly falling functions, based on how well they can describe the background in a given kinematic region. Possible functions, not including normalization factors, for the background description are:

- Bernstein polynomials of third, fourth, or fifth degree. A Bernstein polynomial of degree n is defined as
$$\sum_{\nu=0}^{n} \beta_{\nu}^{\mathrm{bkg}} \binom{n}{\nu} m_{\gamma\gamma}^{\nu} (1 - m_{\gamma\gamma})^{n-\nu} \,, //FIXED \tag{5.4}$$
where $\beta_{\nu}^{\mathrm{bkg}}$ is the Bernstein coefficient for the basis polynomial with index ν. The values of $\beta_{\nu}^{\mathrm{bkg}}$ determine the shape of the polynomial.
- Exponentials of first-, second-, or third-degree polynomials. The definition for a polynomial of degree n is given by
$$\exp\left(- \sum_{\nu=1}^{n} \frac{m_{\gamma\gamma}^{\nu}}{\alpha_{\nu}^{\mathrm{bkg}}} \right), \tag{5.5}$$
where α_{ν} are the coefficients that determine the shape of the spectrum.

Exponentials of second degree polynomials often are well-suited for the description of the

background mass spectrum. The parameters of the background-modeling functions are treated as unconstrained nuisance parameters in the signal-plus-background fit.

In order to decide which background function is best suited for the signal-plus-background fit of the invariant-mass spectrum, studies are performed on mass spectra derived by a combination of simulation and data-based information. The background to the Higgs signal can be categorized into *reducible* and *irreducible* backgrounds. Reducible background consists of events with two reconstructed and identified photon candidates in which at least one of those photon candidates results from a photon-faking jet, denoted by γj or jj. Because it is possible to effectively discriminate between photons and jets from QCD, these events belong to the reducible background. If, on the other hand, two actual photons result from a pp collision that does not involve a Higgs boson decaying to a pair of photons, there is no effective way of discriminating between these and photons from Higgs boson decays. Hence, this type of background is called irreducible.

In order to model the invariant-mass spectrum of non-Higgs diphoton candidates, it is necessary to derive a template for each of the mentioned background categories ($\gamma\gamma$, γj, jj) and sum them, weighted according to their relative contribution. Of the three background components, only the $\gamma\gamma$ background is simulated in sufficient number as to provide reliable shape information in all considered regions of phase space. In order to obtain a template for the mass distribution including all types of background, it is therefore necessary to estimate both the mass spectrum templates and the relative contribution for each of the types of background. Templates for the γj and jj background correspond to $\gamma\gamma$ mass spectra that are reweighted to match mass spectra for events which are enriched in γj and jj events as obtained by a data-driven 2×2D sideband method [197, 198] that involves the reversion of identification and isolation selection criteria. This method is also used to estimate the relative contributions of the various background types to the mass spectrum in the signal region. Thanks to the efficient rejection of photon-faking jets, the irreducible background is considerably larger than the reducible background. In the $m_{\gamma\gamma}$ region from 105 GeV to 160 GeV in the inclusive fiducial phase space, the fraction of irreducible-background events is $75.6^{+3.1}_{-4.8}$ %. The uncertainty is dominated by systematic uncertainties in the definition of the control region.

Given an estimate for the expected invariant-mass distribution in each considered phase-space region, it is important to select a function that is able to model this distribution well. This choice is made for each bin of the differential distributions individually. Since it cannot be expected

that a simple analytic function as given above describes the background perfectly, a bias in the extraction of the signal and background yields has to be assumed and estimated. If the chosen background function underestimates the amount of background in the signal region close to the Higgs boson mass, the extracted $H \to \gamma\gamma$ signal yield correspondingly will be too high, and vice versa. The amount of over- or underestimation is quantified in terms of the *spurious signal*, which is used to perform the choice of background functions. The spurious signal is defined as the maximum value of the absolute extracted signal yield in a sequence of signal-plus-background fits of the *background-only* invariant-mass spectrum for a range of assumed Higgs boson mass values of 121 GeV to 129 GeV. The function describing the background is selected such that the function with the fewest degrees of freedom is chosen which satisfies at least one of the following requirements:

- The spurious signal is smaller than 10 % of the expected signal yield.
- The spurious signal is smaller than 20 % of the expected uncertainty on the signal yield.
- At least one of the two previous requirements are met by the spurious signal minus 2σ, where σ is the statistical uncertainty on the estimated spurious signal.

It is possible that the background template as chosen based on the spurious signal is considerably different from the $m_{\gamma\gamma}$ spectrum in collision data. In order to avoid a possible use of such an unfit background function in the signal-plus-background fit, an additional *F-test* is performed in order to assess the need of a higher-degree version of the initially selected background function: the data sideband, excluding the signal mass region $120\,\text{GeV} < m_{\gamma\gamma} < 130\,\text{GeV}$, is fitted with the background function as chosen based on the spurious signal, as well as with a function from the same category, i.e. exponential or Bernstein functions, but with one additional degree of freedom. The resulting χ^2 values of the fits are denoted with χ^2_1 and χ^2_2, respectively. If the additional degree of freedom does not improve the modeling of the background distribution more than can be statistically expected from the use of an additional degree of freedom, the statistic

$$F = \frac{\frac{\chi^2_1 - \chi^2_2}{p_2 - p_1}}{\frac{\chi^2_2}{n - p_2}}. \tag{5.6}$$

follows the *Fisher* distribution [199]. Here, p_1 denotes the number of degrees of freedom of the function chosen by the spurious-signal method, and p_2 denotes the number of degrees of

freedom of the function with an incremented number of degrees of freedoms. The number of mass bins used in the F-test fits is denoted by n. Based on the Fisher distribution, the probability for observing a value for F as large or larger than the observed value can be determined. If the observed probability is smaller than 5 %, the alternative background function with an additional degree of freedom is chosen.

5.4.3. The Likelihood Function

The signal yield of the signal-plus-background fit is estimated using a maximum-likelihood method. The model parameters resulting in the largest likelihood of observing the measured data correspond to the best-fit values for the parameters. Fitted parameters of the model are the signal yield ν^{sig}, the background yield ν^{bkg}, and the various nuisance parameters θ_k.

For each bin of a given distribution of the measurement, including the inclusive cross section, which corresponds to the case of a single bin, the following likelihood function is constructed:

$$\mathcal{L}(m_{\gamma\gamma}, \nu^{\mathrm{sig}}, \nu^{\mathrm{bkg}}, \theta_k) = \frac{e^{-(\nu^{\mathrm{sig}}+\nu^{\mathrm{bkg}})}}{n!} \prod_{j}^{n} \left[\nu^{\mathrm{sig}} \mathcal{S}(m_{\gamma\gamma}^{j}; \theta_k) + \nu^{\mathrm{bkg}} \mathcal{B}(m_{\gamma\gamma}^{j}; \theta_k) \right], \tag{5.7}$$

where the selected events are labeled with index j, and n corresponds to the number of selected events. The p.d.f.s of the signal and background mass distributions are denoted by $\mathcal{S}$ and $\mathcal{B}$. The factor $e^{-(\nu^{\mathrm{sig}}+\nu^{\mathrm{bkg}})}/n!$ results from the fact that the number of events that enter the fit is a random variable itself that follows a Poisson distribution. A likelihood function as it is shown in Eq. (5.7) is called *extended likelihood function* [163].

The extended likelihood functions for the individual bins in a given considered kinematic variable are multiplied. In addition, the product of the constraints on the nuisance parameters $\prod_k G_k(\theta_k\,; 0, 1)$ is multiplied to the product of extended likelihood functions. That way, the nuisance parameters are correlated over all bins of a kinematic variable.

The nuisance parameter constraints are either Gaussian or log-normal constraints, depending on whether the nuisance parameter should be able to take both positive and negative values. Besides uncertainties on the energy measurement of the photon candidates, uncertainties on the Higgs boson mass and the parameters of the background model are included as nuisance parameters. The nuisance parameters that represent the background shape are not shared between

different bins.

5.5. Correction for Detector Effects

The cross sections given by the ratio of the extracted signal yields and the integrated luminosity cannot be directly compared to predictions or results from other experiments. In order to enable such comparisons, the signal yields must first be corrected for detector effects, that is, inefficiencies and the limited resolution in the determination of event properties. The process of correcting for detector effects is called *unfolding* and usually relies on information from MC simulation. In simulated events, one has access not only to information about events at reconstruction level, but also to information at particle level. Combining information from both reconstruction and particle level allows the creation of a mapping of event and particle properties from reconstruction to particle level, which is the basis of the unfolding process. Several methods of unfolding exist [163], and they can be broadly divided into two types of approaches. First, there are methods of unfolding that rely on a detector response matrix, defined via

$$n_i^{\text{reco}} = \sum_{j=1}^{M} \hat{R}_{ij} \cdot n_j^{\text{ptcl}} , \tag{5.8}$$

where n_i^{reco} is the i-th element of the array that contains the measured signal yields, and n_j^{ptcl} is the j-th element of the array containing the numbers of events in the various bins at particle level. The sum runs up to the number of bins in the particle-level distribution, M. The matrix $\hat{R}_{ij}$ then maps the numbers of events in the various bins at particle level to the measured distribution of signal yields, representing the detector response. As such, it contains information about inefficiencies and migrations between bins due to the finite detector resolution. If an inversion of the response matrix $\hat{R}$ is possible, its application on a spectrum at reconstruction level yields an unfolded spectrum at particle level. This simple approach has zero bias [163], but has the disadvantage that statistical fluctuations as seen in data, i.e. deviations from the expected signal yields, are enhanced by off-diagonal elements of the response matrix, leading to a strongly fluctuating unfolded spectrum and large statistical uncertainties on the unfolded distribution. Several techniques exist to dampen these effects, at the cost of introducing a certain amount of

bias [163].

In this work, another type of unfolding is used; it is based on simple correction factors [163] to account for detector effects, and is called *bin-by-bin* unfolding. Here, the signal yields at reconstruction and particle level in MC simulation, n_i^{reco} and n_i^{ptcl}, respectively, in each considered phase-space region are compared with each other, leading to a correction factor for each bin, given by

$$C_i = \frac{n_i^{\text{reco}}}{n_i^{\text{ptcl}}} \,. \tag{5.9}$$

In order to determine the unfolded cross section for a given bin, the extracted signal yield ν_i^{sig} is divided by the corresponding correction factor and the integrated luminosity L_{int} of the used dataset:

$$\sigma_i = \frac{\nu_i^{\text{sig}}}{C_i \cdot L_{\text{int}}} \,. \tag{5.10}$$

The correction factor generally depends on what the relative contributions from the various Higgs boson production modes in a given phase-space region are. Accordingly, the overall correction factor corresponds to

$$C_i = \frac{\sum_{s=1}^{n_{\text{pm}}} \frac{\sigma_s^{\text{SM}}}{N_s} \cdot n_{\text{fid,s}}^{\text{reco}}}{\sum_{s=1}^{n_{\text{pm}}} \frac{\sigma_s^{\text{SM}}}{N_s} \cdot n_{\text{fid,s}}^{\text{ptcl}}} \,, \tag{5.11}$$

where s is a label for the n_{pm} Higgs boson production modes. The individual expected cross section for a given production mode s is given by σ_s^{SM}. The number of events in the considered phase space at reconstruction and particle level needs to be normalized by the number of all produced events in a given production mode, N_s. By designing the fiducial phase-space volume to include only isolated photons at both reconstruction and particle level, the dependence of the correction factor on the production mode is significantly reduced, which in turn reduces sensitivity to assumptions about the relative contributions from different Higgs boson production modes. Different production modes lead to different amounts of additional radiation. Particularly photons in $t\bar{t}H$ events tend to be less isolated than events corresponding to other production modes due to the relatively large number of jets. If the isolation requirement would only be applied at reconstruction level, the correction factor would have to fully account for isolation inefficiencies.

In general, the bin-by-bin unfolding method leads to a biased unfolding result unless simulation and nature agree in a certain aspect: applying the correction factor as calculated by Eq. (5.9) to the *observed* signal yield, denoted by $n_i^{\text{reco,data}}$, the estimator for the unfolded signal yield in bin i is

$$n_i^{\text{ptcl,data}} = \frac{n_i^{\text{reco,data}}}{C_i} = \frac{n_i^{\text{ptcl}}}{n_i^{\text{reco}}} \cdot n_i^{\text{reco,data}}. \tag{5.12}$$

If one assumes that the actual *true* number of signal events at particle level is not n_i^{ptcl} as predicted by simulation but $\hat{n}_i^{\text{ptcl}}$, and the corresponding expectation value for the *true* number of signal event at reconstruction level is $\hat{n}_i^{\text{reco}}$, the resulting bias of the estimator $n_i^{\text{ptcl,data}}$ is given by

$$\begin{aligned} b &= \langle n_i^{\text{ptcl,data}} - \hat{n}_i^{\text{ptcl}} \rangle = \langle \frac{n_i^{\text{ptcl}}}{n_i^{\text{reco}}} \cdot n_i^{\text{reco,data}} - \hat{n}_i^{\text{ptcl}} \rangle \\ &= \frac{n_i^{\text{ptcl}}}{n_i^{\text{reco}}} \cdot \langle n_i^{\text{reco,data}} \rangle - \hat{n}_i^{\text{ptcl}} = \frac{n_i^{\text{ptcl}}}{n_i^{\text{reco}}} \cdot \hat{n}_i^{\text{reco}} - \hat{n}_i^{\text{ptcl}} \\ &= \left(\frac{n_i^{\text{ptcl}}}{n_i^{\text{reco}}} - \frac{\hat{n}_i^{\text{ptcl}}}{\hat{n}_i^{\text{reco}}} \right) \cdot \hat{n}_i^{\text{reco}}. \end{aligned} \tag{5.13}$$

This means that the bin-by-bin unfolding method in general leads to biased results if the ratio of the expected numbers of events at particle and reconstruction level is different from the ratio of the *true* expectation values for the numbers of events at particle and reconstruction level.

The use of this simple method is warranted if the cross section measurement is statistically limited and if migrations between bins are small. For the latter, either a good resolution must be achieved, or the binning must be chosen sufficiently coarse. The bias introduced by this unfolding method has been studied, and was shown to be small in relation to the expected statistical uncertainties. Moreover, uncertainties on the correction factors from mismodeling of the particle-level cross sections are taken into account in the measurement, as will be described in Section 5.6.2.

5.6. Uncertainties

The uncertainties relevant for the inclusive and differential measurements of the fiducial cross section are discussed in the following sections. In addition to statistical uncertainties from the signal

yield extraction in the mass spectrum fit, systematic uncertainties have to be included: systematic uncertainties in the signal yield extraction, systematic uncertainties in the determination of the correction factors, and the uncertainty on the integrated luminosity of the considered dataset. The uncertainty on the integrated luminosity of the combined 2015–2017 dataset is 2.0 % [200]; see Section 3.5 for information on the luminosity measurement. The diphoton trigger efficiency, which is taken into account by the correction factors, is known with an uncertainty of 0.45 %.

5.6.1. Signal Extraction

The large background from QCD events results in a sizable statistical uncertainty in the signal extraction. There are, however, also systematic uncertainties to be taken into account, which are described below.

Spurious Signal

Among the systematic uncertainties from the signal extraction, the dominant uncertainty is related to the choice of the background modeling function. If the chosen function under- or overestimates the amount of background events in the region close to the Higgs boson mass, the fitted signal yield will be over- or underestimated, respectively. This bias has been studied by performing signal-plus-background fits on a background-only mass spectrum, see Section 5.4.2. The ratio of the spurious signal to the expected signal yield is taken as uncertainty.

Photon Energy Scale and Resolution

The photon energy scale and resolution have influence on the shape of the $m_{\gamma\gamma}$ spectrum and consequently on the extracted signal yield; both are known only with limited accuracy. Several sources of uncertainties exist; these are taken into account by including corresponding nuisance parameters in the signal-plus-background fit. In the case of the energy resolution uncertainties, 9 nuisance parameters are used, which are constrained by log-normal functions. In order to implement uncertainties on the energy scale, 69 nuisance parameters are used; these are constrained by Gaussian functions. The nuisance parameters that encapsulate the resolution uncertainties are generally less constrained than those for the scale uncertainties. Among the largest contributions to the resolution uncertainty are the uncertainty regarding the material

distribution in the inner detector, the limited knowledge of the constant term of the energy resolution as introduced in Section 3.3.3, and the uncertainty in the modeling of pileup effects. The largest contributions to the energy scale uncertainty are the uncertainty due to the relative calibration of different gain settings in the cell energy measurement and the intercalibration of the first and second layers of the EM calorimeter. For details on the determination of energy scale and resolution uncertainties, see Reference [148].

By comparing extracted signal yields from a fit in which all nuisance parameters are floating and a fit in which the considered nuisance parameter θ_k is fixed to a value $\theta_k \pm \Delta\theta_k$, where $\Delta\theta_k$ denotes the uncertainty on the nuisance parameter, the impact of that nuisance parameter on the best-fit signal yield can be determined. For some resolution-related uncertainties, it can be as large as 2 %, while the impact of energy-scale-related uncertainties is generally less than 0.5 %.

In addition to nuisance parameters regarding the photon energy scale and resolution, the signal-plus-background fit is also sensitive to the assumed mass of the Higgs boson. Since that mass is known with only limited precision, it is treated as a nuisance parameter in the fit. The central value of that parameter is 125.09 GeV, corresponding to the measured value [7]. The uncertainty of that measurement is 0.24 GeV, which is reflected in the Gaussian constraint of the nuisance parameter.

5.6.2. Correction Factors

The correction factors used in the unfolding process are based on MC simulation and therefore reflect eventual biases in the SM predictions; such biases need to be estimated and propagated to the correction factors. In addition, experimental uncertainties that affect the cross sections at reconstruction level need to be propagated to the correction factors.

Pileup Reweighting

As described in Section 5.2.2, simulated events are reweighted such that the distribution of the number of pileup interactions per event matches that in the dataset. A mismodeling in the pileup reweighting can lead to biases in the correction factors.

In order to compute the mean value $\mu - 1$ of the Poisson distribution from which the number of pileup interactions is drawn, Eq. (5.1) is used. Thus, the number of pileup interactions that

are added to the hard-interaction event depends on the value of the inelastic cross section σ_{inel}. The modeling of proton-proton interactions in the event generator that is used to simulate pileup interactions, Pythia8, leads to an inelastic cross section that is slightly higher than the measured inelastic cross section [201]. A scale factor relating $\sigma_{\text{inel}}^{\text{data}}$ and $\sigma_{\text{inel}}^{\text{MC}}$ is used in order to take this mismatch into account before pileup reweighting is performed. The scale factor is determined based on the observed number of primary vertices as a function of μ in data and in simulation. The uncertainty on the scale factor of 3 % is propagated to the bin-by-bin correction factors by applying pileup weights based on varied scale factors in the computation of the correction factors and by comparing the resulting correction factors to the nominal values.

Vertex Selection

As described in Section 3.3.2, a multivariate algorithm is used to determine the Higgs boson production vertex. In approximately 75 % of simulated gluon fusion Higgs events, the correct vertex is chosen, defined by the selected reconstructed vertex being in a distance to the true vertex of less than 0.3 mm. The absolute uncertainty on this fraction was estimated to be 5 % by comparing the corresponding values in data and simulation using $Z \to e^+e^-$ events in which the tracks of the electrons from the Z decay are disregarded, see also Figure 3.15.

The assumed location of the Higgs boson production vertex has impact on the reconstructed photon candidate four-momentum because it influences the pseudorapidity assigned to the photon candidate. Via the relation $E_{\text{T}} = E/\cosh(\eta)$ as introduced in Section 3.3.3, this has an effect on the transverse energy of the photon candidates. Moreover, the selection of the Higgs boson production vertex has influence on the track-based isolation variable, for which exclusively the tracks assigned to the hard-interaction vertex are considered. Therefore, the uncertainty of the fraction f of $H \to \gamma\gamma$ events in which the correct vertex has been chosen needs to be propagated to the measured cross section. This requires the determination of the efficiency ε of the diphoton event selection as a function of f,

$$\varepsilon(f) = f \cdot \varepsilon_{\text{corr}} + (1 - f) \cdot \varepsilon_{\text{wrong}} \,. \tag{5.14}$$

In this equation, $\varepsilon_{\text{corr}}$ and $\varepsilon_{\text{wrong}}$ are the diphoton event selection efficiencies in the case of a correct selection of the Higgs boson production vertex, and in the case of an incorrect selection,

respectively. The uncertainty on f is propagated to the selection efficiency $\varepsilon(f)$, and by extension to the correction factors, by comparing $\varepsilon(f)$ for values of f that correspond to its up- and down-variations within the uncertainty Δf, $\varepsilon(f \pm \Delta f)$.

Jets from Pileup Interactions

For an accurate determination of differential cross sections in jet-related variables, it is important to understand the impact of jets from pileup interactions: some jets that pass the selection criteria do not originate in the Higgs boson production vertex but result from pileup interactions. In simulation, particle-level information is exclusively stored for the hard interaction, and not for pileup interactions. Consequently, a jet is considered to be a pileup jet in simulation if it cannot be matched to any particle-level jet from the Higgs boson production vertex with a transverse momentum larger than 10 GeV within $\Delta R < 0.4$. The fraction of selected jets stemming from pileup interactions in simulation is 6 % according to this definition. The efficiency with which pileup jets pass the jet selection cannot be expected to be identical in data and simulation. In order to estimate the effect of this potential difference on the bin-by-bin correction factors for jet-related distributions, 20 % of the selected pileup jets in simulation are randomly removed. This percentage corresponds to an estimate for the relative difference in efficiencies of pileup jets to pass the jet-vertex-tag requirement in data and simulation. The uncertainty from the contribution of pileup jets on the correction factors is assessed by comparing the nominal correction factors with those resulting from events with such modified sets of jets.

Photon Selection

The efficiency of the photon identification and isolation selection in simulation and in data are generally not identical. In order to correct for these differences between events in simulation and in data, scale factors are multiplied as additional factors to the weights of the simulated events. See Chapter 4 for details on the photon identification efficiencies and the corresponding scale factors, given by the ratio of identification efficiencies in data and in simulation. Both identification and isolation efficiency scale factors are known only with limited accuracy. The uncertainties on the identification and isolation efficiency scale factors are of the order 1 % in the relevant photon p_{T} region [147]. In Figures 4.25 and 4.26, the scale factors and uncertainties are

shown for identification efficiencies. In order to propagate uncertainties in the identification and isolation scale factors to the cross section measurement, the scale factors are varied within their uncertainties and the resulting correction factors are compared to the nominal correction factors.

Photon Energy Scale and Resolution

The uncertainty on the photon energy scale and resolution is not only relevant in the signal yield extraction as described in Section 5.6.1, but also in the determination of the correction factors. Systematic variations of the photon energy scale and resolution lead to migrations in and out of the fiducial region and between bins of the p_{T}^{H} and $|y_H|$ distributions. The uncertainty on the energy scale and resolution is propagated to the correction factor uncertainties by computing the difference between the nominal correction factors and the correction factors based on the up- and down-variations of energy scale and resolution.

Jet Calibration and Flavor Tagging

When considering differential distributions in $p_{\mathrm{T}}^{j_1}$ or $N_{b-\mathrm{jets}}$, the systematic uncertainties of the jet energy determination and jet modeling need to be propagated. The calibration of jet energies is outlined in Section 3.3.4. The relevant uncertainties include, but are not limited to, uncertainties within the *in situ* calibration procedure, uncertainties that account for potential mismodeling of the pileup effects, as well as uncertainties in the jet composition. In the case of $N_{b-\mathrm{jets}}$, also uncertainties related to a potential mismodeling of the b-tagging efficiency need to be propagated to the correction factors for the $N_{b-\mathrm{jets}}$ distribution. The uncertainty on the correction factors is determined by quadratically adding differences between the nominal correction factors and correction factors resulting from variations of the relevant jet-related parameters.

Theoretical Uncertainties

The correction factors are sensitive to the modeling of the underlying physics. Several modeling aspects are taken into account in order to estimate the theoretical uncertainty on the correction factors.

Because correction factors for the various Higgs boson production modes differ to some extent, the corrections factors are sensitive to the relative contributions, as can be seen in Eq. (5.11).

The cross sections for the individual production modes that enter this equation are based on SM predictions. By computing the differences between the nominal correction factors and correction factors that are based on varied contributions from different production modes, the uncertainty on the production mode contributions are propagated to the correction factors. In Table 5.3 the up- and down-variations applied to the cross section of six of the production modes independently are shown. These variations are based on References [202–204]. When scaling the cross section of a particular production mode up or down, the cross sections of all other production modes are kept at their SM value. The production modes with the smallest cross sections are not listed in Table 5.3 and are not considered in the variation scheme, that is, their contributions are assumed to be correctly described by the SM. This is justified by their small cross section; variations of these cross sections would result in negligible effects on the correction factors.

$\frac{\sigma_{\text{pm}} \pm \Delta\sigma_{\text{pm}}}{\sigma_{\text{pm}}}$	ggF	VBF	WH	ZH	$t\bar{t}H$	$b\bar{b}H$
Up	1.145	1.203	1.433	1.468	1.500	1.220
Down	0.855	0.797	0.567	0.532	0.700	0.780

Table 5.3. | Orthogonal variations (scaling factors, SM corresponds to 1) of the cross section contributions of individual Higgs boson production modes that are used to determine the modeling uncertainty on the correction factors due to a limited knowledge about the relative contributions from different production modes. Each production mode contribution is varied independently. Values for all production mode variations except $t\bar{t}H$ and $b\bar{b}H$ are based on Reference [202]. The $t\bar{t}H$ and $b\bar{b}H$ variations are based on References [203] and [204], respectively.

Another source of theoretical uncertainty is the sensitivity of the correction factors to the differential distributions in simulation. In order to directly assess the impact of potential mismodeling of the predicted distributions on the unfolded results, alternative sets of correction factors are derived based on distributions from simulated events in which event weights are modified such that the resulting p_{T}^{H} and $|y_H|$ distributions at reconstruction level correspond to the observed distributions. The reweighting factors are derived from a fit of an appropriate function to the observed spectrum and correspond to the ratio of the fitted function to the SM expectation. The resulting reweighting factors, which are smoothed before application, are shown in Figures 5.4a and 5.4b for p_{T}^{H} and $|y_H|$, respectively. Three varied sets of correction factors are produced: one in which only the p_{T}^{H} distribution is modified, one in which only the $|y_H|$ distribution is modified, and one in which both p_{T}^{H} and $|y_H|$ distributions are modified. The maximal deviation of the

three resulting varied correction factors from the nominal correction factor is taken to be the corresponding uncertainty on the correction factor.

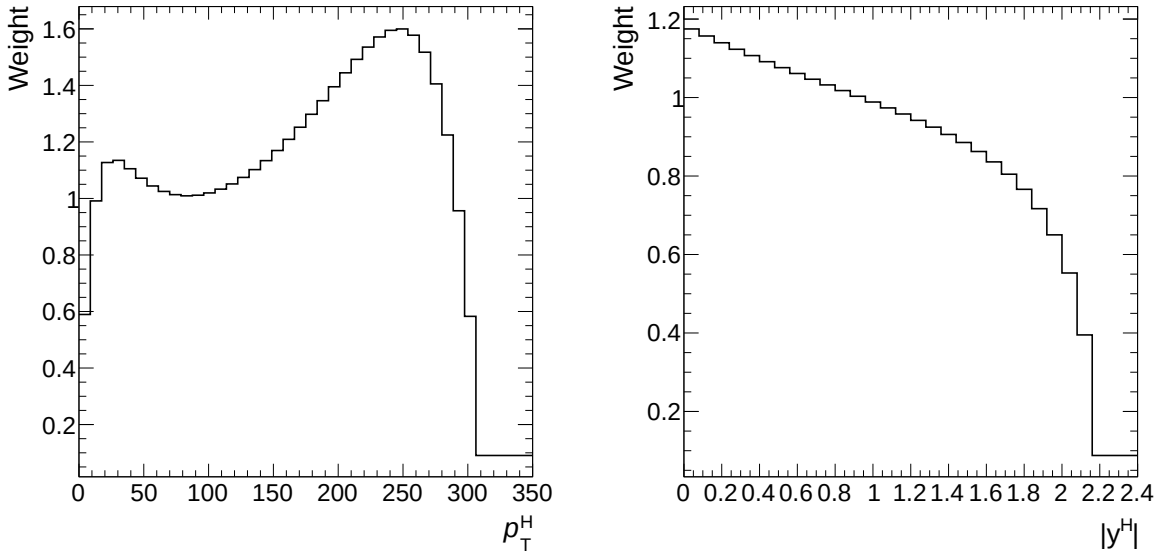

(a) *(b)*

Figure 5.4. | Factors for an event reweighting based on *(a)* p_T^H and *(b)* $|y_H|$ in simulated $H \to \gamma\gamma$ events. By comparing correction factors based on reweighted samples to correction factors from the nominal SM prediction, the impact of a potential mismodeling of differential distributions in simulation on the correction factors is estimated.

Furthermore, an uncertainty due to a potential mismodeling of the underlying event and the parton shower has been taken into account. This uncertainty has been estimated by comparing the nominal correction factors, which are based on the use of Pythia8, with those for which Herwig++ was used as parton shower simulation. For the estimation of this uncertainty, only the effect on the dominant Higgs boson production mode, gluon fusion, was considered. Other production modes, having considerably smaller cross sections, have been omitted here due to the large computational effort that would be necessary for the evaluation of an uncertainty that generally has a small impact on the total uncertainty on the correction factors. Due to a relatively low number of simulated events with Herwig++ as parton shower simulation and resulting statistical fluctuations in some phase-space regions, the uncertainty per bin are estimated based on a linear fit to the distribution of differences between correction factors based on Pythia8 and Herwig++.

The three theoretical uncertainties on the correction factors as described above are combined by taking the envelope of these. A further theoretical uncertainty, an uncertainty related to the

limited knowledge of the Dalitz-events fraction among selected events, is taken into account separately. The sensitivity of the correction factors on the assumed value for the fraction of Dalitz events is estimated by comparing the nominal correction factors to correction factors which are based exclusively on non-Dalitz events.

5.7. Results

5.7.1. Inclusive Cross Section

The measured inclusive Higgs boson production cross section in the diphoton decay channel is

$$\sigma_{\text{fid}} = \left(60.4 \pm 6.1\,(\text{stat.}) \pm 6.0\,(\text{exp.}) \,^{+0.3}_{-0.4}\,(\text{theo.})\right) \text{fb}\,,$$

in the fiducial phase-space volume, which is in good agreement with the SM prediction,

$$\sigma_{\text{fid}}^{\text{SM}} = (63.5 \pm 3.3)\,\text{fb}\,.$$

The relative statistical and systematic uncertainties of the measurement are approximately 10 % each. Thus, in this particular case of a relatively large phase-space region, the statistical uncertainty is similarly small as the combined systematic uncertainties. The systematic uncertainties in the signal yield extraction and the uncertainty on the photon isolation efficiency are the largest systematic contributions to the uncertainty. The uncertainty on the luminosity, being 2 %, is a minor contribution. Theoretical uncertainties on the correction factors are a minor uncertainty contribution, amounting to a relative uncertainty of less than 1 %, which highlights the low model dependence of the measurement. A detailed decomposition of the uncertainty into its various contributions is given in Table 5.4.

5.7.2. Differential Cross Sections

In the following sections, the measured differential cross sections are shown and compared to SM predictions. See Section 2.6.4 for descriptions of the presented predictions. Statistical uncertainties dominate in the differential cross sections, and combined uncertainties generally

Contribution	Relative uncertainty [%]
Fit, statistical uncertainty	10.1
Fit, systematic uncertainty	4.0
Spurious signal	7.3
Dalitz events	0.4
Luminosity	2.0
Trigger efficiency	0.7
Pileup jets & Vertex Selection	0.1
Pileup reweighting	1.9
Photon energy scale & resolution	0.1
Photon isolation efficiency	4.6
Photon identification efficiency	1.3
Theoretical uncertainty	$^{+0.3}_{-0.4}$
Total uncertainty	$^{+14.2}_{-14.2}$

Table 5.4. | Uncertainty contributions in the measurement of the inclusive $H \to \gamma\gamma$ cross section in the fiducial phase-space volume.

are larger than 20 % in all considered phase-space regions. The systematic uncertainties from signal yield extraction are typically the second-largest uncertainty contribution, followed by the correction factor uncertainties, and, finally, by the uncertainty on the integrated luminosity.

The agreement between the measured spectra and the SM predictions can be quantified using the p-value, which is a measure of how probable is to observe deviations from the SM as large or larger than seen in the measured spectrum; see Section 6.3.1 for more information. The covariance matrix that is used for the determination of the p-value includes the statistical and systematic components of the measurement uncertainties as well as the theoretical uncertainties on the SM prediction.

Transverse Momentum of the Higgs Boson

The comparison of the observed differential cross sections in p_{T}^{H} with predictions is shown in Figure 5.5a. The measured spectrum agrees well with the predictions within uncertainties. The compatibility of the measured spectrum with the SM prediction corresponds to a p-value of 31 %. In Figure 5.5b, the relative uncertainty contributions are shown as a function of p_{T}^{H}. The statistical uncertainty is the dominant uncertainty contribution in all bins, ranging from 20 %

to 90 %, followed by signal extraction uncertainties. Uncertainties from unfolding amount to approximately 5 %, shown in Figure 5.5c. The uncertainty on the photon isolation efficiency is the largest contribution to the correction factor uncertainty.

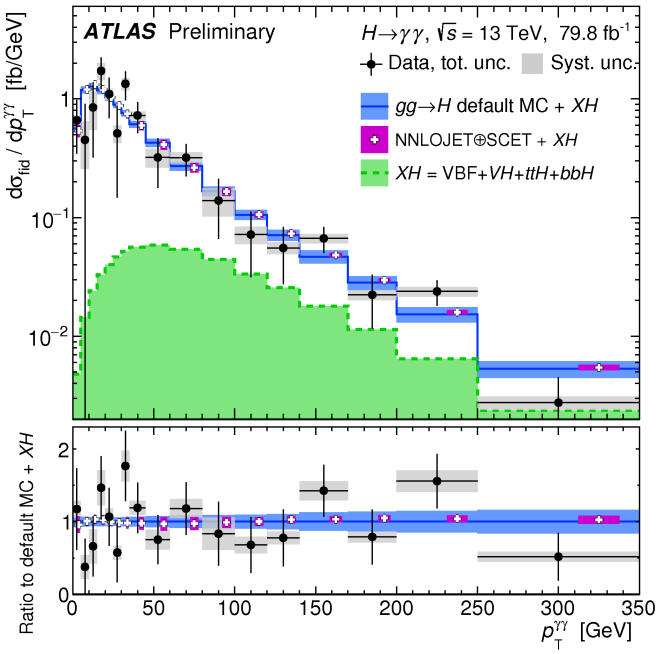

(a)

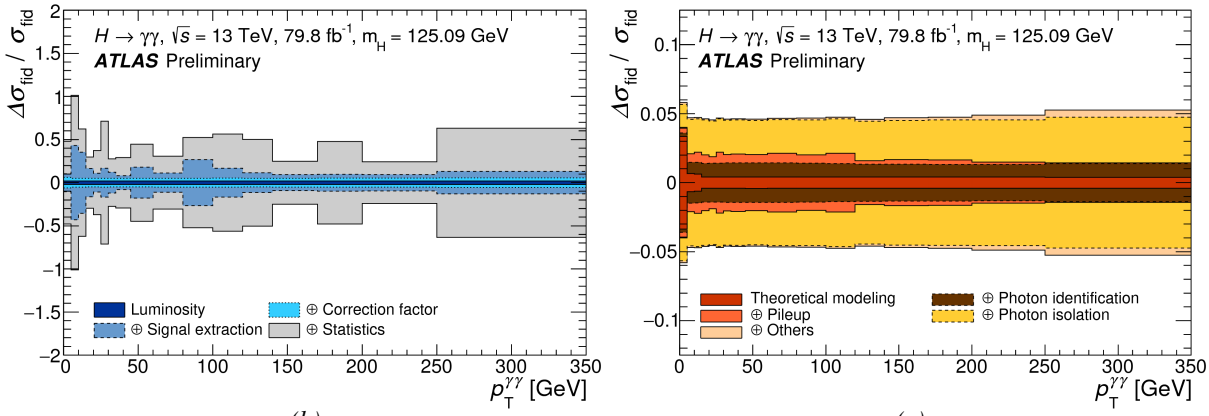

(b) *(c)*

Figure 5.5. | *(a)* Comparison of observed and predicted differential $H \to \gamma\gamma$ cross sections in p_T^H. *(b)* Summary of uncertainties. *(c)* Breakdown of the correction factor uncertainty. Taken from Reference [171].

Transverse Momentum of the Leading Jet

The observed and predicted differential cross sections in $p_T^{j_1}$ are shown in Figure 5.6a. The agreement between predictions and measurement is good, with a p-value of 88 %. In Figures

5.6b and 5.6c, a summary of the uncertainty contributions is given. Combined uncertainties range from 20 % to 50 %. Among the correction factor uncertainties, which are typically smaller than 10 %, the jet energy scale and resolution uncertainties as well as the uncertainty on the photon isolation efficiency are the dominant contributions.

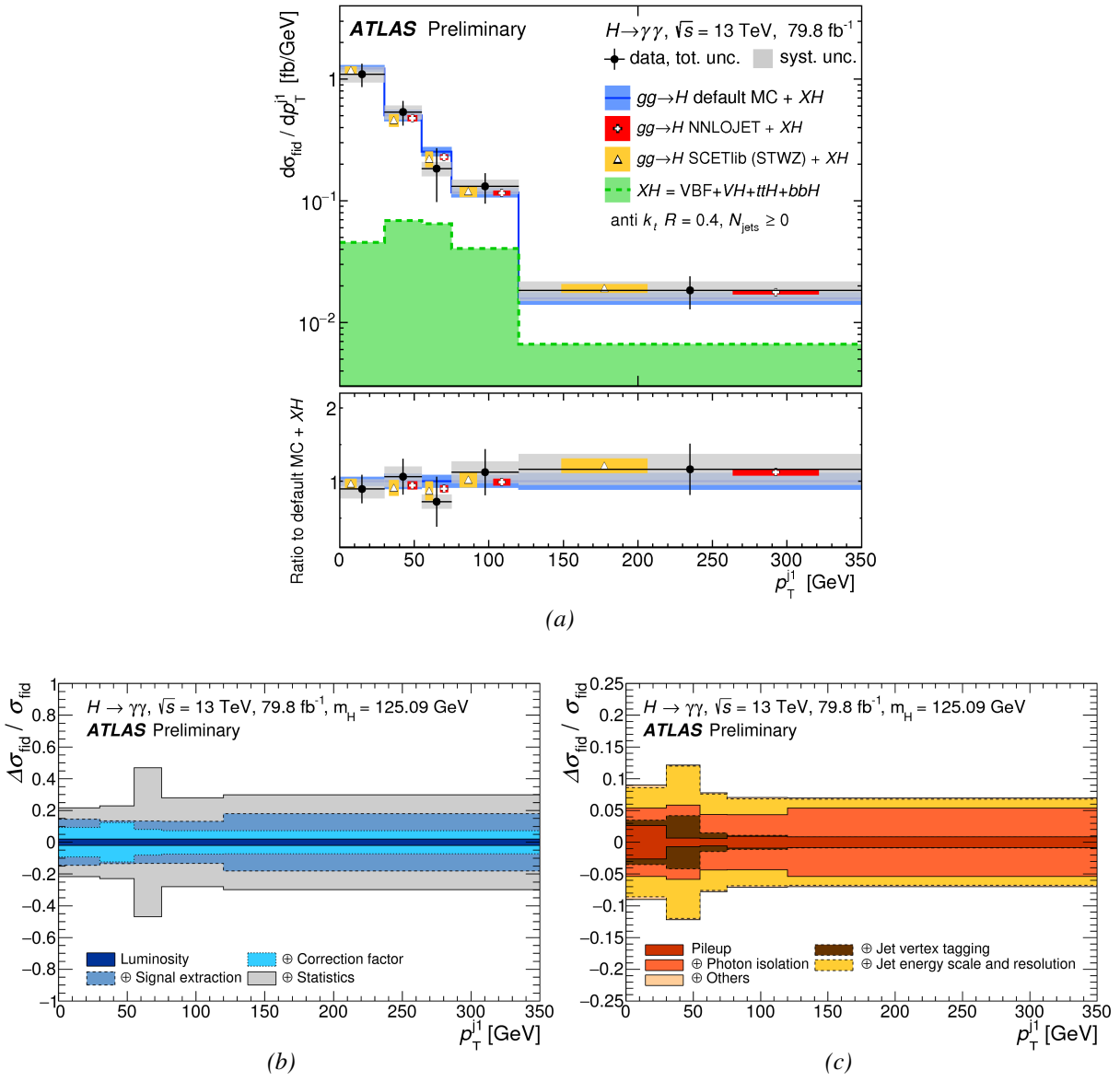

Figure 5.6. | *(a)* Comparison of observed and predicted differential $H \to \gamma\gamma$ cross sections in $p_{\mathrm{T}}^{j_1}$. *(b)* Summary of uncertainties. *(c)* Breakdown of the correction factor uncertainty. Taken from Reference [171].

Higgs Boson Rapidity

The measured differential cross section in the absolute value of the Higgs boson rapidity, $|y_H|$, is shown in Figure 5.7a in comparison with predictions; both distributions are well compatible within the uncertainties, corresponding to a p-value of 56 %. In Figure 5.7b, a summary of the relative uncertainties is shown, while in Figure 5.7c the contributions to the relative uncertainty on the correction factors are presented. The combined uncertainties range from 25 % to 75 %. Being in the range of 20 % to 60 %, the statistical uncertainty is the dominant contribution, followed by signal extraction uncertainties, i.e. the spurious signal and uncertainties on photon energy scale and resolution. Among the correction factor uncertainties, the uncertainty on the photon isolation efficiency is largest.

Number of *b*-jets

The differential cross section in the number of b-jets is shown in Figure 5.8a, explicitly also showing the expected contribution from $t\bar{t}H$, which is substantial at higher b-jet multiplicities. In the region of at least two b-jets, $t\bar{t}H$ is expected to contribute more than 50 % of events, despite its overall small production cross section. There is a good agreement between predicted and measured distributions, corresponding to a p-value of 84 %.

In Figures 5.8b and 5.8c, a summary of the uncertainties on the measured cross sections is shown. The combined uncertainty ranges from about 30 % to 200 %, with the statistical uncertainty being the dominant contribution, particularly so in the bin with at least two reconstructed b-jets. Among the correction factor uncertainties, the uncertainty on the photon isolation efficiency dominates.

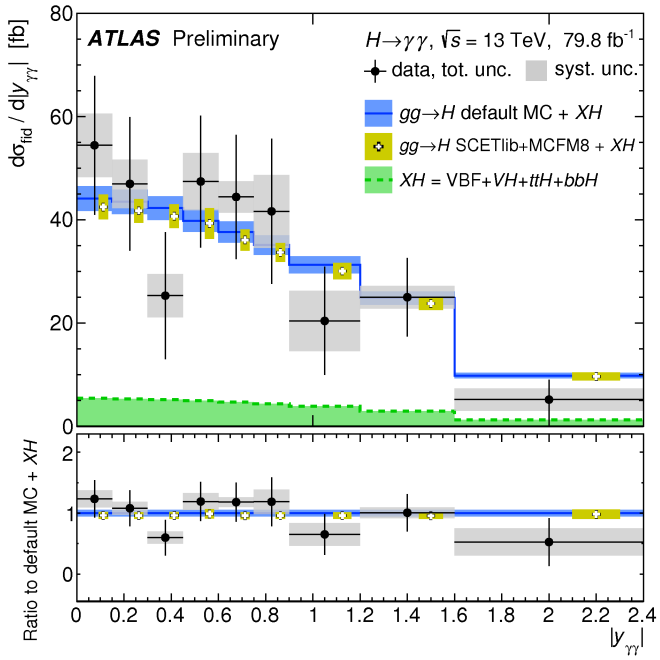

(a)

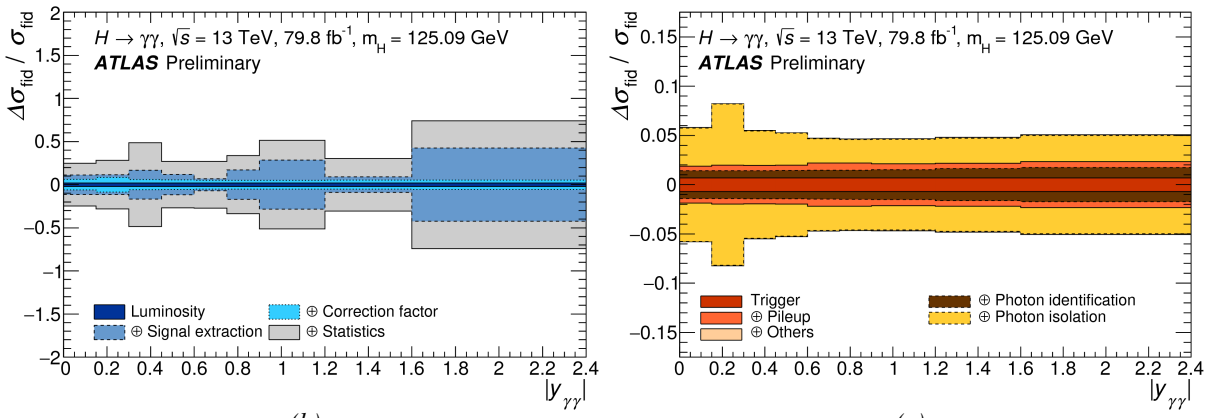

(b) *(c)*

Figure 5.7. | *(a)* Comparison of observed and predicted differential $H \to \gamma\gamma$ cross sections in $|y_H|$. *(b)* Summary of uncertainties. *(c)* Breakdown of the correction factor uncertainty. Taken from Reference [171].

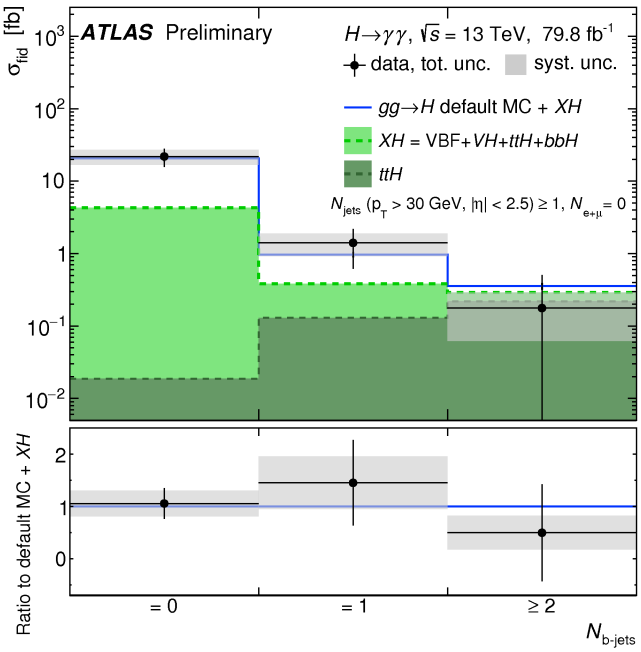

(a)

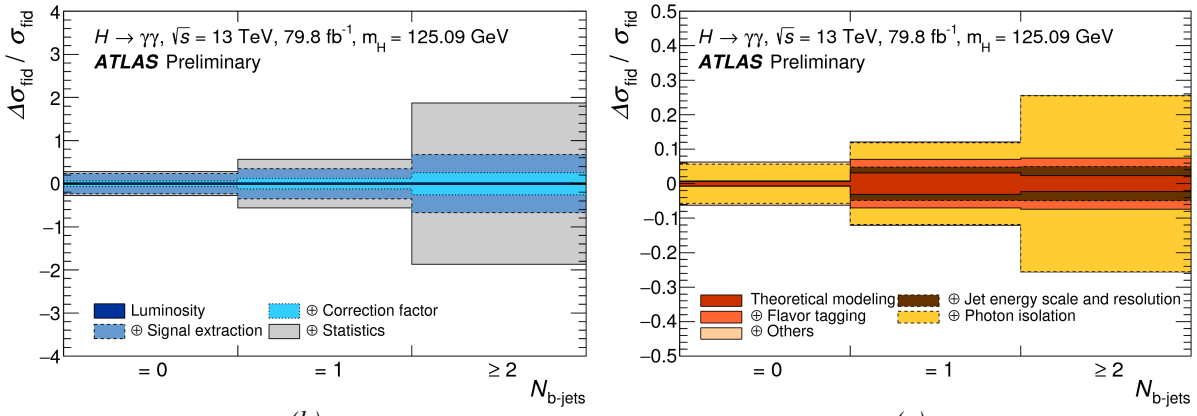

(b) *(c)*

Figure 5.8. | *(a)* Comparison of observed and predicted differential $H \to \gamma\gamma$ cross sections in $N_{b\text{–jets}}$. *(b)* Summary of uncertainties. *(c)* Breakdown of the correction factor uncertainty. Taken from Reference [171].

5.8. Summary

Using pp collision data corresponding to an integrated luminosity of 79.8/fb collected at a center-of-mass energy $\sqrt{s} = 13\,\text{TeV}$, inclusive and differential Higgs boson production cross sections have been measured in the $H \to \gamma\gamma$ decay channel. The considered fiducial phase-space volume is designed to be similar to the detector acceptance, resulting in only a small model dependence of the measurement. Using the bin-by-bin unfolding method, a correction for detector effects of

signal yields from the maximum-likelihood signal-plus-background fit has been performed. The work done within the context of this thesis was focused on the unfolding procedure.

The inclusive cross section for the production of Higgs boson decaying to a pair of photons has been measured to be

$$\sigma_{\text{fid}} = (60.4 \pm 6.1\,(\text{stat.}) \pm 6.0(\text{exp.}) \pm 0.3(\text{theo.}))\,\text{fb},$$

agreeing well with the SM prediction of $\sigma_{\text{fid}}^{\text{SM}} = (63.5 \pm 3.3)\,\text{fb}$. Similarly, the observed differential cross sections in the variables p_{T}^{H}, $p_{\text{T}}^{j_1}$, $|y_H|$, and $N_{b-\text{jets}}$ are also in good agreement with the corresponding SM predictions. For all differential cross sections, the statistical uncertainty is the dominant uncertainty contribution. In the inclusive cross section measurement, the systematic uncertainty is of similar size as the statistical uncertainty. Among systematic uncertainties, signal-extraction-related uncertainties typically largest. In all considered kinematic regions, the uncertainties from the unfolding procedure are relatively small.

6. Measurement of Heavy-Flavor Quark Yukawa Couplings

6.1. Introduction

Because differential cross sections are sensitive to certain model parameters, they can be used to set limits on these parameters. The distribution of the Higgs boson transverse momentum (p_{T}^{H}) is sensitive to the Yukawa couplings between the Higgs boson and quarks; therefore, it is possible to constrain those couplings by a fit to the measured p_{T}^{H} spectrum. This approach can be contrasted with more direct methods of coupling measurements in which events containing final-state quarks resulting from Higgs boson decays or from Higgs boson production in association with quarks are analyzed.

The Higgs boson is predicted to couple to quarks via a Yukawa interaction with a coupling proportional to the mass m_q of the quark flavor in consideration, $y_q^{\mathrm{SM}} = m_q/v$, where v denotes the vacuum expectation value of the Higgs field, see Section 2.3.2. Correspondingly, the Yukawa couplings of the quark types with the largest mass, i.e. the t- and b-quark have been measured most accurately.

6.1.1. Review of Recent Measurements of Quark Yukawa Couplings

The results of the most recent measurements of the t-quark's and the b-quark's coupling to the Higgs boson are well compatible with the SM predictions. In Reference [205], in which data corresponding to an integrated luminosity of 80/fb have been analyzed, the modifier for the t-quark Yukawa coupling,

$$\kappa_t = y_t/y_t^{\mathrm{SM}}, \tag{6.1}$$

has been measured to be $1.02^{+0.11}_{-0.10}$, assuming no beyond-SM decay channels of the Higgs boson. The b-quark Yukawa-coupling modifier

$$\kappa_b = y_b / y_b^{\mathrm{SM}} \tag{6.2}$$

has been determined to be $1.06^{+0.19}_{-0.18}$ in the same publication. In a more recent measurement [206] based on a dataset corresponding to an integrated luminosity of 139/fb using events in which the Higgs boson was produced in association with a $W^{\pm}$ or Z boson and decayed to a pair of b-quarks, the following signal strength was measured:

$$\mu = \frac{\sigma(pp \to VH) \times \mathcal{B}(H \to b\bar{b})}{\sigma_{\mathrm{SM}}(pp \to VH) \times \mathcal{B}_{\mathrm{SM}}(H \to b\bar{b})} = 1.02^{+0.18}_{-0.17},$$

where V corresponds to either the $W^{\pm}$ or the Z boson. Assuming SM couplings between the Higgs boson and the weak gauge bosons, $W^{\pm}$ and Z, this translates to $\kappa_b = 1.02^{+0.22}_{-0.21}$. In summary, both κ_t and κ_b are already well constrained by the Higgs boson couplings measurement and within uncertainties consistent with SM predictions.

The c-quark is a second-generation fermion, a class of particles whose Yukawa couplings are of particular interest after the measured Yukawa couplings of third-generation fermions such as t- and b-quarks as well as the τ lepton are so far consistent with SM predictions [205, 207, 208]. The precise measurement of the Yukawa coupling between fermions with a relatively low mass such as the c-quark and accordingly with a small expected coupling to the Higgs boson is more challenging than in the case of the b- or the t-quark. While the c-quark content in the proton is larger than the b-quark content due to the c-quark's lower mass, the c-quark Yukawa coupling is about $m_b/m_c = 3\,\mathrm{GeV}/0.65\,\mathrm{GeV}$ times smaller than the b-quark Yukawa coupling. Moreover, the tagging of c-jets, i.e. jets resulting from a final-state c-quark, is less efficient than the tagging of b-jets [194].

In References [209] and [210], measurements by the ATLAS and CMS collaboration, respectively, are described that constrain the c-quark Yukawa coupling using events containing pairs of reconstructed c-jets which are consistent with resulting from $H \to c\bar{c}$ decays. In the case of the ATLAS analysis, using a dataset corresponding to an integrated luminosity of 36/fb at

$\sqrt{s} = 13\,\text{TeV}$, the observed upper limit on the signal strength is

$$\mu = \frac{\sigma(pp \to ZH) \times \mathcal{B}(H \to c\bar{c})}{\sigma_{\text{SM}}(pp \to ZH) \times \mathcal{B}_{\text{SM}}(H \to c\bar{c})} < 110$$

at 95 % confidence level. The CMS analysis yields an observed upper limit on

$$\mu = \frac{\sigma(pp \to VH) \times \mathcal{B}(H \to c\bar{c})}{\sigma_{\text{SM}}(pp \to VH) \times \mathcal{B}_{\text{SM}}(H \to c\bar{c})} < 70,$$

using 36/fb of data collected at $\sqrt{s} = 13\,\text{TeV}$. These limits cannot be translated into limits on the c-quark Yukawa-coupling modifier,

$$\kappa_c = y_c / y_c^{\text{SM}}, \tag{6.3}$$

due to their weakness[1]. By analyzing larger datasets, this situation could be improved. However, it is possible to explore alternative ways of measuring the c-quark Yukawa coupling in parallel. A fit of the observed p_{T}^H spectrum in order to set limits on κ_c is such an alternative method. It appears natural to not limit such an alternative method of measuring quark Yukawa couplings to the c-quark. Its application to the Yukawa coupling of b-quarks, which has similar properties as the c-quark, accordingly is also part of this work.

6.1.2. Prediction Model

A measurement of κ_c and κ_b can be performed by comparing the observed p_{T}^H spectrum to predictions for a range of values of κ_c and κ_b. In order to obtain the necessary set of predictions, it is helpful to single out the Higgs boson production modes whose cross section is sensitive to the value of κ_c and κ_b. Only the p_{T}^H spectrum of gluon fusion and c- and b-quark-initiated Higgs boson production ($c\bar{c} \to H$, $b\bar{b} \to H$) depend on these couplings; for all other production modes, SM predictions can be used.

The observed p_{T}^H spectrum used for the fit is based on the combined 2015 – 2018 dataset in the $H \to \gamma\gamma$ decay channel [145]. Its measurement corresponds to an update of the measurement of the differential and inclusive cross sections as presented in Chapter 5 with a larger dataset

[1] In order to set an upper limit on κ_c, the corresponding upper limit on μ has to be smaller than $1/\mathcal{B}(H \to c\bar{c}) = 34.6$.

and slight modifications in the method. The measured cross sections correspond to Higgs boson production cross section multiplied with the $H \to \gamma\gamma$ branching ratio, $\sigma \times B_{\gamma\gamma}$. The $H \to \gamma\gamma$ branching ratio is sensitive to the specific couplings of the Higgs boson to many other particles. As one can deduce from Eq. (2.17), the $H \to \gamma\gamma$ branching ratio is sensitive to the $H \to \gamma\gamma$ decay width as well as to the sum of the decay widths of all other decay channels. This entails a sensitivity to a large number of model parameters; this sensitivity can be reduced by disregarding normalization information and taking into account exclusively information about the shape of the distribution in the fit. In order to achieve this, predictions for the p_{T}^{H} spectrum are normalized to the integrated cross section of the observed spectrum before fitting. Because the $H \to \gamma\gamma$ branching ratio is sensitive to κ_b and κ_c, the inclusion of normalization information would help to constrain these parameters, at the cost of a larger model dependence.

The normalized predicted cross section in a p_{T}^{H} bin with index i is given by

$$\begin{aligned}\sigma^{i}_{\mathrm{pred}}(\kappa_c, \kappa_b) = [&\sigma^{i}_{\mathrm{ggF}}(\kappa_c, \kappa_b) \cdot c^{\mathrm{ggF}}_{\mathrm{np},i} + \sigma^{i}_{b\bar{b}\to H}(\kappa_b) \cdot c^{b\bar{b}\to H}_{\mathrm{np},i} + \sigma^{i}_{c\bar{c}\to H}(\kappa_c) \cdot c^{c\bar{c}\to H}_{\mathrm{np},i} \\ &+ \sigma^{i}_{\mathrm{VBF}} + \sigma^{i}_{VH} + \sigma^{i}_{t\bar{t}H}] \cdot c_{\mathrm{norm}} \cdot c^{\mathrm{norm}}_{\mathrm{np}},\end{aligned} \tag{6.4}$$

where the factors $c^{\mathrm{pm}}_{\mathrm{np},i}$ take the nuisance parameter influence on the predicted spectrum for a given production mode into account; they correspond to

$$c_{\mathrm{np},i} = \prod_{\mathrm{j}} (1 + \lambda^{j}_{\mathrm{np}} \cdot \Delta^{j}_{\mathrm{np},i}). \tag{6.5}$$

Here, $\lambda^{j}_{\mathrm{np}}$ denotes the floating nuisance parameter with index j, which are constrained by Gaussian p.d.f.s. The parameters $\Delta^{j}_{\mathrm{np},i}$ denote the relative shift of the cross section in bin i that results from the variation of nuisance parameter j by one standard deviation from its mean value. The overall normalization factor, which is included for reasons of reduction of model dependence as explained above, is given by

$$c_{\mathrm{norm}} = \left(\sum_{\mathrm{bin\ i}} \sigma^{i}_{\mathrm{meas}} \right) / \sum_{\mathrm{bin\ i}} \sigma^{i}_{\mathrm{pred,\,unnorm}}. \tag{6.6}$$

The application of this factor results in the integrated cross section of the predicted p_{T}^{H} spectrum being equal to the observed spectrum, before an additional, freely floating normalization factor

$c_{\text{np}}^{\text{norm}}$ is included as a factor. The inclusion of the factor $c_{\text{np}}^{\text{norm}}$ improves the quality of the fit in the general case where the shape of the predicted spectrum is not identical with the shape of the observed spectrum.

The dependence of the gluon fusion cross section σ_{ggF} on κ_c and κ_b includes both linear and quadratic terms in these parameters. Quadratic terms result from the squaring of the gluon fusion amplitude, which contains the Yukawa coupling for the quark in the gluon fusion loop, in the cross section calculation. Linear terms result from interferences between gluon fusion processes in which different quark types are running in the gluon fusion loop. In the case of the $c\bar{c} \to H$ and $b\bar{b} \to H$ cross sections, no interference terms exist, resulting in a purely quadratic dependence on κ_c and κ_b, respectively. Combining the gluon fusion contributions, the quark-initiated contributions and all Higgs boson production contributions that are not sensitive to the values of κ_c an κ_b (σ_{other}), while assuming SM t-quark Yukawa coupling ($\kappa_t = 1$), one obtains an expression of the form

$$\begin{aligned}\sigma_{pp\to H}(\kappa_c, \kappa_b) &= \sigma_{\text{ggF}} + \sigma_{b\bar{b}\to H} + \sigma_{c\bar{c}\to H} + \sigma_{\text{other}} \\ &= c_{\text{ggF}}^{tt} + c_{\text{ggF}}^{tb} \cdot \kappa_b + c_{\text{ggF}}^{tc} \cdot \kappa_c + c_{\text{ggF}}^{bc} \cdot \kappa_b\kappa_c \\ &+ (c_{\text{ggF}}^{bb} + c_{b\bar{b}\to H}) \cdot \kappa_b^2 + (c_{\text{ggF}}^{cc} + c_{c\bar{c}\to H}) \cdot \kappa_c^2 + \sigma_{\text{other}}\,. \end{aligned} \tag{6.7}$$

The coefficients c_{ggF}^{qq}, $c_{\text{ggF}}^{qq'}$ correspond to the SM cross section contributions from gluon fusion, and the coefficients $c_{q\bar{q}\to H}$ to the SM cross section contributions from quark-initiated Higgs boson production.

If one varies either κ_c or κ_b individually and calculates the difference to the SM prediction in which $\kappa_c = \kappa_b = 1$, one obtains

$$\Delta\sigma = \sigma(\kappa) - \sigma_{\text{SM}} = a \cdot \left(\kappa + \frac{b}{2a}\right)^2 - \left(a + b + \frac{b^2}{4a}\right), \tag{6.8}$$

with $a = c_{\text{ggF}}^{qq} + c_{q\bar{q}\to H}$ and $b = c_{\text{ggF}}^{tq} + c_{\text{ggF}}^{bc}$. Accordingly, the difference in cross section relative to the SM prediction for a given bin corresponds to a quadratic function of the Yukawa-coupling modifier κ.

6.1.3. Treatment of Uncertainties

The fit of the p_{T}^{H} spectrum based on which limits are set on κ_c and κ_b is performed using the profile likelihood method as described in Section 6.3.1. Uncertainties are incorporated in two different approaches. The statistical and systematic uncertainties on the fitted p_{T}^{H} spectrum as well as theoretical uncertainties on the VH and $t\bar{t}H$ Higgs boson production contributions are taken into account by means of a covariance matrix. All uncertainties on the cross section contributions of gluon fusion and quark-initiated Higgs boson production are taken into account by nuisance parameters. These nuisance parameters are constrained by standard normal distributions, i.e. they are centered at 0 and have a standard deviation of 1. Details on the determination of the corresponding uncertainties are given in Section 6.2.

6.1.4. Fit Range

The low p_{T}^{H} region of the differential cross section is most sensitive to the value of κ_c and κ_b. It has been studied how the inclusion of higher bins of the p_{T}^{H} spectrum affects the sensitivity of the κ_c and κ_b fit; the result is shown in Figure 6.11 in Section 6.4.1. The benefits of including bins at higher p_{T}^{H} are relatively small, although not negligible. The computational effort to produce reliable spectrum templates and uncertainties grows with increasing p_{T}^{H} range as considerable larger numbers of events need to be simulated. As a result, it was decided to limit the fit to the p_{T}^{H} range from 0 GeV to 140 GeV for the present. For future studies, it is planned to take into account the full range in p_{T}^{H}.

6.2. Predictions

For the procedure of setting limits on κ_c and κ_b, it is necessary to be able to predict the p_{T}^{H} spectra for arbitrary values of κ_c and κ_b. In this section, the methods to predict such spectra and determine related theoretical uncertainties for gluon fusion and quark-initiated Higgs boson production are detailed.

6.2.1. Gluon Fusion

Gluon fusion predictions for the Higgs boson p_{T} spectrum have been provided by theorists [104, 105] for all combinations of the κ_c and κ_b values given in Table 6.1. These predictions can be

κ_c:	-10	-5	0	1	5	10
κ_b:	-2	-1	0	1	2	

Table 6.1. | Values for κ_c and κ_b for which gluon fusion predictions have been provided.

used to determine the coefficients c^{qq}_{ggF} and $c^{qq'}_{\mathrm{ggF}}$, $q, q' \in \{t, b, c\}$, introduced in Eq. (6.7): the predictions allow to construct an overconstrained set of equations of the form

$$\begin{aligned}\sigma_{\mathrm{ggF}} = {} & c^{tt}_{\mathrm{ggF}} \cdot \kappa_t^2 + c^{tb}_{\mathrm{ggF}} \cdot \kappa_t \kappa_b + c^{tc}_{\mathrm{ggF}} \cdot \kappa_t \kappa_c + c^{bc}_{\mathrm{ggF}} \cdot \kappa_b \kappa_c \\ & + c^{bb}_{\mathrm{ggF}} \cdot \kappa_b^2 + c^{cc}_{\mathrm{ggF}} \cdot \kappa_c^2 \end{aligned} \tag{6.9}$$

for each bin of the differential p^H_{T} distribution. These sets of equations were solved using a method of least squares, resulting in the above-mentioned coefficients. The coefficients c^{qq}_{ggF}, which correspond to the cross section contributions from gluon fusion processes with a quark of type q in the gluon fusion loop, are generally positive. The interference terms $c^{qq'}_{\mathrm{ggF}}$, on the other hand, can give both positive and negative contributions to the cross section. Numerical values for these coefficients are shown in Figure 6.1. Because the t-quark gluon fusion contribution is much larger than all other contributions, all contributions are scaled up for this plot such that the visibility of their features is improved. In all p^H_{T} bins, the dominant contribution to the ggF cross section results from the t-quark loop, i.e. the coefficient c^{tt}_{ggF}. The interferences of the t-quark gluon fusion loop with the b- and c-quark loop, denoted by c^{tb}_{ggF} and c^{tc}_{ggF}, are comparatively small, but not negligible. They are negative at p^H_{T} values below 80 GeV. The coefficients c^{bb}_{ggF}, c^{cc}_{ggF}, and c^{bc}_{ggF}, are very small.

The gluon fusion predictions for the individual combinations of κ_c and κ_b are computed using RadISH; see Section 2.6.4. For the renormalization, factorization and resummation scale, a central value of $m_H/2$ is assumed. The PDF set used for these predictions is PDF4LHC15_nnlo_mc.

In order to improve the accuracy of the predictions for the p^H_{T} spectra, they are multiplied with

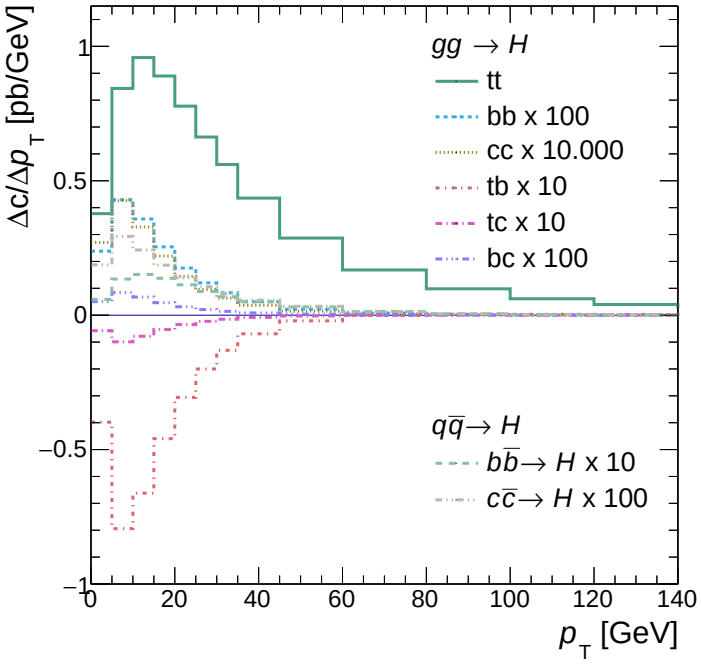

Figure 6.1. | Coefficients for gluon fusion contributions from different quark types in the gluon fusion loop in Eq. 6.9. Additionally, cross section contributions from the $c\bar{c} \rightarrow H$ and $b\bar{b} \rightarrow H$ Higgs boson production modes, described in Section 6.2.2, are shown. Coefficients with relatively small values are scaled up in order to facilitate a comparison.

a scaling factor

$$\sigma_{\mathrm{N^3LO}}/\sigma_{\mathrm{RadISH}}(\kappa_b = 1, \kappa_c = 1) = 1.165\,,$$

where $\sigma_{\mathrm{RadISH}}(\kappa_b = 1, \kappa_c = 1)$ denotes the total cross section of the RadISH prediction at SM parameter values, and $\sigma_{\mathrm{N^3LO}}$ to the inclusive cross section of the state-of-the-art gluon fusion prediction with $\mathrm{N^3LO}$ accuracy for the inclusive cross section, see Section 2.6.4.

The predictions are given for inclusive Higgs boson production in the gluon fusion production mode, its decay was not taken into account at that stage. Therefore, the SM $H \rightarrow \gamma\gamma$ branching ratio has been multiplied to the predicted cross sections. In order to achieve comparability with the observed p_{T}^H spectrum, which was measured in a fiducial phase-space defined by the kinematics and isolation of the photons (see Section 5.3.2), the inclusive gluon fusion predictions need to be corrected for the difference in considered phase-space volume. For this, it is assumed that the correction does not depend on the value of κ_c and κ_b. Ideally, one would derive such acceptance corrections as a function of κ_c and κ_b, but the calculations necessary for this are lacking. The acceptance corrections are determined using the nominal NNLOPS ggF simulation,

see Section 2.6.4, and are shown as a function of p_{T}^{H} in Figure 6.2.

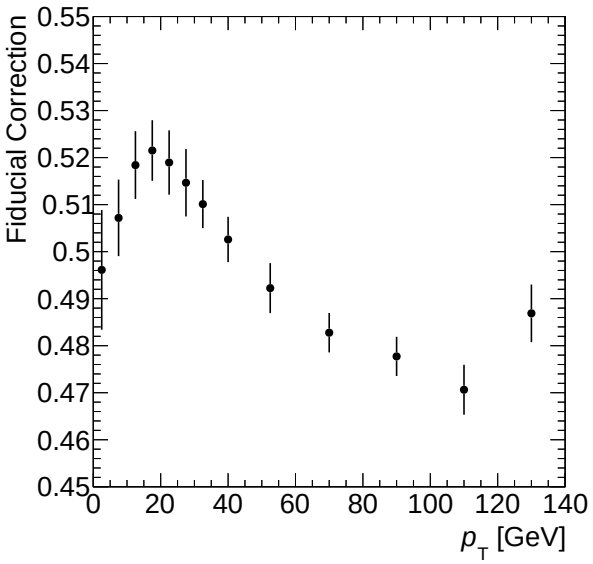

Figure 6.2. | Phase-space corrections to be applied to RadISH predictions as derived from the NNLOPS gluon fusion simulation. The fiducial selection includes requirements on the photon transverse momentum, photon pseudorapidity, and photon isolation. The shown error bars correspond to a combination of PDF uncertainties and uncertainties due to missing higher orders of QCD calculation.

The upper and lower limits of the provided prediction for the p_{T}^{H} spectrum are 0.5 GeV and 245 GeV, respectively. Based on the nominal NNLOPS ggH simulation, this has been extrapolated to 0 GeV and 250 GeV, respectively, in order to be consistent with bin boundaries in the measured p_{T}^{H} distribution.

Uncertainties

The gluon fusion predictions have uncertainties due to the imperfect knowledge of the proton PDF as well as due to missing higher-orders of the QCD calculation. The phase-space corrections for the gluon fusion prediction are subject to these types of uncertainties as well. Correlation between the uncertainties on the phase-space corrections and the cross section predictions in an inclusive phase-space volume are not known; they are treated as uncorrelated in this measurement.

Perturbative uncertainties for the gluon fusion prediction are estimated through variations of the renormalization scale μ_{R}, the factorization scale μ_{F}, and the resummation scale Q around the central value of $m_H/2$. The correlation scheme between the three scale variations has been chosen such that the resulting uncertainty is maximal, corresponding to a simultaneous variation of the renormalization and factorization scales. The resummation scale is varied independently

of the other two scales. In Figure 6.3a the relative effects of corresponding scale variations by factors of 1/2 and 2 are shown. For each value of κ_b and κ_c, the scale variations lead to slightly different relative differences between the nominal cross sections and the cross sections based on varied scales. Among those different values for the relative differences from scale variations at different κ_b and κ_c values, the maximal value is chosen in order to obtain a conservative uncertainty estimate.

The PDF-related uncertainty of the RadISH gluon fusion prediction is estimated using the NNLOPS ggF simulation, which is warranted because the same PDF set is used in both predictions. Uncertainties on the proton PDF are encapsulated in 30 eigenvectors of the covariance matrix of the parameters that describe the PDFs [184, 211]. By repeating the PDF fit on the input data with varied parameters according to the direction in parameter space of these orthogonal eigenvectors, variations of the best-fit PDF set are derived and are accessible in the NNLOPS ggF sample. The relative differences between the differential cross section as computed with the nominal PDF set and the differential cross sections as computed with the varied PDF set serve as input to the overall PDF uncertainty on the measurement of κ_c and κ_b. Not all of these variations, however, lead to significant changes in the differential cross section. The three PDF eigenvectors resulting in the largest deviations from the nominal prediction enter the analysis; see Figure 6.3b for the corresponding relative differences which are used as uncertainties in the κ_c and κ_b fit.

The correction factors that are used to render the ggF predictions comparable to the measured differential cross section, which are given in a fiducial phase-space volume, are derived from the nominal NNLOPS gluon fusion simulation. They are subject to theoretical uncertainties related to missing higher orders of the QCD calculation and to PDF uncertainties. The combined uncertainties are shown as error bars in Figure 6.2.

Bringing the three considered uncertainty contributions to the gluon fusion differential cross section in a fiducial volume into relation to each other, the QCD-scale-related uncertainties dominate, having relative uncertainties of approximately 20 % at larger values of p_{T}^{H} and approximately 10 % at low p_{T}^{H}. The PDF uncertainties on the differential cross section in an inclusive phase-space volume and the combined uncertainties on the phase-space corrections are of the order $O(1\,\%)$.

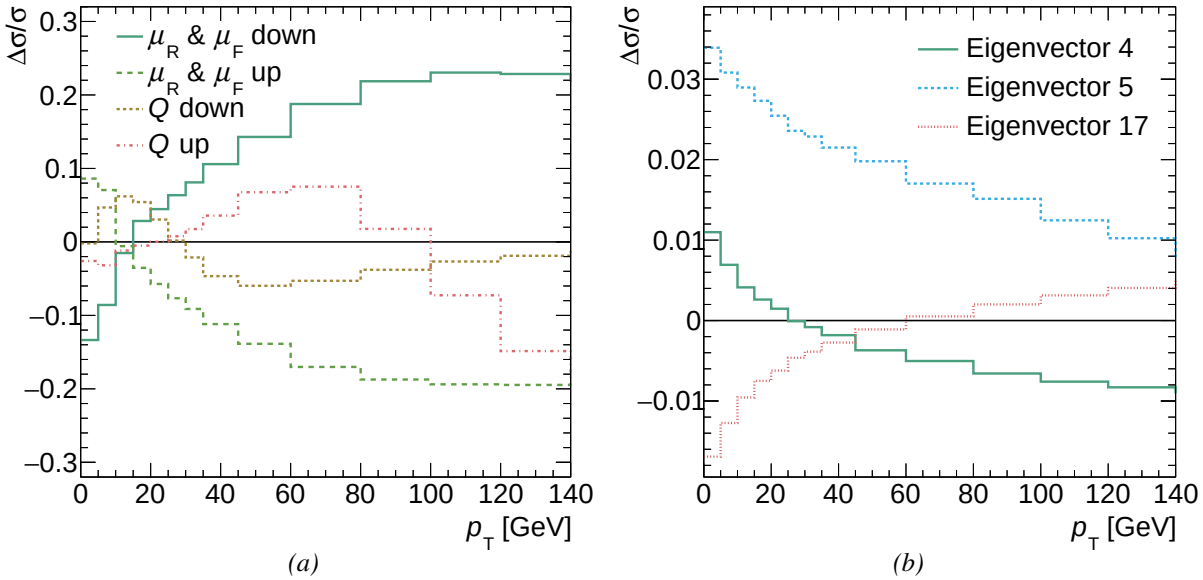

Figure 6.3. | (a) QCD-scale-related uncertainty contributions to the gluon fusion differential cross section. The renormalization and factorization scales μ_R and μ_F are varied simultaneously, while the resummation scale Q is varied independently. (b) PDF-related uncertainty contributions to the gluon fusion differential cross section.

6.2.2. Quark-Initiated Higgs Boson Production

The dependence of the $c\bar{c} \to H$ and $b\bar{b} \to H$ differential cross sections on the Yukawa couplings between the Higgs boson and the c- and b-quark, respectively, is less complicated than in the case of gluon fusion. The $c\bar{c} \to H$ and $b\bar{b} \to H$ cross sections simply scale with κ_c^2 and κ_b^2, respectively. In Section 2.6.5 some aspects of the cross section calculation for the quark-initiated Higgs boson production are discussed. Because the SM cross section prediction for the $c\bar{c} \to H$ process is small, this process was not included in the central ATLAS simulation production. Therefore, c-quark-initiated Higgs boson production had to be simulated in a separate setup. For reasons of consistency, the b-quark-initiated Higgs boson production was simulated in the same, separate setup. The event generator was chosen to be MadGraph5_aMC@NLO [113], which was interfaced to the Pythia8 parton shower simulation, which also was used to simulate the decay of the Higgs boson to a pair of photons. Processes of LO and NLO in QCD are accounted for by the event generator; see Figures 6.4a and 6.4b for the contributing diagrams at LO and NLO, respectively. The PDF set used for the $c\bar{c} \to H$ and $b\bar{b} \to H$ cross section computation is a variant of the `PDF4LHC15_nnlo_mc` PDF set with an improved description of the b-quark PDF, and was obtained from Reference [212]. The central values for the renormalization scale and

the factorization scale have been chosen to be $m_H/2$ and $m_H/4$, respectively. In order to obtain predictions for differential cross sections in a fiducial volume, the generated and showered events are input to a Rivet routine [213], in which the fiducial selection criteria as given in Section 5.3.2 are applied at event level and in which the binning in p_{T}^H is defined.

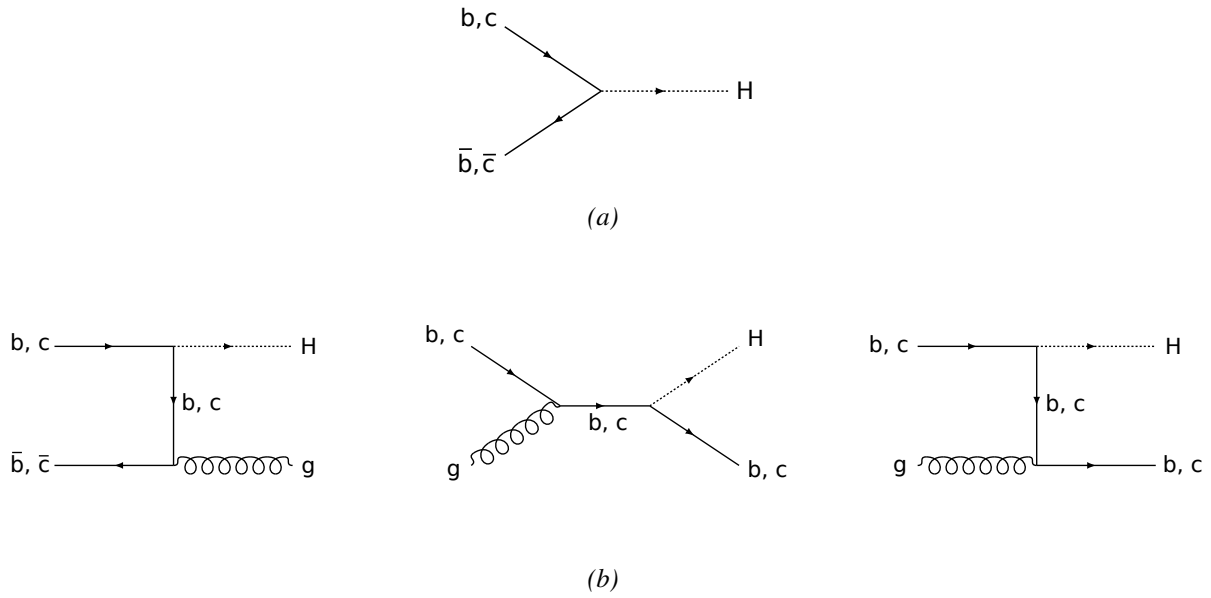

Figure 6.4. | b- and c-quark-initiated Higgs boson production diagrams in the 5FS at LO *(a)*, and NLO *(b)*.

The result for the inclusive cross section of c-quark-initiated Higgs boson production from this simulation setup is $(0.0813 \pm 0.0002)\,\mathrm{pb}$, assuming $\kappa_c = 1$ and not taking into account the $H \to \gamma\gamma$ branching ratio. In an inclusive state-of-the-art computation at NNLO [64], the cross section is predicted to be

$$\sigma_{c\bar{c}\to H} = 1.64 \cdot \frac{m_c^2}{m_b^2} \pm 4.9\,\%(\text{perturbative}) \pm 2.4\,\%(\text{PDF})\,\text{pb}.$$

The quark masses that were set as parameters in the MadGraph5_aMC@NLO simulation are $m_b = 3.0\,\mathrm{GeV}$ and $m_c = 0.65\,\mathrm{GeV}$. These values correspond to the 3-loop running quark masses at a scale of $m_H/2$ in the $\overline{\mathrm{MS}}$ renormalization scheme [214–216], with $m_b(m_b) = 4.18\,\mathrm{GeV}$ and $m_c(3\,\mathrm{GeV}) = 0.65\,\mathrm{GeV}$. Evaluating Eq. (6.2.2) with these values leads to a predicted cross section of $(0.077 \pm 0.004)\,\mathrm{pb}$. In order to improve the accuracy of the MadGraph5_aMC@NLO prediction, which is at NLO, the cross section from the simulation is scaled with a factor $\sigma_{\mathrm{NNLO}}/\sigma_{\mathrm{NLO}} = 0.077\,\mathrm{pb}/0.0813\,\mathrm{pb}$ such that the integrated cross section matches the NNLO

state-of-the-art prediction, which is only available inclusively.

The $b\bar{b} \to H$ differential cross section from MadGraph5_aMC@NLO, which corresponds to an inclusive cross section of 0.55 pb, is normalized to the state-of-the-art prediction [63]

$$\sigma_{b\bar{b}\to H} = 0.529 \pm 9.7\,\%(\text{perturbative})\, ^{+2.2\,\%}_{-3.0\,\%}(\text{parametric})\,\text{pb}.$$

The resulting differential cross sections in p_{T}^{H} for the $c\bar{c} \to H$ and $b\bar{b} \to H$ production modes are shown in Figure 6.1 in comparison with the gluon fusion contributions. As one can see, quark-initiated Higgs boson production cross sections are significantly smaller than the gluon fusion cross section at SM parameter values. Due to the quadratic dependence on κ_c and κ_b, however, the relative size can change considerably when values of κ_c or κ_b very different from $\kappa_{\mathrm{SM}} = 1$ are considered. In Figure 6.13 in Section 6.4.2, a comparison of spectra at different values of κ_c and κ_b is shown.

Uncertainties

The predicted cross sections for the $c\bar{c} \to H$ and $b\bar{b} \to H$ processes are subject to uncertainties due to missing higher orders of the perturbative expansion in α_s, PDF-related uncertainties, as well as an uncertainty related to the parton shower simulation.

In order to assess the uncertainty related to missing higher orders of the QCD calculation, variations of the renormalization and factorization scales around their central values by factors of 1/2 and 2 are performed. As in the case of gluon fusion, both scales are varied simultaneously up and down. The differences between the differential cross section at the nominal scale choice and the differential cross section at the varied scales are used as uncertainty. The result can be seen in Figure 6.5a for the $c\bar{c} \to H$ prediction and in Figure 6.5b for the $b\bar{b} \to H$ prediction. Typically, these uncertainties are in the range from 5 % to 20 %. Effects of statistical fluctuations on the uncertainties at higher p_{T}^{H} values are apparent, related to the fact that Higgs bosons in $c\bar{c} \to H$ and $b\bar{b} \to H$ events tend to have low transverse momenta. For future measurements it is planned to extend the sample size of simulated $b\bar{b} \to H$ and $c\bar{c} \to H$ events, which would result in reduced statistical uncertainties on the estimate of the theoretical uncertainties.

The PDF-related uncertainty for the $c\bar{c} \to H$ prediction is assessed using 100 variations included in the PDF set. These 100 variations are derived from 100 artificial datasets that have been generated using a Monte Carlo method from the input data for the PDF determination [184,

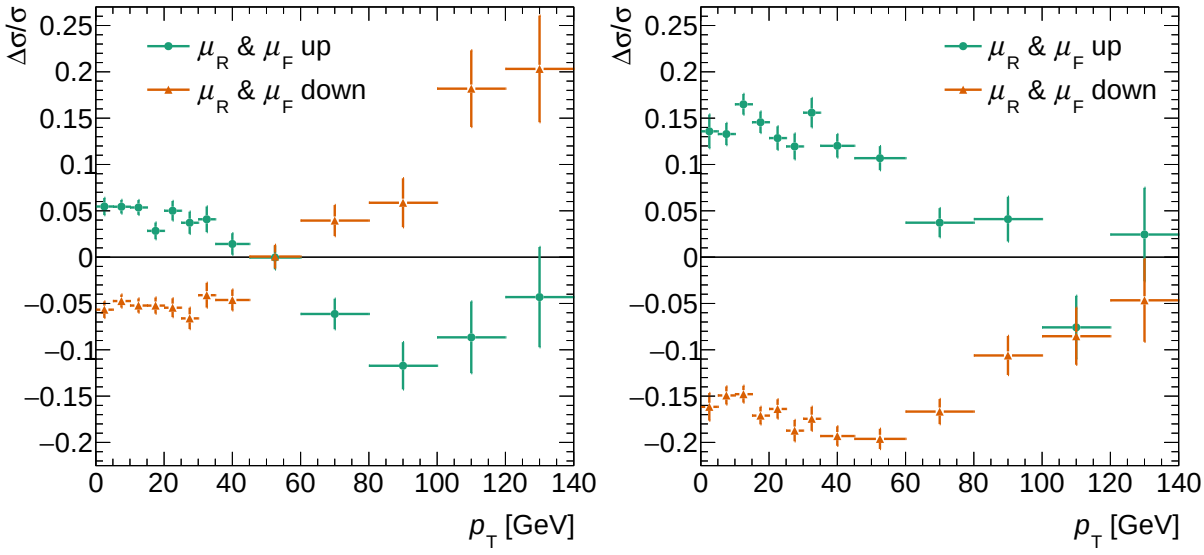

Figure 6.5. | Uncertainties due to missing higher orders in α_s on the differential cross section of c-quark-initiated Higgs boson production *(a)* and b-quark-initiated Higgs boson production *(b)*. Error bars show the statistical uncertainty due to a limited size of the simulated event sample.

217–219]. The uncertainty for a p_{T}^{H} bin i is given by the standard deviation of the cross sections that result from the application of the $N = 100$ PDF variations:

$$\Delta\sigma_i = \sqrt{\frac{1}{N-1}\sum_{j=1}^{100}(\sigma_i^j - \langle\sigma_i\rangle)^2}\,, \tag{6.10}$$

where σ_i^j is the cross section resulting from the PDF variation j, and $\langle\sigma_i\rangle$ is the mean of the cross section σ_i considering all PDF variations. An uncertainty related to the effect of the value of α_s on the PDFs is determined by computing the relative difference in differential cross sections between the cases in which the lower bound on $\alpha_s(m_Z)$ of 0.1165 is used and in which the upper bound of 0.1195 is used, divided by 2. The uncertainties from the PDF variations and from the α_s variations are added in quadrature. The result, amounting typically to about 3 %, is shown in Figure 6.6a, in which the statistical uncertainty on the estimated PDF-related uncertainty is indicated by error bars and is considerable at high p_{T}.

In the case of the $b\bar{b} \to H$ predictions, the major contribution to the uncertainty of the b-quark PDF is not captured reliably by the PDF variations as used for the c-quark PDF uncertainty. Therefore, an alternative method of uncertainty estimation has been used for the $b\bar{b} \to H$

prediction: the b-quark PDF is a quantity that is computed perturbatively, and the corresponding calculation involves the mass of the b-quark, m_b, as well as the energy scale above which the b-quark PDF is assumed to be non-vanishing, μ_b. The central value for these two parameters is assumed to be 4.58 GeV. Both m_b and μ_b are known only with limited precision, and the impact of this uncertainty on the cross section is propagated by explicit variations of m_b and μ_b in the PDF set. The scale μ_b is varied by factors of 1/2 and 2. In the case of m_b, the variation consists in the addition and subtraction of 4 MeV, corresponding to the uncertainty on the b-quark mass. In Figure 6.6b, the envelopes of the relative differences to the nominal $b\bar{b} \to H$ cross section are shown for both variation types. Both uncertainties are of the order of several percent. The uncertainty based on the variation of μ_b tends to be larger than that from the variation of m_b. The impact of statistical fluctuations is considerable, particularly at high p_{T}^H.

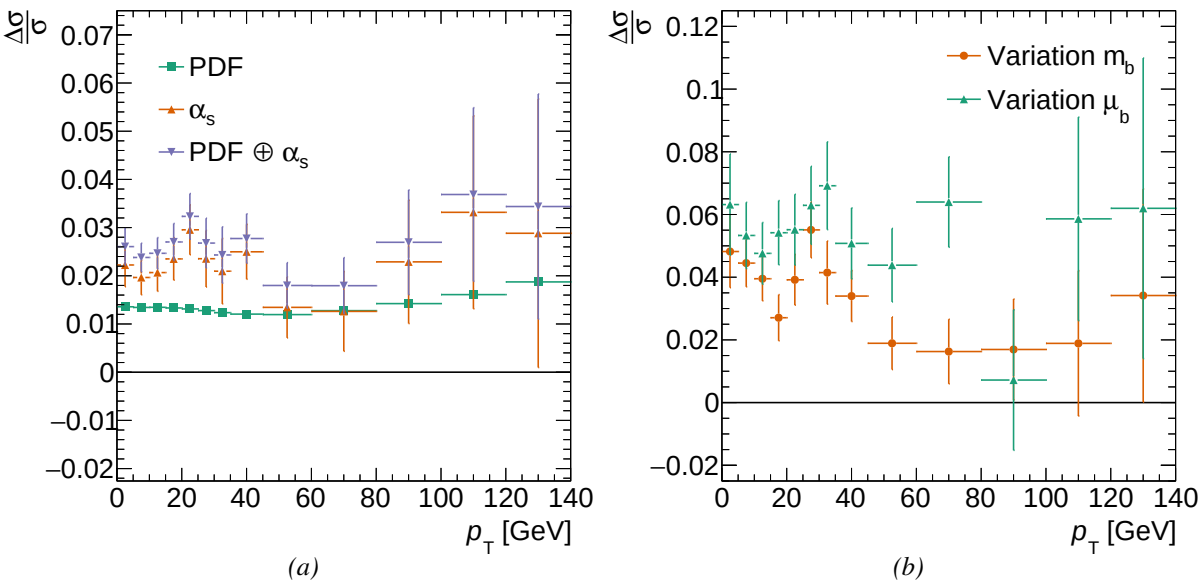

Figure 6.6. | *(a)* PDF-related uncertainty on the differential cross section of c-quark-initiated Higgs boson production. The uncertainties from the PDF variations and from the α_s variation are added quadratically. *(b)* PDF-related uncertainty on the differential cross section of b-quark-initiated Higgs boson production. These uncertainties are determined by comparing the nominal predicted p_{T}^H spectrum with a prediction in which m_b or μ_b in the PDF computation are varied. The relative uncertainties correspond to the envelopes of the up- and down-variations. Error bars indicate the statistical uncertainty due to a limited size of the simulated sample.

Additionally, an uncertainty related to the modeling of the parton shower is considered. The parton shower simulation involves the use of a variety of parameters that encapsulate perturbative and non-perturbative aspects of the showering. A number of observables are used to estimate

appropriate values for these parameters. Examples for these observables are the Z-boson p_{T} spectrum, the distribution of the azimuthal angle between the leading and sub-leading jets, and the fraction of $t\bar{t}$ events in which no jet above a given p_{T} threshold is present in a given rapidity region. The choice for the Pythia8 parameter set (*tune*) in this work is called `A14`. For this tune, five systematic variations are available [182], two of which lead to considerable differences in the differential cross section relative to the nominal tune in the $b\bar{b} \to H$ and $c\bar{c} \to H$ predictions, denoted by *3b* and *3c*. These two *eigentunes* contain varied values for the strong coupling constant α_s as well as for parameters used in the showering of initial- and final-state partons. The *3b* variation contains, besides varied values for the strong coupling constant in both initial- and final-state shower, parameters that modify the matching of emissions described by the matrix element and those that are generated in the parton shower. Variation *3c* consists of a variation in the strong coupling constant used in the initial-state showering.

The resulting uncertainties, corresponding to the difference in differential cross section between the predictions based on the nominal and varied parameter sets, are shown in Figure 6.7a for $c\bar{c} \to H$ and in Figure 6.7b for $b\bar{b} \to H$ predictions. Particularly at low p_{T} the corresponding uncertainty is sizable, being close to 20 % in the case of the *3c* variation.

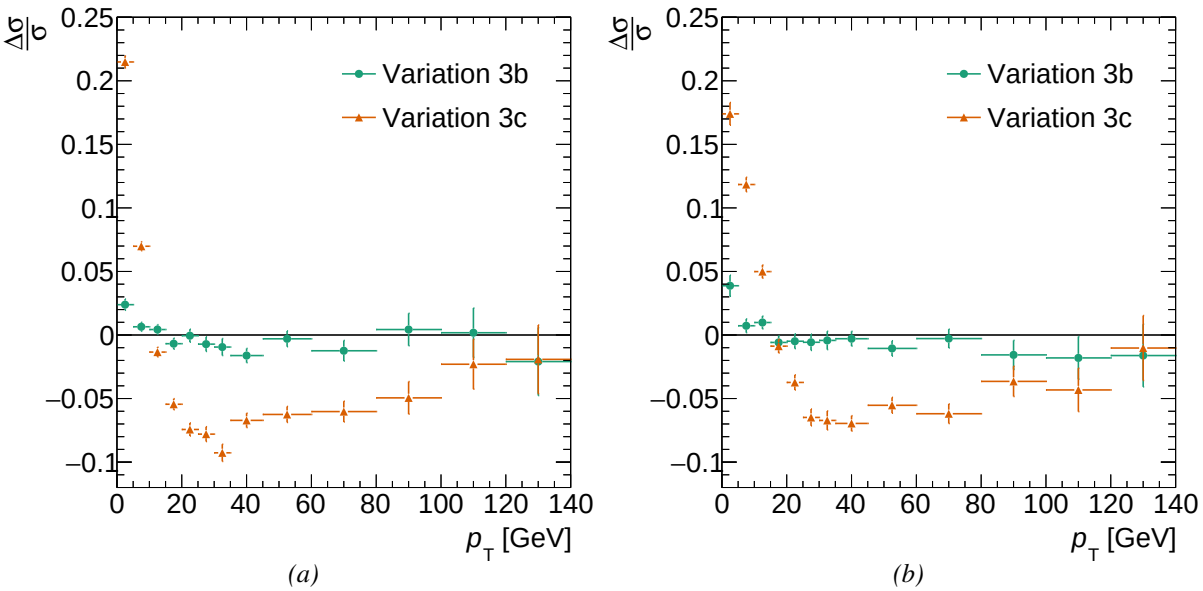

Figure 6.7. | Parton-shower-related uncertainty on the differential cross section of c-quark-initiated Higgs boson production *(a)* and b-quark-initiated Higgs boson production *(b)*. This uncertainty is estimated by comparing the prediction resulting from the nominal Pythia8 parameter set with predicted spectra resulting from systematically varied parameter sets. Error bars indicate the statistical uncertainty due to a limited size of the simulated sample.

6.3. Limit Setting Procedure

Given a way of predicting the fiducial differential Higgs boson production cross section for arbitrary values of κ_c and κ_b, a scan over a range of κ_c or κ_b can be performed, comparing the corresponding predictions with the observed differential cross section. Using a *profile likelihood method*, exclusion intervals can be determined based on the level of agreement between prediction and measurement [220, 221].

6.3.1. The Profile Likelihood Method

In the following explanation of the basic principle of the profile likelihood method, μ and θ denote the collections of parameters of interest and nuisance parameters, respectively. The likelihood of observing a differential cross section consisting of n observed cross sections σ_i in p_{T}^{H} bins indexed with i is given by:

$$\mathcal{L}(\vec{\sigma}\,|\mu,\theta) = \sum_{i=1}^{n} \log f_i(\sigma_i\,|\mu,\theta)\,, \tag{6.11}$$

The p.d.f. according to which the random variable σ_i is distributed is denoted by $f_i(\sigma_i\,|\mu,\theta)$ and depends on the model parameters μ and θ. It contains the prediction model, which in this context is given by Eq. (6.4). The width of the p.d.f. depends on the statistical and systematic uncertainties of the measured differential cross section and the theoretical uncertainties encapsulated by the nuisance parameters.

A commonly used approach to determine best-fit values and confidence intervals for parameters of interest is to *profile out* the nuisance parameters. The best-fit value for the parameter of interest μ is then given by:

$$\hat{\mu} = \arg\max_{\mu} \left\{ \max_{\theta} \{\mathcal{L}(\vec{\sigma}\,|\mu,\theta)\} \right\}. \tag{6.12}$$

This corresponds to the profile likelihood method, which is used in this measurement. An illustration of the principle is shown in Figure 6.8. For each scanned value of the parameter of interest μ, a separate likelihood scan over the nuisance parameter θ is performed, and the maximum likelihood from this separate scan over θ corresponds to the likelihood value for the considered value of μ. The value $\hat{\mu}$ at which this profiled likelihood is maximal is considered to

be the best-fit value for μ.

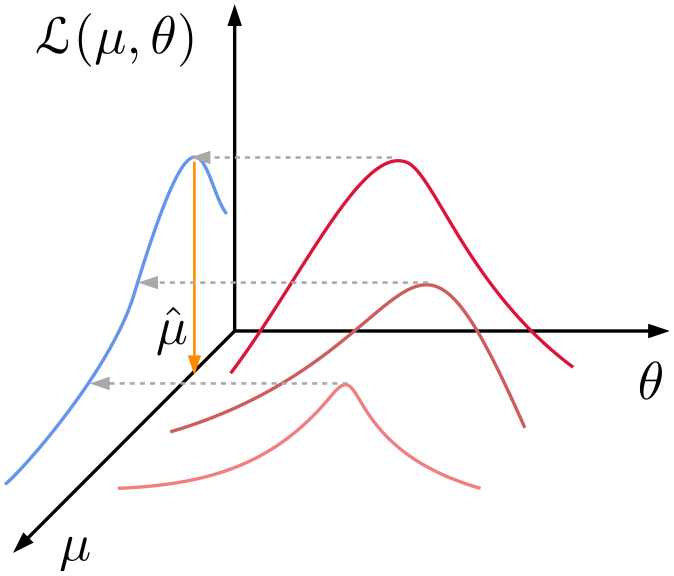

Figure 6.8. | Illustration of the parameter estimation in the profile likelihood method. The nuisance parameter is labeled θ, and the parameter of interest is labeled μ. The likelihood $\mathcal{L}$ is a function of θ and μ. The blue curve, which is the basis for the estimation of the best-fit value of μ, corresponds to the mapping of the term $\max_\theta\{\mathcal{L}(\vec{\sigma}|\mu, \theta)\}$ in Eq. 6.12.

Because likelihoods as defined in Eq. (6.11) tend to have very small values, which can lead to accuracy problems in floating-point number arithmetic performed by computers, it is useful to perform the fit using the negative logarithm of the likelihood:

$$\chi^2(\vec{\sigma}|\mu, \theta) := -2 \ln \mathcal{L}(\vec{\sigma}|\mu, \theta). \tag{6.13}$$

In the process of setting confidence intervals on the fitted parameters, it is helpful to consider the following quantity as the figure of merit, called the *log-likelihood ratio*:

$$\begin{aligned} \Delta\chi^2(\vec{\sigma}|\mu, \theta) &:= \chi^2(\vec{\sigma}|\mu, \hat{\hat{\theta}}(\mu)) - \chi^2(\vec{\sigma}|\hat{\mu}, \hat{\theta}) \\ &= -2\left[\ln \mathcal{L}(\vec{\sigma}|\mu, \hat{\hat{\theta}}(\mu)) - \ln \mathcal{L}(\vec{\sigma}|\hat{\mu}, \hat{\theta})\right] \\ &= -2 \ln \frac{\mathcal{L}(\vec{\sigma}|\mu, \hat{\hat{\theta}}(\mu))}{\mathcal{L}(\vec{\sigma}|\hat{\mu}, \hat{\theta})}, \end{aligned} \tag{6.14}$$

where $\mathcal{L}(\vec{\sigma}|\mu, \hat{\hat{\theta}})$ denotes the likelihood of observing the data $\vec{\sigma}$ assuming that the tested value of μ and the best-fit value of θ at that value of μ are the true parameter values. $\mathcal{L}(\vec{\sigma}|\hat{\mu}, \hat{\theta})$ corresponds to the likelihood of observing the data $\vec{\sigma}$ assuming that the best-fit values of the parameters

μ and θ are the true values, which corresponds to the maximally possible likelihood in the fit. Therefore, the quantity $\Delta\chi^2(\vec{\sigma}|\mu,\theta)$ is a measure of how much less likely an observation is when assuming a value of μ instead of the best-fit value $\hat{\mu}$. Having determined the value of $\Delta\chi^2(\vec{\sigma}|\mu,\theta)$ for a given value of μ (and θ) and observations $\vec{\sigma}$, it can be decided whether these parameters can be excluded with a certain level of confidence. Often, a 95 % *confidence level* (CL) is chosen; this standard is adapted also in this measurement. In order to decide whether a given value of $\Delta\chi^2(\vec{\sigma}|\mu,\theta)$ can be excluded at 95 % CL, the expected distribution of $\Delta\chi^2(\vec{\sigma}|\mu,\theta)$ at the considered value for μ is needed, denoted $g(\Delta\chi^2(\vec{\sigma}|\mu,\theta))$. Based on this distribution it can be determined how probable it is that, assuming the probed value of μ is the true parameter value, a $\Delta\chi^2(\vec{\sigma}|\mu,\theta)$ equal or larger than the observed value $\Delta\chi^2(\vec{\sigma}|\mu,\theta)_{\text{obs}}$ occurs in a measurement. This is called the p-value, and can be computed using the following equation:

$$p-\text{value} = \int_{\Delta\chi^2_{\text{obs}}}^{\infty} g(\Delta\chi^2)\ \mathrm{d}(\Delta\chi^2)\,. \tag{6.15}$$

If for a probed value of μ this probability is below $1-\text{CL} = 1-0.95 = 0.05$, that value is said to be excluded at 95 % CL.

The outcome of the profile likelihood method depends to some extent on how the distribution $g(\Delta\chi^2)$ is estimated. In this work, the profile likelihood method is applied using two different choices of $g(\Delta\chi^2)$. The GammaCombo framework, which is used (version 1.0) for the measurement of κ_c and κ_b, provides an implementation for both choices [222, 223].

6.3.2. Distribution of the Log-Likelihood Ratio

One method to estimate the distribution $g(\Delta\chi^2(\vec{\sigma}|\mu,\theta))$ of the log-likelihood ratio is based on the *asymptotic approximation*, where the log-likelihood ratio $\Delta\chi^2(\vec{\sigma}|\mu,\theta)$ as defined in Eq. (6.14) is assumed to be distributed according to a χ^2 distribution with a number of degrees of freedom equal to the number of fitted parameters of interest [224]. This simplifying assumption is warranted in the large sample limit and if the tested parameter values are not close to possible boundaries of the model. By assuming that $\Delta\chi^2(\vec{\sigma}|\mu,\theta)$ follows a nominal χ^2 distribution, the process of estimating confidence intervals is greatly simplified: in this case, one can rely on the easily accessible cumulative density function of the nominal χ^2 distribution for the computation

of the p-value.

However, the actual distribution of the log-likelihood ratio may deviate significantly from the nominal χ^2 distribution. Therefore, it is advantageous to estimate the actual distribution $g(\Delta\chi^2(\vec{\sigma}|\mu,\theta))$ for a given parameter value by creating numerous pseudo-experiments, also called *toys*. Each of these pseudo-experiments is created by drawing random numbers according to the p.d.f. in Eq. (6.11), where the parameter of interest is set to the considered value for μ. The mean values of the nuisance parameters in the pseudo-experiments are set to the best-fit value for the considered value of μ based on the observed data, i.e. the profile likelihood point. As it is illustrated in Figure 6.8, for a fixed value of μ, the profile likelihood point $\hat{\hat{\theta}}$ corresponds to the θ-value at which the likelihood is maximal, i.e.

$$\hat{\hat{\theta}}(\mu) = \arg\max_{\theta} \mathcal{L}(\vec{x}|\mu,\theta)\,. \tag{6.16}$$

For each of the pseudo-experiments, the log-likelihood ratio for the observation of the result of the pseudo-experiment is determined. It is given by the difference between the log-likelihood of observing the toy result when a) assuming that the tested value of μ is the true value, and b) assuming that the best-fit value for μ for the pseudo-experiment, $\hat{\mu}_{\text{toy}}$, is the true value:

$$\Delta\chi^2_{\text{toy}}(\mu) = \chi^2(\vec{x}_{\text{toy}}|\mu,\hat{\hat{\theta}}_{\text{toy}}) - \chi^2(\vec{x}_{\text{toy}}|\hat{\mu}_{\text{toy}},\hat{\theta}_{\text{toy}})\,. \tag{6.17}$$

By computing this quantity for many pseudo-experiments, the distribution $g\left(\Delta\chi^2(\vec{\sigma}|\mu,\theta)\right)$ can be estimated.

While the pseudo-experiment-based method is computationally more demanding than the method based on the asymptotic approximation, it has better *coverage* properties. The coverage probability is defined as the probability that the estimated confidence interval contains the true parameter value [163]. This means that if the experiment and the analysis would be repeated many times, in a fraction of experiments equal to the coverage probability the estimated confidence intervals would contain the true value for μ. The nominal probability for the estimated confidence interval containing the true value is equal to the confidence level, e.g. 95 %. However, the actual coverage probability of the used method may deviate from this value. The smaller the difference between the nominal coverage probability and the actual coverage probability, the better the

coverage of the method. Because in the pseudo-experiment-based method less simplifying assumptions are made than in the method of asymptotic approximation, the coverage of the former is better than that of the latter. It should be mentioned, however, that also the pseudo-experiment-based method has not necessarily perfect coverage properties, because the nuisance parameter values in the pseudo-experiments are generated based on p.d.f.s that are centered at the profile likelihood point.

6.4. Results

Based on the prediction model and the limit-setting procedure as laid out in the previous sections, a fit of κ_c and κ_b was performed based on the p_{T}^{H} spectrum as measured with the 2015 - 2018 dataset; that measurement is detailed in Reference [145] and corresponds to an updated version of what has been presented in Chapter 5. In addition to one-dimensional fits in κ_c and κ_b individually, in which κ_b and κ_c were fixed to 1, respectively, a two-dimensional fit in κ_c and κ_b has been performed. First, the expected results based on an Asimov dataset [225] derived from the SM predictions are shown, followed by the results based on the observed p_{T}^{H} spectrum. The results from the two different methods of estimating the $\Delta\chi^2$ distribution as described in Section 6.3.2 are compared. Fits that have been performed using pseudo-experiments for that estimation were based on 1000 generated pseudo-experiments. Confidence intervals are given at 95 % CL. In the case of one-dimensional fits of either κ_c or κ_b, the corresponding 95 % CL quantile corresponds to $\Delta\chi^2 = 3.84$. For two-dimensional fits in κ_c and κ_b, the exclusion contours are defined by the corresponding 95 % CL quantile $\Delta\chi^2 = 5.99$ [163].

As can be seen in Figures 6.3a and 6.5, the uncertainties from up- and down-variations of QCD scales, which are used to estimate uncertainties due to missing higher orders in α_s, are not exactly anti-symmetric relative to each other, i.e. $\Delta\sigma(\mu \text{ up}) \neq -\Delta\sigma(\mu \text{ down})$, where μ represents the varied QCD scales. Therefore, uncertainties from both up- and down-variations are included, each associated with its own nuisance parameter. In order to avoid double-counting these uncertainties, they are scaled by a factor of $1/\sqrt{2}$.

6.4.1. Expected Results

In order to obtain the expected limits on κ_c and κ_b, an Asimov dataset has been constructed from the SM prediction, using uncertainties based on a previous measurement of the differential cross section in p_{T}^H using the 2015 – 2017 dataset [171]. In order to make this Asimov dataset comparable to the observed distribution, which is based on an increased amount of collected data, the statistical uncertainties of the Asimov dataset are scaled by a factor of

$$\sqrt{\frac{\mathrm{L}_{\mathrm{int},2015-2017}}{\mathrm{L}_{\mathrm{int},2015-2018}}} = \sqrt{\frac{79.8/\mathrm{fb}}{139.0/\mathrm{fb}}}. \tag{6.18}$$

Based on the expected differential cross section, the expected 95 % CL limits on κ_c and κ_b have been determined; they are listed in Table 6.2 for both methods of estimating the $\Delta\chi^2$ distribution. The limits from both methods are in good agreement. Generally, the expected constraints on κ_b

	κ_c	κ_b
Asymptotic approximation	[-15.1 , 19.1]	[-4.6 , 10.2]
Pseudo-experiments	[-15.1 , 19.0]	[-4.6 , 10.8]

Table 6.2. | Expected confidence intervals at 95 % CL for κ_c and κ_b based on different fit methods.

are stronger than those on κ_c. There is certain asymmetry between the distance from the best-fit value of $\kappa_c = \kappa_b = 1$ to the upper and lower limits, particularly so in the κ_b fit. The reason for this are the linear terms in κ_c and κ_b in Eq. (6.7). At low to intermediate p_{T}^H values, the linear contributions, i.e. those proportional to κ_c or κ_b, to the differential cross section are negative, as can be seen in Figure 6.1. The quadratic contributions, i.e. those proportional to κ_b^2 or κ_c^2, are always positive. Therefore, at positive values for κ_c and κ_b there is a certain cancellation of linear and quadratic contributions to the predicted cross section. The combined effect of the linear and quadratic modifications as a function of κ_c and κ_b for each bin in p_{T}^H can be seen in Appendix D in terms of $\sigma(\kappa_c) - \sigma(\kappa_c = 1)$ and $\sigma(\kappa_b) - \sigma(\kappa_b = 1)$, respectively.

Comparisons of the expected p_{T}^H spectrum with the predicted spectra at values of κ_c and κ_b equal to the expected 95 % CL limits are shown in Figures 6.13a and 6.13b, respectively. As in the fit, the predicted spectra are normalized to the integrated cross section of the expected p_{T}^H spectrum.

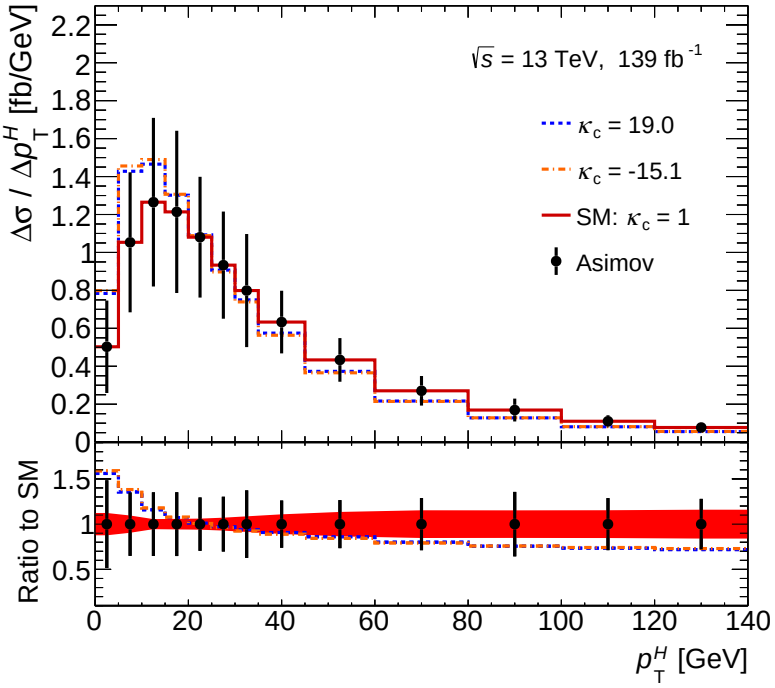

(a)

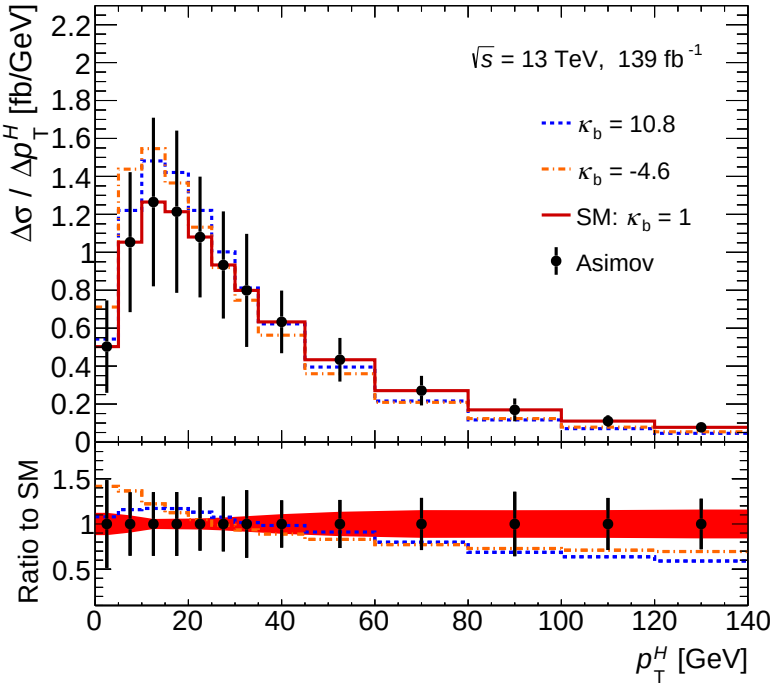

(b)

Figure 6.9. | Asimov dataset compared with non-SM predictions for κ values corresponding to the expected 95 % CL exclusion limits, see Table 6.2. In *(a)*, κ_c is varied and κ_b is fixed to 1, while in *(b)* κ_b is varied and κ_c is fixed to 1. The red uncertainty bands in the lower plots of *(a)* and *(b)* correspond to the theoretical uncertainty on the SM prediction.

In Figure 6.10a, the distribution of p-values based on the Asimov dataset is shown for the κ_c fit, and in Figure 6.10b for the κ_b fit. As expected from an Asimov fit, the best-fit value of the coupling modifiers κ_c and κ_b is the SM value of 1. A comparison of the p-values based on the asymptotic approximation with those based on the pseudo-experiment-based method shows that slight systematic differences are visible at low absolute values of κ_c and κ_b. To a larger extent, these are also present in the fit result based on observed data; an explanation for these differences is given in Section 6.4.3.

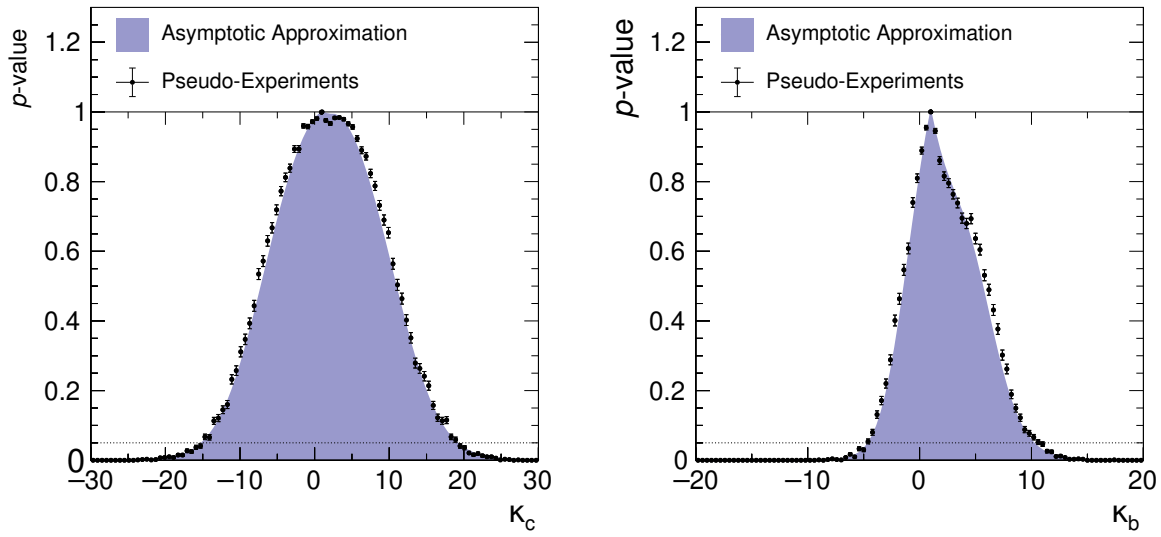

(a) *(b)*

Figure 6.10. | Distributions of p-values as a function of κ_c in *(a)* and κ_b in *(b)*, based on the Asimov dataset. The p-values resulting from the application of the asymptotic approximation are shown as blue-filled curve, while those from the pseudo-experiment-based method are shown as black markers with error bars indicating the statistical uncertainty on the p-values. Lines representing the 95 % CL limit are drawn.

The dependency of the expected confidence intervals on the fitted p_{T}^{H} range is shown in Figure 6.11. The simulation setup that was used to determine the production cross sections for quark-initiated Higgs boson production and the corresponding uncertainties is most reliable at low to intermediate p_{T}^{H}. Moreover, with the current size of the sample of simulated events, the statistical fluctuations of the theoretical uncertainties for $q\bar{q} \to H$ predictions are sizable at large p_{T}^{H}. At the same time, the inclusion of the large p_{T}^{H} region provides relatively small improvements in sensitivity, which is why the fit range has been chosen to be 0 GeV to 140 GeV for this measurement. If, in addition, also the p_{T}^{H} bins between 140 GeV and 250 GeV would be included, the uncertainty would be reduced by 10 % to 15 %. For future measurements it is

planned to include also the high-p_{T}^{H} region.

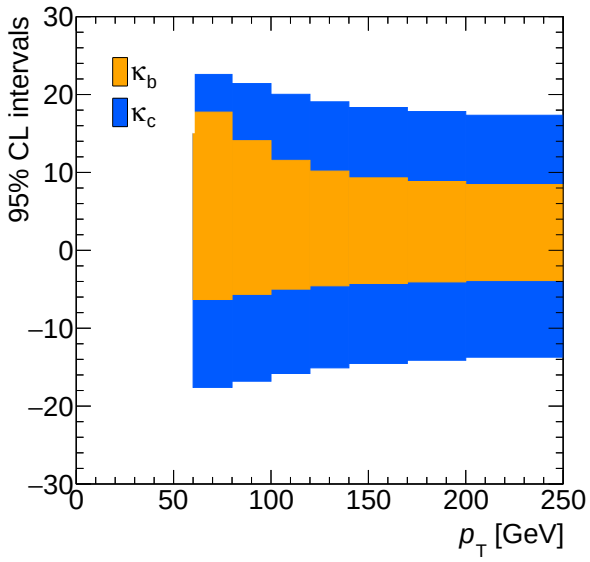

Figure 6.11. | Expected 95 % CL intervals for κ_b and κ_c based on the Asimov dataset as a function of the included p_{T}^{H} range, where in each case 0 GeV is the lower boundary of the fitted range. Due to a considerable decrease of sensitivity below values for the upper boundary of about 60 GeV, corresponding intervals are not shown in this plot.

The expected 95 % CL exclusion contours from a two-dimensional fit to set limits on κ_c and κ_b simultaneously is shown in Figure 6.12. Both fit methods result in exclusion contours that are in good agreement. No strong correlation between the two parameters is seen. Larger deviations of κ_b from the SM value of $\kappa_b = 1$ lead to a stronger constraint on κ_c, and vice versa, resulting in approximately elliptic exclusion contours.

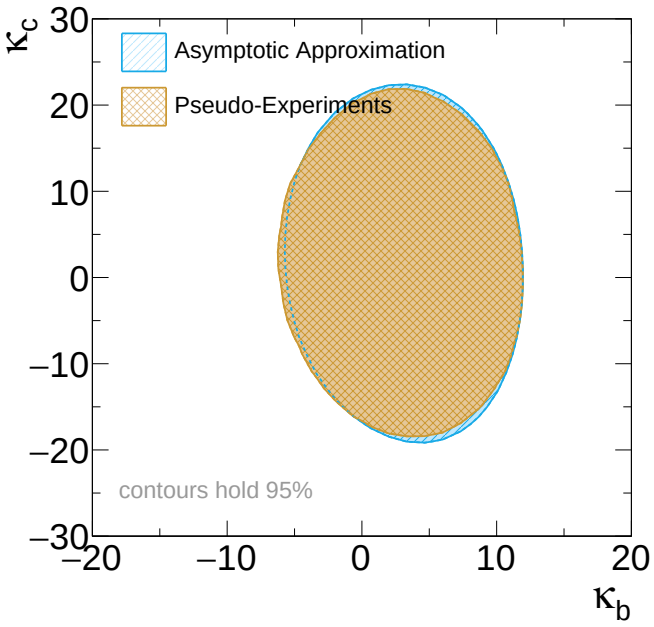

Figure 6.12. | 95 % CL contours for κ_b and κ_c corresponding to $\Delta\chi^2 = 5.99$, based on the *expected* differential cross section in p_{T}^H. Both results from the pseudo-experiment-based method and the asymptotic-approximation method are shown.

6.4.2. Observed Results

The 95 % CL exclusion intervals for κ_c and κ_b based on the observed p_{T}^H spectrum from 2015 – 2018 data-taking are given in Table 6.3. The limits based on the asymptotic approximation and those from the pseudo-experiments-based fitting method agree well with each other. Compared to the expected limits, given in Table 6.2, the observed limits are somewhat weaker. In Figure 6.13

	κ_c	κ_b
Asymptotic approximation	[-18.7 , 24.1]	[-6.0 , 14.8]
Pseudo-experiments	[-19.2 , 24.9]	[-6.3 , 15.5]

Table 6.3. | *Observed* confidence intervals at 95 % CL for κ_c and κ_b based on different fit methods.

(a) and *(b)*, a comparison of the observed spectrum, the SM prediction and the predictions for κ_c and κ_b values corresponding to the exclusion limits is shown, respectively. The p-value distributions are shown in Figures 6.14a and 6.14b for κ_c and κ_b, respectively. The results of a simultaneous fit of κ_c and κ_b is shown in Figure 6.15. Both methods of estimating the $\Delta\chi^2$ distribution lead to similar excluded regions in κ_c and κ_b.

While the excluded parameter regions from both fit methods are in good agreement, the same

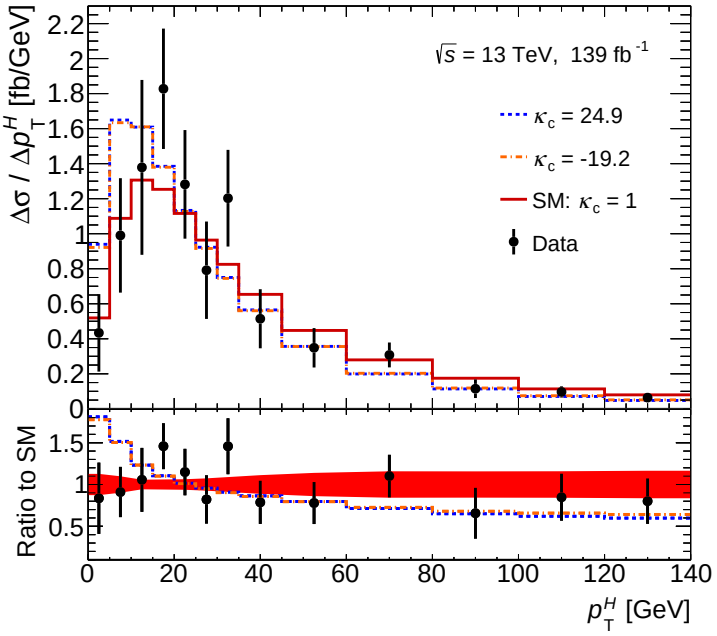

(a)

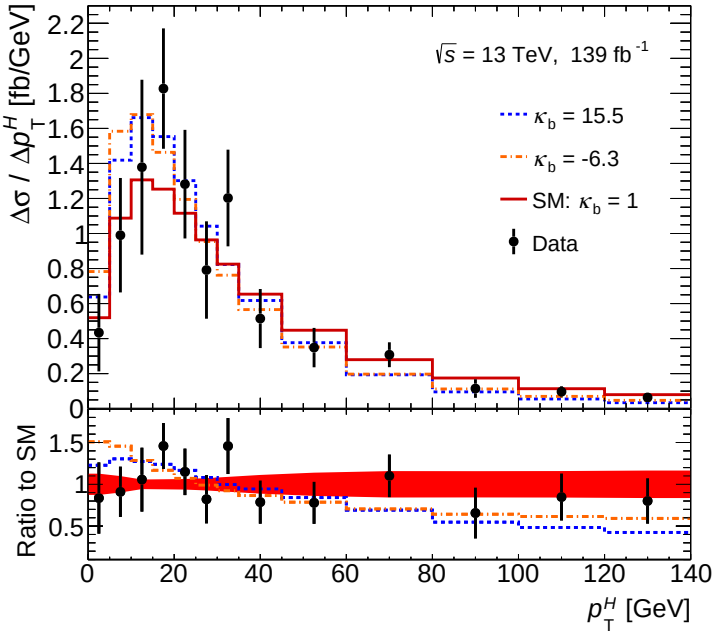

(b)

Figure 6.13. | Observed p_{T}^{H} spectrum compared with the SM prediction as well as non-SM predictions for κ values corresponding to the expected 95 % CL exclusion limits, see Table 6.3. In *(a)*, κ_c is varied and κ_b is fixed to 1, while in *(b)*, κ_b is varied and κ_c is fixed to 1. The red uncertainty bands in the lower plots of *(a)* and *(b)* correspond to the theoretical uncertainty on the SM prediction.

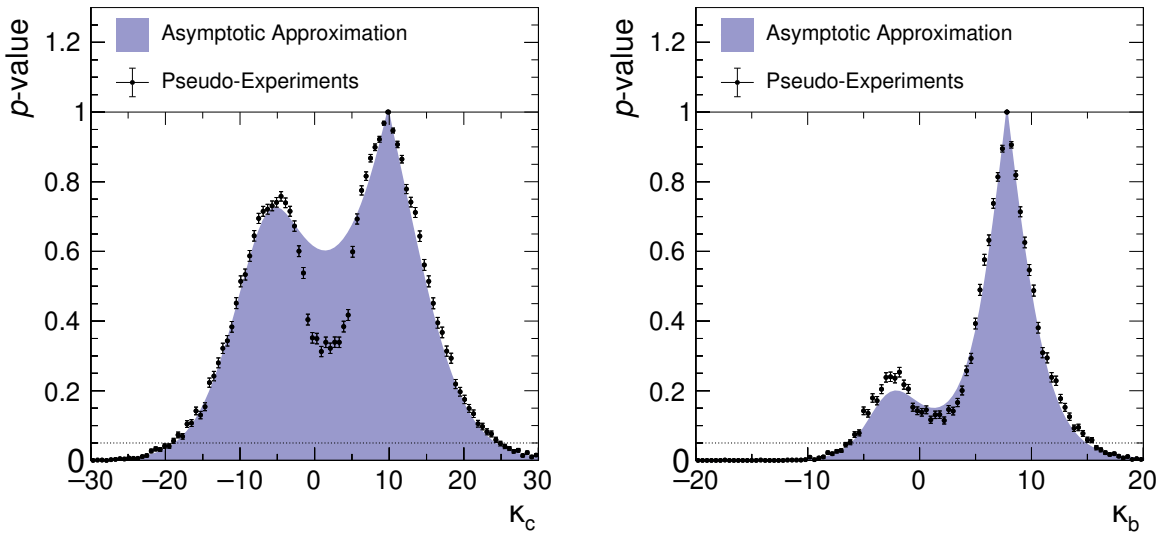

Figure 6.14. | Distributions of p-values as a function of κ_c in *(a)* and κ_b in *(b)* based on the observed differential cross section in p_{T}^{H}. The p-values resulting from the application of the asymptotic approximation are shown as blue-filled curve, while those from the pseudo-experiment-based method are shown as black markers with error bars indicating the statistical uncertainty on the p-values. Lines representing the 95 % CL limit are drawn.

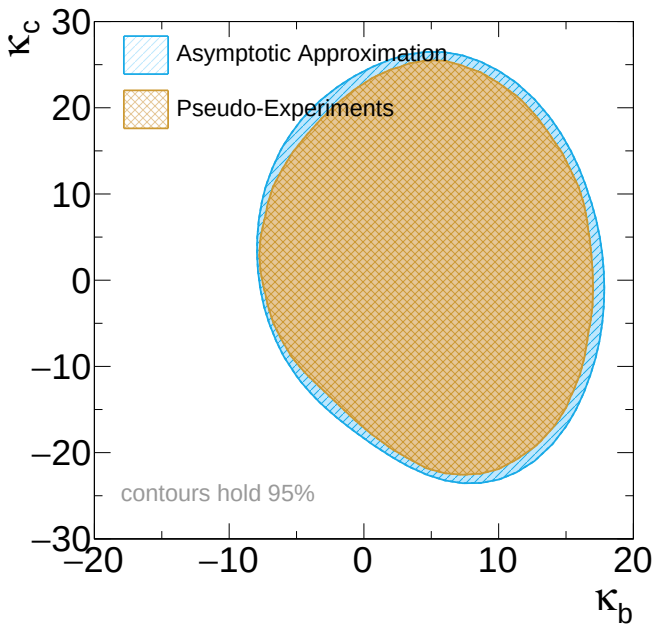

Figure 6.15. | 95 % CL contours for κ_b and κ_c corresponding to $\Delta\chi^2 = 5.99$, based on the *observed* differential cross section in p_{T}^{H}. Both results from the pseudo-experiment-based method and the asymptotic-approximation method are shown.

is not generally true for the p-value distributions within the confidence intervals. As one can see particularly well in Figure 6.14a, the p-values from the pseudo-experiment-based method at small absolute values of κ_c are considerably lower than those from the application of the asymptotic approximation. The reason for this will be discussed in some detail in the following section.

6.4.3. Log-Likelihood-Ratio Distributions and the Prediction Model

The disagreement seen in Figure 6.14a between the p-values from the application of the asymptotic approximation and the pseudo-experiment-based method can be explained by differing distributions of the log-likelihood ratio $\Delta\chi^2$. At low absolute values of κ_c, this disagreement is largest, coinciding with the κ_c region in which the predicted cross section per bin tends to be minimal: the prediction model as given in Eq. (6.7) corresponds to a quadratic function in κ_c and κ_b, with a global minimum that is determined by the interplay between different contributions to the gluon fusion cross section and the cross sections for the $c\bar{c} \to H$ and $b\bar{b} \to H$ processes. In Figure 6.16, the values of κ are shown for which the predicted cross sections in the individual p_{T}^H bins are minimal (κ_{min}), i.e. $\sigma(\kappa_{\mathrm{min}}) = \sigma_{\mathrm{min}}$. The values for κ_{min} range from about 2 at low p_{T}^H to about -1 in the highest considered p_{T}^H bin. In Appendix D, the difference in predicted cross section relative to the SM prediction as a function of κ_c and κ_b is shown for each p_{T}^H bin. It can be shown that the presence of a global minimum in the quadratic prediction model can have a considerable impact on the log-likelihood-ratio distribution as estimated by the generation of pseudo-experiments. Because p-values are determined based on these distributions, this can result in differences between p-values from the asymptotic approximation and the pseudo-experiment-based method.

As described in Section 6.3.2, the pseudo-experiment-based method involves the generation of many pseudo-experiments for each considered value of κ according to the p.d.f. of the observed quantity, i.e. the cross sections per p_{T}^H bin for that value of κ. For each of the generated toys, the log-likelihood ratio $\Delta\chi^2$ is computed. In Figure 6.17 an illustration of this process is shown for a single bin and for two different κ values: one of the κ values (κ_{min}) results in a cross section that is very close to the smallest cross section the model is able to accommodate (σ_{min}). The other κ value results in a predicted cross section that is larger than σ_{min}. Because the pseudo-experiments

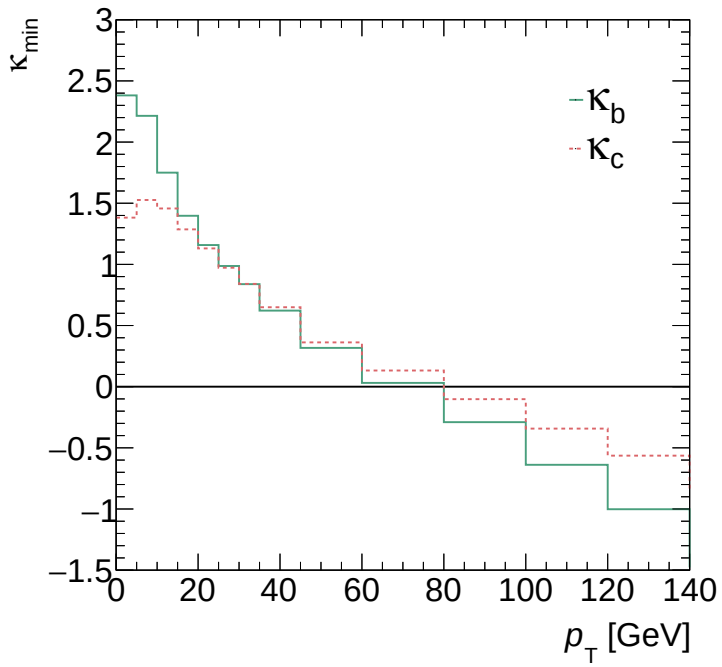

Figure 6.16. | Values of κ_b and κ_c for which the predicted cross section are minimal as a function of p_{T}^{H}.

are generated according to a p.d.f. with a non-zero width, in the former case about half of the generated pseudo-experiments will have a cross section that is *lower* than the lowest cross section that can be accommodated by the prediction model. In the latter case, effectively no pseudo-experiments will be generated with a cross section lower than σ_{min}, under the condition that the width of the p.d.f. is sufficiently small. For each generated pseudo-experiment, the corresponding $\Delta\chi^2$ is determined, i.e. the difference between the log-likelihood of observing the toy result in the case of assuming that the probed value κ is the true parameter value, and in the case of assuming that the best-fit value $\hat{\kappa}_{\mathrm{toy}}$ for the considered toy is the true parameter value, see Eq. (6.17). In the case of $\kappa = \kappa_{\mathrm{min}}$, the best-fit value for κ will be κ_{min} in about 50 % of the pseudo-experiments. Accordingly, the $\Delta\chi^2$ for this fraction of toys will be very close to zero. In the case that the predicted cross section is sufficiently much larger than the minimal cross section of the model, the resulting $\Delta\chi^2$ distribution is able to approximate the nominal χ^2 distribution, which is used in the asymptotic approximation. As a result, the p-values from the asymptotic approximation and from the pseudo-experiment-based method can deviate significantly from each other when $\kappa \approx \kappa_{\mathrm{min}}$. To be more precise, the p-value is expected to be lower for the pseudo-experiment-based method in that parameter region.

The resulting difference depends on the extent of the deviation between prediction and

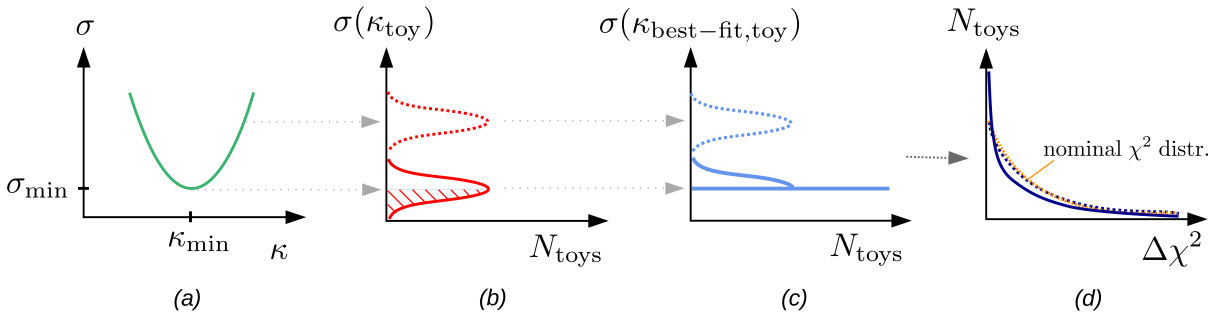

Figure 6.17. | Illustration of the reason for differences between p-values from the application of the asymptotic approximation and the pseudo-experiment-based method. For this illustration, a single p_{T}^{H} bin is assumed for reasons of simplicity. Figure *(a)* schematically shows the quadratic dependency of the predicted cross section on the Yukawa-coupling modifier κ. The corresponding function has a global minimum σ_{min} at κ_{min}. In the pseudo-experiment-based method of determining the $\Delta\chi^2$ distribution, for a given scanned value of κ, numerous pseudo-experiments are generated. The result of this pseudo-experiment generation is shown in *(b)* for the two cases $\kappa \approx \kappa_{\mathrm{min}}$ and $\kappa \gg \kappa_{\mathrm{min}}$. In the course of the calculation of the per-toy $\Delta\chi^2$, the best-fit κ value for each toy is determined. In the third figure, the distributions of the cross sections that correspond to the best-fit κ values for the two cases are shown. While the in the case $\kappa \gg \kappa_{\mathrm{min}}$ the best-fit cross sections are distributed similarly as the toy cross sections in *(b)*, the situation is different when $\kappa \approx \kappa_{\mathrm{min}}$: The toys corresponding to the hatched area in *(b)* are best-fit with the κ value κ_{min}, as it leads to the minimally possible cross section the model can account for. In *(d)*, the resulting distribution of $\Delta\chi^2$ for the two discussed cases is shown, in comparison with a schematic version of the nominal χ^2 distribution with a single degree of freedom. The $\Delta\chi^2$ of a toy quantifies the difference in likelihood of observing the outcome of the pseudo-experiment under the assumption that the scanned value of κ is the underlying true parameter value and under the assumption that the best-fit value of κ is the true parameter value. In the case of $\kappa \approx \kappa_{\mathrm{min}}$, roughly half of the pseudo-experiments have a best-fit κ value very close to the scanned κ value, which leads to very small differences in the likelihood and correspondingly to vanishing values for $\Delta\chi^2$.

observation. If prediction for a given value of κ and observation (or the Asimov dataset) agree well, the value for $\Delta\chi^2_{\text{obs}}$ in Eq (6.15) is small. The sensitivity of the integral in Eq (6.15) to the normalized distribution of $\Delta\chi^2$ vanishes as the lower integration limit $\Delta\chi^2_{\text{obs}}$ approaches zero. Therefore, the disagreement between the p-value distribution from the asymptotic approximation and from the pseudo-experiment-based method is small in the case of the Asimov dataset where in the region $\kappa \approx \kappa_{\text{min}} \approx \kappa_{\text{SM}}$ the predicted spectrum and the reference spectrum agree well. When instead of the Asimov dataset the observed spectrum is used as reference spectrum, relatively large values for $\Delta\chi^2_{\text{obs}}$ result, even at $\kappa \approx \kappa_{\text{min}} \approx \kappa_{\text{SM}}$, allowing the above-described effect of differing $\Delta\chi^2$ distributions to become well visible.

This discussion assumed that only a single bin of the differential cross section was taken into account. By considering multiple bins, the effect of the generation of cross sections with lower values than the minimal cross section of the prediction model is diluted. Even in the case of an identical κ_{min} for each bin, which is not given as can be seen in Figure 6.16, the independent generation of per-bin cross sections of the differential distribution would reduce the fraction of generated toys in which the best-fit value is very close to κ_{min}. An additional reduction of the effect size can be expected from differing values for κ_{min} for different p_{T}^H bins, which, as can be seen in Figure 6.16, is given for both κ_c and κ_b. As a consequence, for any given scanned value for κ_c or κ_b, the effect of the above described phenomenon is further reduced. The variance in κ_{min} for κ_b is larger than for κ_c, which can be expected to result in a better agreement between the p-values from the asymptotic approximation and from the pseudo-experiment-based method. In fact, this difference is relatively small, as can be seen in Figure 6.14b.

In Figure 6.18, four representative examples of $\Delta\chi^2$ distributions from pseudo-experiments are shown in comparison with the nominal χ^2 distribution. In Figure 6.18a and Figure 6.18b, comparisons are given for the cases in which κ_c is close to $\kappa_{c,\text{min}} \approx 1$, and in which κ_c is much larger than $\kappa_{c,\text{min}}$, respectively. As one can see, the pseudo-experiment-based distribution of $\Delta\chi^2$ agrees well with the nominal χ^2 distribution in the latter case, while in the former case the pseudo-experiment-based distribution is relatively strongly peaked at low values of $\Delta\chi^2$. This feature is less pronounced in the case of κ_b, as can be seen in Figures 6.18c and 6.18d.

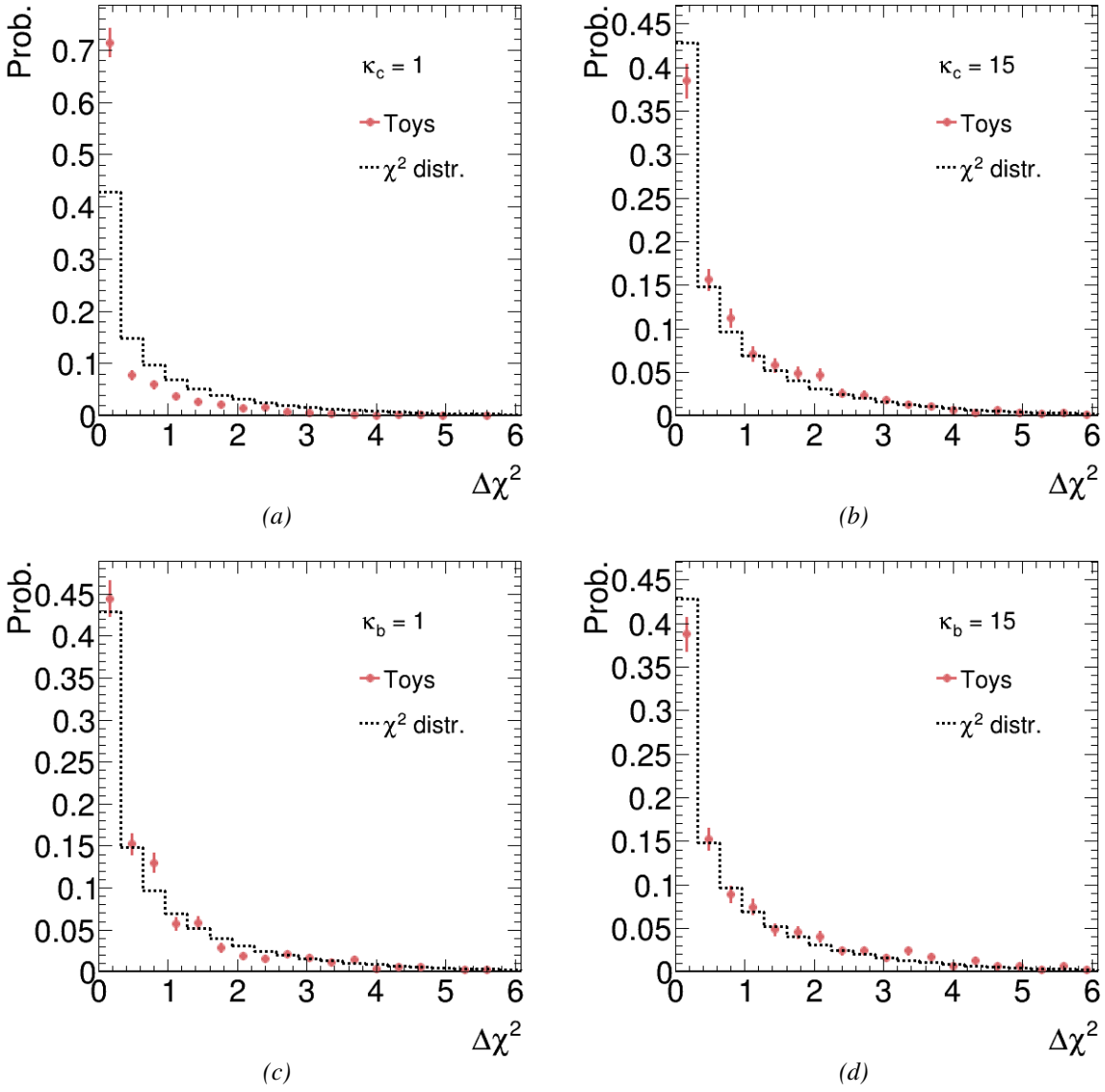

Figure 6.18. | Comparisons of normalized $\Delta\chi^2$ distributions resulting from pseudo-experiments and the nominal χ^2 distribution, which is used in the asymptotic approximation. In *(a)* and *(b)*, the comparison is given for different values of κ_c and $\kappa_b = 1$, and in *(c)* and *(d)* for different values in κ_b and $\kappa_c = 1$. In *(a)* and *(c)*, the κ values are close to the value at which the predicted cross sections are close to the lowest cross section the prediction model can account for.

6.4.4. Impact of Uncertainties

As described in Section 6.1.3, there are several sources of uncertainty, which are incorporated into the fit either via a covariance matrix or via nuisance parameters constrained by Gaussian p.d.f.s. In order to determine the major limiting factors to the measurement, it is of interest to estimate the impact of the various uncertainties on the confidence interval. Because the confidence intervals from the asymptotic approximation generally agree well with those from the pseudo-experiment-based method, it is warranted to perform the following study using the computationally less demanding asymptotic approximation.

The statistical uncertainty contribution is estimated by performing the fit with all uncertainties except the statistical uncertainty set to zero. For all other, i.e. non-statistical uncertainties, the contribution from the considered uncertainty is estimated by computing the quadratic difference between the length of the nominal confidence interval ($\Delta\kappa_{c,b}$) and the length of the confidence interval excluding said uncertainty contribution from the fit, $(\Delta\kappa_{c,b})'$:

$$\Delta\kappa_{c,b}^{\text{contr.}} = \sqrt{(\Delta\kappa_{c,b})^2 - (\Delta\kappa_{c,b})'^2}\,. \tag{6.19}$$

In the case of the experimental systematic uncertainty as well as the VBF-, VH- and $t\bar{t}H$-related theory uncertainties, the uncertainty contribution is excluded by setting the corresponding entries of the covariance matrix to zero. In the case of the other theory uncertainties for gluon fusion and quark-initiated Higgs boson production, the corresponding nuisance parameters are fixed to their best-fit values from the nominal fit.

The contributions to the size of the confidence interval for κ_c and κ_b from the one-dimensional fits are given in Table 6.4 for the expected spectrum, and in Table 6.5 for the observed spectrum. In all fits, the statistical uncertainty on the measured p_{T}^H spectrum is the dominant uncertainty contribution. Systematic experimental uncertainties and uncertainties due to missing higher orders in the perturbation expansion for the gluon fusion prediction are clearly smaller than the statistical uncertainty, but still sizable. The uncertainties due to missing higher orders in the perturbation expansion in the $b\bar{b} \to H$ and $c\bar{c} \to H$ predictions are small in comparison. The PDF uncertainties are minor contributions. For the measurement of κ_b, the PDF uncertainty for the c-quark is practically irrelevant, and vice versa.

Another interesting quantity is the impact of individual nuisance parameters on the best-fit

Contribution	$\Delta\kappa_c^{\text{contr.}}$	$\Delta\kappa_b^{\text{contr.}}$
Total	34.2	14.7
Statistical	27.1	11.6
Systematic	10.0	4.8
QCD Scale (ggF)	16.5	6.7
QCD Scale ($q\bar{q} \to H$)	3.2	3.1
PDF (ggF)	1.2	0.7
PDF (c-quark)	1.0	0.0
PDF (b-quark)	0.0	1.2
Parton Shower Modeling ($q\bar{q} \to H$)	6.3	0.6
VBF, VH, $t\bar{t}H$	0.7	0.4
Acceptance correction (ggF)	0.4	0.2

Table 6.4. | Contributions to the uncertainty corresponding to the 95 % CL confidence intervals from the κ_c and κ_b fits based on the expected differential cross section.

Contribution	$\Delta\kappa_c^{\text{contr.}}$	$\Delta\kappa_b^{\text{contr.}}$
Total	42.8	20.8
Statistical	34.2	17.2
Systematic	6.7	4.5
QCD perturbative (ggF)	20.2	9.3
QCD perturbative ($q\bar{q} \to H$)	4.8	4.2
PDF (ggF)	1.5	0.8
PDF (c-quark)	1.2	0.0
PDF (b-quark)	0.0	1.6
Parton Shower Modeling ($q\bar{q} \to H$)	16.3	4.0
VBF, VH, $t\bar{t}H$	0.5	0.5
Acceptance correction (ggF)	0.4	0.5

Table 6.5. | Contributions to the uncertainty corresponding to 95 % CL confidence intervals from the κ_c and κ_b fits based on the observed differential cross section.

value for κ_c and κ_b. The post-fit impact for a nuisance parameter θ_i is defined as

$$\Delta\kappa_{b,c} = \hat{\kappa}_{b,c}(\theta_i = \hat{\theta}_i \pm \Delta\theta_i) - \hat{\kappa}_{b,c}(\theta_i = \hat{\theta}_i)\,, \tag{6.20}$$

where $\hat{\kappa}_{b,c}$ denotes the best-fit value for κ_b and κ_c. $\hat{\theta}_i$ is the best-fit value for θ_i, and $\Delta\theta_i$ the post-fit uncertainty on that parameter. In the fits that are conducted to determine the impact of a given nuisance parameter, all other nuisance parameters are left floating. In Figures 6.19 and 6.20, the impacts of the individual nuisance parameters on the best-fit value for κ_c and κ_b, respectively, are shown. Additionally, the *pulls* on the nuisance parameters are shown, defined as

$$(\hat{\theta}_i - \theta_{i,0})/\Delta\theta_i\,, \tag{6.21}$$

where $\theta_{i,0}$ is the initially chosen value for the nuisance parameter, which corresponds to zero for the nuisance parameters considered here. Deviations of $\hat{\theta}_i$ from $\theta_{i,0}$ indicate an absorption of features of the fitted spectrum into the nuisance parameter θ_i. The post-fit uncertainties on the nuisance parameters are plotted as error bars to the pull values. The nuisance parameters are not expected to be constrained by the fit; therefore, the expected value for the post-fit uncertainties is 1.

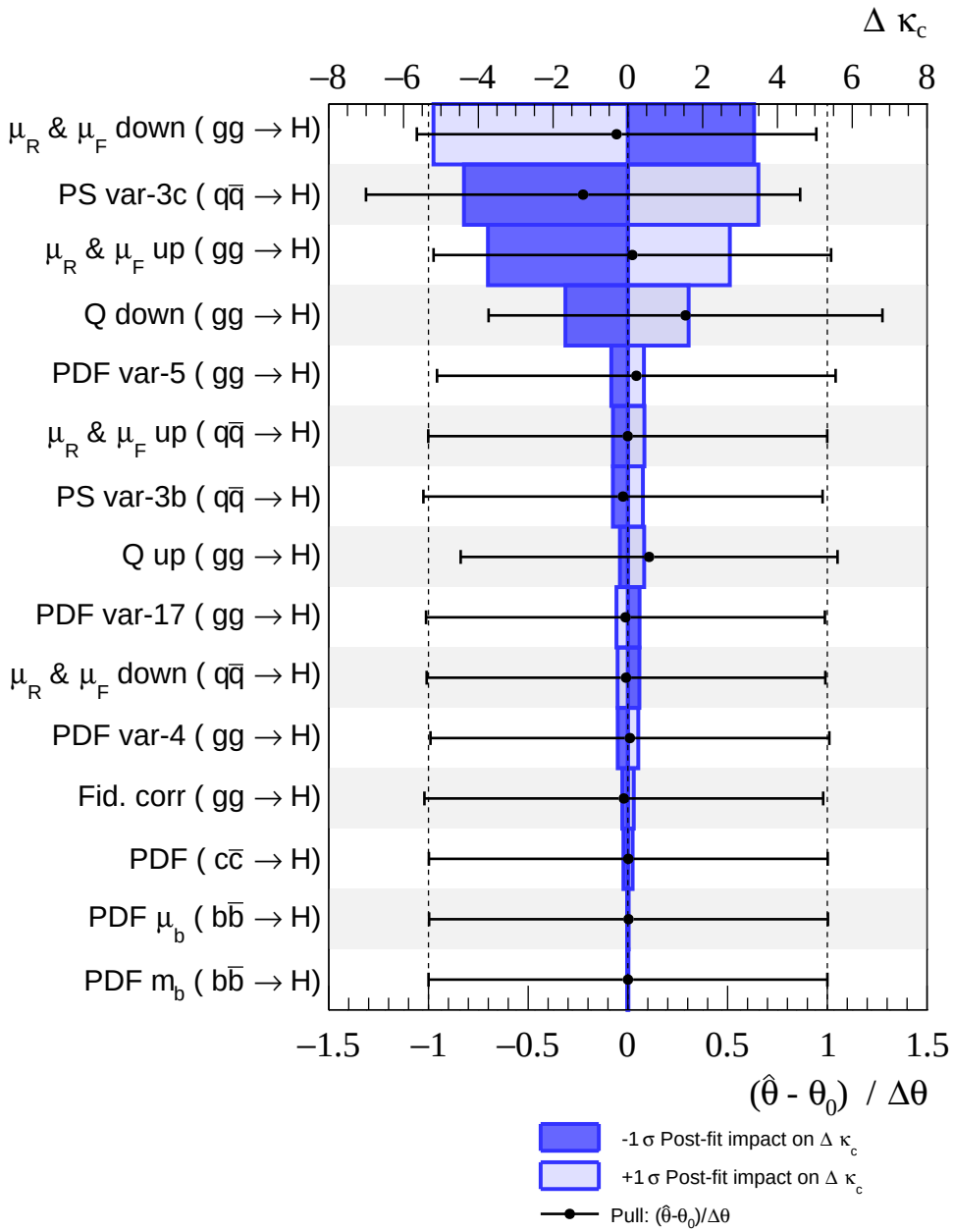

Figure 6.19. | Post-fit impacts of the various nuisance parameters on the best-fit value for κ_c, as well as the nuisance parameter pulls, based on the observed p_{T}^{H} spectrum. The dark-blue bars represent the impact of the down-variation of a given nuisance parameter, while the light-blue bars represent the impact of the up-variation. Pulls on the nuisance parameters, as defined in Equation (6.21), are plotted as black markers in combination with the post-fit uncertainty on θ_i as error bars.

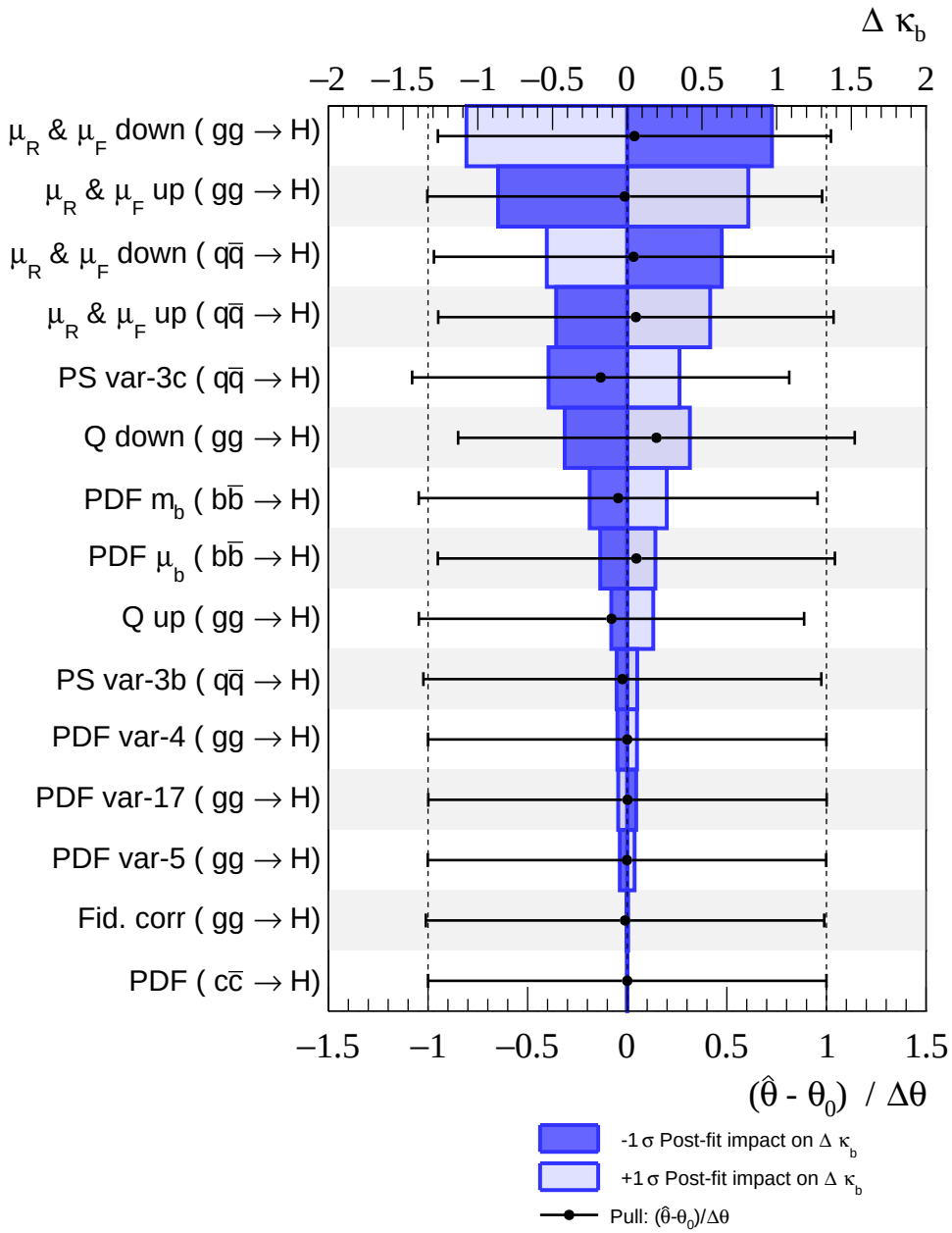

Figure 6.20. | Post-fit impacts of the various nuisance parameters on the best-fit value for κ_b, as well as the nuisance parameter pulls, based on the observed p_{T}^{H} spectrum. The dark-blue bars represent the impact of the down-variation of a given nuisance parameter, while the light-blue bars represent the impact of the up-variation. Pulls on the nuisance parameters, as defined in Equation (6.21), are plotted as black markers in combination with the post-fit uncertainty on θ_i as error bars.

6.5. Summary

The differential cross section in p_{T}^{H} is sensitive to the Yukawa couplings of the Higgs boson to quarks. As a consequence, the measured differential cross section can be used to extract information about these couplings. In this work, limits on the Yukawa couplings of the Higgs boson to the c- and the b-quark were determined. For this, the p_{T}^{H} spectrum as measured in the $H \to \gamma\gamma$ decay channel with the ATLAS dataset collected in the years 2015 – 2018, corresponding to an integrated luminosity of 139.0/fb, was used. The normalization of the p_{T}^{H} spectrum in the diphoton Higgs decay channel, which includes the $H \to \gamma\gamma$ branching ratio, is sensitive to many theory parameters. In order be less model-dependent, only shape information was considered in the fit.

Predictions of the ggF, $b\bar{b} \to H$ and $c\bar{c} \to H$ contributions to the differential cross section needed to be provided for arbitrary values of κ_c and κ_b in order to set limits on the Yukawa-coupling modifiers for the c- and b-quark. For the contributions from other Higgs boson production modes, which are not sensitive to κ_c and κ_b, SM predictions were used. In the case of gluon fusion, a set of resummed NLO predictions for an array of κ_c and κ_b values was used to extract coefficients that allow the prediction of the gluon fusion p_{T}^{H} spectrum for arbitrary values of κ_b and κ_c. The resulting prediction was normalized such that the integrated SM gluon fusion prediction matched the cross section of the state-of-the-art $\mathrm{N^3LO}$ prediction. Moreover, in order for the predictions to be comparable to the measured cross sections in a fiducial phase-space volume, fiducial corrections based on the NNLOPS gluon fusion simulation were applied. NNLOPS predictions were not available for varied values of κ_c or κ_b, and it was assumed that the fiducial corrections are not sensitive to these parameters. Predictions for the quark-initiated Higgs boson production were produced using MadGraph5_aMC@NLO with Pythia8 as parton shower simulation. Theoretical uncertainties related to PDFs, missing higher orders in QCD perturbation theory and the parton shower simulation were taken into account.

The fit of the observed p_{T}^{H} spectrum was performed using a profile likelihood method. The distribution of the log-likelihood ratio was determined by pseudo-experiments. In addition, results based on the asymptotic approximation, i.e. the assumption that the log-likelihood ratio can be approximated by the nominal χ^2 distribution, were shown. Both methods resulted in limits that are in good agreement. The expected values for κ_c and κ_b excluded at 95 % CL

correspond to ($\kappa_c < -15.1$, $\kappa_c > 19.0$) and ($\kappa_b < -4.6$, $\kappa_b > 10.8$), respectively. The exclusion intervals for κ_c and κ_b based on the observed p_{T}^{H} spectrum are given by ($\kappa_c < -19.2$, $\kappa_c > 24.9$) and ($\kappa_b < -6.3$, $\kappa_b > 15.5$), respectively.

These limits on κ_b can be compared to results from analyses using $pp \to VH(\to b\bar{b})$ events. Using a dataset corresponding to an integrated luminosity of 139/fb, the 95 % CL confidence interval in Reference [205] is given by $0.7 < \kappa_b < 1.6$. Therefore, it can be concluded that the more direct method based on $VH(\to b\bar{b})$ events allows setting tighter constraints on κ_b than the method described in this chapter. In the case of the c-quark Yukawa coupling, such a comparison is not yet possible; results based on data corresponding to an integrated luminosity of about 36/fb did not allow setting limits on κ_c [209, 210].

The accuracy of the κ_c and κ_b measurement is at this point clearly limited by the statistical uncertainties from the measurement of the differential cross section in p_{T}^{H}. However, the uncertainties due to missing higher orders of QCD calculation and the experimental systematic uncertainties are not negligible. With an integrated luminosity of approximately 250/fb, the statistical uncertainty can be expected to be of the same size as the current combined systematic and theoretical uncertainties. At that point, advances in the accuracy of theoretical predictions by including higher-order terms of QCD calculations, particularly in differential gluon fusion cross section predictions, and a reduction of experimental uncertainties in the cross section measurement could significantly benefit the precision of this method.

7. Conclusion

One of the central topics of this thesis is the identification of photons in the ATLAS experiment, in particular the efficiency of the identification. A good understanding of photons and their identification is important for photon-based analyses of ATLAS data; accordingly, an accurate measurement of photon identification efficiencies is essential. The identification of photons is performed based on shower-shape variables, which parametrize the shape of the shower in the calorimeter. The method of measuring the photon identification efficiencies that has been applied in this work is called the electron-extrapolation method. It is based on transformations of the shower-shape variables that, if applied to a sample of electrons, results in a sample of pseudo-photons, which has to a good approximation the same distributions of shower-shape variables as a photon sample. By applying such transformations on a pure and unbiased electron sample obtained from data events by a tag-and-probe method applied, the resulting objects can be used to determine the photon identification efficiency in data events. The efficiencies, which have been measured in the transverse momentum region from 25 GeV to 250 GeV, range from approximately 80 % to 100 %, depending on the considered pseudorapidity and transverse momentum. The uncertainties on the measured efficiencies are in the range from about 0.5 % to 3 %. The ratios of the measured efficiencies and those in simulation correspond to efficiency scale factors. These can be used in photon-based analyses to correct weights of events in simulation such that the photon identification efficiency in data and simulation is in good agreement – which is important for the comparability of simulated event samples and event samples from data-taking. The scale factors as determined with the electron-extrapolation method are well compatible with scale factors from the other two methods that are used to measure the photon identification efficiency.

Another central topic of this thesis is the measurement of the properties of the Higgs boson using its decay to a pair of photons. The diphoton decay channel has a clean signature and allows

a robust background subtraction despite its low branching ratio. Accordingly, the $H \to \gamma\gamma$ decay channel has been crucial in the discovery of the Higgs boson, and furthermore allows a precise measurement of Higgs-boson-related observables such as inclusive and differential Higgs boson production cross sections. Based on invariant-mass spectra of events with two reconstructed and identified photon candidates, the numbers of $H \to \gamma\gamma$ events in various phase-space regions can be determined in a signal-plus-background fit. By relating these numbers to the integrated luminosity of the dataset, inclusive and differential cross sections have been measured. In order to make these cross sections comparable to a wider set of theoretical predictions, corrections for detector effects such as inefficiencies and a finite resolution have been applied. Cross sections are measured in a fiducial volume of phase space that closely resembles the detector acceptance, which reduces the model dependence. The inclusive and differential cross sections that were obtained in this way have been compared to SM predictions. The measured value for the inclusive Higgs boson production cross section in the diphoton decay channel is

$$\sigma_{\text{fid}} = \left(60.4 \pm 6.1\,(\text{stat.}) \pm 6.0\,(\text{exp.}) \,{}^{+0.3}_{-0.4}\,(\text{theo.})\right) \text{fb}\,.$$

This result agrees well with SM prediction of (63.5 ± 3.3) fb. The differential cross sections have been measured in the variables p_{T}^{H}, $|y_H|$, $p_{\text{T}}^{j_1}$, and $N_{b-\text{jets}}$ and are, within uncertainties, in good agreement with SM predictions.

The differential cross section in Higgs boson transverse momentum can be used to set limits on Yukawa coupling between the Higgs boson and quarks. In the SM, these couplings are expected to be proportional to the quark masses. The t-quark and b-quark Yukawa couplings are already known relatively precisely, with relative uncertainties of the order of 10 % and 20 %, respectively. In the case of the quark with the third-largest mass, the c-quark, direct measurements using decays of Higgs bosons into a c-quark pair are considerably more challenging. Corresponding limits on this coupling from direct measurements are not yet available. Therefore, it is reasonable to consider alternative paths to the goal of measuring the c-quark Yukawa coupling that can be followed in parallel. Because the spectrum of the Higgs boson transverse momentum is sensitive to the quark Yukawa couplings, including the c-quark Yukawa coupling, a fit of the observed p_{T}^{H} spectrum allows extracting information about the c-quark Yukawa coupling. In addition to a fit with respect to the c-quark Yukawa coupling, the same method has been applied in order

to set limits on the b-quark Yukawa coupling. For the fit, it was necessary to create a method of predicting p_{T}^{H} spectra for arbitrary values of κ_c and κ_b. By taking only the shape of the p_{T}^{H} distribution into account in the fit, the dependence on other theory parameters is reduced. By determining the degree of compatibility of predicted spectra with the observed spectrum for a range of values of the c- and b-quark Yukawa coupling, confidence intervals could be established. For these fits, the dataset collected in the years 2015 – 2018, corresponding to an integrated luminosity of 139/fb, was used. Besides a simultaneous fit of κ_c and κ_b, one-dimensional fits of κ_c and κ_b have been performed, with κ_b and κ_c fixed to their SM value of 1, respectively. For the c-quark Yukawa-coupling modifier $\kappa_c = y_c/y_c^{\mathrm{SM}}$, a 95 % CL confidence interval of $\kappa_c \in [-19, 25]$ was determined. In the case of the b-quark Yukawa-coupling modifier $\kappa_b = y_b/y_b^{\mathrm{SM}}$, the resulting confidence interval corresponds to $\kappa_b \in [-6, 16]$.

Bibliography

[1] The CMS Collaboration. „Observation of a new boson at a mass of 125 GeV with the CMS experiment at the LHC“. *Phys. Lett. B* 716 (2012), pp. 30–61. arXiv: 1207.7235 [hep-ex] (cit. on pp. 1, 16).

[2] The ATLAS Collaboration. „Observation of a new particle in the search for the Standard Model Higgs boson with the ATLAS detector at the LHC“. *Phys. Lett. B* 716 (2012), pp. 1–29. arXiv: 1207.7214 [hep-ex] (cit. on pp. 1, 16, 17).

[3] M. D. Schwartz. *Quantum Field Theory and the Standard Model*. Cambridge University Press, 2014 (cit. on pp. 5, 6, 8, 16, 23, 24, 26).

[4] D. V. Peskin M. E.; Schroeder. *An Introduction to Quantum Field Theory*. Westview Press, 1995 (cit. on pp. 5, 8–11, 13).

[5] D. Griffiths. *Introduction to elementary particles*. Wiley, 2008 (cit. on p. 6).

[6] M. Tanabashi et al. „Review of Particle Physics“. *Phys. Rev. D* 98.3 (2018), p. 030001 (cit. on pp. 7, 8, 15, 23, 27, 37, 99).

[7] The ATLAS Collaboration and the CMS Collaboration. „Combined Measurement of the Higgs Boson Mass in pp Collisions at $\sqrt{s} = 7$ and 8 TeV with the ATLAS and CMS Experiments“. *Phys. Rev. Lett.* 114 (2015). arXiv: 1503.07589 [hep-ex] (cit. on pp. 8, 16, 137, 149, 158).

[8] A. J. G. Aitchison I. J. R.; Hey. *Gauge Theories in Particle Physics, Volume 1, From Relativistic Quantum Mechanics to QED*. 4th ed. CRC Press, 2013 (cit. on p. 10).

[9] A. J. G. Aitchison I. J. R.; Hey. *Gauge Theories in Particle Physics, Volume 2, Non-Abelian Gauge Theories*. CRC Press, 2013 (cit. on pp. 16, 17).

[10] L. Landau. „On the angular momentum of a two-photon system“. *Dokl. Akad. Nauk Ser. Fiz.* 60 (1948) (cit. on p. 17).

[11] C.-N. Yang. „Selection Rules for the Dematerialization of a Particle Into Two Photons“. *Phys. Rev.* 77 (1950) (cit. on p. 17).

[12] The ATLAS Collaboration. „Study of the spin and parity of the Higgs boson in diboson decays with the ATLAS detector“. *Eur. Phys. J. C* 75 (2015). arXiv: 1506.05669 [hep-ex] (cit. on p. 17).

[13] D. de Florian et al. „Handbook of LHC Higgs Cross Sections: 4. Deciphering the Nature of the Higgs Sector“. 2/2017 (Oct. 2016). arXiv: 1610.07922 [hep-ph] (cit. on pp. 17–21, 30, 149).

[14] B. R. Martin. *Particle Physics*. New York: Wiley, 2008 (cit. on p. 17).

[15] The ATLAS Collaboration. „Observation of $H \to b\bar{b}$ decays and VH production with the ATLAS detector“. *Phys. Lett. B* 786 (2018), pp. 59–86. arXiv: 1808.08238 [hep-ex] (cit. on p. 17).

[16] The CMS Collaboration. „Observation of Higgs boson decay to bottom quarks“. *Phys. Rev. Lett.* 121.12 (2018), p. 121801. arXiv: 1808.08242 [hep-ex] (cit. on p. 17).

[17] Aivazis, A. https://feynman.aivazis.com/. Accessed: 2019-08-09 (cit. on p. 18).

[18] LHC Higgs Cross Section Working Group. *SM Higgs production cross sections at* $\sqrt{s} = 13$ *TeV*. https://twiki.cern.ch/twiki/bin/view/LHCPhysics/CERNYellowReportPageAt13TeV. Accessed: 2019-01-11 (cit. on pp. 19–21).

[19] C. Anastasiou et al. „High precision determination of the gluon fusion Higgs boson cross-section at the LHC“. *JHEP* 05 (2016), p. 58. arXiv: 1602.00695 [hep-ph] (cit. on pp. 19, 29, 30).

[20] C. Anastasiou et al. „Higgs Boson Gluon Fusion Production Beyond Threshold in N^3LO QCD“. *JHEP* 03 (2015). arXiv: 1411.3584 [hep-ph] (cit. on pp. 19, 30).

[21] C. Anastasiou et al. „Higgs boson gluon–fusion production at threshold in N^3LO QCD“. *Phys. Lett. B* 737 (2014), pp. 325–328. arXiv: 1403.4616 [hep-ph] (cit. on pp. 19, 30).

[22] C. Anastasiou et al. „Higgs Boson Gluon-Fusion Production in QCD at Three Loops“. *Phys. Rev. Lett.* 114 (2015), p. 212001. arXiv: 1503.06056 [hep-ph] (cit. on pp. 19, 30).

[23] S. Dawson. „Radiative corrections to Higgs boson production“. *Nucl. Phys. B* 359 (1991), pp. 283–300 (cit. on pp. 19, 30).

[24] D. Graudenz, M. Spira, and P. M. Zerwas. „QCD corrections to Higgs boson production at proton proton colliders“. *Phys. Rev. Lett.* 70 (1993), pp. 1372–1375 (cit. on pp. 19, 30).

[25] A. Djouadi, M. Spira, and P. M. Zerwas. „Production of Higgs bosons in proton colliders: QCD corrections“. *Phys. Lett. B* 264 (1991), pp. 440–446 (cit. on pp. 19, 30).

[26] C. Anastasiou and K. Melnikov. „Higgs boson production at hadron colliders in NNLO QCD“. *Nucl. Phys. B* 646 (2002), pp. 220–256. arXiv: hep-ph/0207004 [hep-ph] (cit. on pp. 19, 30).

[27] R. V. Harlander and W. B. Kilgore. „Next-to-next-to-leading order Higgs production at hadron colliders“. *Phys. Rev. Lett.* 88 (2002), p. 201801. arXiv: hep-ph/0201206 [hep-ph] (cit. on pp. 19, 30).

[28] V. Ravindran, J. Smith, and W. L. van Neerven. „NNLO corrections to the total cross-section for Higgs boson production in hadron hadron collisions“. *Nucl. Phys. B* 665 (2003), pp. 325–366. arXiv: hep-ph/0302135 [hep-ph] (cit. on pp. 19, 30).

[29] R. V. Harlander and K. J. Ozeren. „Finite top mass effects for hadronic Higgs production at next-to-next-to-leading order“. *JHEP* 11 (2009), p. 88. arXiv: 0909.3420 [hep-ph] (cit. on pp. 19, 30).

[30] A. Pak, M. Rogal, and M. Steinhauser. „Finite top quark mass effects in NNLO Higgs boson production at LHC“. *JHEP* 02 (2010), p. 25. arXiv: 0911.4662 [hep-ph] (cit. on pp. 19, 30).

[31] R. V. Harlander and K. J. Ozeren. „Top mass effects in Higgs production at next-to-next-to-leading order QCD: Virtual corrections“. *Phys. Lett. B* 679 (2009), pp. 467–472. arXiv: 0907.2997 [hep-ph] (cit. on pp. 19, 30).

[32] R. V. Harlander et al. „Higgs production in gluon fusion at next-to-next-to-leading order QCD for finite top mass“. *Eur. Phys. J. C* 66 (2010), pp. 359–372. arXiv: 0912.2104 [hep-ph] (cit. on pp. 19, 30).

[33] U. Aglietti et al. „Two loop light fermion contribution to Higgs production and decays“. *Phys. Lett. B* 595 (2004), pp. 432–441. arXiv: hep-ph/0404071 [hep-ph] (cit. on pp. 19, 30).

[34] S. Actis et al. „NLO Electroweak Corrections to Higgs Boson Production at Hadron Colliders“. *Phys. Lett. B* 670 (2008), pp. 12–17. arXiv: 0809.1301 [hep-ph] (cit. on pp. 19, 30).

[35] S. Actis et al. „NNLO Computational Techniques: The Cases $H \to \gamma\gamma$ and $H \to gg$“. *Nucl. Phys. B* 811 (2009), pp. 182–273. arXiv: 0809.3667 [hep-ph] (cit. on pp. 19, 30).

[36] C. Anastasiou, R. Boughezal, and F. Petriello. „Mixed QCD-electroweak corrections to Higgs boson production in gluon fusion“. *JHEP* 04 (2009), p. 3. arXiv: 0811.3458 [hep-ph] (cit. on pp. 19, 30).

[37] A. Denner et al. „HAWK 2.0: A Monte Carlo program for Higgs production in vector-boson fusion and Higgs strahlung at hadron colliders“. *Comput. Phys. Commun.* 195 (2015), pp. 161–171. arXiv: 1412.5390 [hep-ph] (cit. on pp. 19, 20).

[38] M. Ciccolini, A. Denner, and S. Dittmaier. „Strong and electroweak corrections to the production of Higgs + 2jets via weak interactions at the LHC“. *Phys. Rev. Lett.* 99 (2007), p. 161803. arXiv: 0707.0381 [hep-ph] (cit. on p. 19).

[39] M. Ciccolini, A. Denner, and S. Dittmaier. „Electroweak and QCD corrections to Higgs production via vector-boson fusion at the LHC“. *Phys. Rev. D* 77 (2008), p. 013002. arXiv: 0710.4749 [hep-ph] (cit. on p. 19).

[40] A. Denner et al. „Electroweak corrections to Higgs-strahlung off W/Z bosons at the Tevatron and the LHC with HAWK“. *JHEP* 03 (2012), p. 75. arXiv: 1112.5142 [hep-ph] (cit. on pp. 19, 20).

[41] A. Denner, S. Dittmaier, and J.-N. Lang. „Renormalization of mixing angles“. *JHEP* 11 (2018), p. 104. arXiv: 1808.03466 [hep-ph] (cit. on p. 19).

[42] P. Bolzoni et al. „Higgs production via vector-boson fusion at NNLO in QCD“. *Phys. Rev. Lett.* 105 (2010), p. 011801. arXiv: 1003.4451 [hep-ph] (cit. on p. 19).

[43] P. Bolzoni et al. „Vector boson fusion at NNLO in QCD: SM Higgs and beyond“. *Phys. Rev. D* 85 (2012), p. 035002. arXiv: 1109.3717 [hep-ph] (cit. on p. 19).

[44] T. Han, G. Valencia, and S. Willenbrock. „Structure function approach to vector boson scattering in pp collisions“. *Phys. Rev. Lett.* 69 (1992), pp. 3274–3277. arXiv: hep-ph/9206246 [hep-ph] (cit. on p. 19).

[45] O. Brein, A. Djouadi, and R. Harlander. „NNLO QCD corrections to the Higgs-strahlung processes at hadron colliders“. *Phys. Lett. B* 579 (2004), pp. 149–156. arXiv: hep-ph/0307206 [hep-ph] (cit. on pp. 19, 20).

[46] O. Brein, R. V. Harlander, and T. J. E. Zirke. „vh@nnlo - Higgs Strahlung at hadron colliders“. *Comput. Phys. Commun.* 184 (2013), pp. 998–1003. arXiv: 1210.5347 [hep-ph] (cit. on p. 20).

[47] R. V. Harlander, S. Liebler, and T. Zirke. „Higgs Strahlung at the Large Hadron Collider in the 2-Higgs-Doublet Model“. *JHEP* 02 (2014), p. 23. arXiv: 1307.8122 [hep-ph] (cit. on p. 20).

[48] L. Altenkamp et al. „Gluon-induced Higgs-strahlung at next-to-leading order QCD“. *JHEP* 02 (2013), p. 78. arXiv: 1211.5015 [hep-ph] (cit. on p. 20).

[49] R. V. Harlander et al. „Soft gluon resummation for gluon-induced Higgs Strahlung“. *JHEP* 11 (2014), p. 82. arXiv: 1410.0217 [hep-ph] (cit. on p. 20).

[50] L. Reina and S. Dawson. „Next-to-leading order results for $t\bar{t}h$ production at the Tevatron“. *Phys. Rev. Lett.* 87 (2001), p. 201804. arXiv: hep-ph/0107101 [hep-ph] (cit. on p. 20).

[51] S. Dawson et al. „Associated top quark Higgs boson production at the LHC“. *Phys. Rev. D* 67 (2003), p. 071503. arXiv: hep-ph/0211438 [hep-ph] (cit. on p. 20).

[52] S. Dawson et al. „Associated Higgs production with top quarks at the large hadron collider: NLO QCD corrections“. *Phys. Rev. D* 68 (2003), p. 034022. arXiv: hep-ph/0305087 [hep-ph] (cit. on p. 20).

[53] W. Beenakker et al. „Higgs radiation off top quarks at the Tevatron and the LHC“. *Phys. Rev. Lett.* 87 (2001), p. 201805. arXiv: hep-ph/0107081 [hep-ph] (cit. on p. 20).

[54] W. Beenakker et al. „NLO QCD corrections to $t\bar{t}H$ production in hadron collisions“. *Nucl. Phys. B* 653 (2003), pp. 151–203. arXiv: hep-ph/0211352 [hep-ph] (cit. on p. 20).

[55] Y. Zhang et al. „QCD NLO and EW NLO corrections to $t\bar{t}H$ production with top quark decays at hadron collider“. *Phys. Lett. B* 738 (2014), pp. 1–5. arXiv: 1407.1110 [hep-ph] (cit. on p. 20).

[56] S. Frixione et al. „Weak corrections to Higgs hadroproduction in association with a top-quark pair“. *JHEP* 09 (2014), p. 65. arXiv: 1407.0823 [hep-ph] (cit. on p. 20).

[57] S. Frixione et al. „Electroweak and QCD corrections to top-pair hadroproduction in association with heavy bosons“. *JHEP* 06 (2015), p. 184. arXiv: 1504.03446 [hep-ph] (cit. on p. 20).

[58] P. Ciafaloni and D. Comelli. „Sudakov enhancement of electroweak corrections“. *Phys. Lett. B* 446 (1999), pp. 278–284. arXiv: hep-ph/9809321 [hep-ph] (cit. on p. 20).

[59] M. Ciafaloni, P. Ciafaloni, and D. Comelli. „Bloch-Nordsieck violating electroweak corrections to inclusive TeV scale hard processes“. *Phys. Rev. Lett.* 84 (2000), pp. 4810–4813. arXiv: hep-ph/0001142 [hep-ph] (cit. on p. 20).

[60] A. Denner and S. Pozzorini. „One loop leading logarithms in electroweak radiative corrections. 1. Results“. *Eur. Phys. J. C* 18 (2001), pp. 461–480. arXiv: hep-ph/0010201 [hep-ph] (cit. on p. 20).

[61] A. Denner and S. Pozzorini. „One loop leading logarithms in electroweak radiative corrections. 2. Factorization of collinear singularities“. *Eur. Phys. J. C* 21 (2001), pp. 63–79. arXiv: hep-ph/0104127 [hep-ph] (cit. on p. 20).

[62] J. M. Butterworth et al. „Jet substructure as a new Higgs search channel at the LHC“. *Phys. Rev. Lett.* 100 (2008), p. 242001. arXiv: 0802.2470 [hep-ph] (cit. on p. 20).

[63] M. Bonvini, A. S. Papanastasiou, and F. J. Tackmann. „Matched predictions for the $b\bar{b}H$ cross section at the 13 TeV LHC“. *JHEP* 10 (2016), p. 53. arXiv: 1605.01733 [hep-ph] (cit. on pp. 20, 34, 35, 185).

[64] R. V. Harlander. „Higgs production in heavy quark annihilation through next-to-next-to-leading order QCD“. *Eur. Phys. J. C* 76.5 (2016), p. 252. arXiv: 1512.04901 [hep-ph] (cit. on pp. 20, 35, 184).

[65] F. Demartin et al. „Higgs production in association with a single top quark at the LHC“. *Eur. Phys. J. C* 75.6 (2015), p. 267. arXiv: 1504.00611 [hep-ph] (cit. on p. 21).

[66] F. Demartin et al. „*tWH* associated production at the LHC“. *Eur. Phys. J. C* 77.1 (2017), p. 34. arXiv: 1607.05862 [hep-ph] (cit. on p. 21).

[67] T. Schörner-Sadenius. *The Large Hadron Collider*. Springer-Verlag, 2015 (cit. on pp. 24, 25).

[68] J. Campbell, J. Huston, and F. Krauss. *The black book of quantum chromodynamics: a primer for the LHC era*. Oxford: Oxford University Press, 2018. URL: https://cds.cern.ch/record/2286381 (cit. on pp. 26, 27).

[69] V. N. Gribov and L. N. Lipatov. „Deep inelastic *ep* scattering in perturbation theory“. *Sov. J. Nucl. Phys.* 15 (1972), pp. 438–450 (cit. on p. 26).

[70] L. N. Lipatov. „The parton model and perturbation theory“. *Sov. J. Nucl. Phys.* 20 (1975), pp. 94–102 (cit. on p. 26).

[71] G. Altarelli and G. Parisi. „Asymptotic Freedom in Parton Language“. *Nucl. Phys. B* 126 (1977), pp. 298–318 (cit. on p. 26).

[72] Y. L. Dokshitzer. „Calculation of the Structure Functions for Deep Inelastic Scattering and e^+e^- Annihilation by Perturbation Theory in Quantum Chromodynamics.“ *Sov. Phys. JETP* 46 (1977), pp. 641–653 (cit. on p. 26).

[73] J. Collins. *Foundations of perturbative QCD*. Vol. 32. Cambridge University Press, Nov. 2013 (cit. on p. 27).

[74] J. C. Collins, D. E. Soper, and G. F. Sterman. „Factorization of Hard Processes in QCD“. Vol. 5. 1989, pp. 1–91. arXiv: hep-ph/0409313 (cit. on p. 27).

[75] A. Buckley et al. „General-purpose event generators for LHC physics“. *Phys. Rept.* 504 (2011), pp. 145–233. arXiv: 1101.2599 [hep-ph] (cit. on pp. 28, 29).

[76] T. Sjöstrand, S. Mrenna, and P. Z. Skands. „PYTHIA 6.4 Physics and Manual“. *JHEP* 05 (2006), p. 26. arXiv: hep-ph/0603175 [hep-ph] (cit. on pp. 29, 32).

[77] T. Sjöstrand, S. Mrenna, and P. Z. Skands. „A Brief Introduction to PYTHIA 8.1“. *Comput. Phys. Commun.* 178 (2008), pp. 852–867. arXiv: 0710.3820 [hep-ph] (cit. on pp. 29, 32, 97, 141).

[78] B. Andersson et al. „Parton fragmentation and string dynamics“. *Physics Reports* 97.2 (1983), pp. 31–145 (cit. on p. 29).

[79] B. Andersson, G. Gustafson, and B. Söderberg. „A General Model for Jet Fragmentation“. *Z. Phys. C* 20 (1983), p. 317 (cit. on p. 29).

[80] T. Sjöstrand. „The merging of jets“. *Physics Letters B* 142.5 (1984), pp. 420–424 (cit. on p. 29).

[81] M. Spira et al. „Higgs boson production at the LHC“. *Nucl. Phys. B* 453 (1995), pp. 17–82. arXiv: hep-ph/9504378 (cit. on p. 30).

[82] R. Harlander and P. Kant. „Higgs production and decay: Analytic results at next-to-leading order QCD“. *JHEP* 12 (2005), p. 15. arXiv: hep-ph/0509189 (cit. on p. 30).

[83] U. Aglietti et al. „Analytic Results for Virtual QCD Corrections to Higgs Production and Decay“. *JHEP* 01 (2007), p. 21. arXiv: hep-ph/0611266 (cit. on p. 30).

[84] R. Bonciani, Giuseppe Degrassi, and A. Vicini. „Scalar particle contribution to Higgs production via gluon fusion at NLO“. *JHEP* 11 (2007), p. 95. arXiv: 0709.4227 [hep-ph] (cit. on p. 30).

[85] C. Anastasiou et al. „Two-loop amplitudes and master integrals for the production of a Higgs boson via a massive quark and a scalar-quark loop“. *JHEP* 01 (2007), p. 82. arXiv: hep-ph/0611236 (cit. on p. 30).

[86] C. Anastasiou, S. Bucherer, and Z. Kunszt. „HPro: A NLO Monte-Carlo for Higgs production via gluon fusion with finite heavy quark masses“. *JHEP* 10 (2009), p. 68. arXiv: 0907.2362 [hep-ph] (cit. on p. 30).

[87] K. Melnikov and A. Penin. „On the light quark mass effects in Higgs boson production in gluon fusion“. *JHEP* 05 (2016). arXiv: 1602.09020 [hep-ph] (cit. on p. 31).

[88] C. W. Bauer, S. Fleming, and M. E. Luke. „Summing Sudakov logarithms in $B \to X_s\gamma$ in effective field theory“. *Phys. Rev. D* 63 (2000), p. 014006. arXiv: hep-ph/0005275 (cit. on p. 32).

[89] T. Becher, A. Broggio, and A. Ferroglia. *Introduction to Soft-Collinear Effective Theory*. Vol. 896. Lecture Notes in Physics. Springer International Publishing, 2015 (cit. on p. 32).

[90] K. Hamilton et al. „NNLOPS simulation of Higgs boson production“. *JHEP* 10 (2013), p. 222. arXiv: 1309.0017 [hep-ph] (cit. on p. 32).

[91] K. Hamilton et al. „Merging H/W/Z + 0 and 1 jet at NLO with no merging scale: a path to parton shower + NNLO matching“. *JHEP* 05 (2013), p. 82. arXiv: 1212.4504 [hep-ph] (cit. on p. 32).

[92] S. Catani and M. Grazzini. „An NNLO subtraction formalism in hadron collisions and its application to Higgs boson production at the LHC“. *Phys. Rev. Lett.* 98 (2007), p. 222002. arXiv: hep-ph/0703012 [hep-ph] (cit. on p. 32).

[93] M. Grazzini. „NNLO predictions for the Higgs boson signal in the $H \to WW \to lvlv$ and $H \to ZZ \to 4l$ decay channels“. *JHEP* 02 (2008), p. 43. arXiv: 0801.3232 [hep-ph] (cit. on p. 32).

[94] M. Grazzini and H. Sargsyan. „Heavy-quark mass effects in Higgs boson production at the LHC“. *JHEP* 09 (2013), p. 129. arXiv: 1306.4581 [hep-ph] (cit. on p. 32).

[95] D. de Florian et al. „Higgs boson production at the LHC: transverse momentum resummation effects in the $H \to \gamma\gamma$, $H \to WW \to lvlv$ and $H \to ZZ \to 4l$ decay modes“. *JHEP* 06 (2012), p. 132. arXiv: 1203.6321 [hep-ph] (cit. on p. 32).

[96] K. Hamilton, P. Nason, and G. Zanderighi. „Finite quark-mass effects in the NNLOPS POWHEG+MiNLO Higgs generator“. *JHEP* 05 (2015), p. 140. arXiv: 1501.04637 [hep-ph] (cit. on p. 32).

[97] R. Boughezal et al. „Color singlet production at NNLO in MCFM“. *Eur. Phys. J. C* 77.1 (2017), p. 7. arXiv: 1605.08011 [hep-ph] (cit. on p. 32).

[98] J. Gaunt et al. „N-jettiness Subtractions for NNLO QCD Calculations“. *JHEP* 09 (2015), p. 58. arXiv: 1505.04794 [hep-ph] (cit. on p. 32).

[99] M. A. Ebert, J. K. L. Michel, and F. J. Tackmann. „Resummation Improved Rapidity Spectrum for Gluon Fusion Higgs Production“. *JHEP* 05 (2017), p. 88. arXiv: 1702.00794 [hep-ph] (cit. on p. 32).

[100] M. A. Ebert et al. *SCETlib: A C++ Package for Numerical Calculations in QCD and Soft-Collinear Effective Theory*. http://scetlib.desy.de (cit. on pp. 32, 33).

[101] I. W. Stewart et al. „Jet p_T resummation in Higgs production at $NNLL' + NNLO$“. *Phys. Rev. D* 89.5 (2014), p. 054001. arXiv: 1307.1808 [hep-ph] (cit. on p. 33).

[102] X. Chen et al. „NNLO QCD corrections to Higgs boson production at large transverse momentum“. *JHEP* 10 (2016), p. 66. arXiv: 1607.08817 [hep-ph] (cit. on p. 33).

[103] X. Chen et al. „Precise QCD Description of the Higgs Boson Transverse Momentum Spectrum“. *Phys. Lett. B* 788 (2019), pp. 425–430. arXiv: 1805.00736 [hep-ph] (cit. on p. 33).

[104] Monni, P. F. and Re, E. and Torrielli, P. „Higgs Transverse-Momentum Resummation in Direct Space“. *Phys. Rev. Lett.* 116.24 (2016), p. 242001. arXiv: 1604.02191 [hep-ph] (cit. on pp. 33, 179).

[105] Banfi, A. and Monni, P. F. and Zanderighi, G. „Quark masses in Higgs production with a jet veto“. *JHEP* 01 (2014), p. 97. arXiv: 1308.4634 [hep-ph] (cit. on pp. 33, 179).

[106] M. Bonvini, A. S. Papanastasiou, and F. J. Tackmann. „Resummation and matching of b-quark mass effects in $b\bar{b}H$ production“. *JHEP* 11 (2015), p. 196. arXiv: 1508.03288 [hep-ph] (cit. on p. 34).

[107] M. Wiesemann et al. „Higgs production in association with bottom quarks“. *JHEP* 02 (2015), p. 132. arXiv: 1409.5301 [hep-ph] (cit. on p. 34).

[108] R. V. Harlander and W. B. Kilgore. „Higgs boson production in bottom quark fusion at next-to-next-to leading order“. *Phys. Rev. D* 68 (2003), p. 013001. arXiv: hep-ph/0304035 [hep-ph] (cit. on p. 34).

[109] S. Dittmaier, M. Krämer, and M. Spira. „Higgs radiation off bottom quarks at the Tevatron and the CERN LHC“. *Phys. Rev. D* 70 (2004), p. 074010. arXiv: hep-ph/0309204 [hep-ph] (cit. on p. 34).

[110] S. Dawson et al. „Exclusive Higgs boson production with bottom quarks at hadron colliders“. *Phys. Rev. D* 69 (2004), p. 074027. arXiv: hep-ph/0311067 [hep-ph] (cit. on p. 34).

[111] F. Maltoni, G. Ridolfi, and M. Ubiali. „b-initiated processes at the LHC: a reappraisal“. *JHEP* 07 (2012). [Erratum: JHEP04,095(2013)], p. 22. arXiv: 1203.6393 [hep-ph] (cit. on p. 34).

[112] B. Jäger, L. Reina, and D. Wackeroth. „Higgs boson production in association with b jets in the POWHEG BOX“. *Phys. Rev. D* 93.1 (2016), p. 014030. arXiv: 1509.05843 [hep-ph] (cit. on pp. 35, 141).

[113] J. Alwall et al. „The automated computation of tree-level and next-to-leading order differential cross sections, and their matching to parton shower simulations“. *JHEP* 07 (2014), p. 79. arXiv: 1405.0301 [hep-ph] (cit. on pp. 35, 141, 183).

[114] C. Kiefer. *Quantum gravity; 2nd ed.* International series of monographs on physics. Oxford Univ. Pr., 2007 (cit. on pp. 35, 36).

[115] M. P. Hobson, G. Efstathiou, and A. N. Lasenby. *General Relativity: An Introduction for Physicists*. New York: Cambridge University Press, 2006 (cit. on p. 35).

[116] X. Calmet, ed. *Quantum aspects of black holes*. Vol. 178. Springer, 2015. URL: http://www.springer.com/978-3-319-10851-3 (cit. on p. 36).

[117] M. Christodoulou and C. Rovelli. „On the possibility of laboratory evidence for quantum superposition of geometries“. *Phys. Lett. B* 792 (2019), pp. 64–68. arXiv: 1808.05842 [gr-qc] (cit. on p. 37).

[118] G. Bertone. *Particle dark matter: observations, models and searches*. Cambridge: Cambridge Univ. Press, 2010. URL: https://cds.cern.ch/record/1235368 (cit. on p. 37).

[119] S. Profumo. *An Introduction to Particle Dark Matter*. Advanced textbooks in physics. World Scientific, 2017. ISBN: 9781786340009 (cit. on p. 37).

[120] J. Baur et al. „Lyman-alpha Forests cool Warm Dark Matter“. *JCAP* 08 (2016), p. 12. arXiv: 1512.01981 [astro-ph.CO] (cit. on p. 37).

[121] O. S. Bruning et al. *LHC Design Report Vol.1: The LHC Main Ring*. 2004 (cit. on pp. 39, 40).

[122] CERN. *Accelerators*. https://home.cern/science/accelerators. [Accessed 23-October-2019] (cit. on p. 39).

[123] The ATLAS Collaboration. *Luminosity Public Results Run2*. https://twiki.cern.ch/twiki/bin/view/AtlasPublic/LuminosityPublicResultsRun2. Accessed: 2019-01-11 (cit. on p. 41).

[124] Z. Marshall. „Simulation of Pile-up in the ATLAS Experiment“. *J. Phys. Conf. Ser.* 513 (2014), p. 022024 (cit. on p. 40).

[125] ATLAS Experiment. *Detector & Technology*. https://atlas.cern/discover/detector. Accessed: 2019-01-11. 2019 (cit. on p. 43).

[126] The ATLAS Collaboration. „The ATLAS Experiment at the CERN Large Hadron Collider“. *JINST* 3 (2008), S08003 (cit. on pp. 42, 45, 48–50, 52–55, 57, 60, 79).

[127] The ATLAS Collaboration. *Technical Design Report for the ATLAS Inner Tracker Pixel Detector*. Tech. rep. CERN-LHCC-2017-021. ATLAS-TDR-030. Geneva: CERN, Sept. 2017. URL: https://cds.cern.ch/record/2285585 (cit. on p. 46).

[128] The ATLAS Collaboration. *Track Reconstruction Performance of the ATLAS Inner Detector at* $\sqrt{s} = 13$ *TeV*. Tech. rep. ATL-PHYS-PUB-2015-018. Geneva: CERN, July 2015. URL: https://cds.cern.ch/record/2037683 (cit. on p. 46).

[129] ATLAS Experiment. *Computer generated image of the ATLAS inner detector*. http://cdsweb.cern.ch/record/1095926. Accessed: 2019-08-05. 2008 (cit. on p. 47).

[130] M. Capeans et al. *ATLAS Insertable B-Layer Technical Design Report*. Tech. rep. CERN-LHCC-2010-013. ATLAS-TDR-19. Sept. 2010. URL: https://cds.cern.ch/record/1291633 (cit. on pp. 48, 60).

[131] ATLAS TRT Collaboration. „The ATLAS Transition Radiation Tracker (TRT) proportional drift tube: design and performance“. *JINST* 3 (2008), P02013. URL: https://cds.cern.ch/record/1094549 (cit. on p. 49).

[132] The ATLAS Collaboration. „Performance of the ATLAS Transition Radiation Tracker in Run 1 of the LHC: tracker properties“. *JINST* 12.05 (2017), P05002. arXiv: 1702.06473 [hep-ex] (cit. on pp. 50, 61).

[133] C. Grupen and B. Schwartz. *Particle detectors*. Vol. 26. Cambridge, UK: Cambridge Univ. Pr., 2008 (cit. on pp. 52, 58, 85).

[134] Ph. Schwemling. „The ATLAS liquid argon calorimeters: Construction, integration, commissioning and performance from selected beam-test results“. *Nucl. Instrum. Meth. A* 598 (2009), pp. 253–257 (cit. on p. 53).

[135] J. Pequenao and P. Schaffner. „How ATLAS detects particles: diagram of particle paths in the detector“. Jan. 2013. URL: https://cds.cern.ch/record/1505342 (cit. on p. 59).

[136] The ATLAS Collaboration. „The upgraded Pixel Detector of the ATLAS Experiment for Run 2 at the Large Hadron Collider“. *Nucl. Instrum. Meth. A* 831 (2016), pp. 65–70 (cit. on p. 60).

[137] The ATLAS Collaboration. „ATLAS event at 13 TeV - 21 May 2015 - Run 265545 Event 5720351“. General Photo. May 2015. URL: https://cds.cern.ch/record/2017716 (cit. on p. 60).

[138] T. Cornelissen et al. *Concepts, Design and Implementation of the ATLAS New Tracking (NEWT)*. Tech. rep. ATL-SOFT-PUB-2007-007. ATL-COM-SOFT-2007-002. Geneva: CERN, Mar. 2007. URL: https://cds.cern.ch/record/1020106 (cit. on pp. 61, 62).

[139] R. Frühwirth. „Application of Kalman filtering to track and vertex fitting“. *Nucl. Instrum. Meth. A* 262 (1987), pp. 444–450 (cit. on p. 61).

[140] Thijs G. Cornelissen et al. „The global chi**2 track fitter in ATLAS“. *J. Phys. Conf. Ser.* 119 (2008), p. 032013 (cit. on p. 62).

[141] The ATLAS Collaboration. *Improved electron reconstruction in ATLAS using the Gaussian Sum Filter-based model for bremsstrahlung*. ATLAS-CONF-2012-047. Geneva, May 2012. URL: https://cds.cern.ch/record/1449796 (cit. on p. 62).

[142] The ATLAS Collaboration. *Early Inner Detector Tracking Performance in the 2015 data at* $\sqrt{s} = 13$ *TeV*. Tech. rep. ATL-PHYS-PUB-2015-051. Geneva: CERN, Dec. 2015. URL: https://cds.cern.ch/record/2110140 (cit. on p. 62).

[143] The ATLAS Collaboration. „Reconstruction of primary vertices at the ATLAS experiment in Run 1 proton–proton collisions at the LHC“. *Eur. Phys. J. C* 77.5 (2017), p. 332. arXiv: 1611.10235 [physics.ins-det] (cit. on p. 63).

[144] The ATLAS Collaboration. „Measurement of Higgs boson production in the diphoton decay channel in pp collisions at center-of-mass energies of 7 and 8 TeV with the ATLAS detector“. *Phys. Rev. D* 90.11 (2014), p. 112015. arXiv: 1408.7084 [hep-ex] (cit. on p. 65).

[145] The ATLAS Collaboration. *Measurements and interpretations of Higgs-boson fiducial cross sections in the diphoton decay channel using 139* fb^{-1} *of pp collision data at* $\sqrt{s} = 13$ *TeV with the ATLAS detector*. ATLAS-CONF-2019-029. Geneva, 2019 (cit. on pp. 65, 149, 175, 193).

[146] The ATLAS Collaboration. *Electron and photon reconstruction and performance in ATLAS using a dynamical, topological cell clustering-based approach*. Tech. rep. ATL-PHYS-PUB-2017-022. Geneva: CERN, Dec. 2017. URL: https://cds.cern.ch/record/2298955 (cit. on p. 66).

[147] The ATLAS Collaboration. „Electron and photon performance measurements with the ATLAS detector using the 2015–2017 LHC proton-proton collision data“. *JINST* 14.12 (2019), P12006. arXiv: 1908.00005 [hep-ex] (cit. on pp. 66, 67, 69, 70, 72, 73, 131, 133, 134, 160).

[148] The ATLAS Collaboration. „Electron and photon energy calibration with the ATLAS detector using 2015–2016 LHC proton-proton collision data“. *JINST* 14.03 (2019), P03017. arXiv: 1812.03848 [hep-ex] (cit. on pp. 70, 158).

[149] J. J. Apostolakis et al. *Elementary particles: Subvolume B. Detectors for Particles and Radiation, Part 1, Principles and Methods*. Ed. by C. W. Fabjan and H. Schopper. Landolt-Börnstein. New series. Group 1 Elementary particles, nuclei and atoms. Berlin: Springer, 2011 (cit. on pp. 70, 85).

[150] The ATLAS Collaboration. „Electron reconstruction and identification in the ATLAS experiment using the 2015 and 2016 LHC proton-proton collision data at $\sqrt{s} = 13$ TeV“. *Eur. Phys. J. C* 79.8 (2019), p. 639. arXiv: 1902.04655 [physics.ins-det] (cit. on pp. 73, 74, 101).

[151] M. Cacciari, G. P. Salam, and G. Soyez. „The anti-k_t jet clustering algorithm“. *JHEP* 04 (2008), p. 63. arXiv: 0802.1189 [hep-ph] (cit. on p. 74).

[152] The ATLAS Collaboration. „Jet energy scale measurements and their systematic uncertainties in proton-proton collisions at $\sqrt{s} = 13$ TeV with the ATLAS detector“. *Phys. Rev. D* 96.7 (2017), p. 072002. arXiv: 1703.09665 [hep-ex] (cit. on p. 76).

[153] The ATLAS Collaboration. „Determination of jet calibration and energy resolution in proton-proton collisions at $\sqrt{s} = 8$ TeV using the ATLAS detector“ (2019). arXiv: 1910.04482 [hep-ex] (cit. on p. 76).

[154] M. Cacciari and G. P. Salam. „Pileup subtraction using jet areas“. *Phys. Lett. B* 659 (2008), pp. 119–126. arXiv: 0707.1378 [hep-ph] (cit. on p. 76).

[155] S. Catani et al. „Longitudinally-invariant $k_\perp$-clustering algorithms for hadron-hadron collisions“. *Nucl. Phys. B* 406.CERN-TH-6775-93. LU-TP-93-2 (Feb. 1993), 187–224. 38 p. URL: https://cds.cern.ch/record/246812 (cit. on p. 76).

[156] The ATLAS Collaboration. „Jet energy measurement with the ATLAS detector in proton-proton collisions at $\sqrt{s} = 7$ TeV“. *Eur. Phys. J. C* 73.3 (2013), p. 2304. arXiv: 1112.6426 [hep-ex] (cit. on p. 76).

[157] The ATLAS Collaboration. „Muon reconstruction performance of the ATLAS detector in proton–proton collision data at $\sqrt{s} = 13$ TeV“. *Eur. Phys. J. C* 76.5 (2016), p. 292. arXiv: 1603.05598 [hep-ex] (cit. on pp. 77, 144).

[158] The ATLAS Collaboration. „Performance of the ATLAS Trigger System in 2015“. *Eur. Phys. J. C* 77.5 (2017), p. 317. arXiv: 1611.09661 [hep-ex] (cit. on p. 78).

[159] The ATLAS Collaboration. „Luminosity determination in pp collisions at $\sqrt{s} = 8$ TeV using the ATLAS detector at the LHC“. *Eur. Phys. J. C* 76.12 (2016), p. 653. arXiv: 1608.03953 [hep-ex] (cit. on p. 79).

[160] P. Grafström and W. Kozanecki. „Luminosity determination at proton colliders“. *Progress in Particle and Nuclear Physics* 81 (2015), pp. 97–148. ISSN: 0146-6410. URL: http://www.sciencedirect.com/science/article/pii/S0146641014000878 (cit. on p. 80).

[161] The ATLAS Collaboration. „Measurement of the photon identification efficiencies with the ATLAS detector using LHC Run 2 data collected in 2015 and 2016“. *Eur. Phys. J. C* 79.3 (2019), p. 205. arXiv: 1810.05087 [hep-ex] (cit. on pp. 86, 93, 95).

[162] L. Devroye. *Non-Uniform Random Variate Generation*. Springer-Verlag New York, 1986 (cit. on p. 89).

[163] G. Cowan. *Statistical Data Analysis*. Oxford science publications. Clarendon Press, 1998. ISBN: 9780198501558 (cit. on pp. 92, 153–155, 192, 193).

[164] S. Alioli et al. „NLO vector-boson production matched with shower in POWHEG“. *JHEP* 07 (2008), p. 60. arXiv: 0805.4802 [hep-ph] (cit. on p. 97).

[165] N. Chamandy et al. *Estimating Uncertainty for Massive Data Streams*. Tech. rep. Google, 2012 (cit. on p. 119).

[166] C. Blocker. *Uncertainties on Efficiencies*. Tech. rep. CDF/MEMO/STATISTICS/PUBLIC/7168. 2004. URL: https://www-cdf.fnal.gov/physics/statistics/notes/cdf7168_eff_uncertainties.ps (cit. on p. 122).

[167] A. Valassi and R. Chierici. „Information and treatment of unknown correlations in the combination of measurements using the BLUE method“. *Eur. Phys. J. C* 74 (2014), p. 2717. arXiv: 1307.4003 [physics.data-an] (cit. on p. 131).

[168] L. Lyons, D. Gibaut, and P. Clifford. „How to Combine Correlated Estimates of a Single Physical Quantity“. *Nucl. Instrum. Meth. A* 270 (1988), p. 110 (cit. on p. 131).

[169] The ATLAS Collaboration. „The ATLAS Simulation Infrastructure“. *Eur. Phys. J. C* 70 (2010), pp. 823–874. arXiv: 1005.4568 [physics.ins-det] (cit. on pp. 140, 141).

[170] The ATLAS Collaboration. *A study of the Pythia 8 description of ATLAS minimum bias measurements with the Donnachie-Landshoff diffractive model*. Tech. rep. ATL-PHYS-PUB-2016-017. Geneva: CERN, Aug. 2016. URL: https://cds.cern.ch/record/2206965 (cit. on p. 140).

[171] The ATLAS Collaboration. *Measurements of Higgs boson properties in the diphoton decay channel using 80 fb^{-1} of pp collision data at $\sqrt{s} = 13$ TeV with the ATLAS detector*. ATLAS-CONF-2018-028. Geneva, July 2018. URL: https://cds.cern.ch/record/2628771 (cit. on pp. 140, 147, 166, 167, 169, 170, 194).

[172] P. Nason. „A New method for combining NLO QCD with shower Monte Carlo algorithms“. *JHEP* 11 (2004), p. 40. arXiv: hep-ph/0409146 [hep-ph] (cit. on p. 141).

[173] S. Frixione, P. Nason, and C. Oleari. „Matching NLO QCD computations with Parton Shower simulations: the POWHEG method“. *JHEP* 11 (2007), p. 70. arXiv: 0709.2092 [hep-ph] (cit. on p. 141).

[174] S. Alioli et al. „A general framework for implementing NLO calculations in shower Monte Carlo programs: the POWHEG BOX“. *JHEP* 06 (2010), p. 43. arXiv: 1002.2581 [hep-ph] (cit. on p. 141).

[175] P. Nason and C. Oleari. „NLO Higgs boson production via vector-boson fusion matched with shower in POWHEG“. *JHEP* 02 (2010), p. 37. arXiv: 0911.5299 [hep-ph] (cit. on p. 141).

[176] G. Luisoni et al. „$HW^{\pm}$/HZ + 0 and 1 jet at NLO with the POWHEG BOX interfaced to GoSam and their merging within MiNLO“. *JHEP* 10 (2013), p. 83. arXiv: 1306.2542 [hep-ph] (cit. on p. 141).

[177] H. B. Hartanto et al. „Higgs boson production in association with top quarks in the POWHEG BOX“. *Phys. Rev. D* 91.9 (2015), p. 094003. arXiv: 1501.04498 [hep-ph] (cit. on p. 141).

[178] http://powhegbox.mib.infn.it/. Accessed: 2020-04-06 (cit. on p. 141).

[179] M. Bahr et al. „Herwig++ Physics and Manual“. *Eur. Phys. J. C* 58 (2008), pp. 639–707. arXiv: 0803.0883 [hep-ph] (cit. on p. 141).

[180] J. Bellm et al. „Herwig 7.0/Herwig++ 3.0 release note“. *Eur. Phys. J. C* 76.4 (2016), p. 196. arXiv: 1512.01178 [hep-ph] (cit. on p. 141).

[181] The ATLAS Collaboration. „Measurement of the Z/γ^* boson transverse momentum distribution in pp collisions at $\sqrt{s} = 7$ TeV with the ATLAS detector“. *JHEP* 09 (2014), p. 145. arXiv: 1406.3660 [hep-ex] (cit. on p. 141).

[182] The ATLAS Collaboration. *ATLAS Pythia 8 tunes to 7 TeV data*. Tech. rep. ATL-PHYS-PUB-2014-021. Geneva: CERN, Nov. 2014. URL: https://cds.cern.ch/record/1966419 (cit. on pp. 141, 188).

[183] H.-L. Lai et al. „New parton distributions for collider physics“. *Phys. Rev. D* 82 (2010), p. 074024. arXiv: 1007.2241 [hep-ph] (cit. on p. 141).

[184] J. Butterworth et al. „PDF4LHC recommendations for LHC Run II“. *J. Phys. G* 43 (2016), p. 023001. arXiv: 1510.03865 [hep-ph] (cit. on pp. 141, 182, 185).

[185] E. Bothmann et al. „Event Generation with Sherpa 2.2“. *SciPost Phys.* 7.3 (2019), p. 34. arXiv: 1905.09127 [hep-ph] (cit. on p. 141).

[186] T. Gleisberg et al. „Event generation with SHERPA 1.1“. *JHEP* 02 (2009), p. 7. arXiv: 0811.4622 [hep-ph] (cit. on p. 141).

[187] S. Schumann and F. Krauss. „A Parton shower algorithm based on Catani-Seymour dipole factorisation“. *JHEP* 03 (2008), p. 38. arXiv: 0709.1027 [hep-ph] (cit. on p. 141).

[188] S. Agostinelli et al. „GEANT4: A Simulation toolkit“. *Nucl. Instrum. Meth. A* 506 (2003), pp. 250–303 (cit. on p. 141).

[189] J. Allison et al. „Geant4 developments and applications“. *IEEE Trans. Nucl. Sci.* 53 (2006), p. 270 (cit. on p. 141).

[190] J. Allison et al. „Recent developments in Geant4“. *Nucl. Instrum. Meth. A* 835 (2016), pp. 186–225 (cit. on p. 141).

[191] The ATLAS Collaboration. „Performance of electron and photon triggers in ATLAS during LHC Run 2“. *Eur. Phys. J. C* 80.1 (2020), p. 47. arXiv: 1909.00761 [hep-ex] (cit. on p. 143).

[192] The ATLAS Collaboration. *Tagging and suppression of pileup jets with the ATLAS detector*. ATLAS-CONF-2014-018. Geneva, May 2014. URL: https://cds.cern.ch/record/1700870 (cit. on p. 144).

[193] The ATLAS Collaboration. „Performance of pile-up mitigation techniques for jets in pp collisions at $\sqrt{s} = 8$ TeV using the ATLAS detector“. *Eur. Phys. J. C* 76.11 (2016), p. 581. arXiv: 1510.03823 [hep-ex] (cit. on p. 144).

[194] The ATLAS Collaboration. „Performance of b-Jet Identification in the ATLAS Experiment“. *JINST* 11.04 (2016), P04008. arXiv: 1512.01094 [hep-ex] (cit. on pp. 144, 174).

[195] T. Skwarnicki. „A study of the radiative CASCADE transitions between the Upsilon-Prime and Upsilon resonances“. PhD thesis. Cracow, INP, 1986. URL: http://www-library.desy.de/cgi-bin/showprep.pl?DESY-F31-86-02 (cit. on p. 149).

[196] The ATLAS Collaboration. „Search for Scalar Diphoton Resonances in the Mass Range $65-600$ GeV with the ATLAS Detector in pp Collision Data at $\sqrt{s} = 8$ TeV“. *Phys. Rev. Lett.* 113.17 (2014), p. 171801. arXiv: 1407.6583 [hep-ex] (cit. on p. 149).

[197] The ATLAS Collaboration. „Measurement of the inclusive isolated prompt photon cross section in pp collisions at $\sqrt{s} = 7$ TeV with the ATLAS detector“. *Phys. Rev. D* 83 (2011), p. 052005. arXiv: 1012.4389 [hep-ex] (cit. on p. 151).

[198] The ATLAS Collaboration. „Measurement of the isolated di-photon cross-section in pp collisions at $\sqrt{s} = 7$ TeV with the ATLAS detector“. *Phys. Rev. D* 85 (2012), p. 012003. arXiv: 1107.0581 [hep-ex] (cit. on p. 151).

[199] Milton Abramowitz. *Handbook of Mathematical Functions, With Formulas, Graphs, and Mathematical Tables,* USA: Dover Publications, Inc., 1974. ISBN: 0486612724 (cit. on p. 152).

[200] The ATLAS Collaboration. *Luminosity determination in pp collisions at $\sqrt{s} = 13$ TeV using the ATLAS detector at the LHC*. ATLAS-CONF-2019-021. Geneva, June 2019. URL: https://cds.cern.ch/record/2677054 (cit. on p. 157).

[201] The ATLAS Collaboration. „Measurement of the Inelastic Proton-Proton Cross Section at $\sqrt{s} = 13$ TeV with the ATLAS Detector at the LHC“. *Phys. Rev. Lett.* 117.18 (2016), p. 182002. arXiv: 1606.02625 [hep-ex] (cit. on p. 159).

[202] CMS Collaborations ATLAS. „Measurements of the Higgs boson production and decay rates and constraints on its couplings from a combined ATLAS and CMS analysis of the LHC pp collision data at $\sqrt{s} = 7$ and 8 TeV“. *JHEP* 08 (2016), p. 45. arXiv: 1606.02266 [hep-ex] (cit. on p. 162).

[203] The ATLAS Collaboration. „Evidence for the associated production of the Higgs boson and a top quark pair with the ATLAS detector“. *Phys. Rev. D* 97.7 (2018), p. 072003. arXiv: 1712.08891 [hep-ex] (cit. on p. 162).

[204] The ATLAS Collaboration. „Observation of $H \to b\bar{b}$ decays and VH production with the ATLAS detector“. *Phys. Lett. B* 786.arXiv:1808.08238 (Aug. 2018), 59–86. 28 p. URL: https://cds.cern.ch/record/2636066 (cit. on p. 162).

[205] The ATLAS Collaboration. „Combined measurements of Higgs boson production and decay using up to 80 fb^{-1} of proton-proton collision data at $\sqrt{s}$ = 13 TeV collected with the ATLAS experiment“. *Phys. Rev. D* 101.1 (2020), p. 012002. arXiv: 1909.02845 [hep-ex] (cit. on pp. 173, 174, 212).

[206] The ATLAS Collaboration. *Measurements of WH and ZH production in the $H \to b\bar{b}$ decay channel in pp collisions at 13 TeV with the ATLAS detector*. ATLAS-CONF-2020-006. Geneva, Apr. 2020. URL: https://cds.cern.ch/record/2714885 (cit. on p. 174).

[207] The ATLAS Collaboration. „Cross-section measurements of the Higgs boson decaying into a pair of τ-leptons in proton-proton collisions at $\sqrt{s}$ = 13 TeV with the ATLAS detector“. *Phys. Rev. D* 99 (2019), p. 072001. arXiv: 1811.08856 [hep-ex] (cit. on p. 174).

[208] The CMS Collaboration. *Combined Higgs boson production and decay measurements with up to 137 fb^{-1} of proton-proton collision data at $\sqrt{s}$ = 13 TeV*. Geneva, 2020. URL: https://cds.cern.ch/record/2706103 (cit. on p. 174).

[209] The ATLAS Collaboration. „Search for the Decay of the Higgs Boson to Charm Quarks with the ATLAS Experiment“. *Phys. Rev. Lett.* 120.21 (2018), p. 211802. arXiv: 1802.04329 [hep-ex] (cit. on pp. 174, 212).

[210] The CMS Collaboration. „A search for the standard model Higgs boson decaying to charm quarks“. *JHEP* 2003 (Dec. 2019), 131. 54 p. eprint: 1912.01662. URL: https://cds.cern.ch/record/2703386 (cit. on pp. 174, 212).

[211] J. Pumplin et al. „Uncertainties of predictions from parton distribution functions. 2. The Hessian method“. *Phys. Rev. D* 65 (2001), p. 014013. arXiv: hep-ph/0101032 (cit. on p. 182).

[212] *PDFs for bbH process*. https://www.ge.infn.it/~bonvini/bbh/. [Accessed 15-April-2019] (cit. on p. 183).

[213] A. Buckley et al. „Rivet user manual“. *Comput. Phys. Commun.* 184 (2013), pp. 2803–2819. arXiv: 1003.0694 [hep-ph] (cit. on p. 184).

[214] G. 't Hooft and M. Veltman. „Regularization and renormalization of gauge fields“. *Nuclear Physics B* 44.1 (1972), pp. 189–213 (cit. on p. 184).

[215] G. 't Hooft. „Dimensional regularization and the renormalization group“. *Nuclear Physics B* 61 (1973), pp. 455–468 (cit. on p. 184).

[216] W. A. Bardeen et al. „Deep-inelastic scattering beyond the leading order in asymptotically free gauge theories“. *Phys. Rev. D* 18 (11 Dec. 1978), pp. 3998–4017 (cit. on p. 184).

[217] L. Del Debbio et al. „Unbiased determination of the proton structure function F_2^p with faithful uncertainty estimation“. *JHEP* 03 (2005), p. 80. arXiv: hep-ph/0501067 (cit. on p. 185).

[218] L. Del Debbio et al. „Neural network determination of parton distributions: The Nonsinglet case“. *JHEP* 03 (2007), p. 39. arXiv: hep-ph/0701127 (cit. on p. 186).

[219] R. D. Ball et al. „A Determination of parton distributions with faithful uncertainty estimation“. *Nucl. Phys. B* 809 (2009). [Erratum: Nucl.Phys.B 816, 293 (2009)], pp. 1–63. arXiv: 0808.1231 [hep-ph] (cit. on p. 186).

[220] O. Behnke et al. *Data Analysis in High Energy Physics*. Wiley-VCH, 2013 (cit. on p. 189).

[221] K. Cranmer. *Practical Statistics for the LHC*. 2015. arXiv: 1503.07622 (cit. on p. 189).

[222] The LHCb Collaboration. „Measurement of the CKM angle γ from a combination of LHCb results“. *JHEP* 12 (2016), p. 87. arXiv: 1611.03076 [hep-ex] (cit. on p. 191).

[223] *GammaCombo*. https://gammacombo.github.io/. [Accessed 21-March-2019] (cit. on p. 191).

[224] S. S. Wilks. „The Large-Sample Distribution of the Likelihood Ratio for Testing Composite Hypotheses“. *Annals Math. Statist.* 9.1 (1938), pp. 60–62 (cit. on p. 191).

[225] G. Cowan et al. „Asymptotic formulae for likelihood-based tests of new physics“. *Eur. Phys. J. C* 71 (2011). [Erratum: Eur. Phys. J.C73,2501(2013)], p. 1554. arXiv: 1007.1727 [physics.data-an] (cit. on p. 193).

A. Feynman Diagrams for Associated Higgs Boson and Single-Top-Quark Production

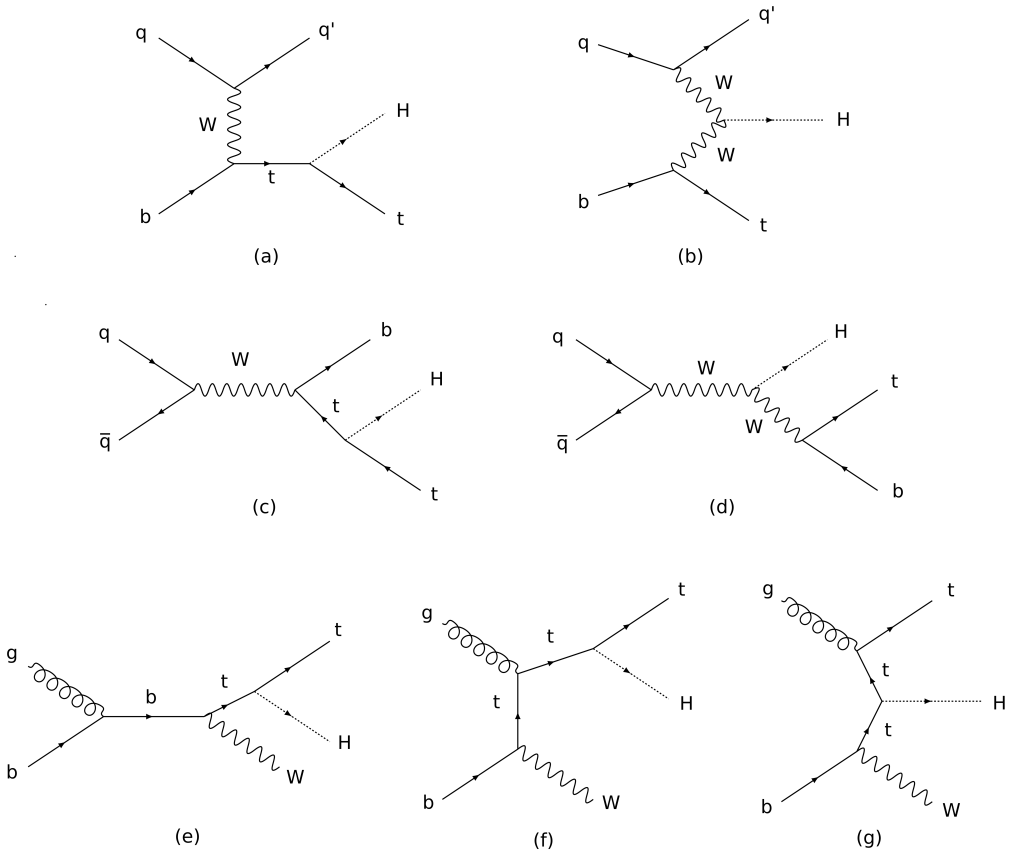

Figure A.1. | The leading-order Feynman diagrams in the 5-flavor-scheme (see Section 2.6.2) for Higgs boson production in association with a single t-quark. All of these diagrams involve a W boson. In the first row the t-channel diagrams are shown, in the second row the s-channel diagrams, and in the last row the diagrams with an on-shell W boson are shown.

B. Photon Identification Efficiencies

Pseudorapidity	Transverse momentum [GeV]	Measured efficiency	Total uncertainty
$0.0 < \|\eta\| < 0.6$	$25 < p_{\mathrm{T}} < 30$	0.827	0.019
	$30 < p_{\mathrm{T}} < 35$	0.869	0.027
	$35 < p_{\mathrm{T}} < 40$	0.898	0.022
	$40 < p_{\mathrm{T}} < 45$	0.904	0.026
	$45 < p_{\mathrm{T}} < 50$	0.920	0.029
	$50 < p_{\mathrm{T}} < 60$	0.929	0.031
	$60 < p_{\mathrm{T}} < 80$	0.948	0.020
	$80 < p_{\mathrm{T}} < 100$	0.958	0.010
	$100 < p_{\mathrm{T}} < 125$	0.967	0.013
	$125 < p_{\mathrm{T}} < 150$	0.971	0.008
	$150 < p_{\mathrm{T}} < 175$	0.971	0.009
	$175 < p_{\mathrm{T}} < 250$	0.981	0.008
$0.6 < \|\eta\| < 1.37$	$25 < p_{\mathrm{T}} < 30$	0.827	0.022
	$30 < p_{\mathrm{T}} < 35$	0.861	0.025
	$35 < p_{\mathrm{T}} < 40$	0.893	0.022
	$40 < p_{\mathrm{T}} < 45$	0.918	0.019
	$45 < p_{\mathrm{T}} < 50$	0.935	0.016
	$50 < p_{\mathrm{T}} < 60$	0.946	0.015
	$60 < p_{\mathrm{T}} < 80$	0.962	0.010
	$80 < p_{\mathrm{T}} < 100$	0.965	0.012
	$100 < p_{\mathrm{T}} < 125$	0.979	0.005
	$125 < p_{\mathrm{T}} < 150$	0.983	0.005
	$150 < p_{\mathrm{T}} < 175$	0.981	0.005
	$175 < p_{\mathrm{T}} < 250$	0.983	0.005
$1.52 < \|\eta\| < 1.81$	$25 < p_{\mathrm{T}} < 30$	0.823	0.018
	$30 < p_{\mathrm{T}} < 35$	0.843	0.021
	$35 < p_{\mathrm{T}} < 40$	0.879	0.017
	$40 < p_{\mathrm{T}} < 45$	0.895	0.018
	$45 < p_{\mathrm{T}} < 50$	0.919	0.015
	$50 < p_{\mathrm{T}} < 60$	0.937	0.012
	$60 < p_{\mathrm{T}} < 80$	0.946	0.013
	$80 < p_{\mathrm{T}} < 100$	0.961	0.010
	$100 < p_{\mathrm{T}} < 125$	0.967	0.010
	$125 < p_{\mathrm{T}} < 150$	0.972	0.009
	$150 < p_{\mathrm{T}} < 175$	0.981	0.010
	$175 < p_{\mathrm{T}} < 250$	0.970	0.005
$1.81 < \|\eta\| < 2.37$	$25 < p_{\mathrm{T}} < 30$	0.824	0.025
	$30 < p_{\mathrm{T}} < 35$	0.870	0.021
	$35 < p_{\mathrm{T}} < 40$	0.897	0.019
	$40 < p_{\mathrm{T}} < 45$	0.907	0.017
	$45 < p_{\mathrm{T}} < 50$	0.929	0.013
	$50 < p_{\mathrm{T}} < 60$	0.937	0.013
	$60 < p_{\mathrm{T}} < 80$	0.948	0.009
	$80 < p_{\mathrm{T}} < 100$	0.962	0.005
	$100 < p_{\mathrm{T}} < 125$	0.966	0.007
	$125 < p_{\mathrm{T}} < 150$	0.973	0.009
	$150 < p_{\mathrm{T}} < 175$	0.975	0.009
	$175 < p_{\mathrm{T}} < 250$	0.964	0.007

Table B.1. | Photon identication efficiencies and absolute uncertainties for converted photons as measured by the electron-extrapolation method, based on the data collected in 2015 – 2017.

Pseudorapidity	Transverse momentum [GeV]	Measured efficiency	Uncertainty
$0.0 < \|\eta\| < 0.6$	$25 < p_{\mathrm{T}} < 30$	0.858	0.018
	$30 < p_{\mathrm{T}} < 35$	0.865	0.024
	$35 < p_{\mathrm{T}} < 40$	0.886	0.020
	$40 < p_{\mathrm{T}} < 45$	0.896	0.016
	$45 < p_{\mathrm{T}} < 50$	0.911	0.013
	$50 < p_{\mathrm{T}} < 60$	0.918	0.013
	$60 < p_{\mathrm{T}} < 80$	0.927	0.012
	$80 < p_{\mathrm{T}} < 100$	0.928	0.013
	$100 < p_{\mathrm{T}} < 125$	0.932	0.018
	$125 < p_{\mathrm{T}} < 150$	0.931	0.021
	$150 < p_{\mathrm{T}} < 175$	0.924	0.024
	$175 < p_{\mathrm{T}} < 250$	0.928	0.032
$0.6 < \|\eta\| < 1.37$	$25 < p_{\mathrm{T}} < 30$	0.839	0.015
	$30 < p_{\mathrm{T}} < 35$	0.857	0.018
	$35 < p_{\mathrm{T}} < 40$	0.876	0.018
	$40 < p_{\mathrm{T}} < 45$	0.888	0.016
	$45 < p_{\mathrm{T}} < 50$	0.899	0.016
	$50 < p_{\mathrm{T}} < 60$	0.911	0.014
	$60 < p_{\mathrm{T}} < 80$	0.921	0.014
	$80 < p_{\mathrm{T}} < 100$	0.925	0.013
	$100 < p_{\mathrm{T}} < 125$	0.931	0.020
	$125 < p_{\mathrm{T}} < 150$	0.935	0.023
	$150 < p_{\mathrm{T}} < 175$	0.934	0.023
	$175 < p_{\mathrm{T}} < 250$	0.920	0.022
$1.52 < \|\eta\| < 1.81$	$25 < p_{\mathrm{T}} < 30$	0.850	0.016
	$30 < p_{\mathrm{T}} < 35$	0.863	0.013
	$35 < p_{\mathrm{T}} < 40$	0.889	0.008
	$40 < p_{\mathrm{T}} < 45$	0.893	0.011
	$45 < p_{\mathrm{T}} < 50$	0.912	0.008
	$50 < p_{\mathrm{T}} < 60$	0.926	0.008
	$60 < p_{\mathrm{T}} < 80$	0.933	0.006
	$80 < p_{\mathrm{T}} < 100$	0.933	0.007
	$100 < p_{\mathrm{T}} < 125$	0.937	0.006
	$125 < p_{\mathrm{T}} < 150$	0.940	0.006
	$150 < p_{\mathrm{T}} < 175$	0.945	0.006
	$175 < p_{\mathrm{T}} < 250$	0.947	0.006
$1.81 < \|\eta\| < 2.37$	$25 < p_{\mathrm{T}} < 30$	0.849	0.015
	$30 < p_{\mathrm{T}} < 35$	0.859	0.012
	$35 < p_{\mathrm{T}} < 40$	0.879	0.010
	$40 < p_{\mathrm{T}} < 45$	0.879	0.007
	$45 < p_{\mathrm{T}} < 50$	0.886	0.007
	$50 < p_{\mathrm{T}} < 60$	0.895	0.003
	$60 < p_{\mathrm{T}} < 80$	0.900	0.005
	$80 < p_{\mathrm{T}} < 100$	0.906	0.006
	$100 < p_{\mathrm{T}} < 125$	0.902	0.011
	$125 < p_{\mathrm{T}} < 150$	0.912	0.017
	$150 < p_{\mathrm{T}} < 175$	0.908	0.013
	$175 < p_{\mathrm{T}} < 250$	0.893	0.019

Table B.2. | Photon identication efficiencies and absolute uncertainties for unconverted photons as measured by the electron-extrapolation method, based on the data collected in 2015 – 2017.

C. Shower-Shape Distributions

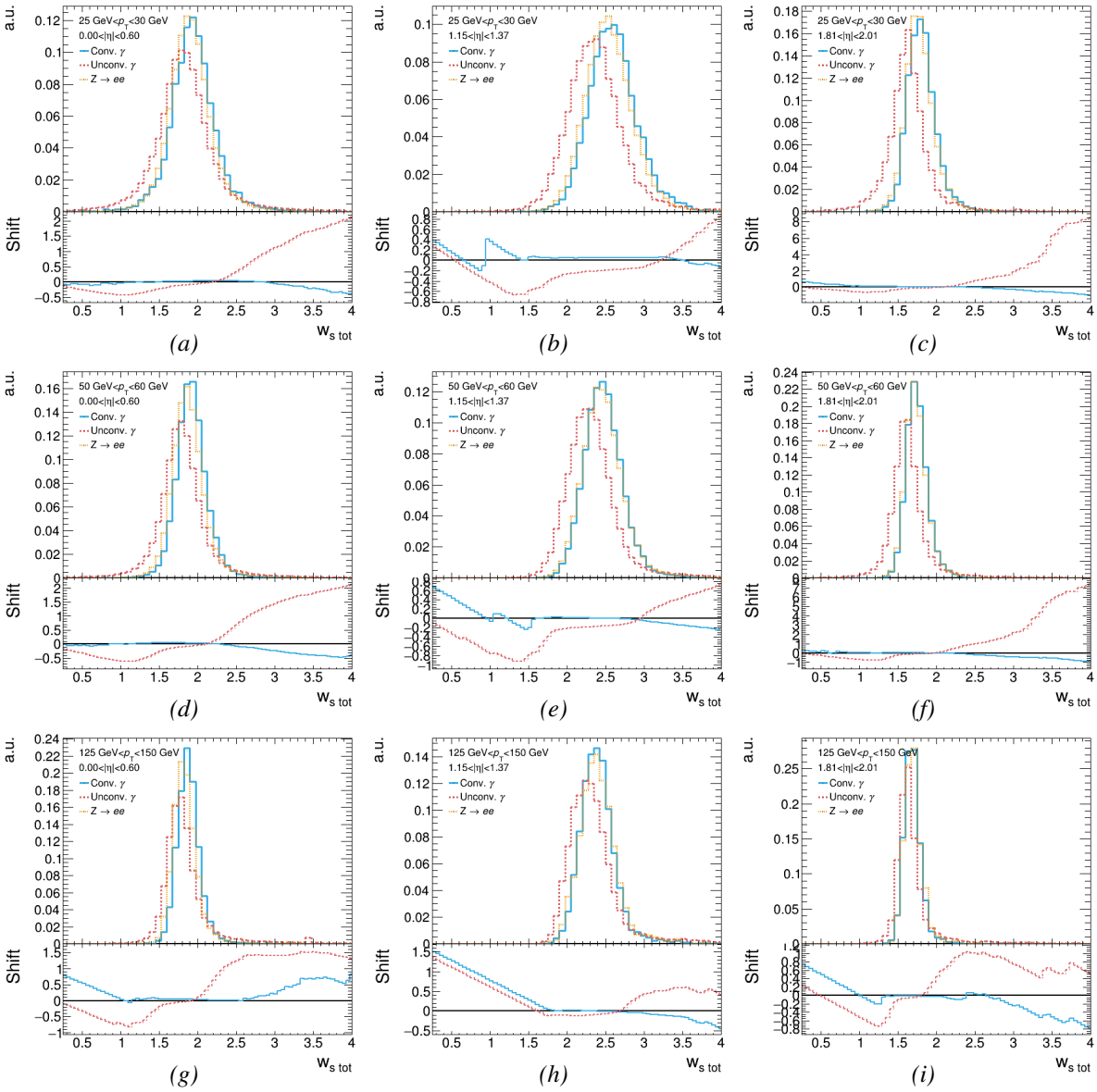

Figure C.1. | Distribution of the shower-shape variable $w_{s\,\mathrm{tot}}$ for different kinematic regions. The distributions are shown for electrons, converted and unconverted photons. In addition, the effective shift corresponding to the shower-shape variable transformations is shown, $x_{\mathrm{pseudo}-\gamma} - x_e$.

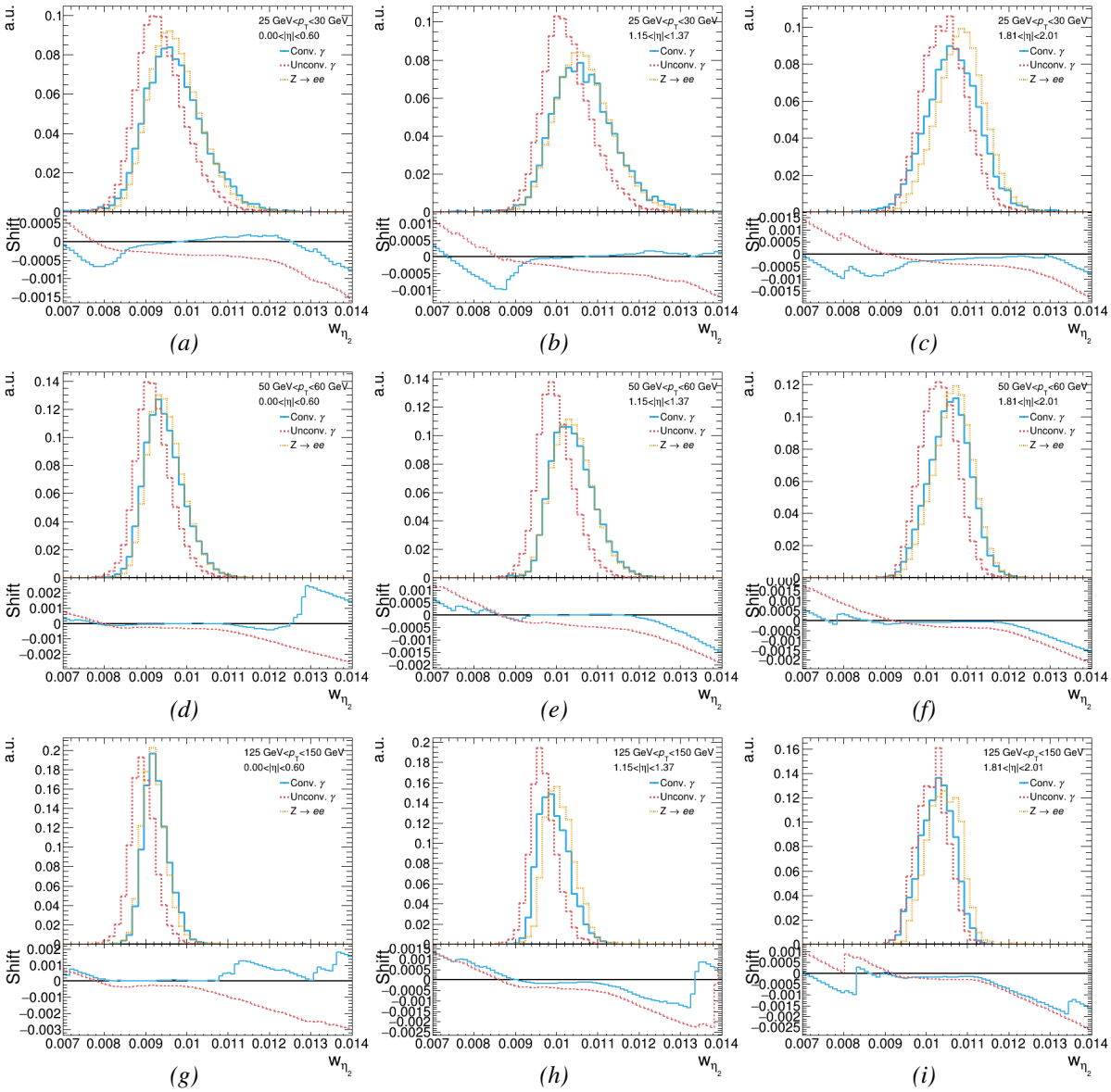

Figure C.2. | Distribution of the shower-shape variable w_{η_2} for different kinematic regions. The distributions are shown for electrons, converted and unconverted photons. In addition, the effective shift corresponding to the shower-shape variable transformations is shown, $x_{\text{pseudo}-\gamma} - x_e$.

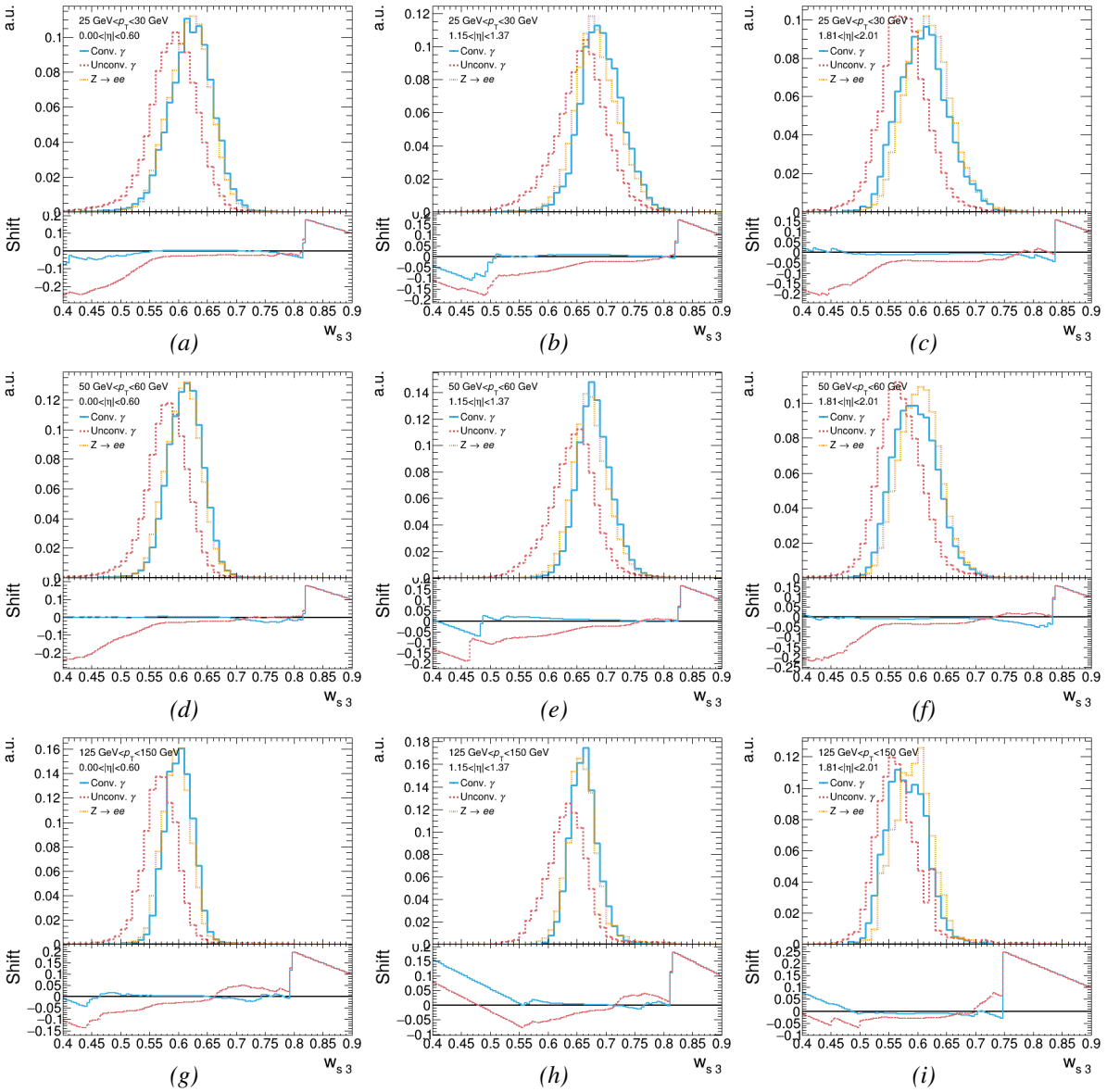

Figure C.3. | Distribution of the shower-shape variable w_{s3} for different kinematic regions. The distributions are shown for electrons, converted and unconverted photons. In addition, the effective shift corresponding to the shower-shape variable transformations is shown, $x_{\text{pseudo}-\gamma} - x_e$.

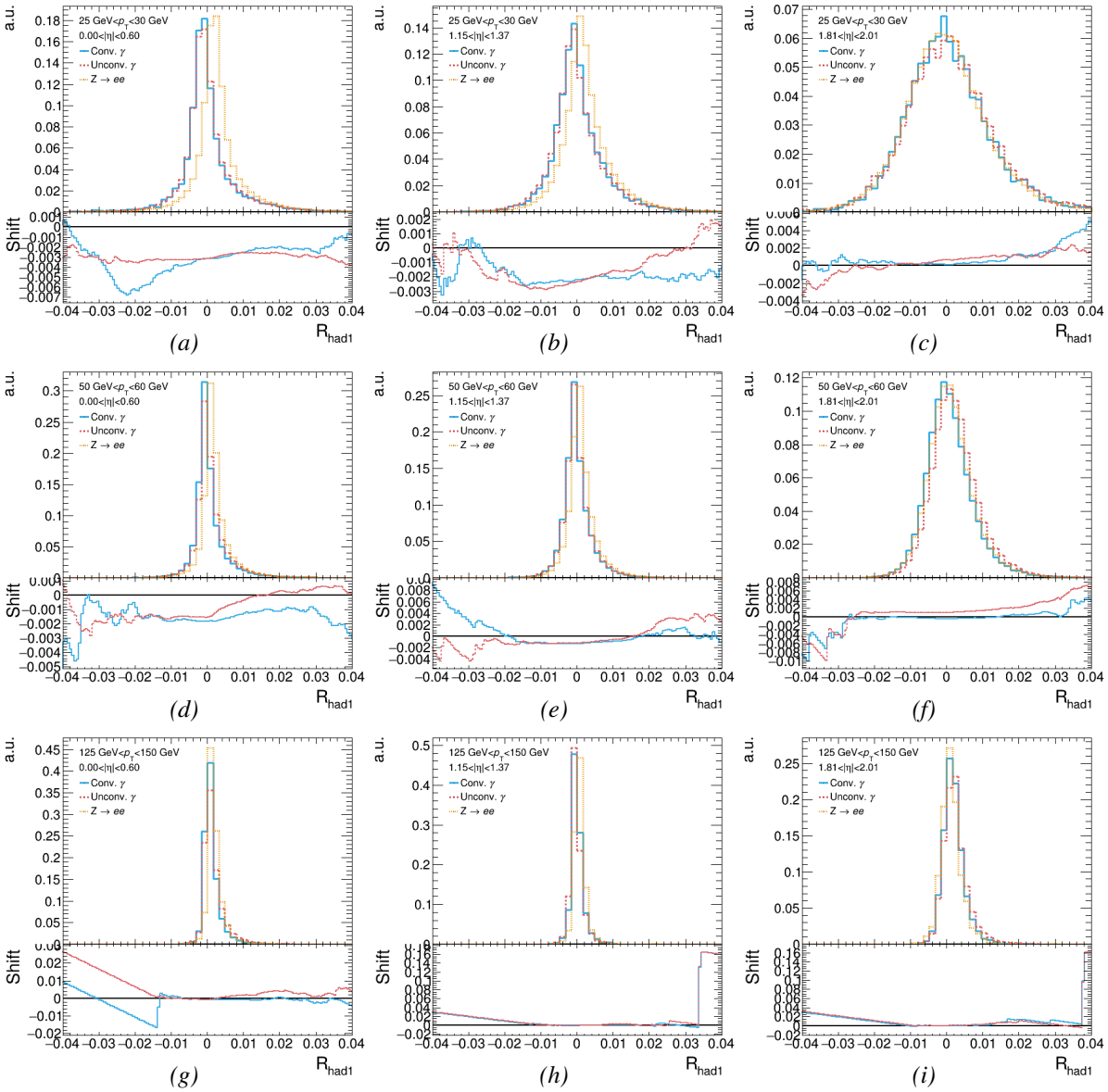

Figure C.4. | Distribution of the shower-shape variable R_{had1} for different kinematic regions. The distributions are shown for electrons, converted and unconverted photons. In addition, the effective shift corresponding to the shower-shape variable transformations is shown, $x_{\text{pseudo}-\gamma} - x_e$.

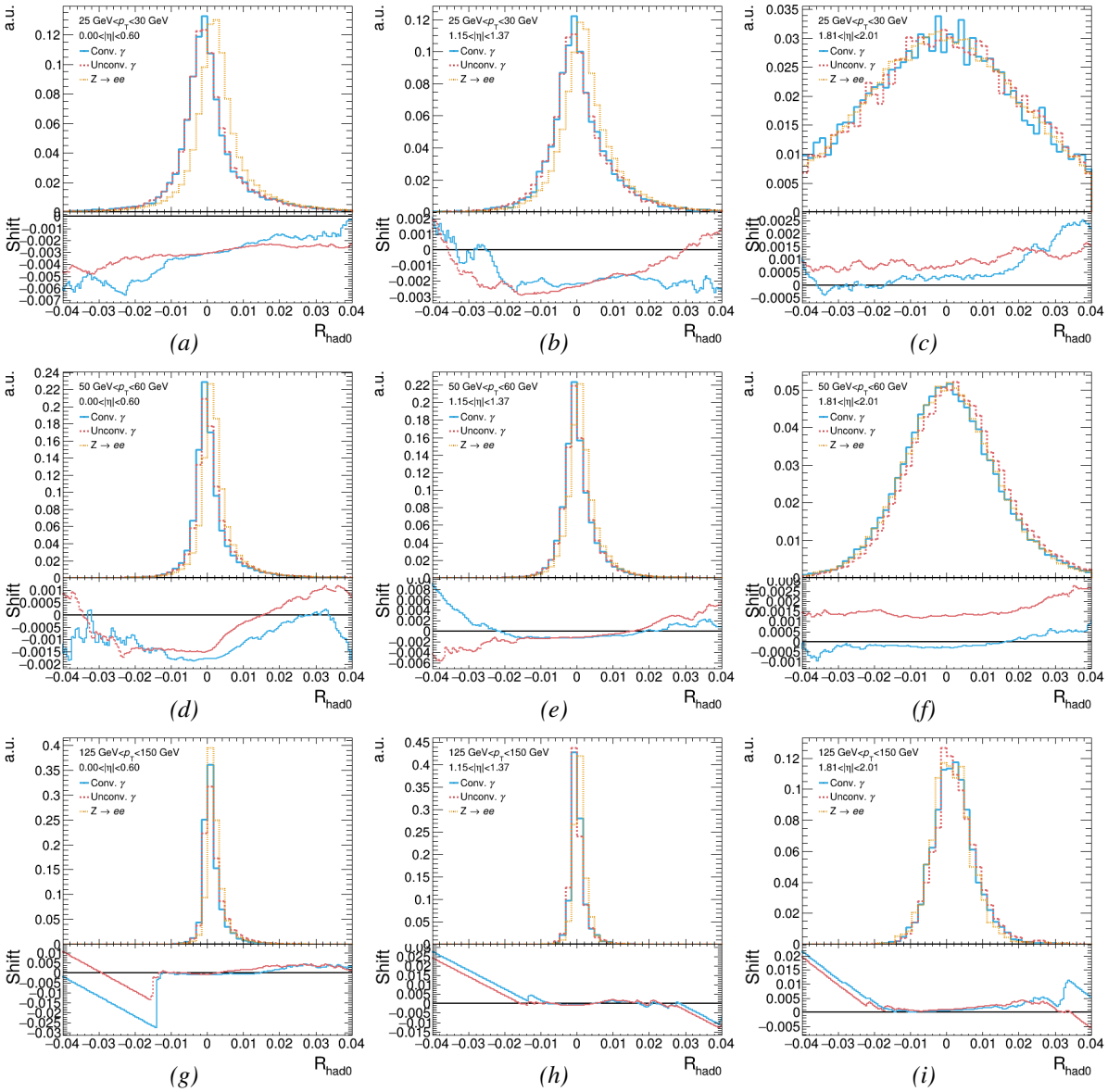

Figure C.5. | Distribution of the shower-shape variable R_{had} for different kinematic regions. The distributions are shown for electrons, converted and unconverted photons. In addition, the effective shift corresponding to the shower-shape variable transformations is shown, $x_{\text{pseudo}-\gamma} - x_e$.

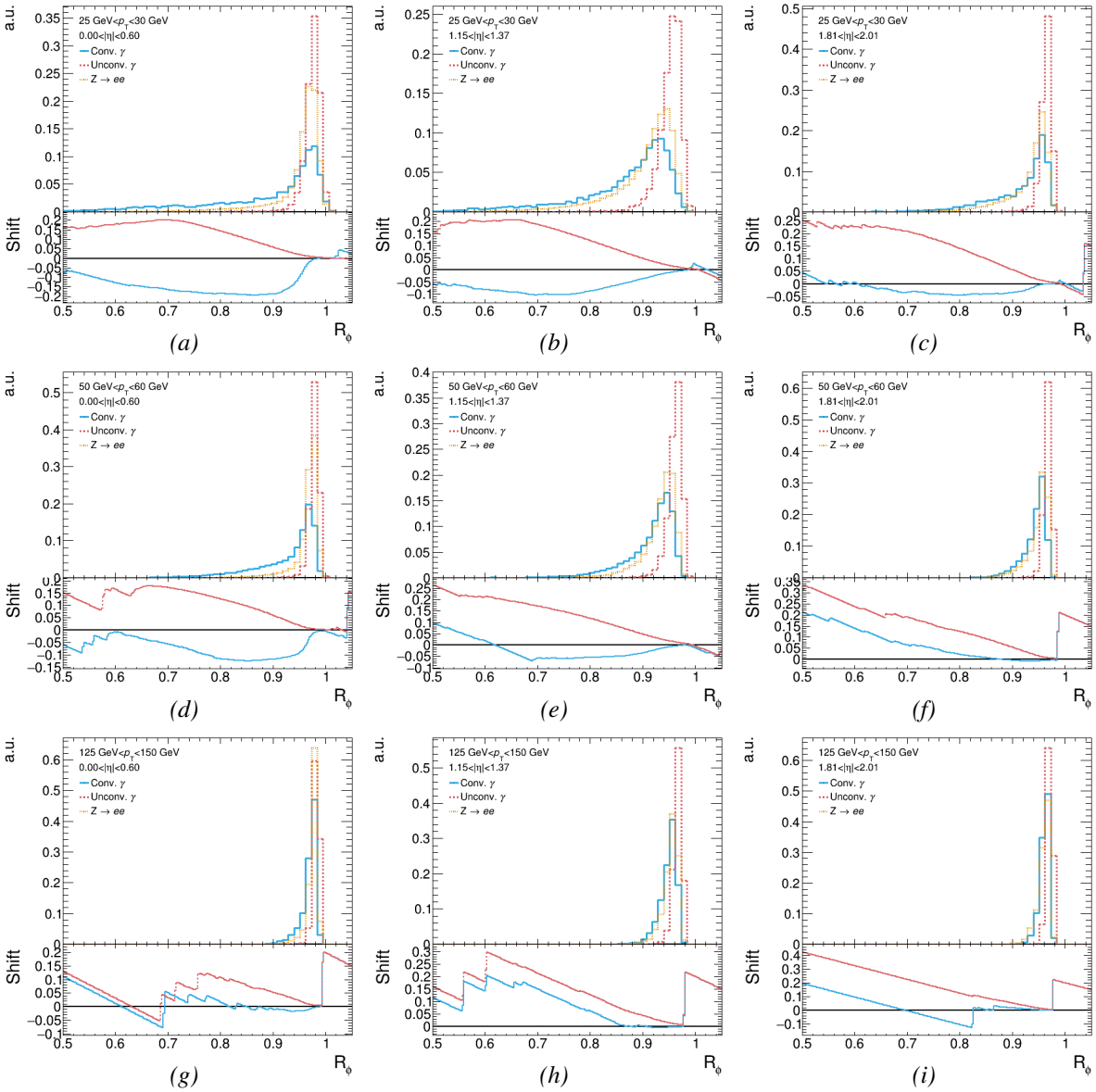

Figure C.6. | Distribution of the shower-shape variable R_ϕ for different kinematic regions. The distributions are shown for electrons, converted and unconverted photons. In addition, the effective shift corresponding to the shower-shape variable transformations is shown, $x_{\text{pseudo}-\gamma} - x_e$.

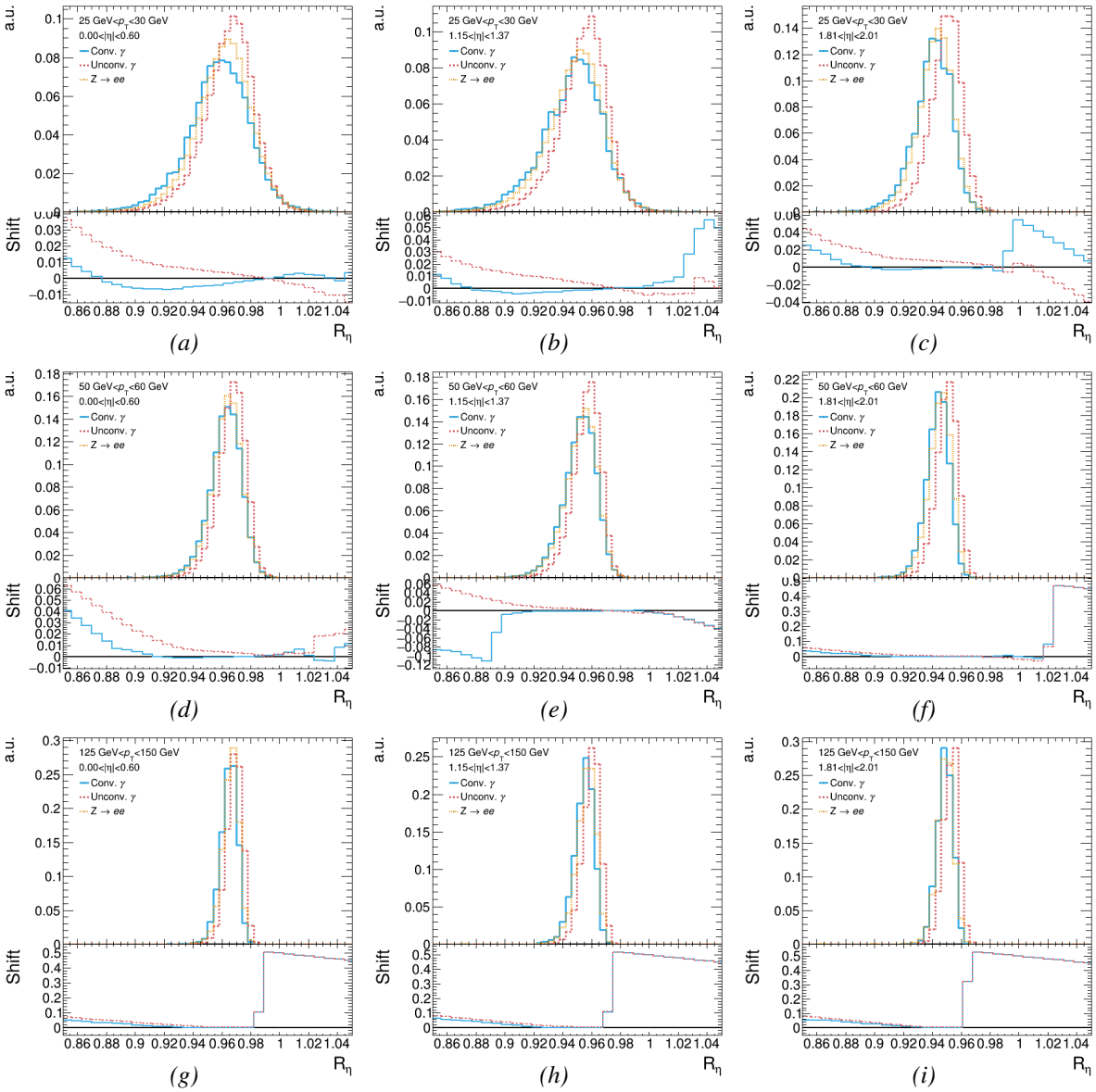

Figure C.7. | Distribution of the shower-shape variable R_η for different kinematic regions. The distributions are shown for electrons, converted and unconverted photons. In addition, the effective shift corresponding to the shower-shape variable transformations is shown, $x_{\text{pseudo}-\gamma} - x_e$.

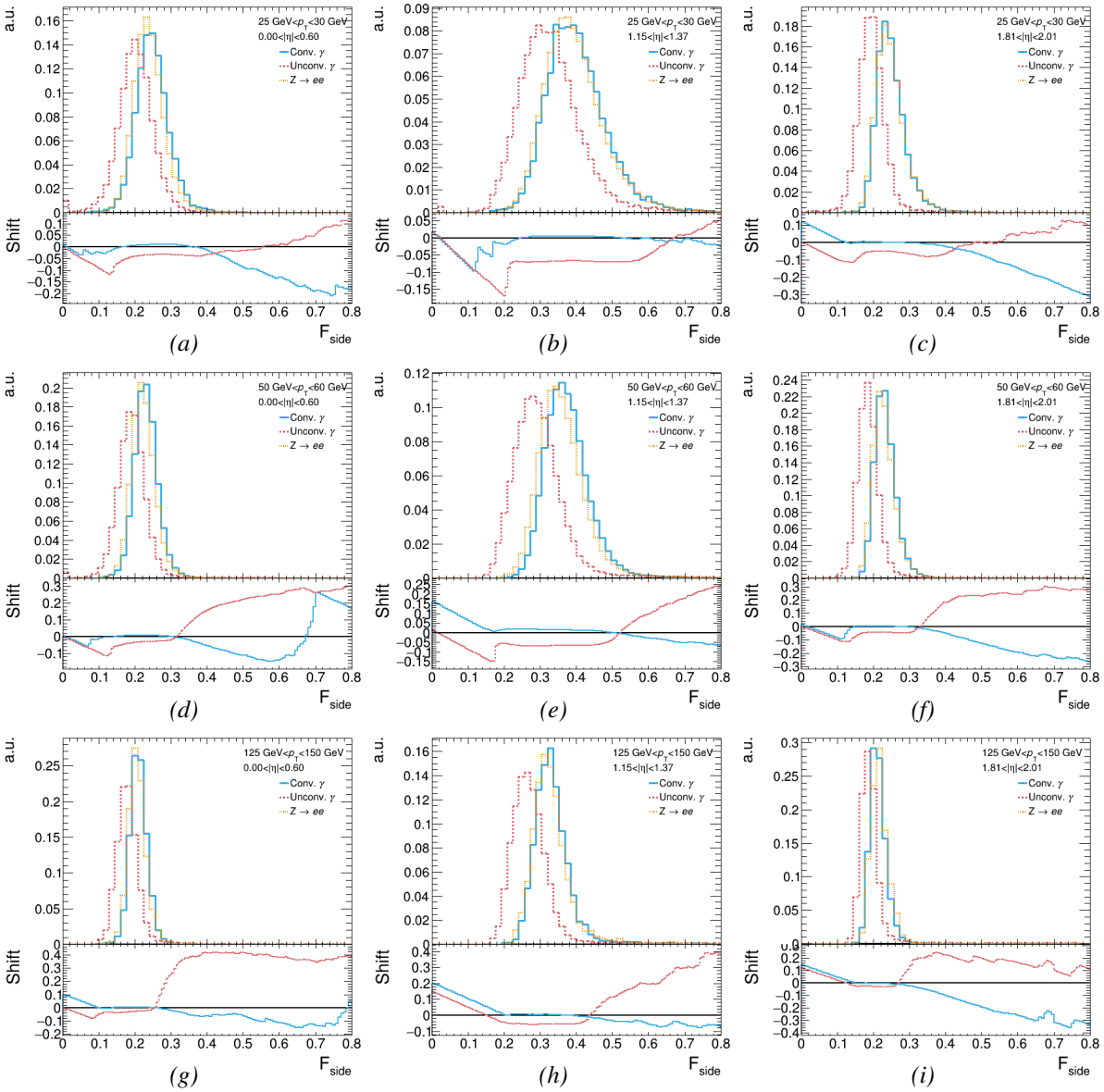

Figure C.8. | Distribution of the shower-shape variable F_{side} for different kinematic regions. The distributions are shown for electrons, converted and unconverted photons. In addition, the effective shift corresponding to the shower-shape variable transformations is shown, $x_{\text{pseudo}-\gamma} - x_e$.

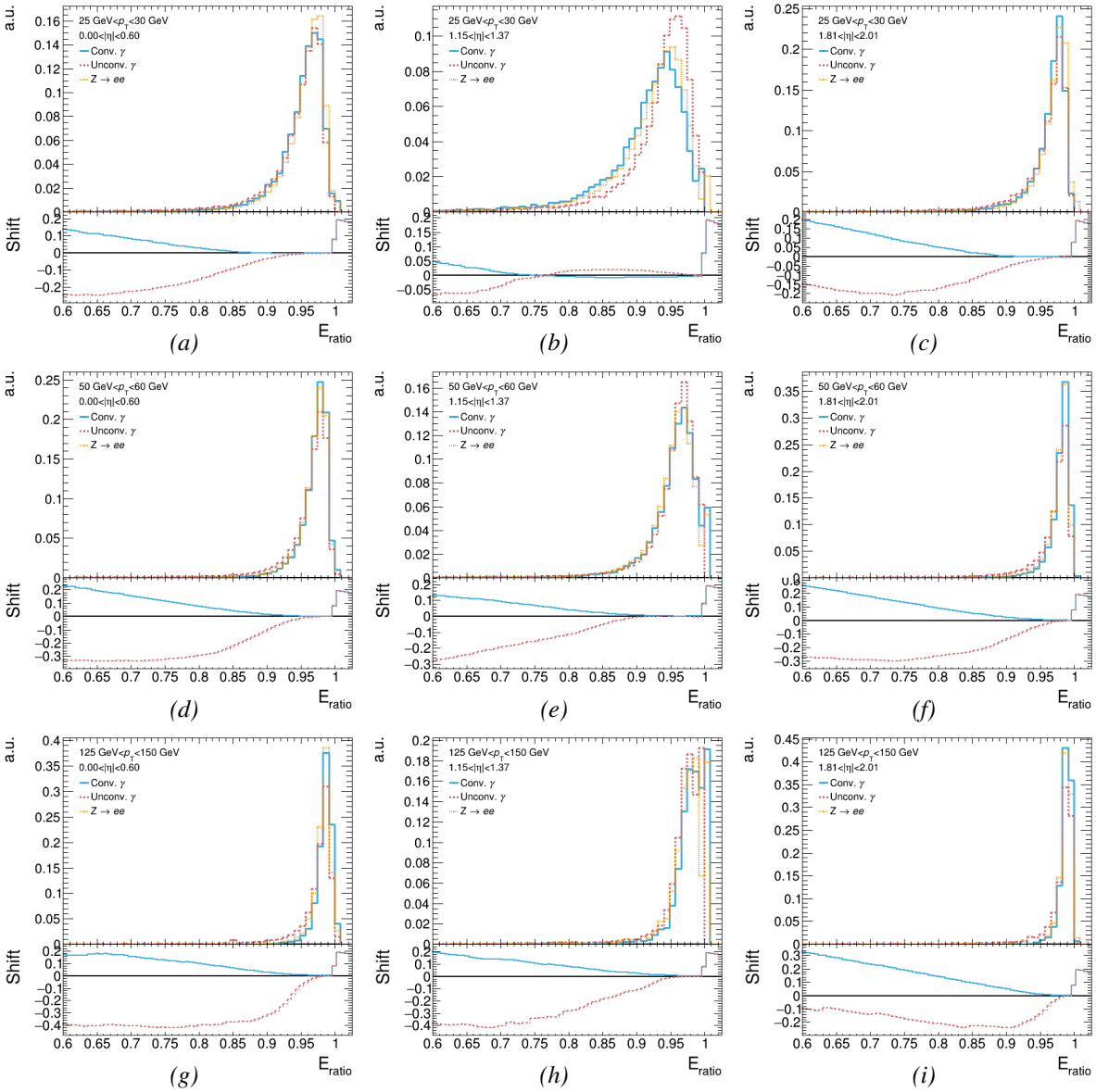

Figure C.9. | Distribution of the shower-shape variable E_{ratio} for different kinematic regions. The distributions are shown for electrons, converted and unconverted photons. In addition, the effective shift corresponding to the shower-shape variable transformations is shown, $x_{\text{pseudo}-\gamma} - x_e$.

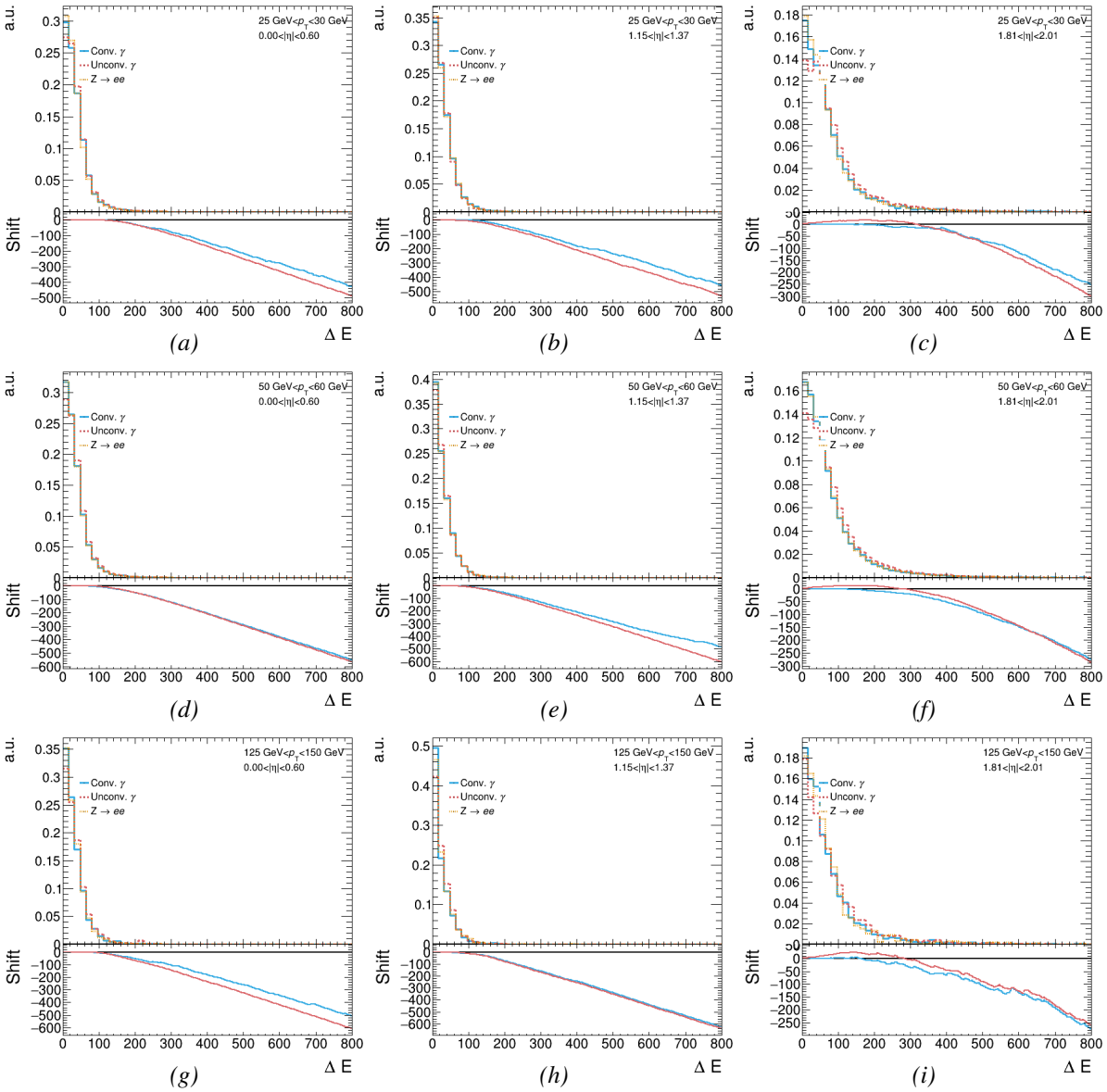

Figure C.10. | Distribution of the shower-shape variable ΔE_s for different kinematic regions. The distributions are shown for electrons, converted and unconverted photons. In addition, the effective shift corresponding to the shower-shape variable transformations is shown, $x_{\text{pseudo}-\gamma} - x_e$.

D. The p_{T}^{H} Distribution as a Function of κ_c and κ_b

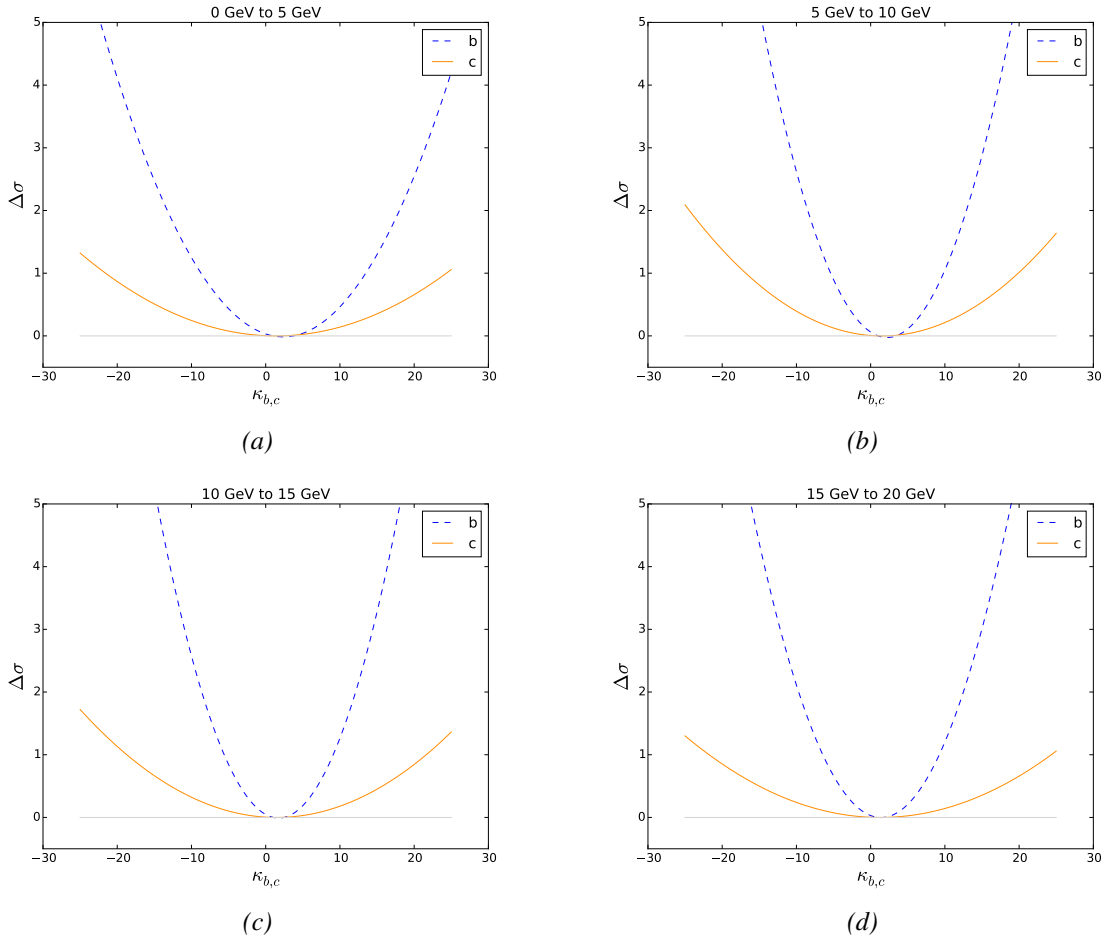

Figure D.1. | Difference of the predicted cross section to the SM cross section prediction for individual bins in p_{T}^{H} as a function of κ_b and κ_c.

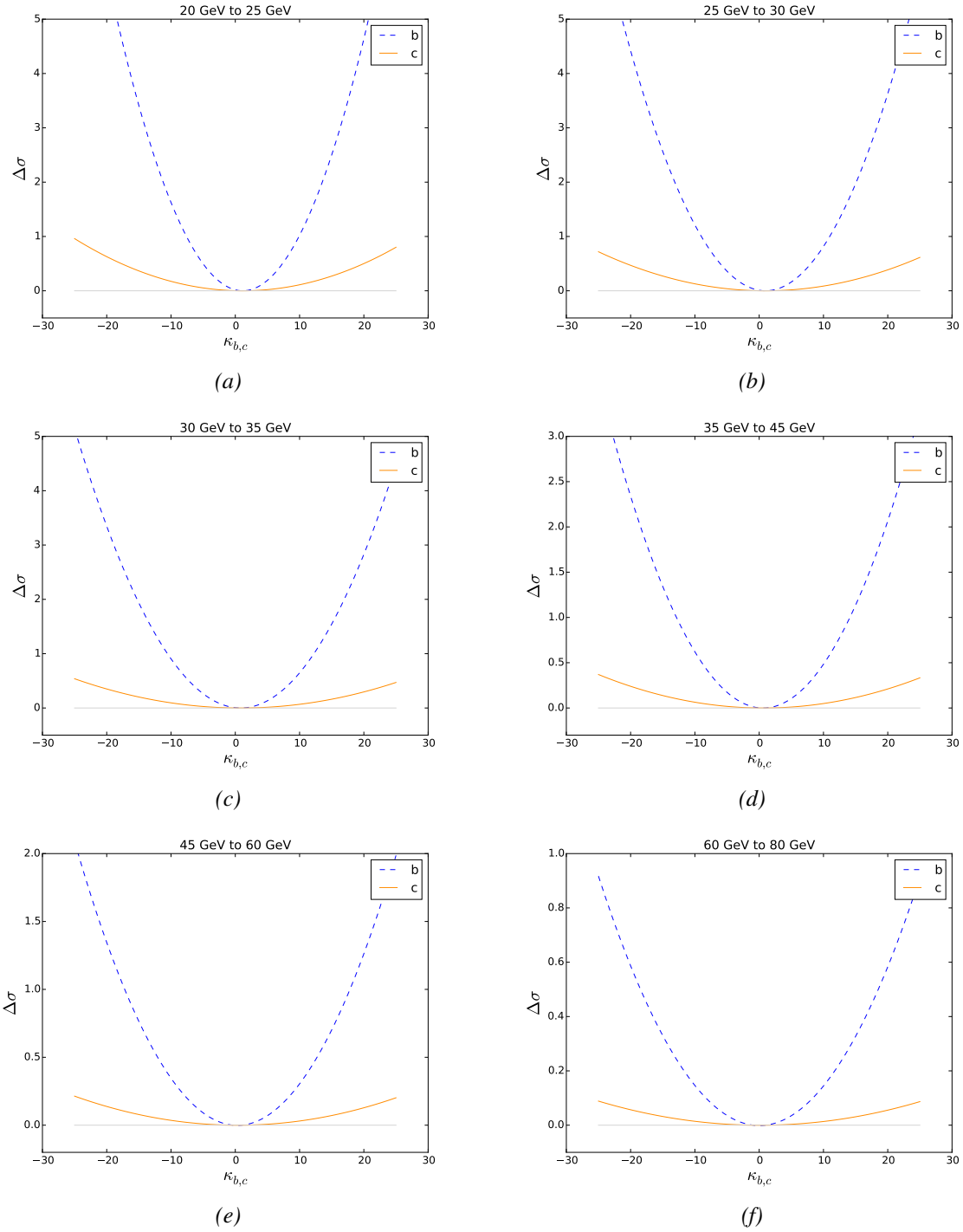

Figure D.2. | Difference of the predicted cross section to the SM cross section prediction for individual bins in p_{T}^{H} as a function of κ_b and κ_c.

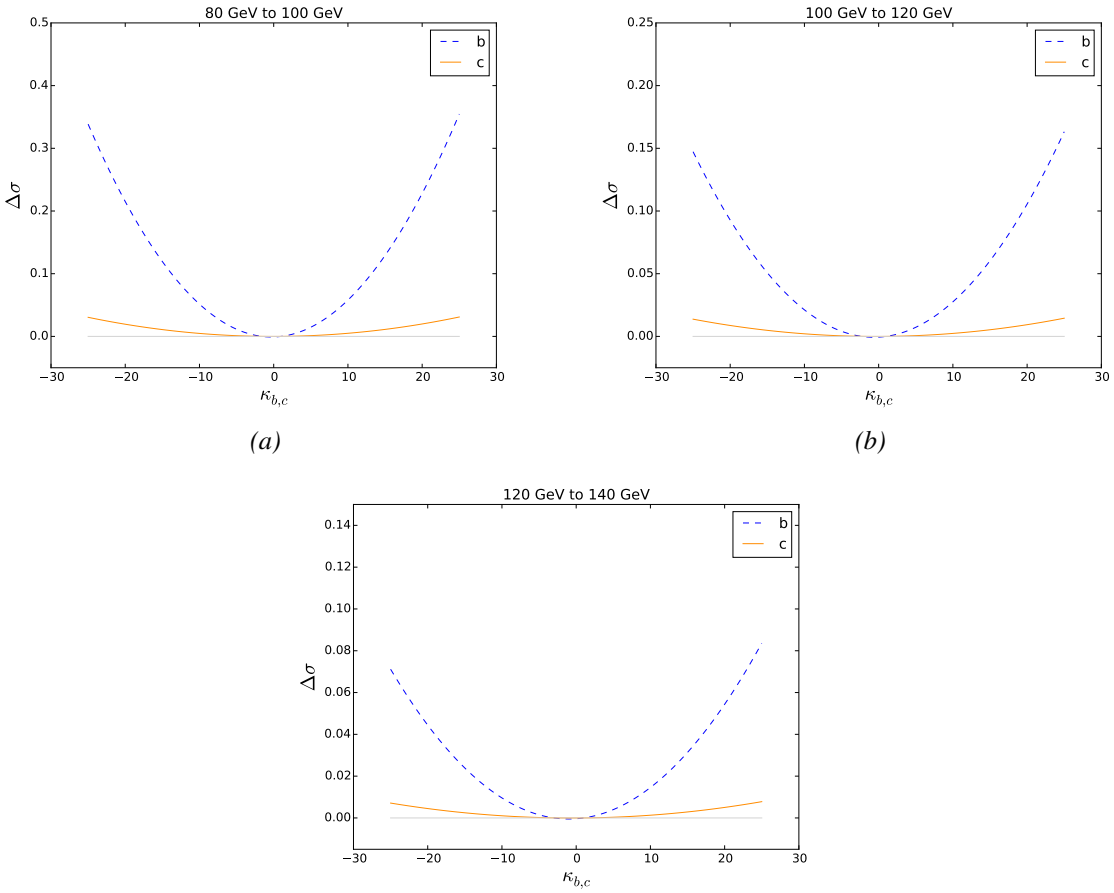

Figure D.3. | Difference of the predicted cross section to the SM cross section prediction for individual bins in p_{T}^{H} as a function of κ_b and κ_c.